Comprehensive characterization of laser-driven neutron sources and a pathway towards miniaturization

Umfassende Charakterisierung von lasergetriebenen Neutronenquellen und ein Weg zur Miniaturisierung

Zur Erlangung des Grades eines Doktors der Naturwissenschaften (Dr. rer. nat.)
Genehmigte Dissertation von Stefan Scheuren aus Bad Homburg v. d. Höhe
Tag der Einreichung: 15.07.2024, Tag der Prüfung: 14.10.2024

1. Gutachten: Prof. Dr. Markus Roth
2. Gutachten: Prof. Dr. Stephan Kuschel
Darmstadt, Technische Universität Darmstadt

TECHNISCHE UNIVERSITÄT DARMSTADT

Fachbereich Physik
Institute for Nuclear Physics
AG Markus Roth

Comprehensive characterization of laser-driven neutron sources and a pathway towards miniaturization
Umfassende Charakterisierung von lasergetriebenen Neutronenquellen und ein Weg zur Miniaturisierung

Accepted doctoral thesis by Stefan Scheuren

Date of submission: 15.07.2024
Date of thesis defense: 14.10.2024

Darmstadt, Technische Universität Darmstadt

Nur wenige wissen, wie viel man wissen muss, um zu wissen, wie wenig man weiß.
- Werner Heisenberg

Für meine Familie und Freunde

In Gedenken an Günter Scheuren
*13.09.1961 †16.07.2021

Erklärungen laut Promotionsordnung

§ 8 Abs. 1 lit. d PromO

Ich versichere hiermit, dass zu einem vorherigen Zeitpunkt noch keine Promotion versucht wurde. In diesem Fall sind nähere Angaben über Zeitpunkt, Hochschule, Dissertationsthema und Ergebnis dieses Versuchs mitzuteilen.

§ 9 Abs. 1 PromO

Ich versichere hiermit, dass die vorliegende Dissertation – abgesehen von den in ihr ausdrücklich genannten Hilfen – selbstständig verfasst wurde und dass die „Grundsätze zur Sicherung guter wissenschaftlicher Praxis an der Technischen Universität Darmstadt“ und die „Leitlinien zum Umgang mit digitalen Forschungsdaten an der TU Darmstadt“ in den jeweils aktuellen Versionen bei der Verfassung der Dissertation beachtet wurden.

§ 9 Abs. 2 PromO

Die Arbeit hat bisher noch nicht zu Prüfungszwecken gedient.

Darmstadt, 15.07.2024

S. Scheuren

Zusammenfassung

In den letzten zehn Jahren haben lasergetriebene Neutronenquellen (LDNS) als kompakte, kostengünstige Alternative zu etablierten Neutronenquellen großes Interesse geweckt. In dieser Zeit hat sich das Gebiet der laserbasierten Neutronenquellen von frühen Untersuchungen, die sich auf die Eigenschaften des erzeugten Neutronenfeldes konzentrierten, bis hin zu ersten Demonstrationen von Anwendungen weiterentwickelt. In dieser Arbeit wird eine umfassende Charakterisierung einer LDNS vorgestellt, die als Grundlage für künftige Experimente und den möglichen Bau einer laserbasierten Neutronenanlage dienen soll. Die Charakterisierung basiert auf eingehenden Monte-Carlo-Simulationen, die mit experimentellen Messungen verglichen und validiert werden. Die Monte-Carlo-Simulationen ermöglichen die Untersuchung der einzelnen Bestandteile der vermessenen Neutronenspektren an der Position der Detektoren. Außerdem werden der Beitrag der Neutronenstreuung und die Neutronenauflösungsfunktion für die verwendeten Detektoren bestimmt. Auf diese Weise konnte gezeigt werden, dass bis zu $25\,\%$ der Neutronen an der Detektorposition von außerhalb des Konverters stammen und dass bis zu $90\,\%$ der Neutronen durch Streuung beeinflusst werden.

In dieser Arbeit wurde auch die Machbarkeit der thermischen Neutronenresonanzabbildung an LDNS in einem Demonstrations-Experiment nachgewiesen. Während des Experiments wurde die energieabhängige Abschwächung einer Cadmium Probe gemessen, was die Bestimmung ihrer Position im Neutronenbild ermöglichte.

Es wird auch ein Konzept für den Betrieb hocheffizienter LDNS auf der Grundlage von laserbeschleunigten Elektronenstrahlen vorgestellt. Diese Quellen sind als kompakte LDNS im Labormaßstab sehr vielversprechend. Es konnte gezeigt werden, dass elektronenbasierte Quellen bei niedrigen Laserpulsenergien höhere Konversionseffizienzen bieten sollten als ionenbasierte Quellen.

Schließlich wurde eine neue Methode zur Analyse und Berechnung von Neutronenfluenzen auf Basis von Bubble Detektor Messungen entwickelt. Die Methode wurde zur Analyse der Messergebnisse der Characterisierungskampagne verwendet. Monte-Carlo-Simulation experimenteller Messungen weisen eine gute Übereinstimmung mit den aus Bubble Detektor Messung errechneten Neuronenfluenzen auf. Die mit der neuen Methode berechneten Neutronenfluenzen sind bis zu $55\,\%$ niedriger als Fluenzen die mit bisher etablierten Methode berechnet wurde.

Abstract

Over the past decade, laser-driven neutron sources (LDNS) have garnered much interest as a compact, cost-efficient alternative to established neutron sources. During this time, the field of laser-driven neutron sources has progressed from early investigations focusing on the characteristics of the generated neutron field to the first proof-of-principle demonstration of applications. This work presents a comprehensive characterization of a LDNS intended to be used as a blueprint for future experiments and the eventual design of a laser-based neutron facility. The characterization is based on in-depth Monte Carlo simulations that are compared and validated by experimental measurements. The Monte Carlo simulations allow for investigation into the constituents that make up the neutron fluence at the position of the detectors. Furthermore, the contribution of neutron scattering and the neutron resolution function for the detectors used during the experimental campaign are determined. In this way, it could be demonstrated that up to $25\,\%$ of the neutrons at the detector position originate outside the catcher and that up to $90\,\%$ of the neutrons are affected by scattering.

This thesis also demonstrated the viability of thermal neutron resonance imaging at LDNS in a proof-of-principle experiment. During the experiment, the energy-dependent attenuation of a Cd sample was measured, allowing for the determination of its position in the neutron image.

A concept for driving highly efficient LDNS based on laser-accelerated electron beams is also presented. These sources hold much promise as compact, laboratory-scale LDNS. It could be demonstrated that electron-based sources should perform much better than ion-based sources for low laser pulse energies.

Finally, a new method for analyzing and calculating neutron fluences from bubble detector measurements was developed. The method was used to analyze the data recorded during the characterization campaign, and the results from the Monte Carlo simulations showed good agreement. Compared to previously used methods, the neutron fluences calculated by the new method are up to $55\,\%$ lower than those calculated from previously used methods.

Contents

1. Introduction

Since James Chadwick discovered the neutron in 1932 (Chadwick 1932b), neutrons have assumed a vital role in many fields, from nuclear physics to material science to medicine and energy generation (Parise 2006; Rinaldi et al. 2009). The great interest in neutrons stems from their unique interaction characteristics with matter. Due to their lack of charge, the interaction of neutrons in matter is primarily governed by the strong nuclear force (Lamarsh, Baratta, et al. 2001; Stacey 2007). Thus, neutron interactions depend on the configuration of the nucleus of the material, making it distinctly different from the interaction of charged particles or photons with matter. As a result of these characteristics, neutrons are most strongly attenuated by low-Z materials, such as hydrogen, with the attenuation of high-Z materials significantly reduced in comparison. Due to their increased sensitivity to low-Z materials, neutrons are ideally suited for investigating organic matter enclosed in high-Z materials (IAEA 2008).

Furthermore, since neutrons are unaffected by the Coulomb field of the nucleus, they exhibit high penetration depth in most materials, giving them the unique possibility to investigate bulk samples that are otherwise inaccessible (IAEA 2008).

Despite their importance to many different areas of research, access to neutron beams is limited due to the required financial, personnel, and machine effort to provide usable, stable neutron beams. These beams, found at research reactors (Gläser 2002) and spallation-based sources (Lisowski and Schoenberg 2006), are large-scale, complex, and expensive facilities to build and run.

Within the past 10+ years, a consolidation towards fewer, large-scale neutron sources has been taking place in Europe, leading to an overall reduction in available beamtime and, thus, access to neutrons(Sciences and Group 2015). This consolidation is primarily driven by the phasing-out of many European research reactors (Sciences and Group 2015; 2019), with the planned replacement being the brightest neutron source in the world, the European Spallation Source (ESS) in Lund, Sweden (Garoby et al. 2017). This phasing-out of research reactors leads to centralization in the accessibility of neutron beams, which can limit progress within the neutron community. Furthermore, difficulties in accessing neutrons can also negatively impact the adoption of neutron techniques for industrial and other applications.

However, many neutron experiments do not require the highest achievable neutron fluxes to deliver meaningful results and would benefit from decentralizing access to neutron beams. Therefore, a growing trend is to build smaller, compact, application-specific accelerator-driven neutron sources, such as the High Brightness Source project in Jülich (Rücker et al. 2016). Within this line of thinking, laser-driven neutron sources (LDNS) have relatively recently emerged as promising contenders to convention accelerator-based compact neutron source concepts (Alvarez et al. 2014; Alejo, Ahmed, et al. 2015; Yogo, Arikawa, et al. 2023). The defining characteristics of LDNS are their compact size, comparatively low acquisition and operating costs, the short primary neutron pulse duration relevant to energy-resolved neutron detection, and their high instantaneous flux and flexibility.

Laser-driven neutron sources utilize high peak power, ultra-short pulse lasers to accelerate charged particles, which are directed into a suitable converter material to generate neutrons. The most commonly employed mode of operation is the so-called pitcher-catcher scheme, in which the charged particle source is

separate from the neutron generating source (Roth, D. Jung, et al. 2013).

Light ions, such as protons or deuterium, are accelerated from the pitcher and converted into neutrons inside the catcher using intense laser pulses. Much effort went into optimizing these sources, and peak fluences of 3×10^{11} neutrons per shot have been reported (Yogo, Lan, et al. 2023). Additionally, different neutron applications have been demonstrated at these sources recently (Zimmer, Scheuren, Kleinschmidt, et al. 2022; Yogo, Lan, et al. 2023).

Although the field of laser-driven neutron sources garnered much attention, decisively advancing the concept remains challenging since no laser system is dedicated to neutron production. The lack of a dedicated source significantly limits the impact and adaptation of LDNS since the experimental investigation is limited to user facilities, which prevents the optimization of existing concepts and setups.

A laser facility dedicated to generating neutron beams is needed for laser-driven neutron sources to unfold their full potential. Designing such a facility requires a deep understanding of the characteristics, challenges, and requirements of LDNS. The main goal of this thesis is to provide a basis for developing such a dedicated source by providing a comprehensive characterization of an LDNS. An experimental campaign at the $1\,\mathrm{PW}$ DRACO laser system (Ziegler, Albach, et al. 2021) at the Helmholtz-Zentrum Dresden-Rossendorf was conducted to achieve this goal. In-depth Monte Carlo simulations of the experimental setup are combined with experimental measurements to analyze and quantify the source performance and the individual contributions to the detector signals. Thereby highlighting the influence of secondary source terms, the shielding setup, and the experimental area on the source performance. The knowledge gained from the experimental campaign should be used to aid the design of a dedicated source.

An additional challenge addressed in this work is the scalability of LDNS with high repetition rates. A neutron generation concept based on laser wakefield accelerated (LWFA) electron beams is proposed to drive a compact, highly efficient neutron source. Due to the laser requirements of LWFA, these electron-based sources have the potential to miniaturize LDNS sources further to the laboratory scale. Such a source could directly counteract the centralization in the accessibility of neutron beams by providing a compact, cost-efficient alternative.

Lastly, in a proof-of-principle experiment conducted at the PHELIX laser system (Bagnoud et al. 2010), neutron resonance imaging could be demonstrated for the first time at an LDNS. For this demonstration, moderated neutron beams were used to resolve the position of a ^{113}Cd sample by looking at different energy regions around its resonance. Furthermore, energy-selective neutron imaging using fast neutrons could also be demonstrated at PHELIX.

Thesis Structure

This thesis is divided into seven chapters, with the first being the introduction in the section above. The second chapter briefly introduces the most relevant concepts necessary for understanding this work, including short pulse laser matter interaction, plasma physics, laser-based particle acceleration, neutron physics and Monte Carlo simulations.

Chapter 3 introduces methods that were developed and used throughout this thesis.

Chapter 4 discusses the characterization of a laser-driven neutron source setup used at DRACO. In this discussion the stability and reproducibility of the neutron generation is detailed. Afterwards, the influence and contribution of different particle species, that are associated with laser-particle acceleration, on the neutron performance and flux is discussed. This discussion is based on the comparison of experimental measurements, as well as Monte Carlo simulations. Finally, neutron scattering and its influence is investigated

using Monte Carlo simulations and recommendations are given regarding the design of experiments at LDNS.

Chapter 5 deals with the neutron imaging experiments conducted at the PHELIX laser system. These measurements are compared to a measurement conducted at a conventional neutron source. The comparison is conducted to evaluate the competitiveness of LDNS and to approximate require fluxes and repetition rates.

Chapter 6 uses Monte Carlo simulations to investigate the neutron performance of a concept for laboratory scale LDNS, which can offer a pathway towards further miniaturization. The concept is based on laser-accelerated electrons, to drive the neutron source. The chapter concludes with an outlook on a potential use-case of these sources, leveraging the specific characteristics of the electron-based approach. Furthermore, a method is proposed to further increase the achievable neutron flux.

Chapter 7 concludes this work by summarizing the main results.

2. Theoretical Foundations

This chapter establishes and discusses the theoretical background necessary to understand and describe laser-driven neutron sources. Herein, the most relevant concepts of plasma physics as well as the interaction of ultra-short laser pulses with matter will be introduced. Afterwards, the concept of laser particle acceleration is summarized, which is the foundation of laser-driven neutron sources. Finally, the unique properties and interaction characteristics of neutrons, as well as selected applications of neutron beams are discussed. The chapter concludes with a description of the state-of-the-art of laser-driven neutron sources.

2.1. Fundamentals of laser-matter interaction and plasma physics

The field of plasma physics studies the behavior of a special state of matter, the so-called plasma, in which the atoms are either partially or fully ionized, meaning the electrons are not bound to the atomic nucleus anymore. The defining characteristics of a plasma are its quasi-neutrality and its long-range collective behavior, which is meditated through electric and magnetic fields. The quasi-neutrality means that the plasma contains the same amount of positive and negative charges. While its natural occurrence on earth is very limited, it makes up more than $99\,\%$ of the visible universe and is therefore the most common state of matter (American Physical Society 2024).

A plasma can be generated through a variety of different mechanisms, for example, applying heat to a neutral gas or subjecting matter to strong electric fields. The generation process most relevant to this thesis is the application of strong electromagnetic fields to matter, which are supplied by ultra-short pulse, high intensity laser systems. High intensity laser pulses are capable of ionizing atoms, even if the energy of a single photon is not sufficient to elevate an electron from a bound to a free state. In this case, four different processes play a dominant role, ranging from lowest to highest required laser intensity: multi-photon ionization (MPI), above-threshold ionization, tunneling ionization and barrier suppression ionization.

When a laser beam is focused to intensities of around $10^{10}\,\mathrm{W/cm^2}$ the photon density becomes so high, that an electron can absorb multiple photons, leading to the transfer of an electron to an unbound state, effectively ionizing the atom. This process is the previously mentioned MPI. Further increasing the laser intensity to about $10^{13}\,\mathrm{W/cm^2}$ leads to the above-threshold ionization regime. The difference between this regime and MPI is that an electron absorbs more photons than is necessary for ionization. The difference in energy is carried away by the electron in the form of kinetic energy (Gibbon 2005).

Once the laser intensity reaches approximately $10^{14}\,\mathrm{W/cm^2}$ the laser field strength becomes comparable to the field strength of atoms. Thereby, the electric potential of the atom is modified, i.e. suppressed by the laser's electric field. The reduction in height of the Coulomb potential wall leads to an increase in tunneling probability. This process is known as tunnel ionization, as the electron can tunnel through the potential of the atom, resulting in an unbound electron. Further increasing the laser intensity to $10^{16}\,\mathrm{W/cm^2}$ and beyond leads to the complete suppression of the atomic potential and the electron is immediately transferred to an unbound state, leading to ionization of the atom. All four processes described above ultimately lead to the generation of plasma (Gibbon 2005). The freed electrons can now interact directly with the laser field.

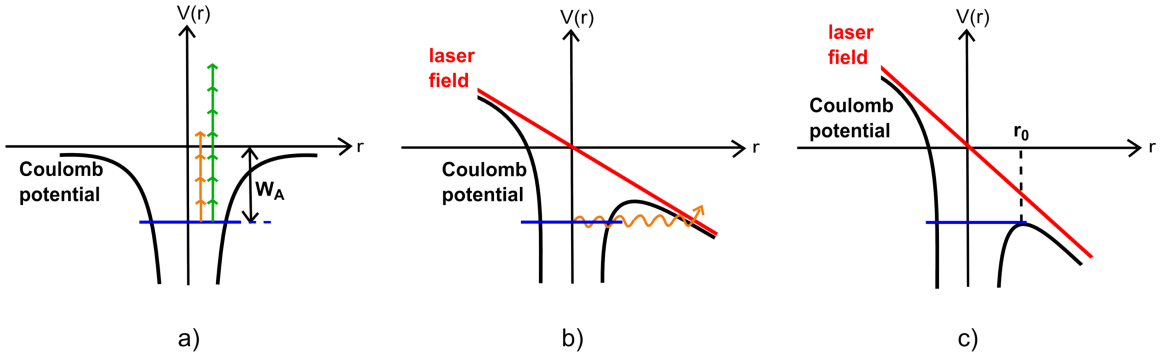

Figure 2.1.: Visual representation of different ionization processes. Multi-photon ionization, represented by the orange arrows, as well as above threshold ionization (green arrows) are displayed in a). W_A is the energy required to cause ionization. The colored arrows represent the energy of a single photon. In figure b) partial barrier suppression due to the laser field can be seen, which leads to a higher probability of tunnel ionization. For even higher intensities the laser field completely suppresses the atomic potential barrier and the electron is instantly freed, as depicted in c). Adapted from (Hoffmeister 2014).

2.1.1. Motion of charged particles in laser fields

To understand the interaction between plasmas and short laser pulses, it is helpful to understand the motion of a single charged particle within a laser light field. The interaction between the electromagnetic wave of the laser field and the charged particle can be described by the Lorentz force

$$\vec{F}_L = \frac{\mathrm{d}\vec{p}}{\mathrm{d}t} = m\ddot{\vec{r}} = q \cdot \left(\vec{E} + \vec{v} \times \vec{B}\right), \tag{2.1}$$

where $\vec{E}$ and $\vec{B}$ are the electric and magnetic field components of the electromagnetic wave, q is the particles charge, m its mass, $\ddot{\vec{r}}$ the second derivative of its position vector with respect to time and $\vec{v}$ its corresponding velocity. The electric- and magnetic fields of an electromagnetic wave are linked through the equation

$$\vec{B} = 1/\mathrm{c} \cdot \vec{k} \times \vec{E},$$

where $\vec{k}$ is the wave vector and c is the speed of light in vacuum. As a consequence of this equation, $\vec{B}$ is smaller than $\vec{E}$ by a factor of c and can be neglected in the non-relativistic case. Thus Equation 2.1 can be simplified to

$$m\ddot{\vec{r}} = q \cdot \vec{E}. \tag{2.2}$$

Assuming, for simplicity, a linearly polarized plane wave traveling along the z-axis, $\vec{E}$ and $\vec{B}$ are given by

$$\begin{aligned} \vec{E}\,(\vec{r},t) &= \vec{E}_0\,(\vec{r}) \cdot \sin\left(\omega_L t - kz\right) \\ \vec{B}\,(\vec{r},t) &= \vec{B}_0\,(\vec{r}) \cdot \sin\left(\omega_L t - kz\right), \end{aligned} \tag{2.3}$$

with the angular frequency $\omega_L = 2\pi \mathrm{c}/\lambda_L$ and λ_L the wavelength of the laser. Inserting Equation 2.3 for $\vec{E}$ in Equation 2.2 and integrating once yields the velocity $\vec{v}$ that is picked up by the charged particle as a result of the interaction with the laser pulse:

$$\frac{\mathrm{d}\vec{v}}{\mathrm{d}t} = \frac{q\vec{E}_0(\vec{r})}{m} \sin(\omega_L t - kz) \tag{2.4}$$

$$\begin{aligned} \longrightarrow \vec{v}(\vec{r},t) &= -\frac{q\vec{E}_0(\vec{r})}{m\omega_L} \cos(\omega_L t - kz) + \vec{v}_0 \\ &= \vec{v}_{\mathrm{osc}} \cos(\omega_L t - kz) + \vec{v}_0. \end{aligned} \tag{2.5}$$

Here $\vec{v}_0$ is the initial velocity of the particle before interacting with the electromagnetic wave. The velocity vector $\vec{v}_{\mathrm{osc}}$ is referred to as the quiver velocity of the charged particle. Notably, no net energy is transferred from the electromagnetic wave to the electron, as the electron returns to rest at its original position, once the electromagnetic wave has passed (Eliezer 2002; Gibbon 2005).

From this quiver velocity, an important parameter can be derived by dividing the maximum quiver velocity $|\vec{v}_{\mathrm{osc,max}}|$ by the speed of light c. This is the so-called normalized vector potential of the laser, denoted by a_0

$$a_0 := \frac{|\vec{v}_{\mathrm{osc,max}}|}{\mathrm{c}} = \frac{|-q\vec{E}_0|}{m\omega_L \mathrm{c}}. \tag{2.6}$$

In the case that the quiver velocity approaches the speed of light, $|\vec{v}_{\mathrm{osc,max}}| \to \mathrm{c}$, the normalized amplitude a_0 approaches 1. Therefore, $a_0 \gtrsim 1$ is called the relativistic threshold at which the relativistic effects need to be taken into account by substituting $\vec{p}_q = m\vec{v} \to \gamma(\vec{v}) m_0 \vec{v}$ in Equation 2.1. Strictly speaking, the momentum of the quiver motion becomes relativistic $p_{\mathrm{osc}}/(m_0\mathrm{c}) \gtrsim 1$ as the velocity cannot equal or exceed the speed of light (Gibbon 2005). The added subscript 0 denotes the rest mass of the particle. The oscillation momentum can be defined via

$$\begin{aligned} p_{\mathrm{osc}} = m|\vec{v}_{\mathrm{osc}}| &= \frac{|-q\vec{E}_0|}{\omega_L} \\ \longrightarrow a_0 &\propto p_{\mathrm{osc}} \propto |\vec{E}_0|. \end{aligned} \tag{2.7}$$

The factor $\gamma(\vec{v}) = 1/\sqrt{1-(\vec{v}/\mathrm{c})^2} = \sqrt{1+p^2/(m_0\mathrm{c})^2}$ is the relativistic Lorentz factor and m_0 is the rest mass of the charge carrying particle. Additionally, the effect of the magnetic field $\vec{B}$ can no longer be neglected and needs to be accounted for when calculating the particle trajectory (Gibbon 2005). The effects and consequences of this relativistic oscillation will become important in later sections with the introduction of the ponderomotive force and laser particle acceleration.

From Equation 2.6 the threshold electric fields and thus the laser intensities can be calculated for different particles. For example, using a laser that emits at a wavelength of $800\,\mathrm{nm}$, the relativistic intensity for electrons is greater than $2.1 \times 10^{18}\,\mathrm{W/cm^2}$, whereas $7.2 \times 10^{24}\,\mathrm{W/cm^2}$ are required for protons.

2.1.2. Plasma frequency and dispersion relation

Considering Equation 2.5 for an electron in the non-relativistic limit, where $a_0 \ll 1$ and assuming $\vec{v}_0 = 0$, it can be seen, that the particle gains velocity in the direction of the electric field of the electromagnetic wave. Integration in time yields the trajectory of the particle

$$\vec{r} = \frac{\mathrm{e}\vec{E}_0\left(\vec{r}\right)}{m\omega_L^2}\sin\left(\omega_L t - kz\right). \tag{2.8}$$

Equation 2.8 results in a displacement of the electron due to the varying electric field, with it returning to its original position once the wave has passed.

Applying such a displacement to the electrons inside a quasi-neutral plasma leads to charge separation. In the case of a plasma, the electrons are displaced first, as they have the lowest mass, and ions can be assumed stationary (F. F. Chen 2016). Due to the displacement and the resulting charge separation, the electrons experience a restoring force which can be approximated as

$$\mathrm{m_e}\ddot{\vec{r}} = -eE_{\mathrm{sep}} \tag{2.9}$$

$$= \frac{n_\mathrm{e}\mathrm{e}^2}{\epsilon_0}\vec{r}, \tag{2.10}$$

where E_{sep} is the electric field resulting from the charge separation, e is the electron charge, $\mathrm{m_e}$ the electron mass, n_e the electron density and ϵ_0 is the vacuum permittivity (Stroth 2011). This equation has the same form as the harmonic oscillator with its characteristic eigenfrequency

$$\omega_p = \sqrt{\frac{n_\mathrm{e}\mathrm{e}^2}{\epsilon_0 \mathrm{m_e}}}, \tag{2.11}$$

which is referred to as the plasma frequency. This is the maximum frequency with which the electrons inside the plasma can oscillate and therefore react to and follow an electromagnetic wave.

An alternative approach to derive the plasma frequency is to consider the polarization caused by the periodical displacement of the electrons. The polarization for a given electron density n_e can be expressed through (Demtröder 2019)

$$\vec{P} = -\mathrm{e}n_\mathrm{e}\vec{r}_\mathrm{e} \tag{2.12}$$

$$= -\frac{\mathrm{e}^2 n_\mathrm{e}}{\mathrm{m_e}\omega_L}\cdot\vec{E}\left(\vec{r},t\right).$$

From Maxwell's equations the wave equation for electromagnetic waves in vacuum and matter can be derived, which for the electric field takes the following form (Demtröder 2019)

$$\vec{\nabla}^2\vec{E} = \frac{1}{\mathrm{c}_0^2}\frac{\partial^2}{\partial t^2}\vec{E} + \frac{1}{\epsilon_0\mathrm{c}_0^2}\frac{\partial^2}{\partial t^2}\vec{P}. \tag{2.13}$$

Inserting Equation 2.12 into $\vec{P}$ in Equation 2.13 results in the full wave equation for the electric field of a laser propagating through a plasma

$$\vec{\nabla}^2\vec{E} - \frac{1}{\mathrm{c}_0^2}\left(1 - \frac{e^2 n_\mathrm{e}}{\epsilon_0 \mathrm{m_e}\omega_L^2}\right)\frac{\partial^2}{\partial t^2}\vec{E} = 0. \tag{2.14}$$

The term $\epsilon = 1 - \frac{e^2 n_\mathrm{e}}{\epsilon_0 \mathrm{m_e} \omega_L^2}$ in the equation above is referred to as the permittivity of the plasma. To propagate through the plasma ϵ needs to be larger than 0. If $\epsilon \leq 0$, the electromagnetic wave is damped and cannot propagate through the plasma. From this expression, a frequency that divides the regime of wave propagation from damping is obtained

$$\epsilon = 0 \longrightarrow \omega_p^2 = \frac{e^2 n_\mathrm{e}}{\epsilon_0 \mathrm{m_e}}.$$

This is the plasma frequency as defined above in Equation 2.11. To reiterate, the plasma frequency can be understood as a separation frequency that divides the region where an electromagnetic wave can pass through a plasma from where the wave is absorbed/reflected.

When inserting Equation 2.3 into Equation 2.14, the dispersion relation for an electromagnetic wave inside a (cold) plasma can be obtained

$$\omega_L^2 = \omega_p^2 + k_L^2 \mathrm{c}_0^2. \tag{2.15}$$

The dispersion relation enforces a minimum laser frequency ω_L to propagate into the plasma, which is given by ω_p. k_L becomes imaginary in the case of $\omega_L < \omega_p$, resulting in the absorption and reflection of the wave. The wave can propagate inside the plasma only in the case of $\omega_L > \omega_p$. The dispersion relation defines the refractive index of a plasma, which can be expressed as

$$n = \sqrt{\epsilon} = \sqrt{1 - \omega_p^2 / \omega_L^2}. \tag{2.16}$$

Notably, the index of refraction is always smaller than unity for waves capable of propagating through the plasma. It is also readily apparent that when the laser frequency is lower than the plasma frequency, the index of refraction becomes imaginary, resulting in an exponential dampening of the electromagnetic wave inside the plasma.

From the plasma frequency and dispersion relation, another important quantity can be defined, the so-called critical plasma density n_cr. A plasma density that results in $\omega_p = \omega_L$ is said to be critical because the electro-magnetic wave cannot propagate past this density; it acts as a reflective boundary

$$n_\mathrm{cr} = \frac{\epsilon_0 \mathrm{m_e} \omega_L^2}{\mathrm{e}^2}. \tag{2.17}$$

Plasmas with $n_\mathrm{e} > n_\mathrm{cr}$ are considered over-dense, making them opaque to the incoming electromagnetic wave. In contrast, a plasma is referred to as being under-dense in the case of $n_\mathrm{e} < n_\mathrm{cr}$, allowing for propagation inside the plasma. For a wavelength of $800\,\mathrm{nm}$ the critical density is $n_\mathrm{cr} \approx 1.7 \times 10^{21}\,1/\mathrm{cm}^3$.

So far, the solutions derived above have been obtained for slowly varying, plane electromagnetic waves. However, relevant to this work are ultra-short laser pulses with a finite pulse duration of $< 1\,\mathrm{ps}$, which are tightly focused to spot sizes of several micrometers. The tight focusing introduces strong radial intensity gradients, altering the motion of charged particles inside the electric field. At the same time, ultra-short laser pulses are highly dispersive (Gibbon 2005). These characteristics of short laser pulses give rise to the ponderomotive force, which will be discussed in the next section.

2.1.3. Finite pulse duration and the ponderomotive force

The influence of the finite laser pulse duration can be accounted for by multiplying a temporal envelope function $f(t)$ to the electric field of Equation 2.3, therefore taking the form

$$\vec{E}(\vec{r},t) = \vec{E}_0(\vec{r})\, f(t) \cdot \sin(\omega_L t - kz). \tag{2.18}$$

If $f(t)$ varies slowly compared to electromagnetic wave oscillation, i.e. $\mathrm{d}f/\mathrm{d}t \ll \omega_L f$, then $\vec{E}_0(\vec{r})$ in Equation 2.5 and 2.8 can be substituted for $\vec{E}_0(\vec{r})\, f(t)$. The resulting electron motion exhibits the same characteristics as before, first the electron returns to rest after the laser pulse has passed, but the electron is displaced along the direction of the electric field while conserving the transversal momentum, as described by Equation 2.7 (Gibbon 2005).

The effects of tight focusing and the resulting strong radial intensity gradients cannot be handled in such a straightforward way. When introducing radial gradients in the intensity and consequently also in the electric field, charged particles experience different accelerations, according to Equation 2.4, depending on their distance from the center of the laser pulse. Particles that move away from the beam center in the first half of the cycle experience a lower electric field at this new position, leading to a reduced acceleration in the second half of the electric field cycle. Expanding the electric field in a Taylor series and subsequently averaging over one electric field cycle returns the ponderomotive force (Lamb and Morales 1983; Bauer et al. 1995)

$$F_p = -\frac{q^2}{4 m_q \omega_L^2} \frac{\partial \vec{E}_0^2(\vec{r})}{\partial \vec{r}}. \tag{2.19}$$

This force pushes charged particles away from regions of high intensity (electric field strength) towards lower-intensity regions. The fully relativistic expression of the ponderomotive force has been derived by (Bauer et al. 1995) and (Startsev and McKinstrie 1997)

$$\vec{F}_p = -\frac{c_0^2}{\gamma}\left(\vec{\nabla} m_{\text{eff}} + \frac{\gamma - 1}{\vec{v}_q^2}\left(\vec{v}_q \cdot \vec{\nabla} m_{\text{eff}}\right)\vec{v}_q\right), \tag{2.20}$$

here m_{eff} denotes the relativistic mass. The important result from Equation 2.20 is the conversion of oscillatory energy into directed energy, as particles pick up an additional velocity component along the laser propagation direction. The particles are thus accelerated at an ejection angle θ, which is given by $\cos(\theta) = \sqrt{(\gamma - 1)/(\gamma + 1)}$ (Bauer et al. 1995; Gibbon 2005). The transferred energy from the laser field to the electron can be considered a heating of the electrons, resulting in a distribution of so-called hot or energetic electrons (Roth and Schollmeier 2017).

The above introduced concepts play an important role in laser-based particle acceleration, especially in the case of laser ion acceleration. Laser particle acceleration will be discussed in more detail in chapter 2.2. To understand the acceleration of electrons in a laser-plasma accelerator, it is helpful to take a closer look at non-linear wave propagation in plasma. The following section will go into more detail on plasma waves, their wakefields and wavebreaking.

2.1.4. Non-linear plasma waves and wavebreaking

In this section, defining characteristics of non-linear plasma waves will be discussed. The original derivation of the equations can be found in (Akhiezer and Polovin 1956), the corresponding generic solutions are found in (Decoster 1978) and the solution to longitudinal plasma oscillations originates from (Noble 1985). However, the derivation presented in this section follows Gibbon's approach (Gibbon 2005).

Here, the properties of cold non-linear plasma waves will be derived and the correction for thermal plasmas will be introduced, but not derived. For rigorous derivations of the equations of motion for relativistic thermal plasmas, the reader is referred to (Coffey 1971; Katsouleas and W. Mori 1988). Finally, the Lorentz force and Maxwell-fluid equations in their cgs formulation will be used for the description of the plasma:

$$\frac{\partial \vec{p}}{\partial t} + \left(\vec{v}\cdot\vec{\nabla}\right)\vec{p} = -\mathrm{e}\left(\vec{E} + \frac{1}{\mathrm{c}}\vec{v}\times\vec{B}\right), \tag{2.21}$$

$$\vec{\nabla}\cdot\vec{E} = 4\pi\mathrm{e}\left(n_0 - n_\mathrm{e}\right), \tag{2.22}$$

$$\vec{\nabla}\times\vec{E} = -\frac{1}{\mathrm{c}}\frac{\partial\vec{B}}{\partial t}, \tag{2.23}$$

$$\vec{\nabla}\times\vec{B} = -\frac{4\pi}{\mathrm{c}}\mathrm{e}n_\mathrm{e}\vec{v} + \frac{1}{\mathrm{c}}\frac{\partial\vec{E}}{\partial t}, \tag{2.24}$$

$$\vec{\nabla}\cdot\vec{B} = 0, \tag{2.25}$$

with $\vec{p} = \gamma m\vec{v}$ the relativistic momentum, γ the relativistic factor, as defined above, and n_0 the ion (charge) density. Introducing $\tau = t - \vec{e}_i\cdot\vec{r}/v_p$, with $v_p = \omega_p/k_p$ and $\vec{e}_i$ the unit vector in the direction of wave propagation allows solutions to take the form $f(\tau)$ (Gibbon 2005). Due to the time shift, the derivatives need to be adjusted accordingly: $\frac{\partial}{\partial t} \to \partial_\tau := \frac{\partial}{\partial\tau}$; $\vec{\nabla}\cdot \to -\frac{\vec{e}_i}{v_p}\partial_\tau\cdot$ and $\vec{\nabla}\times \to -\frac{\vec{e}_i}{v_p}\partial_\tau\times$. Substituting the derivatives in Equation 2.21 - 2.25 and integrating Equation 2.23 once with respect to τ yields the following equations:

$$\left(\frac{\vec{e}_i\cdot\vec{v}}{v_p} - 1\right)\frac{\mathrm{d}\vec{p}}{\mathrm{d}\tau} = \mathrm{e}\left(\vec{E} + \frac{1}{\mathrm{c}}\vec{v}\times\vec{B}\right), \tag{2.26}$$

$$-\vec{e}_i\cdot\frac{\mathrm{d}\vec{E}}{\mathrm{d}\tau} = 4\pi\mathrm{e}v_p\left(n_0 - n_\mathrm{e}\right), \tag{2.27}$$

$$\vec{B} = \frac{\mathrm{c}}{v_p}\vec{e}_i\times\vec{E}, \tag{2.28}$$

$$-\vec{e}_i\times\frac{\mathrm{d}\vec{B}}{\mathrm{d}\tau} = -\frac{4\pi}{\mathrm{c}}\mathrm{e}v_p n_\mathrm{e}\vec{v} + \frac{v_p}{\mathrm{c}}\frac{\mathrm{d}\vec{E}}{\mathrm{d}\tau}, \tag{2.29}$$

$$\vec{e}_i\cdot\frac{\mathrm{d}\vec{B}}{\mathrm{d}\tau} = 0. \tag{2.30}$$

One interesting aspect of (plasma) waves is the behavior of the electron density n_e. Taking the dot product of Equation 2.29 with the waves' propagation vector $\vec{e}_i$ and inserting Equation 2.27 for the electric fields, returns a relation for the electron density in dependence on the plasma phase and fluid velocity

$$n_\mathrm{e} = \frac{v_p n_0}{v_p - \vec{e}_i\cdot\vec{v}} = \frac{\beta_p n_0}{\beta_p - \vec{e}_i\cdot\vec{u}}. \tag{2.31}$$

Here $\beta_p = v_p/\mathrm{c}$ and $\vec{u} = \vec{v}/\mathrm{c}$. Equation 2.31 reveals an important feature of plasma waves, namely the electron density becomes very large (infinite) when the fluid velocity of the plasma approaches (equals) the phase velocity. To obtain a set of coupled equations for the longitudinal and transverse fields of the plasma wave, $\vec{e}_i\times$ is first applied to Equation 2.26 which returns an explicit expression for $\vec{B}$ depending on $\mathrm{d}\vec{p}/\,\mathrm{d}\tau$. Likewise, by applying $\vec{e}_i\times$ to Equation 2.29 and inserting Equation 2.28 yields an expression for $\mathrm{d}\vec{B}/\,\mathrm{d}\tau$. Subtracting the two resulting equations leaves the transverse plasma wave equation

$$\vec{e}_i \times \frac{\mathrm{d}^2\vec{p}}{\mathrm{d}\tau^2} + \frac{\omega_p^2\beta_p^2}{\beta_p^2 - 1}\frac{\beta_p}{\beta_p - \vec{e}_i\cdot\vec{u}} = 0 \tag{2.32}$$

with $\omega_p^2 = 4\pi\mathrm{e}^2 n_0/\mathrm{m_e}$. Note the normalization to $\mathrm{cm_e}$, leading to $\vec{p} = \gamma\vec{u}$. In a similar manner an expression for the longitudinal component can be found. Starting by taking $\vec{e}_i\cdot$ of Equation 2.26 and differentiating in τ, then using the expression for $\vec{B}$ (Equation 2.28), obtained during the derivation of the transversal wave equation can again be used to eliminate $\vec{B}$. Inserting Equation 2.31 yields the resulting differential equation for the longitudinal component. For a detailed derivation see (Gibbon 2005). Assuming the wave travels along the z-axis ($\vec{e}_i = \vec{e}_z$), the following equation is obtained for the longitudinal wave component:

$$\frac{\mathrm{d}}{\mathrm{d}\tau}\left((u_z - \beta_p)\frac{\mathrm{d}p_z}{\mathrm{d}\tau} + u_x\frac{\mathrm{d}p_x}{\mathrm{d}\tau} + u_y\frac{\mathrm{d}p_y}{\mathrm{d}\tau}\right) = \frac{\omega_p^2\beta_p^2 u_z}{\beta_p - u_z} \tag{2.33}$$

The electric field, its potential and the magnetic field can be found after solving for $\vec{p}$ in Equation 2.33. In this equation the term $\mathrm{d}/\,\mathrm{d}\tau(u_i\,\mathrm{d}p_i/\,\mathrm{d}\tau)$ with $i \in [x, y]$ can be understood as a pump term, driving a plasma wave. Details of the derivation can be found in (Gibbon 2005). Equation 2.33 will play a central role when wakefield generation by a laser pulse is introduced in the next section. In the context of particle acceleration, the longitudinal electric field component is one of the important quantities and was derived by (Noble 1985)

$$\vec{E}(\tau) = \pm\sqrt{2}\frac{\omega_p \mathrm{c_0 m_e}}{\mathrm{e}}\left(\gamma_{\mathrm{max}} - \gamma(\tau)\right)^{1/2}. \tag{2.34}$$

The γ factors are defined as before, but $\vec{u} \to \vec{u}(\tau)$ and γ_{max} is the relativistic factor of the maximum supported oscillation velocity $(v/\mathrm{c_0})_{\mathrm{max}} = u_{\mathrm{max}}$ (Gibbon 2005). From Equation 2.31 and 2.34 the characteristic sawtooth electric field and spiked electron density can be obtained, similar to what is displayed in Figure 2.2. These characteristics will play a central role in section 2.2.1.

To properly utilize the acceleration of particles in such a plasma wave, it is essential to know the maximum longitudinal electric field strength that can be supported, before the wave starts to break down. The break down of a plasma wave is typically referred to as wavebreaking and can be thought of as the wave "tumbling" over itself. This usually occurs when part of the wave starts to outrun the phase velocity of the wave, i.e. $u_{\mathrm{max}} \geq u_p$, leading to part of the wave/the electrons crossing over each other (Gibbon 2005). A popular analogy is the breaking of a wave near the beach. Wavebreaking is relevant to the maximum electric field achievable and plays a vital role in the injection process of electrons into the plasma wakefield (Kuschel et al. 2018; Kuschel 2018), which will be discussed in section 2.2.1.

With the knowledge that wavebreaking occurs when parts of the wave start to outrun the phase velocity, a simpler, non-relativistic solution for the maximum field strength can be found from Equation 2.34. In this case $\gamma_{\mathrm{max}} = \gamma_p$ and $|\vec{E}(\tau)|$ is maximized when setting $\gamma(\tau) = 1$, leading to

$$|E_{\text{max}}| = \sqrt{2}\frac{\omega_p \mathrm{c_0 m_e}}{\mathrm{e}} \left(\gamma_p - 1\right)^{1/2}. \tag{2.35}$$

For non-relativistic phase velocities this leads to the expression $E_{\text{max}} = \omega_p v_p \mathrm{m_e/e} \simeq \mathrm{m_e}\omega_p \mathrm{c/e}$, known as the cold wavebreaking limit (J. Dawson and Oberman 1962). *"In this picture, wavebreaking can be thought of as the crossing of neighboring charge sheets, accompanied by a density singularity"*, taken from (Gibbon 2005, page 63). In the case of a warm, relativistic plasma, corrections must be included to account for the relativistic fluid momenta and the suppression of density singularities due to the plasma pressure. The solution including these considerations was obtained by (Katsouleas and W. Mori 1988)

$$E_{\text{max}} = \frac{\omega_p \mathrm{c_0 m_e}}{\mathrm{e}} \mu^{-1/4} \left(\ln(2)\gamma_p^{1/2}\mu^{1/4}\right)^{1/2}, \tag{2.36}$$

where $\mu = 3\mathrm{k_B}T_\mathrm{e}/(\mathrm{m_e}v_p^2)$ includes the thermal correction due to the electron temperature T_e. This expression holds in the case that the phase velocity of the plasma is much greater than the velocity of the thermal motion. The maximum longitudinal electric field in a thermal plasma is therefore typically lower than in the case of the cold plasma (V. Malka 2020).

2.1.5. Laser-driven Wakefield generation

Previous sections established the fundamental equations regarding the propagation of plasma waves, Equation 2.32 and 2.33 and the maximum electric field that can be supported by the wave in Equation 2.35 and 2.36. This section deals with the generation of laser-driven plasma waves and the wakefield potential caused by these. Here, only the case for small pump strength $a_0 \lesssim 1$ will be derived in the quasi-static approximation, as done in (Gibbon 2005). The case for arbitrary pump strength will not be derived explicitly here due to its length and for the reason that the exact derivation is out of scope for this work, but can also be found in (Gibbon 2005). An elegant approach to the relativistic derivation can be found in (Kuschel 2018), where the relativistic Hamiltonian of a charged particle in an electromagnetic field was used.

It is assumed that the electric field of the laser oscillates along the y-axis. Starting point is a linearized version Equation 2.33, retaining the non-linear pump term $\mathrm{d}/\,\mathrm{d}\tau(u_y\,\mathrm{d}p_y/\,\mathrm{d}\tau)$ from the same equation. Here linearization means setting $p_{x,y,z}/(\mathrm{m_e c_0}) \ll 1$ and assuming $u_z \ll \beta_p$. In the case of small pump strength, i.e. $a_0 < 1$ the following equation is obtained:

$$\frac{\mathrm{d}^2 u_z}{\mathrm{d}\tau^2} + \omega_p^2 u_z = \frac{1}{\beta_p}\frac{\mathrm{d}}{\mathrm{d}\tau}\left(u_y \frac{\mathrm{d}p_y}{\mathrm{d}\tau}\right). \tag{2.37}$$

Defining n as the perturbation of the electron density yields

$$\begin{aligned} n \equiv n_\mathrm{e} - n_0 &= \frac{n_0 u_z}{\beta_p - u_z} \\ &\simeq \frac{n_0 u_z}{\beta_p} \end{aligned} \tag{2.38}$$

which is obtained by substituting Equation 2.31 for n_e. Expressing u_z in terms of n and n_0 and substituting u_z in Equation 2.37 results in the following differential equation for n:

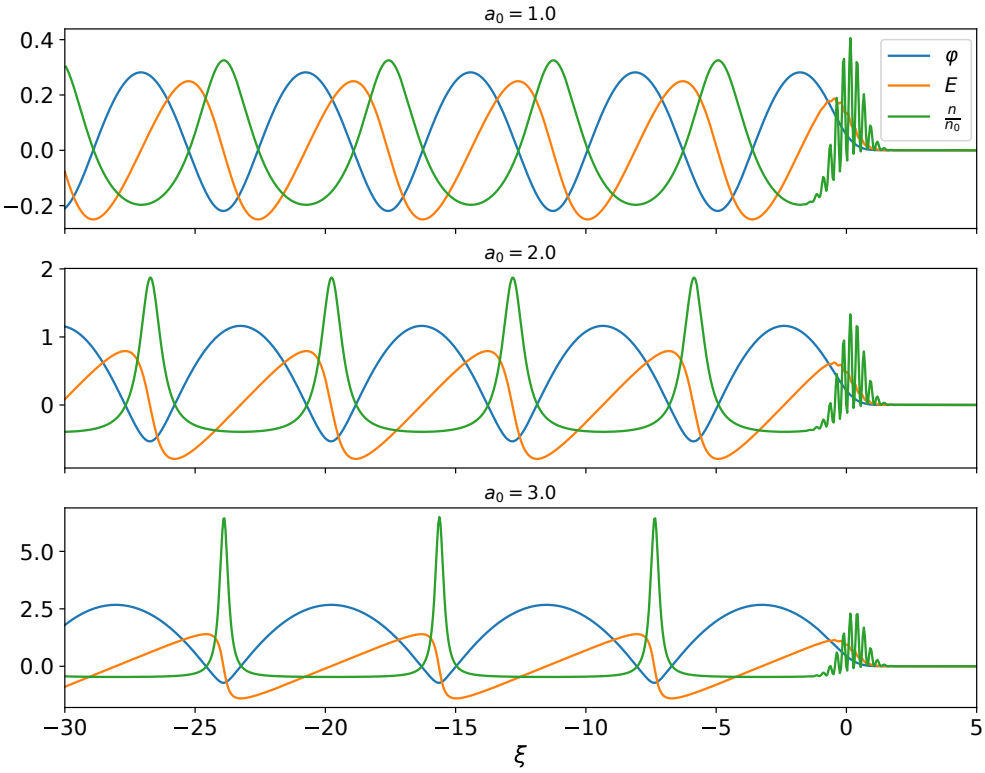

Figure 2.2.: Numerical solutions for Equation 2.40 - 2.42. As a reminder, the derivation presented here is only valid for small pump strengths $a_0 \lesssim 1$. In this limit, the plasma wave is a harmonic oscillation, as seen in the top image. This is no longer the case for relativistic intensities $a_0 > 1$, as shown by the lower plots. In the non-linear, case a spike in the density distribution and the characteristic sawtooth electric field is observed. The Python script for generating the plots was provided courtesy of Stephan Kuschel.

$$\frac{\partial^2 n}{\partial t^2} + \omega_p^2 n = \frac{n_0}{2}\frac{\partial^2}{\partial z^2}\frac{v_y^2}{\mathrm{c}_0^2}. \tag{2.39}$$

Here, the equation was transformed back to its original variables t and z of Equation 2.21-2.25. Within the non-relativistic limit established at the start of this section, Equation 2.39 describes a laser-driven plasma wave (Gibbon 2005).

The goal is to find an expression for the longitudinal electric field that can be utilized for particle acceleration. Before an expression can be obtained, another coordinate transformation to a co-moving coordinate system, propagating with $v_g \simeq \mathrm{c}_0$ is helpful, with $\xi = x - \mathrm{c}_0 t$ and $\tau = t$. In the quasistatic approximation, the differentials are given by $\partial/\partial x = \partial/\partial\xi$ and $\partial/\partial t = \partial/\partial\tau - \mathrm{c}_0\partial/\partial\xi \simeq -\mathrm{c}_0\partial/\partial\xi$. The differential in τ can be neglected as τ varies slowly while the pulse propagates through the plasma (Gibbon 2005). After the transformation and applying Equation 2.6 to the right side of Equation 2.39, the density perturbation can be expressed in terms of the normalized laser potential $a_0 = v_y/\mathrm{c}$

$$\left(\frac{\partial^2}{\partial\xi^2} + k_p^2\right) n = \frac{n_0}{2}\frac{\partial^2}{\partial\xi^2} a_0^2. \tag{2.40}$$

As a last step Equation 2.22 is used to replace n in the equation above, resulting in the following expressions for the longitudinal component of the electric field E and its potential φ of the plasma wave:

$$\left(\frac{\partial^2}{\partial\xi^2} + k_p^2\right) E = \frac{k_p^2}{4}\frac{\partial}{\partial\xi}a_0^2 \tag{2.41}$$

$$\left(\frac{\partial^2}{\partial\xi^2} + k_p^2\right) \varphi = -\frac{k_p^2}{4}a_0^2, \tag{2.42}$$

where $-\partial\varphi/\partial\xi = E$ is used. A couple of observations can be made from the two differential equations: Firstly, the pump term driving the plasma wave is the ponderomotive force, caused by the intensity gradient of the laser pulse. The electrons experience an impulse or "kick" from the ponderomotive force thus expelling electrons from regions of high intensity towards regions of lower intensity in the forward direction. As the laser's electric field reverses its sign after half the cycle period, the electrons experience a second impulse from the ponderomotive force. This impulse can be used to amplify the longitudinal electric field, when the oscillation period of the plasma roughly matches the pulse duration of the laser, leading to the condition $\lambda_p \approx c_0\tau_{\text{Laser}}$ (Gibbon 2005). Driving a wakefield inside a plasma can efficiently accelerate electrons to the MeV to GeV energy range.

2.2. Laser particle acceleration

The concept of compact, table-top laser plasma particle accelerators goes back to 1979 and was proposed by Tajima and Dawson (Tajima and J. M. Dawson 1979). These table-top accelerators allow for high acceleration electric fields over very short distances due to the characteristics of plasmas, making them a compelling alternative to conventional RF-based accelerator technologies. The first demonstration of electron acceleration utilizing plasma waves was reported in 1995 (Modena et al. 1995), with the demonstration of quasi mono-energetic electron beam acceleration reported around 2004 (Albert et al. 2021). Experimental demonstration of ion acceleration using a laser-plasma accelerator was reported in 2000 (Snavely et al. 2000; Wilks, Langdon, et al. 2001). Since then, much effort has gone into optimizing the performance and stability of these source, to establish them as viable platforms for charged particle acceleration. In this section, the concepts behind the two most widely used acceleration schemes will be introduced, as they play a key role in the realization of laser-driven neutron sources.

Laser-ion acceleration will be introduced first, followed by a description of electron acceleration utilizing non-linear plasma waves.

Target normal sheath acceleration

Target Normal Sheath acceleration (TNSA) is a mechanism whose primary goal is the acceleration of ions. Using TNSA, proton energies reaching up to $150\,\text{MeV}$ have recently been achieved (Ziegler, Göthel, et al. 2024). A key characteristic of ion beams accelerated by TNSA is the spectral distribution of the ion beam, which decays exponentially towards higher energies (Roth and Schollmeier 2017) and exhibits a half-opening divergence angle of 20 to $30°$, with higher energetic ions located closer to the beam axis (Brack et al. 2020). Another key aspect is the bunch duration $< 1\,\text{ns}$, which is in the order of the laser pulse length (Zeil et al. 2010). A schematic drawing of the TNSA mechanism is shown in Figure 2.3.

In a typical TNSA experiment, an ultra-short laser pulse ($\tau_\text{L} \lesssim 1\,\text{ps}$) is focused to a spot size measuring only a couple of µm in diameter and directed on a micrometer-thin plastic or metal foil target, leading to the disintegration of the target in the form of an expanding plasma. Laser intensities on the target exceed $10^{18}\,\text{W/cm}^2$

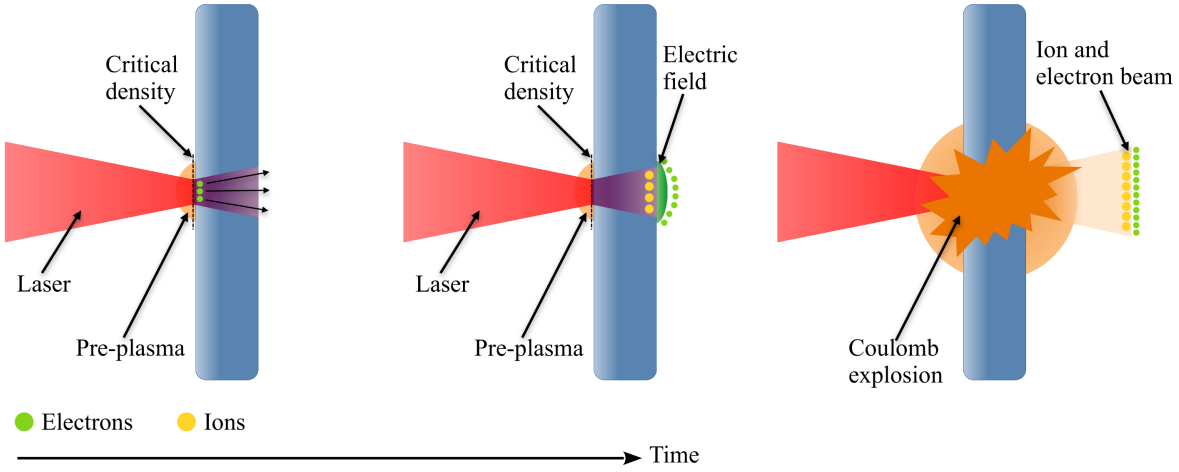

Figure 2.3.: Schematic drawing of the TNSA process. An ultra-high intensity laser beam is directed onto a suitable target, for example a μm thin plastic foil. Before the main peak of the laser pulse arrives, the target is ionized by the rising edge of the laser, leading to an expanding pre-plasma. The main laser pulse propagates through the pre-plasma up to the critical density, where it is absorbed and reflected. At the boundary electrons are continuously heated and pushed through the target, as the ponderomotive force peaks at the boundary. Electrons leaving the backside of the target generate an electric sheath field due to charge separation, which ionizes the target back layer. The ions can then be accelerated in the electric sheath field, disintegration the target in the process.

($a_0 > 1$), thus leading to electrons oscillating with relativistic velocities, according to Equation 2.6. During the interaction with the laser pulse, the electrons are heated through a variety of different heating mechanisms, such as sheath inverse bremsstrahlung (Catto and More 1977) ($\sim 10^{12}$ to $10^{15}\,\mathrm{W/cm^2}$), Brunel heating (Brunel 1987) ($\sim 10^{15}$ to $10^{18}\,\mathrm{W/cm^2}$), and/or $\vec{j} \times \vec{B}$ heating (W. L. Kruer and Estabrook 1985) ($> 10^{18}\,\mathrm{W/cm^2}$). While many different ion acceleration mechanisms/regimes at laser-plasma accelerators exist, only TNSA is relevant to this work and therefore elaborated on.

The laser propagates through the expanding plasma up to the critical density (see Equation 2.17), where it is absorbed and partially reflected. Therefore, the intensity gradient is maximized at the critical density in forward direction, which maximizes the ponderomotive force (see Equation 2.19 and 2.20), pushing the heated electrons through the critical density and deeper into the target. Beyond the critical density the electrons no longer experience a restoring force (see section 2.1) and can further traverse the target. If the target is thinner than the range of these electrons (inside the target material), they can exit the rear surface of the target. In this work, the most energetic electrons that escape from the target are referred to as hot electrons. The current of hot electrons induces a magnetic field, according to Lenz's law, causing a return current of background electrons, thereby preventing less energetic electrons from escaping. These less energetic electrons (compared to the hot electrons) that cannot are referred to as energetic electrons. These energetic electrons can accumulate at a certain distance from the target and circulate back and forth between the front and rear sides of the target for as long as the laser irradiates and heats the target. The return current causes a close-to-zero net current and is an important property of the TNSA mechanism, ensuring that energy conservation holds (Roth and Schollmeier 2017).

Due to the recirculation between the target's front and rear side, an electron sheath can be formed on either side by the energetic electrons. The electron sheath invokes a strong electric field in the range of TV/m (Eliezer 2002) and can be described by:

$$E(z) = \frac{2\mathrm{k_B}T_\mathrm{e}}{\mathrm{e}} \cdot \frac{1}{z + \sqrt{2\exp(1)}\lambda_\mathrm{D}}, \tag{2.43}$$

according to (Macchi 2013; Roth and Schollmeier 2017), with T_e the electron temperature. Following (Wilks, W. Kruer, et al. 1992) the electron temperature in keV can be estimated by $T_\mathrm{e} = 511\,\mathrm{keV} \cdot \left(\sqrt{1 + 0.73 I_L \lambda_L^2} - 1\right)$ where I_L and λ_L are the laser intensity in $10^{18}\,\mathrm{W/cm^2}$ and wavelength in µm. The variable λ_D is the so-called Debye length (Debye and Hückel 1923), describing the distance after which the electric field decreases to $1/e$ due the screening effects of other electrons, and is given by

$$\lambda_\mathrm{D} = \sqrt{\frac{\epsilon_0 T_\mathrm{el} \mathrm{k_b}}{\mathrm{e}^2 n_\mathrm{e}}}.$$

The strong electric field ionizes the atoms, mainly consisting of a hydrocarbon contamination layer, on the front/rear side of the target. Subsequently, these ions are accelerated in the electric sheath field, resulting in energetic ions with MeV kinetic energy. The ions are accelerated according to their charge-to-mass ratio, which results in electrons being accelerated first, with carbon ions trailing behind. The ions accelerated first modulate the accelerating sheath field, decreasing its effective strength, which is the reason for the exponential decay in the number of ions towards higher energies (Snavely et al. 2000). The acceleration process occurs on the time scale of the laser pulse duration and once the laser passes, a mixture of ions (protons, carbon ions) and electrons fly from the target position. The acceleration process is accompanied by a strong component of highly energetic photons due to the recirculation of the electron. This photonic component is commonly referred to as the γ-flash.

For specific applications, such as neutron generation, it can be beneficial to accelerate specific ion species, here deuterium ions. Two approached can be employed to achieve this. Firstly, doping the contamination layer with the ion species of interest can efficiently accelerate the desired ions. Secondly, a suitable choice of target bulk material is also a viable strategy without requiring fine control over the contamination layer. However, bulk material acceleration using TNSA is less efficient than accelerating ions from the contamination layer, since the contamination layer is accelerated first modulating the accelerating sheath field. For efficient acceleration of bulk material, a different acceleration mechanism needs to be utilized, such as laser break-out afterburner (Yin et al. 2006) or relativistically induced transparency acceleration (Akhiezer and Polovin 1956; Vshivkov et al. 1998; Sahai et al. 2013).

For neutron generation, the accelerated ions are directed into a suitable converter material, where they cause nuclear reactions. Different types of reactions are detailed in section 2.3.2.

2.2.1. Laser Wakefield Acceleration

Laser wakefield acceleration (LWFA) describes a method for the acceleration of electrons, utilizing the strong longitudinal electric field in a plasma due to the excitation of a plasma wave. Energies up to $8\,\mathrm{GeV}$ (Gonsalves et al. 2019) and bunch charges in the range of $700\,\mathrm{nC}$ (Shaw et al. 2021) have been reported. The defining characteristics of laser wakefield accelerated electron beams are low divergence (compared to TNSA ion beams) in the range of several mrad, see for example (Kuschel et al. 2018; Wenz and S. Karsch 2020; V. Malka 2020), as well as the option to generate quasi mono-energetic electron beams. In the case of quasi mono-energetic beams, the electrons are peaked around a central energy E_mean; see (S. P. Mangles et al. 2006) for example. Similar to TNSA, the electron beam bunch duration is in the order of the laser pulse duration. Acceleration of electrons using plasma waves is a complex process; different acceleration

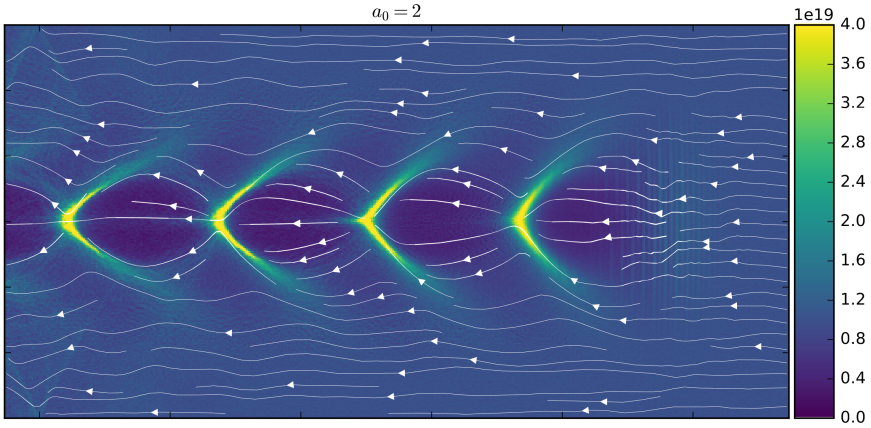

Figure 2.4.: 2D PIC simulation of a laser generated plasma wake in the non-linear regime. The color scale indicates the electron density. The (mostly) electron free bubble and multiple wakefield ”buckets” are clearly visible. Streamlines indicate the movement of electrons. In this figure no electrons were injected into the plasma wake. Courtesy of Stephan Kuschel.

regimes and explanations can be found in the literature. Here, the focus is on the so-called bubble regime (Pukhov and Meyer-ter-Vehn 2002; Kostyukov et al. 2004; W. Lu et al. 2007). The regime is characterized by a (nearly) spherical region in the plasma, where the laser pulse almost entirely expels the electrons.

The LWFA acceleration mechanism is a combination of plasma waves to generate a longitudinal accelerating electric field, see Equation 2.37 and (among others), wavebreaking (Equation 2.35 and 2.36) to inject electrons into the wake of the wave. Only by precisely controlling both, the accelerating field and the injection into the wake, high quality electron beams can be obtained (Kuschel 2018; V. Malka 2020).

In a LWFA experiment, a ultra-short laser pulse (typically $\tau_\mathrm{L} < 100\,\mathrm{fs}$) is focused on a gaseous target, where the pulse causes ionization and thus generates a plasma. Commonly a normalized vector potential a_0 between 2 and 4 is chosen for LWFA. When the laser passes through the plasma, the ponderomotive force of the laser pulse expels electrons radially from the focus, resulting in the formation of the eponymous bubble. This cavity is surrounded by the expelled electrons, which stream along the outside of the bubble, intersecting at the rear side, opposite of the laser. In this way, multiple cavities, sometimes called ”buckets”, can be formed, with a spacing in the range of the plasma wavelength λ_p. A snapshot of a 2D PIC simulation of the described mechanism is displayed in Figure 2.4. The movement of the electron is indicated by the white arrows and the color scale represents the electron density, clearly showing the accumulation of the electrons at the end of the buckets. The structure of electron density distribution seen in the figure can be described by Equation 2.40, with the corresponding longitudinal electric field described by Equation 2.41. The middle figure of Figure 2.2 show the corresponding electric field and density of Figure 2.4.

If enough electron accumulate at the back of the bubble and the plasma wave grows sufficiently large, the wavebreaking limit described by Equation 2.35 and 2.36 can be exceeded, resulting in the injection of electrons into the bubble. These injected electrons become trapped inside the bubble and are subsequently accelerated along the laser axis (W. Lu et al. 2007; V. Malka et al. 2002) by the electric field of the plasma wave. The described mechanism for injecting electrons into the bubble is known as self-injection. Many different injection schemes exist, each with its own requirements, advantages, and disadvantages. A discussion of these is out of the scope of this work; instead the reader is referred to (V. Malka 2020; Wenz and S. Karsch 2020) for an overview of different schemes. Due to the fact that injection only occurs at the back end of the bubble, the phase-space volume occupied by the injected electrons is limited, leading to the generation of quasi mono-energetic electron beams.

Electrons will gain energy until one of three events occurs: First, the laser pulse expends its energy and the intensity a_0 is no longer sufficient to continue driving the wave. The distance over which the laser expands its energy is known as the depletion length $L_{\text{depletion}}$. The depletion length can be estimated by:

$$L_{\text{depletion}} \simeq \frac{\omega_p^2}{\omega_{\text{L}}^2} \cdot \text{c}\tau_{\text{L}}, \tag{2.44}$$

where ω_{L} is the laser frequency, τ_{L} the laser pulse duration and ω_p the plasma frequency (W. Lu et al. 2007). Second, electrons start to outrun the plasma wave, thus reaching the decelerating part of the electric field, see Figure 2.2. The latter condition defines the so-called dephasing length, given by

$$L_{\text{dephasing}} \simeq \frac{2}{3\pi}\sqrt{a_0}\lambda_{\text{L}}\left(\frac{n_{\text{cr}}}{n_{\text{e}}}\right)^{3/2}. \tag{2.45}$$

Here, a_0 denotes the normalized vector potential, n_{cr} is the critical density, λ_{L} the wavelength of the laser and n_{e} is the electron density. (Wenz and S. Karsch 2020). To achieve the highest performance of a laser wakefield accelerator, the depletion and dephasing length should be matched. Remembering the matching condition for efficiently driving a plasma wake $\lambda_p \approx \text{c}_0\tau_{\text{L}}$ from section 2.1.5 allows the pump and depletion length to be matched (W. Mori 1997). In practice this requires either laser pulse durations of $\tau_{\text{L}} < 50\,\text{fs}$ or low plasma densities for longer pulses, which results in short depletion length according to Equation 2.44.

Under experimental conditions, the laser pulse is typically focused to focal spot size w_0 in the range of several µm, leading to the third mechanism that limits LWFA: Diffraction. Beyond the focal point, the laser beam diffracts, which reduces a_0 and thus the pulse's ability to drive the plasma wave. The cross-sectional area of a focused laser beam doubles after a distance z_{R}, known as the Rayleigh length. This length is usually shorter than either $L_{\text{dephasing}}$ or $L_{\text{depletion}}$, leading to an early breakdown of the acceleration. Thus, to match the acceleration distance to the depletion and dephasing length, the premature breakdown needs to be circumvented. This can be achieved by guiding the laser pulse through the plasma, utilizing an effect known as relativistic self-focusing (Sun et al. 1987; Sprangle, Joyce, et al. 1988). To access the regime of relativistic self-focusing in a plasma, the laser pulse power P_{L} needs to exceed the critical power P_{cr} (in GW) defined through (Litvak 1970; Max et al. 1974; Sprangle, Tang, et al. 1987)

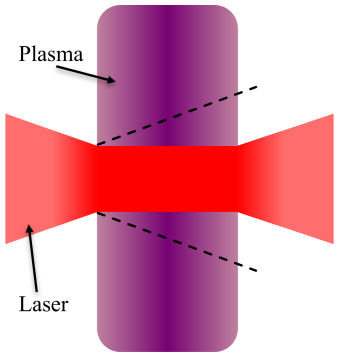

Figure 2.5.: Schematic drawing of the effect of relativistic self-focusing. The dashed lines corresponds to a pulse that does not experience self-focusing and therefore diffracts beyond its focal point. In contrast, the self-focused beam is guided through the length of the plasma.

$$P_{\text{cr}} \simeq 17\left(\frac{\omega_{\text{L}}}{\omega_p}\right)^2. \tag{2.46}$$

Relativist self-focusing arises from the modification of the plasma's index of refraction. An interplay between the electrons' relativistic mass increase and the ponderomotive force causes the alteration. Due to

the relativistic electron motion inside the laser field, described by Equation 2.5, the mass of the electron increases in dependence on the intensity. This leads to an increase in the index of refraction on the laser axis relative to the fringes of the laser pulse, which effectively focuses the beam (Max et al. 1974; Pukhov 2002). The ponderomotive force also modifies the refractive index by pushing electrons out of regions with higher intensity, again resulting in an increased index of refraction on the laser propagation axis. In this way, the beam does not diffract while propagating through the plasma (Del Pizzo and Luther-Davies 1979). Figure 2.5 shows a schematic drawing of the effect of relativistic self-focusing.

Lu *et al.* (W. Lu et al. 2007) developed a phenomenological framework for the design of a laser wakefield accelerated in the bubble regime for self-guided pulses. From this framework important electron beam Quantities such as the energy E_{mean} and the charge Q_{beam} of the electron beam can be calculated. The framework is based on the idea that efficient acceleration occurs when the radius of the bubble R_{bubble} matches the laser (focus) spot size w_0. Resulting in the so-called matching condition:

$$k_{\text{p}} w_0 = 2\sqrt{a_0}, \tag{2.47}$$

from which the optimal laser spot size can be determined for a given plasma density. As a reminder, $k_{\text{p}} = \omega_{\text{p}}/\text{c}$ is the wave vector of the plasma, with ω_{p} the plasma frequency. Note, this expression only holds for $a_0 \gtrsim 2$ and $P_{\text{L}} > P_{\text{cr}}$.

Expressing the matching condition in terms of the critical power P_{cr} yields:

$$a_0 \simeq 2\left(\frac{P_{\text{L}}}{P_{\text{cr}}}\right)^{1/3}. \tag{2.48}$$

Combining Equation 2.47 and 2.48, a condition for the matched spot size based on a set of laser parameters can be found (W. Lu et al. 2007). The condition for the matched spot size diameter d_{FWHM} can be written as:

$$d_{\text{FWHM}} = 2\sqrt{2\ln(2)}\frac{c}{\omega_{\text{p}}} \cdot \sqrt{2\left(\frac{P_{\text{L}}}{P_{\text{cr}}}\right)^{1/3}}. \tag{2.49}$$

To make use of Equation 2.49 three laser parameters need to be know, the laser pulse energy, the pulse length (FWHM) and the wavelength, as well as the plasma frequency. From this equation the energy of the electron beam E_{mean} can be estimated by

$$E_{\text{mean}} \simeq \frac{2a_0}{3}\left(\frac{\omega_{\text{L}}}{\omega_{\text{p}}}\right)^2 \text{m}_{\text{e}}\text{c}^2, \tag{2.50}$$

where a_0 needs to satisfy Equation 2.47 and depends on d_{FWHM}. Based on Lu's framework and according to (Wenz and S. Karsch 2020) the beam charge can be calculated by

$$Q_{\text{beam}} \simeq \frac{\pi \text{c}^3}{\text{e}^2}\sqrt{\frac{\text{m}_{\text{e}}^3 \epsilon_0^3}{n_{\text{e}}}} a_0^{\frac{3}{2}}, \tag{2.51}$$

Furthermore, the spot size w_0 should roughly match the length of the laser pulse $\text{c}\tau_{\text{L}}$, resulting in $2w_0 \gtrsim \text{c}\tau_{\text{L}}$ (W. Lu et al. 2007; Wenz and S. Karsch 2020), in order for these formulations to hold.

In chapter 6, Equation 2.49-2.51 are used to calculate the expected electron beam for a high repetition rate, high average power laser system. These electron beam parameters are then used to calculate the neutron yield performance of such a laser system.

2.3. Introduction into neutron physics, production and detection

The neutron was first experimentally observed by James Chadwick in 1932 (Chadwick 1932a), generated from interaction between beryllium and α particles. It is similar in mass to the proton, with its defining feature being the lack of electric charge, allowing neutrons to interact with matter purely through the strong nuclear force. Since its discovery, the neutron has assumed an important role in everyday life, ranging from power generation in nuclear reactors, to material analysis, to microprocessor testing, medical isotope production and many more. As neutron generation, detection and their application are central aspects of this thesis, an introduction to the most relevant topics of neutron physics is given in this chapter, starting with the classification of neutrons.

2.3.1. Neutron classification

The interaction of neutrons with matter depends strongly on its energy. Whereas neutrons with high energies ($>$ MeV) are highly penetrating, neutrons with low energies ($\sim$ eV) can be absorbed or captured within very short distances, depending on the material. It is therefore common practice to classify neutrons according to their kinetic energy (Lapp and Howard 1972). In the context of this thesis, the following neutron classifications will be used, going from low to high energy:

Cold	$\lesssim 10\,\mathrm{meV}$
Thermal	0.01 to $0.5\,\mathrm{eV}$
Epi-thermal	0.5 to $100\,\mathrm{eV}$
Intermediate	0.1 to $100\,\mathrm{keV}$
Fast	0.1 to $50\,\mathrm{MeV}$
High-energy	$\gtrsim 50\,\mathrm{MeV}$

Strictly speaking, thermal neutrons are in thermal equilibrium with the surrounding matter, meaning they have the same energy as the atoms of the surrounding material. A temperature of $20\,^{\circ}\mathrm{C}$ corresponds to an energy of $25.3\,\mathrm{meV}$, which can be calculated by $E = \mathrm{k_b}T$, where $\mathrm{k_b}$ is Boltzmann's constant and T the absolute temperature. In the context of this thesis neutrons with energies less than $0.5\,\mathrm{eV}$ are considered thermal neutrons.

In order to conduct neutron measurements, beams of free neutrons are needed. However, since neutrons are radioactive and decay via beta decay, with a half-life of $10.2\,\mathrm{min}$ (Bondarenko et al. 1978), they are not found as free particles in nature but only as part of the nucleus. Additionally, due to the lack of electric charge, neutron beams cannot be generated the same way ion or electron beams are. Generating free neutrons and neutron beams relies on nuclear reactions of suitable particle combinations. The following section will establish the neutron generation mechanisms most relevant to this thesis. All neutron production channels discussed below share a common attribute: the emitted neutrons posses an initial energy range spanning from tens of keV to the MeV range, typically cutting off around the maximum energy of the reaction inducing particle.

2.3.2. Neutron generation

Many different methods can be utilized to generate neutron beams. Commonly used methods are nuclear fission and fusion, spallation reactions, ion induced reactions below the spallation threshold and photo-disintegration of the nucleus. The most relevant generation processes for this work are ion induced reactions

below the spallation threshold and photo-nuclear reactions. For the ion based reactions, proton- and deuteron-induced reactions, denoted as (p,n) and (d,n), play a prominent role but carbon based reactions (C,n) can also occur. Ions in the context of this work are generated via the above explained TNSA mechanism. These types of reactions will be introduced first. The second neutron generation process explored is based on the interaction of high energy γ-rays with the nucleus, resulting in photo-nuclear reaction (γ,n) or photo-disintegration/photo-fission of the nucleus (γ,f). The γ-rays are generated by impinging a high energy electron beam on a high-Z material, where the electrons are decelerated and produce bremsstrahlung. This reaction channel will be explained last. Concluding the section on neutron generation is a short account of how a thick target influences neutron production.

Ion-induced reactions

In ion induced reactions, two ion projectile species important to laser-driven neutron sources. The first species is the proton and the second is the deuteron. With regard to protons and deuterons, two reaction types dominate neutron production: direct reactions and the formation of a compound nucleus (Lapp and Howard 1972; Bermejo and Sordo 2013). The direct reaction can further be distinguished, among others, into nuclear knockout reactions, which are most relevant but not exclusive to proton reactions and stripping reactions, most relevant in the case of deuteron or multi-nucleon projectiles (Lapp and Howard 1972). Differences between direct and compound reactions are the time scales at which they occur. Whereas neutron emission caused by direct reactions takes place on timescales similar to the time that projectiles need to traverse the nucleus (10^{-22} to 10^{-21} s), compound reactions require much longer times (10^{-18} to 10^{-15} s) (Lapp and Howard 1972; Bethge et al. 2007; Bermejo and Sordo 2013). Another difference between the two reaction types is the angular and spectral distribution of the emitted neutrons.

Knockout reactions, as part of the direct reactions, are discussed first in the context of proton induced reactions (although they apply to ions in general), followed by a description of stripping reactions for deuterium induced reactions. Direct reactions resulting in the emission of nucleons mostly take place in the outer perimeter of the nucleus, where the incoming projectile ($\hat{p}$), here a proton (p) imparts energy on a single nucleon, here a neutron (n), of the target material's nucleus (T). Thus, the neutron has a high probability of leaving the nucleus without interacting with the other nucleons (Butler 1957). This reaction results in a favored emission at $0°$ relative to the incoming proton and the highest neutron energies can be obtained in this direction. The schematic of this reaction is given in Equation 2.52 and visualized in Figure 2.6.

$$\hat{p} + T \rightarrow C^* \rightarrow \mathrm{n} + X, \tag{2.52}$$

where X is the reaction product. The total energy of the reaction needs to be conserved, such that $Q + E^{\mathrm{kin}}_{\hat{p}} + E^{\mathrm{kin}}_{T} = E^{\mathrm{kin}}_{\mathrm{n}} + E^{\mathrm{kin}}_{X}$ holds true, with Q the reactions value defined as $Q = (\mathrm{m}_{\hat{p}} + m_T - [\mathrm{m}_{\mathrm{n}} + m_X]) \cdot \mathrm{c}^2$. Further E^{kin}_{i} and m_i with $i \in (p, T, \mathrm{n}, X)$ are the kinetic energy and mass of the respective particles. Following calculations carried in (Petrov et al. 2013) yields

$$E^{\mathrm{kin}}_{\mathrm{n}}(\theta) \approx E^{\mathrm{kin}}_{\hat{p}} + Q + 2\sqrt{\frac{\mathrm{m}_{\hat{p}}\mathrm{m}_{\mathrm{n}}}{m_X^2}\left(1 + \frac{Q}{E^{\mathrm{kin}}_{\hat{p}}}\right)E^{\mathrm{kin}}_{\hat{p}}}\cos(\theta) \tag{2.53}$$

for the kinetic energy of the neutron in dependence on its emission angle θ. Again, θ is measured with respect to the incoming projectile. Equation 2.53 shows, that the highest energetic neutron are found at $0°$. In the case of a proton projectile and $\mathrm{m_p}, \mathrm{m_n} \ll m_X$ the expression can be simplified to

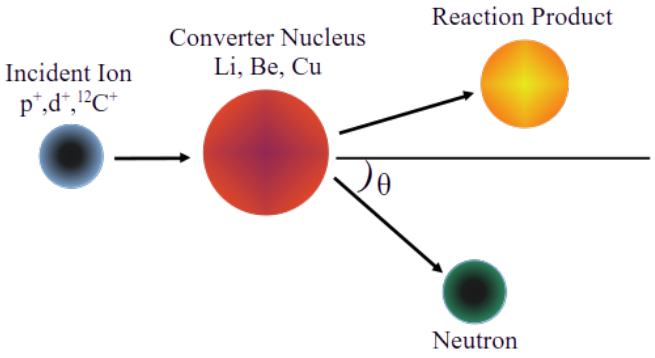

Figure 2.6.: Schematic drawing of the direct knockout reaction. The incoming projectile (dark blue) collides with the target (red), emitting a neutron (dark green) at an angle θ and a reaction product (orange). Figure adapted from (Petrov et al. 2013).

$$E_{\mathrm{n}}^{\mathrm{kin}} \approx E_{\mathrm{p}}^{\mathrm{kin}} + Q. \tag{2.54}$$

From Equation 2.54, the highest achievable neutron energy can be calculated, which is specific to the combination of projectile and target material, due to the Q.

The description of the stripping reaction in this section is limited to the deuteron and its (d,n) reaction channel, as it is most relevant to the neutron production of LDNS. The reaction channel (d,p) is not discussed. When a deuteron approaches a nucleus of the target material, the Coulomb potential of the nucleus will repel the proton, leading to polarization of the deuteron. If the Coulomb force acting on the proton is strong enough to overcome the binding energy of $E_{\mathrm{B}} = 2.225\,\mathrm{MeV}$ (Kazi et al. 1961), the deuteron can break-up in the Coulomb field, with the neutron continuing along the original trajectory. Consequently, emission in the forward direction $\theta = 0°$ is favored (Hamburger et al. 1961). This is primarily the case for high-Z target materials, such as tungsten. When low-Z target materials are used, such as lithium or beryllium, the break-up is caused by nuclear forces through stripping processes (Serber 1947; Hamburger et al. 1961; Parfenova and Zhukov 2001), namely proton stripping.

The cross section of proton stripping in the case of the deuteron can be calculated using perturbation theory in the distorted wave Born approximation (DWBA) (Hashimoto, Y. Iwamoto, et al. 2014a). In simple terms, the proton stripping process can be described as follows for light nuclei: If the deuteron comes close enough to the target nucleus, the wave functions of the proton and the target nucleus start to overlap. Thus, the wave functions become distorted. Consequently, the proton can merge with the target nucleus and form a new compound nucleus while the neutron continues to move along the original trajectory. However, when the target nucleus fuses with the deuteron, meaning the entire deuteron is absorbed, the neutron is emitted quasi-isotropically and an unstable intermediate reaction product remains (Ye et al. 2009). This process is comparable to the compound nuclear reaction, which will be elaborated on next.

With the direct reactions introduced above, the focus is now on neutron generation via compound reactions. This type of reaction is responsible for the dominantly isotropic emission of neutrons in the energy range of up to $\sim 10\,\mathrm{MeV}$ (Bermejo and Sordo 2013). The reaction channel is characterized by multiple interactions between nucleons, a key difference from direct reactions. When a projectile (proton) penetrates the Coulomb barrier and interacts with the target nucleus via the nuclear force, the projectile and target nucleus become indistinguishable and form compound nucleus. Due to the energy added by the projectile, this newly formed compound nucleus is in an excited state (Lapp and Howard 1972).

The nucleons of this compound nucleus rapidly "thermalize", i.e. distributing the energy among all constituents; this process typically takes less than $1\,\mathrm{fs}$, which is a long time with regard to nuclear time scales (Bermejo and Sordo 2013). If, during the thermalization process, enough energy is concentrated into a neutron to overcome the binding energy ($\simeq 2$ to $8\,\mathrm{MeV}$ depending on the nucleus), emission of the neutron from the compound nucleus can occur. The energetic distribution of the neutrons is given by

$$\frac{\mathrm{d}\Phi}{\mathrm{d}E} = \sqrt{\frac{E}{\pi\left(\mathrm{k_B}T\right)^3}} \cdot \exp\left(-\frac{E}{\mathrm{k_B}T}\right), \tag{2.55}$$

in this case, T is the temperature of the nucleus (Bertsch et al. 1996). Consequences of the thermalization process are the much delayed particle emission compared to direct reactions, the loss of original directionality, leading to a primarily isotropic emission and emission energies in the range of the binding energy (Lapp and Howard 1972).

To conclude ion induced neutron reactions, the so-called pre-equilibrium reaction, first described by (Griffin 1966), needs to be mentioned. It can be thought of as a mix of direct and compound reactions (Hofmann 2008). The energies of the emitted neutrons are between those emitted from direct and compound reactions, whereas the angular distribution resembles the distribution of the compound reactions. For a more detailed, theoretical description of the pre-equilibrium reaction, the reader is referred to (Koning, Akkermans, et al. 1999) and (Hofmann 2008, Chapter 9).

Photo-nuclear reactions

Photo-nuclear reactions, leading to the emission of a nucleon, can occur when the photon exceeds the binding energy of the target nucleus (J. Levinger 1957; J. S. Levinger 1960). Photon-induced reactions are predominately found at electron-based neutron sources. At these sources, electrons are accelerated to several MeV and directed into a high-Z target material such as lead or tungsten, where the electrons are decelerated, thereby emitting bremsstrahlung γ-rays (Kramers 1923; Sommerfeld 1931; Bermejo and Sordo 2013). Following the emission of bremsstrahlung, the γ-ray photons can interact with the target nuclei and cause photo-nuclear reactions or induce photo-fission (Lapp and Howard 1972).

According to (Kramers 1923) the bremsstrahlung γ-ray photon distribution is determined by

$$\frac{\mathrm{d}E_\gamma}{\mathrm{d}\lambda} \propto Z\left(\frac{\lambda E_{\mathrm{el}}^{\mathrm{kin}}}{\mathrm{hc}_0} - 1\right)\frac{1}{\lambda^3}, \tag{2.56}$$

where Z is the atomic number of the target material, h is Planck's constant and $E_{\mathrm{el}}^{\mathrm{kin}}$ the electron kinetic energy. The highest γ-ray energy achievable is thereby limited by the maximum electron energy (Duane 1915). For neutron emission to occur, the photon's energy needs to exceed the binding energy E_B of the neutron (Bermejo and Sordo 2013); this requirement constitutes a threshold energy. Above the threshold energy, neutron production can be separated into three distinguished processes: the giant dipole resonance (GDR), the quasi-deuteron effect and photopion generation (Swanson 1979; Bermejo and Sordo 2013).

The GDR regime ranges from the threshold energy up to $\sim 30\,\mathrm{MeV}$ (Swanson 1979), depending on the material. In this regime, neutron production is caused by a photon-induced oscillation of the nucleus in which the protons and neutrons are displaced relative to each other, leaving the nucleus in an excited state. The energy excess is then released by the emission of a neutron (Swanson 1979; Bermejo and Sordo 2013). Neutron emission occurs isotropically and the energy peaks around $1\,\mathrm{MeV}$ with the maximum neutron

energy in the order of the binding energy arising from neutron evaporation. The generation of neutrons is dominated by the GDR, with cross sections reaching up to the several hundred milli-barn level. If a photon's energy is greater than $x \cdot E_{\text{threshold}}$ with $x \in \mathbb{N}$, up to x neutrons can be emitted by the target in a (γ,xn) reaction, albeit at a reduced probability/cross section. The neutron distribution generated by the GDR can be approximated (Bermejo and Sordo 2013) by a Watt fission spectrum (Watt 1952)

$$\frac{\mathrm{d}\Phi}{\mathrm{d}E} = \sqrt{\frac{\pi E}{4k_{\text{fis}}^3}} \cdot \exp\left(-\frac{E}{k_{\text{fis}}}\right), \tag{2.57}$$

with $k_{\text{fis}} \approx 1.4\,\text{MeV}$. When measuring the neutron flux generated from electrons with energies exceeding $\sim 30\,\text{MeV}$, a high energy tail $E > 20\,\text{MeV}$ in the neutron spectrum will be visible. This tail is the result of direct reactions and can therefore not be described by Equation 2.57.

Above the GDR $E_\gamma \gtrsim 30\,\text{MeV}$, neutrons are generated through direct reactions. The first such reaction is the so-called quasi-deuteron effect, in which the photon interacts with the dipole moment of a neutron-proton pair inside the nucleus rather than the entire nucleus (J. S. Levinger 1960). Post interaction, the quasi-deuteron decays, with each particle typically acquiring half the energy of the incoming photon E_γ, due to the quasi-two-body final state of the interaction (Swanson 1979). Both particles can subsequently interact with the remaining nucleons, with the neutron commonly emitted from the nucleus. Neutrons with energies between $E_{\text{B}} < E \lesssim E_\gamma/2$ predominantly originate from the quasi-deuteron effect and follow approximately

$$\frac{\mathrm{d}\Phi}{\mathrm{d}E} \approx E^{-\alpha}, \tag{2.58}$$

where α is a material specific constant, ranging from $\alpha = 3.0 - 3.3$ for heavy nuclei (Z=73-83) and $\alpha \approx 3.6$ for fissionable nuclei (Swanson 1979). It should be noted that for $E_\gamma \gtrsim 10\,\text{MeV}$ photo-fission of fissionable nuclei, e.g. ^{235}U or other heavy elements can occur, further increasing the neutron yield (Haxby et al. 1941; Baldwin and Klaiber 1947; Doré et al. 2006; Silano and Karwowski 2018).

Lastly, at $E_\gamma > 140\,\text{MeV}$, neutrons are generated via photopion production, resulting in highly energetic neutrons ($E > 100\,\text{MeV}$). Average neutron energies of $E \approx 200\,\text{MeV}$ can be expected at photon energies well above the pion threshold (Swanson 1979). Production of high energy neutrons and pions is of major importance concerning radiation protection, as pions decay into muons, which are also highly penetrating. For this reason, energies at electron accelerators are commonly limited to 140 MeV to avoid the radiation protection implications from muon production.

Neutron generation inside a thick converter target

The reaction channels described above considered the interaction of a single projectile, either an ion or a photon, with a nucleus of the converter target. Under experimental conditions, the neutron production rate, i.e. the conversion efficiency η_{n} from projectile to neutron, must be maximized. Hence, the use of thick targets is strongly suggested.

The converter should be thick enough to (almost) stop all incoming ions to maximize the neutron generation potential for each ion. The range of the ions inside the material thereby determines the thickness in the case of ion projectiles. The range of ions inside matter can be calculated using the Bethe-Block equation (Bohr 1913; Bethe 1930; Bloch 1933)

$$-\frac{\mathrm{d}E_i}{\mathrm{d}l} = \frac{4\pi}{\mathrm{m_e c_0^2}} \cdot \left(\frac{\mathrm{e}^3}{4\pi\epsilon_o}\right)^2 \cdot \frac{z_p^2 \mathrm{N_A}\rho}{A_T \mathrm{M_u}} \cdot \frac{Z_T}{\beta^2} \cdot \left[\ln\left(\frac{2\mathrm{m_e c_0^2}\beta^2}{I(1-\beta^2)}\right) - \beta^2\right], \tag{2.59}$$

where I denotes the mean excitation potential, z_p the charge of the projectile, $\mathrm{N_A}$ Avogadro's constant, $\mathrm{M_u}$ the molar mass constant and A_T, Z_T the mass and atomic number of the converter target, respectively. In the continuous slowing-down approximation, the range can then be calculated by integrating the reciprocal of Equation 2.59 over the particle's energy (Carron 2006).

Circling back to neutron production, the probability P of a neutron producing reaction occurring can be written as

$$P = \sigma(E_i)\frac{N_T}{A_s}, \tag{2.60}$$

where $\sigma(E_i)$ is the ion energy dependent reaction cross section, N_T is the number of target nuclei and A_s the irradiated area of the target. The amount of generated neutrons is thus given by $N_{\text{Neutron}} = P \cdot n_i$, with n_i the amount of ion projectiles. Note, in the case of LDNS the number of projectiles depends on the energy as a result of the TNSA mechanism, $n_i \to n_i(E_i)$. For thin targets, the yield can be expressed as

$$\mathrm{d}N_{\text{Neutron}} = \sigma(E_i) n_i \rho_T \,\mathrm{d}l \tag{2.61}$$

$$= \sigma(E_i) n_i \rho_T \,\mathrm{d}E_i \frac{\mathrm{d}l}{\mathrm{d}E_i}, \tag{2.62}$$

with the particle density of the converter $\rho_T = \frac{\mathrm{N_A}\rho}{M_m}$. ρ is the density of the material and M_m is its molar mass. Finally, the thick target neutron yield for ions can be calculated from Equation 2.62 by integrating over the projectile's energy

$$N_{\text{Neutron}} = \int_{E_{\text{max}}}^{0} \frac{\sigma(E_i) n_i \rho_T}{-\frac{\mathrm{d}E_i}{\mathrm{d}l}} \,\mathrm{d}E_i. \tag{2.63}$$

From this equation, it is evident that neutron production is inversely proportional to the stopping power of the converter target's material. This can be interpreted as the projectile passing by fewer nuclei, thus reducing the probability of inducing a neutron-emitting reaction. The implication is that high-Z materials generate fewer neutrons for comparable neutron production cross sections for protons below ~ 40 to 60 MeV (Rücker et al. 2016).

Photo-nuclear reaction based converter targets are more involved, as the production ordinarily involves a two-step process in which an electron beam needs to interact with the material, thus generating γ-rays with sufficient energy. Equation 2.60 still holds in this case, with $\sigma(E_i)$ now the cross section for (γ,xn) reactions and the neutron production is given by

$$N_{\text{Neutron}} = \int_{E_{\text{B}}}^{E_{\text{max}}} \sigma(E_\gamma)\phi_\gamma(E_\gamma) \,\mathrm{d}E_\gamma, \tag{2.64}$$

where $\phi_\gamma(E_\gamma)$ is the spectral photon distribution which can be calculated from Equation 2.56. In contrast to the case of ions, Equation 2.63 is no longer applicable as γ-rays are not continuously slowed down in

matter but transfer energy/change direction in discrete interaction events. For this reason, determining the converter target dimensions for an electron-based neutron source is an elaborate process, oftentimes requiring Monte Carlo simulations (see section 2.4) for optimizations (Jallu et al. 1999; Huang et al. 2005; Petwal et al. 2007).

2.3.3. Neutron propagation and moderation in matter

Moving on from neutron generation, understanding how neutrons interact with matter is paramount for designing and utilizing neutron sources. The focus is therefore shifted to the propagation of neutrons in matter. Crucial to the quantification of neutron propagation is the attenuation model, which states that neutron interactions with matter can completely be described by the total nuclear cross section $\sigma(E)$. Similar to neutron production, the probability of a neutron interacting through a specific reaction channel can be calculated by Equation 2.60 when adjusting the cross section to the corresponding reaction channel $\sigma_{rc}(E)$. Thus, the number of reactions taking place in an infinitesimally thin material layer can be written as in the case of Equation 2.61, where $\mathrm{d}N_{\text{Neutron}}$ now stands for the number of reactions occurring and n_i for the number of neutrons passing through the layer.

Setting the number of reactions equal to the change in neutron flux Φ yields the differential equation

$$\frac{\mathrm{d}\Phi}{\mathrm{d}l} = -\sigma_{rc}(E)\rho_T\Phi, \tag{2.65}$$

solving the differential equation leads to an expression for the attenuation of neutrons in matter, caused by reaction channel rc. It has the same form as the Lambert-Beer law (Bouguer 1729; Lambert 1760; Beer 1852) for attenuation

$$\Phi(l) = \Phi_0 \cdot e^{-\sigma_{rc}(E)\rho_T l} \tag{2.66}$$

In this equation l is the thickness of the material and Φ_0 is the unattenuated flux, before entering the material. When the total attenuation is of interest the total neutron cross section needs to be used in Equation 2.66, $\sigma_{rc}(E) \rightarrow \sigma_t(E) = \sum_{rc}\sigma_{rc}$.

If the material is composed of different elements, the total attenuation is given by the individual contributions of each element

$$\begin{aligned}\Phi(l) &= \Phi_0 \cdot \Pi_k e^{-f_k\rho_T l\cdot\sum_{rc}\sigma_{k,rc}(E)} \\ &= \Phi_0 \cdot \Pi_k e^{-f_k\rho_T l\cdot\sigma_{t,k}(E)}\end{aligned} \tag{2.67}$$

where f_k is the fraction of element k in the material (Lamarsh, Baratta, et al. 2001; Stacey 2007). The mean free path λ_{fp} is an important quantity in the context of neutron propagation in materials, which describes the distance that neutrons can travel inside a material until only $1/e \approx 0.368$ of the incoming neutrons are left unscattered. This can be described by the condition $\Phi(l) = \Phi_0/e$. Using this condition and Equation 2.67 leads to

$$\begin{aligned}\lambda_{\text{fp}} &= \left(\rho_T \cdot \Sigma_k f_k \sigma_k(E)\right)^{-1} \\ &= 1/\Sigma_t.\end{aligned} \tag{2.68}$$

Σ_t is called the macroscopic cross section of the material and should not be confused with the symbol for summation.

Neutron scattering and moderation

Neutrons are ”born” in the fast energy region. However, many neutron applications require neutrons in the epi-thermal energy region or below. Obtaining neutrons in the energy region of interest can be achieved by moderation, a process in which a neutron interacts with a material, the moderator, thereby transferring energy via elastic and inelastic scattering processes. With proper moderator design and material selection, the final neutron spectrum can span up to 12 orders of magnitude in energy.

During inelastic neutron scattering, the nucleus of the moderator material, refereed to as just the nucleus for the rest of this section, obtains kinetic energy and is left in an excited state. Inelastic scattering exhibits an energetic threshold, which depends on the level structure of the nucleus and corresponds to the excitation energy. Following the scattering event, the nucleus de-excites through the emission of a γ-ray. In this reaction, the total kinetic energy is not conserved. Inelastic scattering only plays a minor role regarding neutron moderation. However, it is sometimes employed to moderate high energy neutrons down to energies where elastic scattering dominates.

The dominant process through which energy transfer occurs is elastic scattering with the nuclei of the moderator. In these events, the total kinetic energy is conserved and part of the neutron's kinetic energy is passed to the nucleus of the moderating material. Two types of elastic scattering exist, resonance elastic scattering and potential scattering (Stacey 2007). During resonance elastic scattering, a compound nucleus is formed, with subsequent neutron emission that has a reduced kinetic energy. Potential scattering can be understood quantum mechanically as hard sphere (s-wave) scattering (Stacey 2007) and can be described by the partial wave analysis formalism (Griffiths 2012; Sakurai, Napolitano, et al. 2014).

Approaching the scattering of hard spheres from the point of view of classical mechanics and taking a look at the kinematics involved (Balashov and Pontecorvo 1997), the energy of the neutron after an elastic scattering event E_f can be written as

$$E_f = \frac{E_i}{(A+1)^2} \cdot \left(\cos\theta + \sqrt{A^2 - \sin^2\theta}\right)^2, \tag{2.69}$$

with E_i the initial neutron energy, A the atomic mass of the scattering nucleus and θ the scattering angle. For large atomic masses, the final neutron energy after the scattering event is close to the initial energy and only a small amount of energy is transferred. E_f is minimized with small values for A, meaning that the highest energy transfer occurs in a scattering event with hydrogen. Setting $A = 1$ in Equation 2.69 and averaging over the scattering angle reveals that a neutron loses, on average, half its energy in an elastic collision with hydrogen, making hydrogen-rich materials highly moderating. This is the reason why neutron beams are more strongly attenuated by low-Z materials. A consequence of Equation 2.69 is that moderators are made from light materials, such as polyethylene, beryllium, graphite, among others.

2.3.4. Neutron detection

Detecting neutrons poses a unique challenge since they lack an electric charge, rendering direct detection methods almost impossible. Measurement of neutrons relies on choosing suitable nuclear reactions that produce secondary charged particles such as (n,α), (n,^{3}H), (n,p) and (n, elastic) reactions. The energy of the neutron determines the reactions of choice and can be divided into three categories: high-energy/fast, intermediate and epi-thermal neutrons. Utilizing this subdivision, the epi-thermal range includes all neutrons with energies in the epi-thermal regions and below, see section 2.3.1.

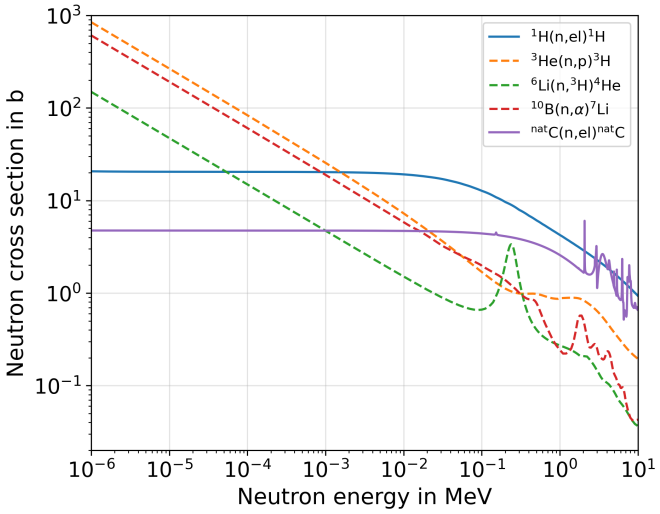

Figure 2.7.: Cross sections for a selection of commonly used neutron detection reactions. Solid lines represent reactions used to detect fast neutrons and the dashed line is for detection of the epi-thermal and intermediate neutron class. The cross section data is obtained from JENDL-4.0 nuclear data files (Shibata et al. 2011).

As discussed in subsection 2.3.3, the cross section governs the interaction of neutrons in matter. Therefore, neutron detection strongly depends on the cross section for the different reaction channels. Figure 2.7 shows the energy dependent cross sections for commonly used detection reactions.

The detection of fast neutrons and above is almost exclusively done by measuring elastic scattering reactions in hydrogen- or carbon-rich materials, like organic scintillators (Knoll 2010; Leo 2012) or diamond based semiconductor detectors (Liu et al. 2023; Millán-Callado 2023). In the context of this work, fast neutrons are primarily detected using organic plastic scintillators and bubble detectors. Bubble detectors will be introduced below.

Elastic neutron scattering in the scintillator material results in kinetic energy transfer from the neutron to the nucleus, resulting in a recoil ion. Recoil ions can obtain energies of several MeV, which they subsequently deposit along their trajectory inside the detector material, with their range and energy loss determined by Equation 2.59. Due to energy deposition, the scintillator material is elevated into an excited state, with the ensuing emission of photons returning the scintillator to the ground state. Photomultiplier tubes (PMTs) (Hamamatsu Photonics 2007) can be used to detect and amplify the photon signal, delivering a measurable current. Signals obtained by scintillators are therefore proportional to the amount of energy deposited, with the detection probability described by the cross section. Special care needs to be taken when analyzing the signals of plastic scintillators, as the light yield can be affected by quenching/saturation effects with high energy deposition density (J. B. Birks 1951; J. B. Birks 2013). Note, that this is not the only method to detect fast neutrons. Other detection mechanisms, neutron induces fission in the detector (Ingle et al. 1970; Guan et al. 2019) or neutron activation (Zankl et al. 1981) are also commonly used.

An unusual type of ”fast neutron detectors” in use at LDNS are Bubble Detectors (BDs), which were originally intended to be used as personal neutron dosimeters (Ing et al. 1997; Ing 2001). BDs are insensitive to γ- and x-rays, making them especially suitable for the environment of LDNS (Kleinschmidt et al. 2018). They are made from a plastic tube filled with a polymer gel in which super-heated halogen droplets are suspended. When a neutron interacts with the gel of the bubble detector, it generates recoil ions which

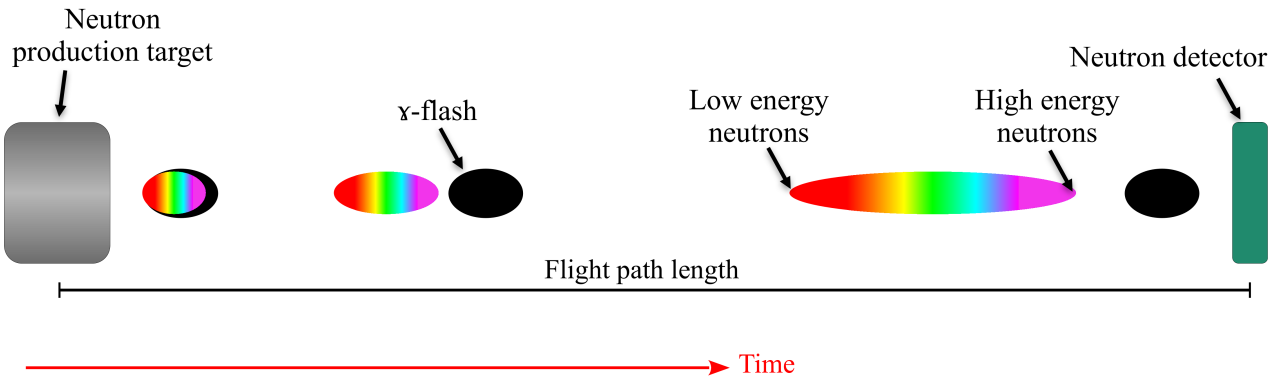

Figure 2.8.: Schematic drawing of a typical neutron time-of-flight measurement. Neutrons of all energies originate at the source with the primary pulse duration determined by the driver beam. During the propagation towards the detector the beam disperses due to the different velocities of the neutrons, leading to an elongated neutron pulse.

deposit their energy inside the gel. The energy deposition results in the expansion of the super-heated bubbles which can be counted and allow for neutron dose determination (Ing et al. 1997; Olsher et al. 2007).

In contrast to fast neutrons, epi-thermal and less energetic neutrons are mainly detected through neutron capture reactions. Commonly used reactions for the detection of slow neutrons are ^{10}B(n,α)^{7}Li, ^{6}Li(n,^{3}H)^{4}He and ^{3}He(n,p)^{3}H. All mentioned reactions follow a $1/v_{\text{neutron}}$ dependence in this energy region (Stacey 2007), see Figure 2.7. Boron and helium-based detectors are often used in the form of gas-filled tubes. However, boron-doped microchannel plates (MCPs) (Wiza et al. 1979) are also deployed. Lithium-based detectors appear as scintillation-based detectors, where a scintillating material is doped with ^{6}Li. The scintillation signal can either be measured with PMTs or an image-intensified camera.

Detection of intermediate neutrons is a more problematic undertaking, due to their energy being situated between fast and epi-thermal neutrons. Their energy is not sufficient enough to generate (measurable) scintillation signals, but their energy is in a region where the cross section, for most charged particle producing reactions, has fallen off significantly (see Figure 2.7). The reduction is a result of the $1/v_{\text{Neutron}}$ dependence of the cross section. Nonetheless, intermediate neutrons can be detected using the same reactions as used for slow/epi-thermal neutrons. ^{6}Li-based detectors are often used in this case, albeit at a much reduced detection efficiency.

Under experimental conditions, the energy of a neutron is determined through the Time-of-Flight (ToF, or in the case of neutrons nToF) technique. Direct energy determination is difficult due to the interaction properties of neutrons with matter due to their lack of charge. Therefore, the energy is calculated through the neutrons velocity, which can be obtained by measuring the flight path length between the source d_{ToF} and the time the neutron takes to reach the detector t_{n}. From these two quantities the velocity can be obtained $n_{\text{n}} = d_{\text{ToF}}/t_{\text{n}}$ and in the non-relativistic case the kinetic energy is thus calculated from $E_{\text{kin}} = \frac{1}{2}\text{m}_{\text{n}}v_{\text{n}}^2$. For neutrons exceeding $\gtrsim 0.5$ to 1 MeV the energy is calculated through the relativistic kinetic energy

$$E_{\text{kin}} = (\gamma - 1)\text{m}_{\text{n}}\text{c}^2, \tag{2.70}$$

where γ is the relativistic factor as defined in section 2.1.1. In this way, it is evident that neutrons that arrive earlier at the detector must possess higher energies. A schematic of a typical time-of-flight measurement is shown in Figure 2.8.

2.4. Monte Carlo method for particle transport

Monte Carlo (MC) simulations are a valuable tool in the world of nuclear radiation and neutron physics, which has been around since 1945 (Haghighat 2021). They can be used for source, beamline and detector design, as well as the optimization of experimental setups and radiation protection calculations. Concerning LDNS, they play a prominent role in the design, optimization and analysis of experiments. Especially during the analysis of experimentally obtained data, MC simulations play an essential role, as measured signals can be a superposition of many different signals caused by different particle species. Monte Carlo simulations must be utilized to properly separate the signals of interest from the noise caused by the harsh environment. The **P**article and **H**eavy **I**on **T**ransport code **S**ystem (PHITS or Phits) (Sato et al. 2023) version 3.32, developed by the Japanese Atomic Energy Agency, is the MC code of choice for this work. Benchmark studies demonstrating Phits' reliability can be found in (Y. Iwamoto et al. 2022). Following (Carter and Cashwell 1975) and (Haghighat 2021), this section will briefly introduce the field of MC simulations.

2.4.1. Overview

The basis of the Monte Carlo method for particle transport forms the Boltzmann transport equation, here given in its integral form (Carter and Cashwell 1975; Haghighat 2021)

$$\hat{\Omega} \cdot \vec{\nabla}\phi\left(\vec{r}, E, \hat{\Omega}\right) + \Sigma_t\left(\vec{r}, E\right)\phi\left(\vec{r}, E, \hat{\Omega}\right) = \int_0^\infty \int_{4\pi} \Sigma_s'\left(\vec{r}, E' \to E, \hat{\Omega} \cdot \hat{\Omega}'\right)\phi\left(\vec{r}, E', \hat{\Omega}'\right) \mathrm{d}\Omega' \, \mathrm{d}E' + S\left(\vec{r}, E, \hat{\Omega}\right), \tag{2.71}$$

$\phi\left(\vec{r}, E, \hat{\Omega}\right) = v(E) \cdot \hat{n}\left(\vec{r}, E, \hat{\Omega}\right)$ is the angular flux in phase space, with $v(E)$ its velocity, corresponding to energy E, $\hat{n}$ the particle density in phase space, Σ_t the macroscopic cross section, Σ_s' is the macroscopic scattering cross section and $S\left(\vec{r}, E, \hat{\Omega}\right)$ an (external) source term. $\hat{\Omega}$ is the angular distribution of the particles in phase space. Σ_s' includes all scattering reactions, such as elastic or inelastic scattering events, as well as neutron multiplication reactions, i.e. (n,2n) (Carter and Cashwell 1975). Equation 2.71 balances particle losses on the left side and particle production on the right side (Haghighat 2021). Each term represents a specific transport event: the first term describes particle propagation in phase space, with the second term representing a particle undergoing a collision. The third term describes particle scattering, with the fourth term describing the initial source distribution of the primary particles.

Solving for ϕ is a complex undertaking and analytical solutions only exist for special geometries and under specific assumptions (Haghighat 2021). However, the Monte Carlo method can simulate an ensemble of particles, in which known macroscopic cross sections are used to determine their behavior. In this way the individual contributions of the terms in Equation 2.71 can be approximated by averaging over individual particle histories. Thus, the average behavior of particles, such as the flux $\phi\left(\vec{r}_p, E, \hat{\Omega}\right)$ at given position p, can be determined (Carter and Cashwell 1975; J. P. Dabruck 2018; Haghighat 2021).

2.4.2. Nuclear Monte Carlo method

The simulation of radiation transport, using PHITS, follows a "simple" loop. From Equation 2.66 the probability of propagation without collision is given by $\exp(-\Sigma_t l)$ and the probability for an interaction in a distance $\mathrm{d}l$ is given by $\Sigma_t \, \mathrm{d}l$. Again Σ_t is the total macroscopic cross section. The probability an interaction occurring between l and $l + \mathrm{d}l$ is thus described by $p(l)\,\mathrm{d}l = \Sigma_t e^{-\Sigma_t l}\,\mathrm{d}l$ (Carter and Cashwell 1975) and leads to

$$P(l) = \int_0^l \Sigma_t e^{-\Sigma_t l'} \, \mathrm{d}l' = \xi$$
$$\rightarrow \xi = 1 - e^{-\Sigma_t l}. \tag{2.72}$$

Therefore, the distance to the next interaction point, assuming only one region/material, is given by $l = -\ln(\xi)/\Sigma_t$. For multiple regions/materials this method becomes inefficient (Haghighat 2021) and the distance to the next interaction point is sampled in terms of the mean free path (Equation 2.68) leading to

$$b = \frac{l}{\lambda_{\text{fp}}} = -\ln \xi.$$

To determine the region/material of the next collision point, $b_k = \sum_i r_i/\lambda_{\text{fp},i}$ is calculated for each region/material along the current flight path. Afterwards, a random number ξ is generated and the particle is moved until the inequality

$$b_{k-1} < -\ln \xi \leq b_k \tag{2.73}$$

is satisfied. Thereby determining the region of the next collision to be in k. Finally, the interaction point l_k inside the region is determined by (Haghighat 2021)

$$l_k = -\frac{\ln \xi + b_{k-1}}{\Sigma_{t,k}}.$$

With the position of the interaction point determined, the next step is to sample the interaction type from the underlying nuclear cross section data or reaction models. The probability of interaction i (out of N possible interactions) can be calculated by using $p_i = \Sigma_i/\Sigma_t$ where the individual probabilities need to satisfy $P_n = \sum_i^n p_i$, with $n \leq N$. A new random number ζ is generated. If it satisfies the inequality $P_{n-1} < \zeta \leq P_n$, then the interaction of type n will be selected for the collision (Haghighat 2021). Once the type of interaction is determined, the result of the interaction is sampled from a new set of random numbers, which determine the scattering angle and the energy of the particle after the collision, again following the procedure of Equation 2.73.

The scattering angle and energy distribution is based on experimentally measured nuclear data libraries like JENDL-4.0 (Shibata et al. 2011). If any secondary particles are generated during the interaction, they are added to the particle stack and transported once the previous particles are terminated. Particles can be terminated in different ways. They can either be absorbed in an interaction or leave the simulation space boundary. Moreover, if the energy of a particle drops below a user-defined energy cut-off, they are also terminated (Carter and Cashwell 1975; Haghighat 2021).

This is a very brief description of the Monte Carlo method as applied to nuclear physics. There are other important parameters and features of this technique, such as particle weight, variance reduction, dose rate and activation calculations, as well as tallying quantities of interest. As this is a vast topic, it will not be discussed here and the reader is instead referred to (Carter and Cashwell 1975; Booth 1985; Stacey 2007; Haghighat 2021; Kulesza et al. 2022).

2.5. Laser-driven neutron sources

The first experimental demonstration of laser-driven neutron sources, short LDNS, dates back to the late 80s, early 90s (Key et al. 1998; Disdier et al. 1999). At that point neutron, production from high intensity laser beams was mostly a by-product of fusion research (Yogo, Arikawa, et al. 2023). With the advent of laser-driven particle acceleration, the first experiments that used separate sources for charged particle acceleration and neutron neutron generation were conducted in the early 2000s (Lancaster et al. 2004). The concept of spatially separating the charged particle from the neutron source would come to be known as the "pitcher-catcher" scheme, the predominant scheme to drive LDNS today. A schematic of a standard pitcher-catcher setup is shown in Figure 2.9. Nowadays, laser-accelerated ions and electrons are utilized to drive LDNS, e.g (Roth, D. Jung, et al. 2013; Feng et al. 2020), with the ion-based implementation being more commonly pursued.

In a typical pitcher-catcher setup, the laser pulse is directed onto a target, resulting in the generation of a charged particle beam by means of either TNSA or LWFA. LDNS based on TNSA commonly employ thin (solid state) foil target as the pitcher, with thicknesses of 0.1 to $1\,\mu$m. These foil targets are disintegrated by the laser pulse during the acceleration process, making them single-use. The implications of this will be elaborated on later in this section. Laser wakefield acceleration typically relies on gas jets/nozzles or gas cells for the pitcher, in which the laser pulse drives a non-linear plasma wave, resulting in an energetic electron beam. Depending on the pitched particle species, different catchers need to be used. For ions the choice of catcher material has the highest influence on the neutron generation efficiency, with the geometry chosen in such a way that the entire ion beam is stopped within the catcher. Common materials are lithium (or Li-based materials such as LiF), beryllium and copper (Alvarez et al. 2014; Alejo, Ahmed, et al. 2015; Yogo, Arikawa, et al. 2023). For electrons both the catcher material and the geometry of the moderator play an important role, which is investigated and discussed in chapter 6. Suitable materials are high-Z materials such as tungsten, tantalum, lead or uranium.

Achievable neutron fluences per solid angle can reach up to $2.3 \times 10^{10}\,\mathrm{n/sr/shot}$ (Yogo, Lan, et al. 2023) for ion-based sources employing the TNSA mechanism. Reported total neutron yields in 4π reach up to $3 \times 10^{11}\,\mathrm{n/shot}$ (Yogo, Lan, et al. 2023). A review of LDNS studies shows that for ion-based sources, the neutron production per unit of laser energy peaks at around 10^6 to $10^8\,\mathrm{n/sr/J}$ (Yogo, Arikawa, et al. 2023). In contrast, LDNS based on laser wakefield acceleration is only sparsely reported. For these sources, the highest measured neutron fluence is around $2.5 \times 10^6\,\mathrm{n/sr/shot}$, with a total production of $3.2 \times 10^7\,\mathrm{n/shot}$ (Feng et al. 2020). The neutron production per unit of laser energy is thus around $9 \times 10^5\,\mathrm{n/sr/J}$, which is lower than what is reported by other state-of-the-art LDNS experiments.

Using LDNS, a wide range of neutron energies were measured. Ranging from up 50 to $80\,\mathrm{MeV}$ (Zimmer, Scheuren, Kleinschmidt, et al. 2022) on the fast end of the energy spectrum, to less than $5\,\mathrm{meV}$ on the low end (Mirfayzi, Yogo, et al. 2020).

Unique characteristics of LDNS are: 1) their comparatively small form factor, with potential for further miniaturization; 2) potentially high mobility; 3) lower acquisition and operating costs; 4) sub-ns primary neutron pulse durations; 5) high instantaneous neutron fluence; 6) low expected machine activation and 7) multi-source capabilities.

Elaborating on a few selected characteristics mentioned above, the primary neutron pulse duration is an essential parameter of neutron sources for energy-resolved measurements. Since the energy determination of neutrons relies on the time-of-flight technique, a long primary pulse duration results in significant uncertainties for the energy determination. The short pulse durations should make LDNS sources ideal candidates for applications requiring fast neutrons, such as fast neutron imaging (Mizutani et al. 2020; Yogo, Arikawa, et al. 2023).

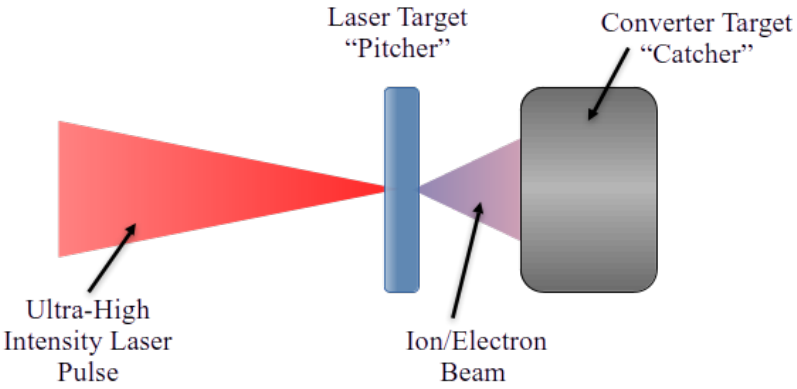

Figure 2.9.: Schematic drawing of the pitcher-catcher scheme. The experimental setup needs to adjusted based on the type of particle (ions vs. electrons) that is used for neutron generation. In the case of electrons the pitcher is usually a gas jet (nozzle) or gas cell, with the catcher made from a high-Z material, e.g. W, Pb. For ions the target is typically a thin foil with a thickness of 0.1 to $1\,\mu$m. Common catcher materials are LiF, Be or Cu.

Additionally, lower activation of machine parts is expected, compared to conventional sources, due to the working principle of LDNS. During normal operation, the intensity of the laser pulse outside the focus is not high enough to cause ionization or nuclear reactions. Thus, only the catcher and parts/materials directly near the generation point can become activated, reducing the amount of nuclear waste generated by the source.

The last point highlights the flexibility of LDNS. While the main goal is to generate neutrons, the acceleration process (TNSA) and neutron production are usually accompanied by high energy γ-rays. These γ-rays can drive a dual-purpose/dual-use source. Furthermore, the accelerated ion beam can also be utilized (Alvarez et al. 2014; Yogo, Arikawa, et al. 2023). LDNS based on electron acceleration using LWFA could additionally be used as a compact muon source if the provided electron beams have sufficient energy (Swanson 1979).

While the field of LDNS has made significant progress in recent years, with the first proof-of-principle demonstrations of established neutron techniques (Mizutani et al. 2020; Zimmer, Scheuren, Kleinschmidt, et al. 2022; Yogo, Lan, et al. 2023), many challenges remain. These challenges must be overcome for these source to be adopted by the scientific community or industry. One of the biggest issues is the scaling of LDNS. State-of-the-art implementations utilize laser systems that provide laser pulses with a repetition rate in the range of one shot per minute to one shot per hour (Zimmer, Scheuren, Kleinschmidt, et al. 2022; Yogo, Lan, et al. 2023; Lelièvre et al. 2023). These low reposition rates result in low average neutron fluxes and severely limit the type of measurements that can be conducted at LDNS. With high repetition rate laser systems now becoming available (Mourou et al. 2011), targetry has become the focus and, in part, the limiting factor with regard to scalability. Ion-based LDNS are especially affected by the problems plaguing currently employed targetry systems, due to the disintegration of the target after each shot and the reliance on solid state foil target. The challenge regarding self-replenishing, high repetition rate capable targets has led to the emergence of an entire field of research (Morrison et al. 2018; A. S. Tebartz 2018; Treffert 2023). In contrast, targetry systems used in electron acceleration, based on LWFA, are inherently self-replenish since they are gas-based. Thus, the above described problems do not apply to electron-based laser-driven neutron sources.

Finally, another critical issue for LDNS is their scaling with laser pulse energy. Laser energies typically needs to be reduced for laser systems to become more compact and operate at higher repetition rates. This

results from heat build-up and thermal effects (Patrizio 2020), which negatively impact the acceleration performance without adequate compensation. However, since the neutron yield for ion-based sources scales approximately with E_{Laser}^{2-4} (Zimmer 2020; Yogo, Lan, et al. 2023), reducing the laser energy leads to a significant decrease in neutron flux. If the energy is reduced by a factor of 10, the repetition rate needs to be increased by a factor of 10^2 to 10^4 in order to achieve the same neutron flux as before. Therefore, ion-based LDNS are not the ideal platform for compact, laboratory-scale neutron sources.

However, a promising alternative for an efficient and scalable low laser energy neutron source exists. It is based on the acceleration of electrons with the LWFA mechanism. Due to their lower mass, electrons can be accelerated to high energies with laser energies in the range of $\sim 1\,\text{J}$ (S. P. Mangles et al. 2006; V. Malka 2020; Wenz and S. Karsch 2020). These high energy electron beams can efficiently generate neutrons via (γ,n) reactions. For this reason and in combination with the inherently high repetition rate capable targetry system, laser-accelerated electron-based neutron sources hold immense potential as table-top, laboratory-scale neutron sources. Since electron-based LDNS have not been studied as thoroughly as ion-based LDNS, much optimization potential remains unused, which will be addressed in chapter 6.

Neutron (resonance) imaging at LDNS

A wide range of neutron applications exist, many of which are feasible at laser-driven neutron sources (Alvarez et al. 2014). During this work, energy-selective neutron imaging is investigated, both in the thermal and fast neutron energy range. Neutron imaging experiments were conducted in three separate beamtimes utilizing a laser-driven neutron source. Here, the basic principles of neutron imaging required for the analysis of the experimental data presented in chapter 5 are introduced.

Neutron imaging is a method in which the 2D spatial neutron distribution of a neutron beam is measured after it passes through a sample under investigation. The resulting image is called a neutron radiography or (neutron) transmission image. The transmission through the sample strongly depends on the isotopic composition of the sample, as well as the energy of the neutrons (Anderson et al. 2009). To gain insight into a sample's composition, two different types of neutron images must be recorded. One of the images required is the so-called flat field (FF) or open beam image, during which no sample is placed on the neutron beam. Only the neutron distribution as emitted by the source is recorded during this image. The other image is the sample image, in which the object under investigation is placed in the neutron beam. The flat field image and the sample image are related to each other via the Lambert-Beer attenuation law (see Equation 2.67):

$$I(d) = I_{\text{FF}} \cdot e^{-\rho_T d \cdot \sigma_t(E)},$$

where d is the thickness of the sample, ρ_T the particle density and $\sigma_t(E)$ the total neutron cross section. I_{FF} is the neutron intensity of the flat field and $I(d)$ the intensity behind the sample. Dividing the sample intensity by the flat field intensity returns the normalized transmission image

$$I_T = \frac{I(d)}{I_{\text{FF}}} = e^{-\rho_T d \cdot \sigma_t(E)}.$$

From this equation, properties of the object under investigation can be inferred, such as its density, thickness or material composition. By carefully selecting the energies E at which an image is recorded, the distribution of specific isotopes within a sample can be identified (Losko and S. Vogel 2022). Identification is made possible by the unique neutron resonance structure, in the (epi-) thermal energy region of each isotope. If the selected energy E matches the energy of a resonance, then the neutron beam is strongly

attenuated by the sample. The resonance structure is caused by the nuclear energy levels of the isotope and the energy levels of the reaction product (Lapp and Howard 1972). This type of imaging is known as neutron resonance imaging and is commonly conducted using (epi-) thermal neutron beams. Due to the strong attenuation in this energy region, thin samples are most suitable for investigation using this method.

In contrast, the high penetrability of fast neutrons can be leveraged to investigate bulk samples. This type of neutron imaging is referred to as fast neutron imaging. This type of imaging is especially well suited to non-destructively investigate low-Z materials housed inside a high-Z shell (Aswal et al. 2022).

Neutron imaging is a versatile technique to investigate complex samples that has been adopted by in the field of (fusion) research, civil engineering, industrial and nuclear inspections, as well as in the (nuclear) security sector (Imaging 2008; Nelson et al. 2018; Aswal et al. 2022). For example, in the nuclear technology sector neutron imaging can be used to assess (spend) nuclear fuel to determine the distribution of fissile material (Losko and S. Vogel 2022). Furthermore, neutron imaging can be applied to find organic matter that is shielded by high-Z materials, which is of great importance in the security sector, where it can be used to find explosives and other illicit materials in containers (Buffler 2004; Buffler and Tickner 2010; Mor, Dangendorf, et al. 2015).

3. Detector evaluation methods for absolute neutron numbers and spectra

This chapter serves as an introduction to different methods essential to this thesis. It involves the basic settings of Monte Carlo simulations, the reconstructions of absolute neutron spectra based on organic scintillator measurements, and the energy-dependent response of bubble detectors. The reconstruction algorithm for organic scintillators implemented throughout this work is influenced by the approach detailed in (Mirfayzi, Kar, et al. 2015). Reconstruction of the neutron flux using bubble detectors (Ing et al. 1997; Ing 2001) is based on a new approach developed as part of this dissertation.

3.1. Fundamental setup of PHITS simulations

This work uses the PHITS (Sato et al. 2024) Monte Carlo code, Version 3.31, developed by the Japan Atomic Energy Agency (JAEA). The reliability of the code has been demonstrated in several benchmark studies, e.g. (Y. Iwamoto et al. 2022). Several nuclear reaction models combined with nuclear data cross section libraries are used. Whenever possible, nuclear data libraries are used to model reactions. For proton reactions, the JENDL-4.0HE (Kunieda et al. 2016; Konno 2023) data library is used for proton energies up to $200\,\mathrm{MeV}$. If cross section libraries are unavailable, the interaction of light ions such as protons and deuterons is simulated using the INCL (Intra-Nuclear Cascade of Liège) model (Boudard et al. 2013). The Kurotama model (Iida et al. 2007) is used to augment the INCL model for proton-nucleus reactions at intermediate energies. Additionally, low proton and deuteron energy ($E < 100\,\mathrm{MeV}$) reactions are modeled using a combination of intra-nuclear cascade models and distorted wave Born approximation (Hashimoto, O. Iwamoto, et al. 2014; Hashimoto, Y. Iwamoto, et al. 2014b).

In order to simulate the interaction of heavy ion collisions such as carbon and lithium, the JAERI quantum molecular dynamics model (Ogawa et al. 2015) is used. Photon and electron transport is handled by the Electron-Gamma Shower code (Hirayama et al. 2005), version 5 (EGS5), which is included in the PHITS package. Cross sections for photo-nuclear reactions are based on the TENDL-2019 (Koning, Rochman, et al. 2019) nuclear data library and JENDL-5.0 (O. Iwamoto et al. 2023) in the case of uranium. JENDL-5.0 is used for uranium as it more closely reproduces results published in (Barber and George 1959; Gayther and Goode 1967; Alsmiller Jr and Moran 1967; Lai and Y. Yang 2022). Neutron transport uses the JENDL-4.0 (Shibata et al. 2011; Matsuda et al. 2019) nuclear data library up to a neutron energy of $20\,\mathrm{MeV}$; above this energy, nuclear reaction models are used. All simulations assume a temperature of $20\,^{\circ}\mathrm{C}$.

3.2. Neutron spectrum reconstruction from organic scintillators

Characterizing a neutron source requires the measurement of both the generated neutron number and their energetic distribution. Measurements of neutron spectra are most commonly conducted in a time-of-flight (ToF) setup, where the time the neutron takes to cover the distance from the source to the detector is converted into kinetic energy. Neutrons are generally generated around $1\,\mathrm{MeV}$ and are thus classified as

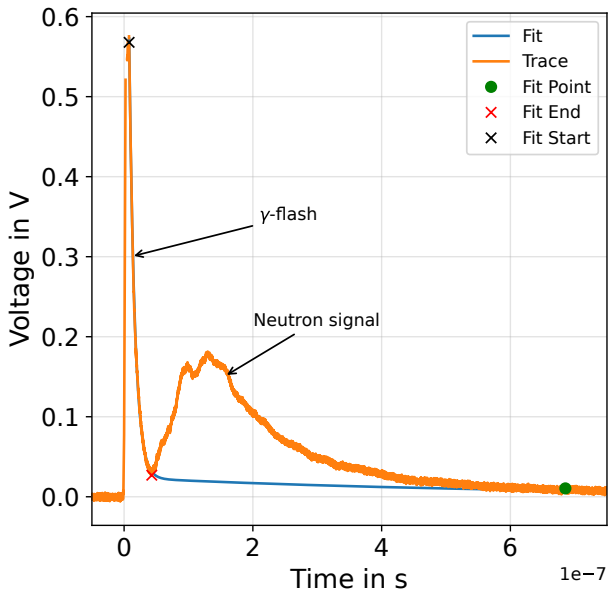

(a) Raw measured scintillator trace.

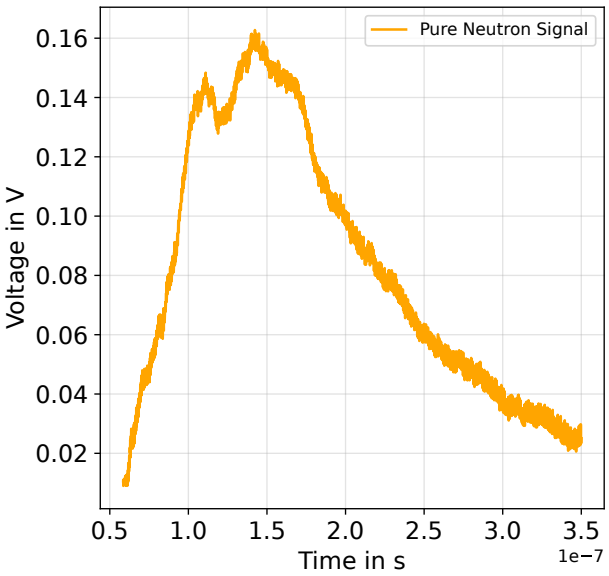

(b) Scintillator trace after γ-flash subtraction.

Figure 3.1.: (a) shows the full signal recorded by the oscilloscope. The blue line is a fit to the falling edge of the γ-flash. The line is fitted between the red and black cross. In order to include potential offsets and the slow decay components of the scintillator, the fit also takes data points to the right of the green dot into account. (b) shows the pure neutron signal after subtraction of the γ-flash. This is the signal fed to the reconstruction algorithm.

fast neutrons. As discussed in chapter 2, fast neutron detection relies on recoil nuclei, mainly hydrogen, which are generated when (fast) neutrons interact with the detector. Due to the short pulse duration of the neutron beam and the corresponding high neutron flux at LDNS, fast neutron detectors at laser-based sources are mostly used in current mode. Therein, individual neutron events cannot be resolved anymore, rather the measured neutron peak can be considered a large pile-up event of around 10^5 neutrons arriving within a short time window.

Here, fast neutron detection is based on an EJ232Q organic scintillator manufactured by Eljen Technology (Eljen Technology 2021) that is coupled to a Hamamatsu R2083 photomultiplier tube (PMT) (Hamamatsu 2020). The recoil nuclei cause the scintillator to emit photons with wavelengths between 400 to $450\,\mathrm{nm}$, which in turn are able to generate free electrons in the photo-cathode of the PMT. The efficiency with which free electrons are generated in the photo-cathode is called the quantum efficiency, which for the R2083 is $q_{\mathrm{eff}} = 0.27$ for the wavelength region of interest (Hamamatsu 2020). Subsequently, the (free) electron signal is amplified by the PMT through a series of dynodes, where the amplified signal is proportional to the original signal at the photo-cathode. The amplification of the PMT is controlled by the supply voltage U_{PMT} and the overall amplification strength is referred to as gain factor g, which is given by (Hamamatsu 2020)

$$g = 7.24534 \times 10^{-12} \cdot U_{\mathrm{PMT}}^{5.04619}, \tag{3.1}$$

For experimental data presented in this thesis, U_{PMT} was set to $1.3\,\mathrm{kV}$ unless stated otherwise. Finally, the amplified signal is recorded by a fast oscilloscope, which measures the time-dependent voltage signal $U(t)$.

The signal $U(t)$ measured at the oscilloscope can be related to the (time-dependent) number of photons $\Delta N_{\mathrm{ph}}(t)$ arriving within a time window Δt, which generates the primary electron signal in the photo-cathode.

The relation can be obtained from Ohm's law and results in

$$\frac{\Delta N_{\text{ph}}(t)}{\Delta t} = \frac{U(t)}{g \cdot q_{\text{eff}} \cdot R \cdot \text{e}}, \tag{3.2}$$

where e is the elementary charge, $U(t)$ the voltage measured by the oscilloscope and $R = 50\,\Omega$ the impedance of the oscilloscope channel. Equation 3.2 forms the basis for converting the measured scintillator signal, also called trace, into a neutron spectrum. An example of a measured can be seen in Figure 3.1a. In the trace, two peaks are visible, corresponding to the γ-rays flash (left, larger peak) and the neutron signal (right, smaller peak).

To convert the trace to a neutron spectrum, the γ-flash needs to be subtracted from the overall signal. This is done by fitting a function (blue line in Figure 3.1a) to the γ-flash and subtracting the fit from the trace, leaving only the neutron signal as displayed in Figure 3.1b. In order to make use of Equation 3.2 and convert the data of Figure 3.1b into a neutron spectrum, the neutron induced photon production $\Delta N_{\text{ph}}(t)/\Delta t$ in the scintillator needs to be calculated.

Central to the photon generation from recoil nuclei is the scintillation efficiency. The scintillation efficiency given in photons per MeV_{ee} is $2900\,\text{photons}/\text{MeV}_{\text{ee}}$ for the EJ232Q scintillator used in this work (Eljen Technology 2021). This measure returns the amount of generated photons per $1\,\text{MeV}$ deposited by electrons in the scintillator material (obtained from the manufacturer). However, as described above and in subsection 2.3.4, neutrons deposit energy through recoil protons, not electrons. Therefore, the scintillation efficiency must first be converted into photons per MeV deposited by protons. The scintillation efficiency of energy deposited by protons is lower when compared to electrons due to the proton's higher localized ionization potential, which leads to quenching effects in the scintillator (Chou 1952a; Laplace et al. 2022), thus reducing the scintillation efficiency. A theory describing the scintillation efficiency and quenching effects has been developed by Birks (J. Birks 1951; J. B. Birks 2013) and was later adapted by Chou (Chou 1952b; Chou 1952a). Discussion of the theory of scintillators is out of the scope of this work and the reader is referred to literature instead.

In this work, the conversion of scintillation efficiency for electrons to the scintillation efficiency of protons is achieved by fitting a polynomial function $l_{\text{fit}}(E_{\text{dep}})$ to experimentally measured light yield for mono-energetic protons reported in (Gooding and Pugh 1960; D. Smith et al. 1968; Madey and F. Waterman 1972; Madey, F. M. Waterman, et al. 1978; O'Rielly et al. 1996). The fit to the data and a comparison of the light yield from electrons is displayed in Figure 3.2a. For electrons, the scintillation efficiency is linear in the energy region of interest, indicated by the dashed black line.

With the help of $l_{\text{fit}}(E_{\text{dep}})$, the light yield per unit of deposited energy for protons can be calculated relative to the light yield for electrons. Therefore, the light yield for electrons is calculated first by using the scintillation efficiency obtained from the manufacturer:

$$Y_{\text{electron}} = 2900\,\frac{\text{photons}}{\text{MeV}_{\text{ee}}} \cdot E_{\text{dep}}.$$

Y_{electron} is then multiplied by the ratio of the red and black curve in Figure 3.2a for a given amount of deposited energy E_{dep} to obtain the light yield from protons. For example, electrons depositing $25\,\text{MeV}$ generate 7.3×10^4 photons, whereas $25\,\text{MeV}$ deposited by protons only generates 4.7×10^4 photons.

Since the energy transfer from neutrons to protons in an elastic scattering event is non-discrete, the energy transfer here is characterized by the average energy deposition per neutron at a given energy E_{n}.

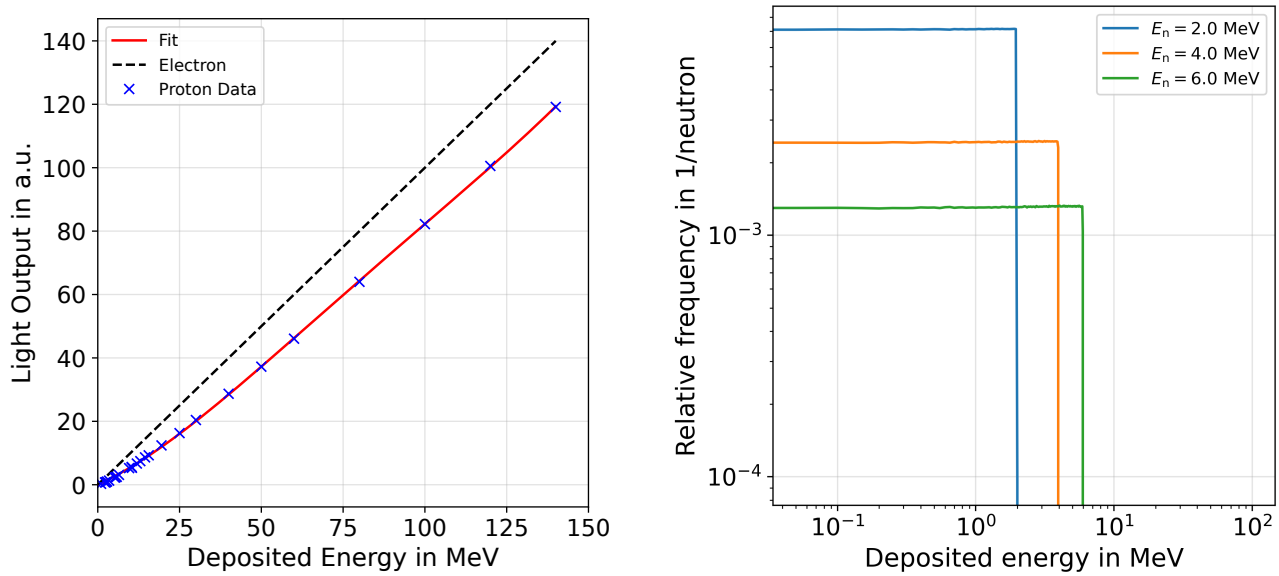

(a) Scintillator light output.

(b) Neutron energy deposition.

Figure 3.2.: (a) comparison of the scintillation efficiency between energy deposition by electrons and protons. Blue crosses indicate data points taken from literature and the red line is a fit to the data points. (b) shows the relative frequency for energy deposited by recoil protons calculated using PHITS. The recoil protons are produced during scattering events with mono-energetic neutrons of energy E_n.

The average energy deposition for a given neutron energy and its interaction probability with the scintillator is determined from Monte Carlo simulations. Figure 3.2b shows the energy deposition from a single elastic scattering event for mono-energetic neutrons of different energy. In total, 36 different neutron energies E_n are simulated and the average light yield for each energy is calculated. E_n is narrowly spaced between 0.3 to $20\,\mathrm{MeV}$, with the spacing increasing towards higher energies, up to a maximum neutron energy of $90\,\mathrm{MeV}$. Neutron interactions are divided into two categories: single interactions and multiple interactions. Single interactions refer to the first interaction between a neutron and the scintillator. Every additional interaction is classified as multiple interactions and the energy deposition resulting from these extra interactions is scored separately.

The resulting light yield from single interactions in the scintillator is then fitted by

$$f_\mathrm{single} = a_1 \cdot E_\mathrm{n} \cdot \tanh\left(E_\mathrm{n}\right) - a_2 \cdot E_\mathrm{n}^{a_3} \tag{3.3}$$

to allow for interpolation between data points. From the fit the fit parameters a_i are determined to be $a_1 = -18 \pm 2$, $a_2 = -343 \pm 11$ and $a_3 = 0.44 \pm 0.02$. Similarly, the light yield from multiple neutron interactions is fitted by

$$f_\mathrm{multi} = \frac{b_1}{E_\mathrm{n}^{b_2}} \cdot \frac{1}{\exp\left(b_3/E_\mathrm{n}\right) - 1} \tag{3.4}$$

with the fit parameter b_i returned as $b_1 = 692 \pm 139$, $b_2 = 1.2 \pm 0.1$ and $b_3 = 1.33 \pm 0.03$. The same procedure is applied to the interaction probabilities for single and multiple neutron interactions. Light yields

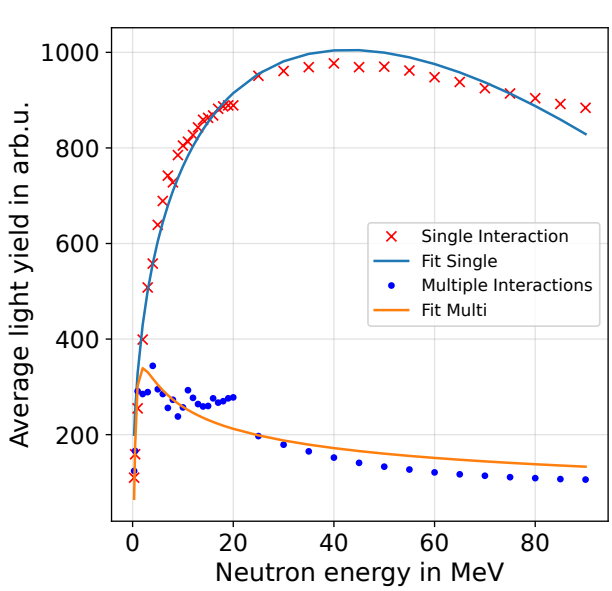

(a) Neutron induced light yield from the scintillator.

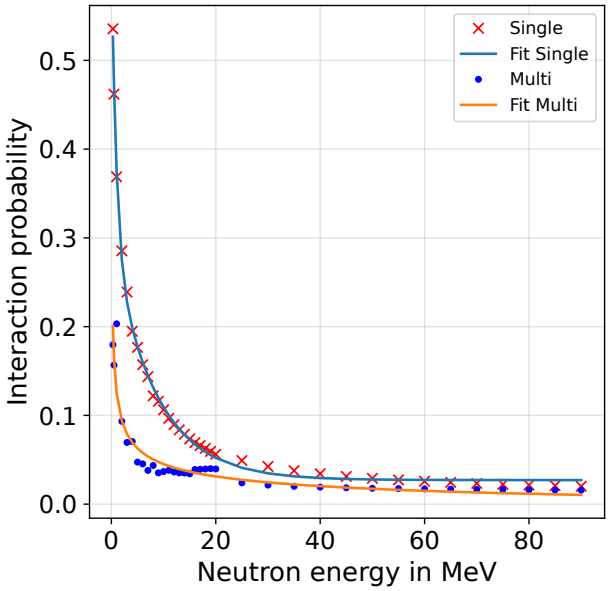

(b) Neutron detection probability of the scintillator.

Figure 3.3.: (a) Average expected light yield from mono-energetic neutrons interacting with the scintillator based on Monte Carlo simulations (red crosses and blue dots). Single interaction describes the first scattering event of a neutron in the scintillator, with multiple interactions summarizing subsequent scattering events. The data for multiple interaction events excludes the first scattering interaction. The blue line is the fit corresponding to Equation 3.3 and the orange line corresponds to a fit using Equation 3.4. (b) show the interaction probability at a given neutron energy.

for the different neutron energies, weighted by their interaction probability, are shown in Figure 3.3a.Figure 3.3b shows the interaction probability for single and multiple interactions.

Once the average light yield for a neutron at a given energy is determined, the time-dependent voltage signal needs to be converted into a neutron energy-dependent (E_n) voltage signal. This can be achieved by the following transformation

$$\begin{aligned}\frac{\mathrm{d}N_\mathrm{ph}}{\mathrm{d}E_\mathrm{n}} &\approx \frac{\Delta N_\mathrm{ph}}{\Delta E_\mathrm{n}} \\ &= \frac{\Delta N_\mathrm{ph}}{\Delta t} \cdot \frac{\Delta t}{\Delta E_\mathrm{n}},\end{aligned} \tag{3.5}$$

where $\Delta N_\mathrm{ph}/\Delta t$ is given by Equation 3.2 and ΔE_n and Δt are the width of the energy and time bins, respectively. In the case where the time bins Δt become infinitesimally short $\Delta t \to 0$, Equation 3.5 turns into

$$\begin{aligned}\frac{\mathrm{d}N_\mathrm{ph}}{\mathrm{d}E_\mathrm{n}} &= \lim_{\Delta t \to 0} \frac{\Delta t}{\Delta E_\mathrm{n}} \cdot \frac{\Delta N_\mathrm{ph}}{\Delta t} \\ &= \frac{1}{\dot{E}_\mathrm{n}} \cdot \frac{\mathrm{d}N_\mathrm{ph}}{\mathrm{d}t},\end{aligned} \tag{3.6}$$

with $\dot{E}_\mathrm{n}$ is the first derivative in time t_n of the relativistic kinetic energy $E_\mathrm{n} = (\gamma - 1) \cdot \mathrm{m_n c^2}$. Since $\Delta t \to 0$ is not satisfied for the detector used in this work, neutron spectra reconstruction is based on Equation 3.5.

Next, the contribution of neutrons interacting multiple times with the scintillator is subtracted from $\frac{\mathrm{d}N_\mathrm{ph}}{\mathrm{d}E_\mathrm{n}}$ using Equation 3.4. Lastly, the neutron number can be calculated by using Equation 3.3 and 3.2, in combination with the probability $p(E)$ of a neutron interacting with a hydrogen nucleus in the scintillator:

$$\frac{\mathrm{d}N}{\mathrm{d}E_\mathrm{n}} = \frac{1}{f_\mathrm{single}(E_\mathrm{n}) \cdot p(E_\mathrm{n})} \frac{\mathrm{d}N_\mathrm{ph}}{\mathrm{d}E_\mathrm{n}}. \tag{3.7}$$

At laser-driven neutron sources, neutron detectors based on scintillators are typically surrounded by lead shielding to suppress the influence of the γ-flash. However, the lead shielding also attenuates the neutron beam. Therefore, the attenuation caused by the lead needs to be considered for each energy E_n

$$\frac{\mathrm{d}N_\mathrm{corr}}{\mathrm{d}E_\mathrm{n}} = \frac{1}{T(E_\mathrm{n})} \cdot \frac{\mathrm{d}N}{\mathrm{d}E_\mathrm{n}}, \tag{3.8}$$

where $T(E_\mathrm{n})$ is the neutron transmission through the lead for a given energy. The transmission is again determined from PHITS simulations. Equation 3.8 is the final expression that is used to reconstruct fast neutron spectra from a measurement using an organic scintillator in current mode.

The approach described in this section has limitations, which will be discussed briefly. The method is quite sensitive to the subtraction of the γ-flash and the overlap in time between the γ-flash and the neutron signal. An improper fit can lead to an offset, which leads to an over- or underestimation of the neutron flux. Ensuring sufficient separation between the γ-flash and the neutron signal is essential. This separation requirement is what drives the use of sizable lead shielding assemblies around scintillators.

During the reconstruction, it is assumed that only the interaction of neutrons with hydrogen atoms causes the scintillator to emit light. However, recoil carbon nuclei also contribute to the light yield of the scintillator (Satoh, Sato, et al. 2006; Satoh and Sato 2022). Neglecting the carbon contributions leads to underestimating the average light yield per neutron, thus overestimating the reconstructed neutron fluence. Expanding the method implemented in this work should include carbon contributions, which can be calculated from codes such as SCINFUL (Dickens 1988), NRESP (Dietze and Klein 1982) or SCINFUL-QMD (Satoh, Sato, et al. 2006).

Moreover, the influence of scattered neutrons or photons overlapping with the neutron signal is also neglected, which can lead to an overestimation of the measured neutron flux if significant scattering occurs close to the detector. Additionally, the scintillator's decay behavior and its pulse shape is not considered during the reconstruction, meaning that the pulse overlap is not included. To implement a correction for the decay behavior, the detector would need to be absolutely calibrated by measuring the pulse shape $P(E_\mathrm{n})$ of the scintillator at various neutron energies. The number of photons N_ph can then be corrected via

$$N_\mathrm{ph}(t) = N_\mathrm{ph}(t) - \left(\sum_{i=1}^{n} N_\mathrm{ph}(t - i \cdot \Delta t) \cdot P(t - i \cdot \Delta t, E) \right), \tag{3.9}$$

where $P(t, E_\mathrm{n})$ is the normalized pulse shape of a scintillation event caused by a neutron with energy E_n (Lelièvre et al. 2023). Δt is the width of time bins, determined by the sampling rate of the oscilloscope and $n \cdot \Delta t < t$.

3.3. Calculating neutron fluences from bubble detector measurements

Bubble detectors have emerged as the de facto standard to characterize and compare the neutron number per solid angle at laser-driven neutron sources. Their insensitivity to electromagnetic interference, be it EMP or γ-radiation, makes them well suited for the high noise environment found at LDNS (Kleinschmidt 2017). The detectors are manufactured by Bubble Technology Industries (BTI) (Bubble Technology Industries 2023). A detailed account of the working principle can be found in (Ing et al. 1997). The basic working principle is that visible gas bubbles are formed within a gel after irradiating bubble detectors with neutrons. The amount of bubbles after irradiation is proportional to the neutron dose received by the detector. From the dose or rather the number of bubbles in a detector, the neutron fluence can be calculated. Figure XY shows an image of a bubble detector after irradiation.

The common way to calculate the neutron number per solid angle $\hat{N}$ from a number of bubbles b follows the approach summarized in (Kleinschmidt et al. 2018)

$$\hat{N} \left[\frac{1}{\mathrm{sr}} \right] = \frac{b \cdot d^2}{\bar{c} \cdot s_0}, \tag{3.10}$$

where d is the distance from source to detector in cm, s_0 the sensitivity of the bubble detector in bubbles per mrem and $\bar{c}$ is an average value for the neutron energy-dependent response curve $c(E_\mathrm{n})$ of bubble detectors. The response function was measured by the manufacturer and published in (Ing et al. 1997), the data of the response function was obtained from the manufacturer and is displayed in Figure 3.5. Commonly an average value of $\bar{c} = (3.0 \pm 0.4) \times 10^{-5} \, \frac{\mathrm{b \cdot cm^2}}{\mathrm{neutron}}$ is used as a value for the detector response, for a detector with a sensitivity of $1\,\mathrm{bubble/mrem}$ is assumed (Kleinschmidt et al. 2018).

The interaction behavior of neutrons with matter is strongly governed by its kinetic energy. Thus an approach that averages the energy-dependent response function can lead to over-/underestimation of neutron fluence for a couple of reasons. Averaging the response function removes the influence that the neutron spectrum has on the calculation and therefore excludes characteristics of the reaction that generates the neutrons.

An adapted methodology was developed during the course of this thesis to account for the energy dependency of the response functions properly. It is based on calculating a setup-specific effective value for $c(E_\mathrm{n})$ that takes the emitted neutron spectrum into account. This effective value c_eff depends on the parameters of the experimental setup, for example, the pitcher-catcher combination, the angle under which the bubble detectors are placed and the shape of the neutron spectrum. The method was developed with the help of Dr. Benedikt Schmitz and a manuscript discussing the approach has been submitted to and is under review at Review of Scientific Instruments (Scheuren, Millan-Callado, et al. 2024). The developed code is available on Gitlab[1] under the Creative Commons Attribution 4.0 license.

Figure 3.4.: A bubble detector after irradiation. The orange circle contains the detector signal. These are the bubbles indicated by variable b in Equation 3.11.

A second minor correction to the neutron flux calculation includes a correction for the temperature dependence of the sensitivity s_0 of bubble detectors. The value for s_0 supplied by BTI is a reference value for 20 °C. In (Buckner et al. 1994; Ing et al. 1997), BTI published the experimentally determined temperature dependence of the bubble detectors' sensitivity $s(T)$, which is used as the foundation of the temperature correction. Finally, since s_0 is subject to tolerances/variation of the calibration, resulting in deviations of the quoted (given by BTI) to the actual/measured sensitivity (Ing 2001), a correction factor for the calibration is also determined.

Basics of the new approach

The proposed new methodology is based on effective values for the response c_eff and sensitivity s_eff, which take the spectral shape of the neutron beam, the temperature of the bubble detectors, as well as production variances into account. The biggest correction originates from the inclusion of the energy dependency of $c_\mathrm{eff}(E_\mathrm{n})$, which at its core is based the convolution of normalized neutron spectra with the the response function $c(E_\mathrm{n})$. The neutron spectra can either be based on experimental measurements or deducted from Monte Carlo simulation. From these effective values, the neutron number/fluence N can be calculated following Equation 3.10

$$N\left[\frac{1}{\mathrm{sr}}\right] = \frac{b \cdot d^2}{c_\mathrm{eff}(E_\mathrm{n}) \cdot s_\mathrm{eff}(T)}. \tag{3.11}$$

As the variables are independent of each other, the uncertainty corresponding to Equation 3.11 is calculated via Gaussian error propagation and is given by

[1] https://git.rwth-aachen.de/surrogat-models/bubbledetectors

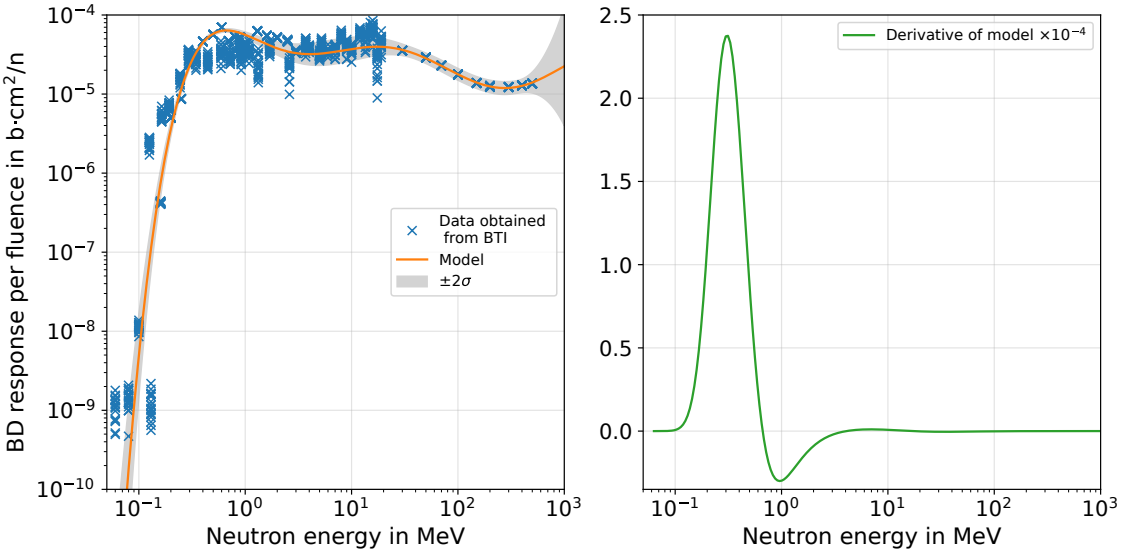

Figure 3.5.: The left plot shows the reconstructed BD response curve in orange. The reconstruction was implemented and retrieved by Dr. Benedikt Schmitz. The markers represent the measured and simulated response, for a bubble detector with a sensitivity of $1\,\mathrm{mrem/bubble}$. The data was provided by BTI. The response data was also published in (Ing et al. 1997) (measurements) and (M. Smith et al. 2015) (simulations). The plot on the right shows the first derivative with respect to neutron energy of the reconstructed response curve.

$$(\Delta N)^2 = \sum_i \left(\frac{\partial N}{\partial x_i} \cdot \Delta x_i\right)^2 \tag{3.12}$$

$$= \left(\frac{d^2 \cdot \Delta b}{c_{\mathrm{eff}} \cdot s}\right)^2 + \left(\frac{2b \cdot d \cdot \Delta d}{c_{\mathrm{eff}} \cdot s}\right)^2 + \left(-\frac{b \cdot d^2 \cdot \Delta c_{\mathrm{eff}}}{c_{\mathrm{eff}}^2 \cdot s}\right)^2 + \left(-\frac{b \cdot d^2 \cdot \Delta s_0}{c_{\mathrm{eff}} \cdot s_0^2 \cdot f(T)}\right)^2$$
$$+ \left(-\frac{b \cdot d^2 \cdot \Delta T}{c_{\mathrm{eff}} \cdot s_0 \cdot f^2(T)} \cdot \frac{\partial f(T)}{\partial T}\right)^2 + \left(-\frac{b \cdot d^2 \cdot \Delta E_n}{s \cdot c_{\mathrm{eff}}^2} \cdot \frac{\partial c_{\mathrm{eff}}(E_n)}{\partial E_n}\right)^2, \tag{3.13}$$

where $x_i \in [b, d, c_{\mathrm{eff}}, s_{\mathrm{eff}}, E_{\mathrm{n}}, T]$ are the variables of Equation 3.11 and $\Delta x_i \in [\Delta b, \Delta d, \Delta c_{\mathrm{eff}}, \Delta s_{\mathrm{eff}}, \Delta T, \Delta E_n]$ the uncertainty of the associated variables.

To calculate the convolution of the neutron flux $\phi(E_{\mathrm{n}})$ with the response function $c(E_{\mathrm{n}})$, an analytical expression needs to be found. This is done by reconstructing the function based on the measured (Ing et al. 1997) and simulated (M. Smith et al. 2015) data via bootstrapping and Gaussian Process Regression.

The temperature correction is based on a polynomial fit $f(T)$ to the data published by BTI (Buckner et al. 1994; Ing et al. 1997) and the correction factor k_{dev} to take deviations from the factory quoted to the actual sensitivity of the detectors is calculated based on data published in (Ing 2001). The method was implemented with the help of Dr. Benedikt Schmitz who supplied the reconstruction algorithm for determining $c(E_{\mathrm{n}})$.

Reconstruction of $c(E_\mathrm{n})$ and its derivative

Looking at the energy dependency of the response data (crosses) and the reconstructed curve (orange line), displayed in the left plot of Figure 3.5, it can be seen that the response is higher for neutrons with energies from 0.4 to $1.8\,\mathrm{MeV}$ compared to $\gtrsim 2\,\mathrm{MeV}$ neutrons, thus making the detectors more sensitive to neutrons below $2\,\mathrm{MeV}$, resulting in the generation of more bubbles. The data shown is based on the simulated (red crosses) and measured (blue crosses) data provided by BTI.

As the response function is rather complex, a surrogate model is applied for the reconstructions based on Gaussian process regression from the SMT toolbox (Saves et al. 2024). During the reconstruction, the uncertainty of each data point is accounted for by applying a parametric bootstrap. In case of significant differences between measured and simulated data, the experimentally measured data is given precedence over the simulated data points, which explains the „peak“ around 600 to $800\,\mathrm{keV}$ in Figure 3.5.

Crucially, the model $\mathfrak{f}$ is trained on the logarithmic ($\log_{10}$) values of the supplied data points displayed in Figure 3.5. This is done to achieve greater stability, as the data points span almost six orders of magnitude. The model thus also returns the logarithmic response function c_sm

$$c_\mathrm{sm}(E_\mathrm{n}) = \mathfrak{f}\left(\log_{10}(E_\mathrm{n})\right), \tag{3.14}$$

and the response in Figure 3.5 (orange curve) is obtained from

$$\begin{aligned} c(E_\mathrm{n}) &= 10^{c_\mathrm{sm}(E_\mathrm{n})} \\ &= 10^{\mathfrak{f}(\log_{10}(E_\mathrm{n}))}. \end{aligned} \tag{3.15}$$

The derivative of $c(E_\mathrm{n})$ is needed to calculate the uncertainty in neutron number ΔN based on Equation 3.13 and is given by

$$\frac{\partial c}{\partial E_\mathrm{n}}(E_\mathrm{n}) = \frac{\mathfrak{f}'\left(\log_{10}(E_\mathrm{n})\right)}{E_\mathrm{n}} \cdot 10^{\mathfrak{f}(\log_{10}(E_\mathrm{n}))}. \tag{3.16}$$

The derivative $\mathfrak{f}'$ of the fit function can be obtained from the surrogate model output.

Determination of c_eff

To calculate c_eff, the output of the surrogate model $c(E_\mathrm{n})$ is convoluted with the differential neutron spectrum obtained from Monte Carlo simulations.

The neutron spectrum used here is obtained from PHITS simulations. In the simulations, a TNSA proton beam recorded during an experimental campaign at the DRACO laser is used to generate neutrons in different converter materials, which are commonly discussed in the context of LDNS. Experimentally measured neutron spectra can also be used to calculate the effective response value, as long as they are normalized. c_eff is calculated by

$$c_\mathrm{eff}(E_\mathrm{n}) = \frac{1}{\eta} \cdot \int_{E_0}^{E_u} c(E_\mathrm{n}) \cdot \frac{d\varphi}{dE_\mathrm{n}} dE_\mathrm{n}. \tag{3.17}$$

$$= \frac{1}{\eta} \cdot \int_{E_0}^{E_u} c(E_\mathrm{n}) \cdot \phi(E_\mathrm{n}) dE_\mathrm{n}, \tag{3.18}$$

where E_0 and E_u are the upper and lower energy limits for which $c(E_\mathrm{n})$ or $\phi(E_\mathrm{n})$ are defined. η is the normalization factor, calculated through

$$\eta = \int_{E_i}^{E_f} \phi(E_\mathrm{n}) dE_\mathrm{n}, \tag{3.19}$$

with E_i and E_f being the lowest and highest neutron energies recorded in the spectrum, respectively.

Table 3.1 contains a comparison of c_eff values for different neutron-generating target materials that hold relevance to LDNS. The neutrons in these examples are scored at $0°$ relative to the proton beam. The differences are the results of the spectral distribution of the neutrons, which can be seen in Figure 3.6. Furthermore, the energy and number of emitted neutrons depends on the emission angle of the neutrons relative to the incoming proton beam and thus, c_eff also depends on this angle. In Figure 3.7a the neutron spectra for a LiF converter are shown at different angles and Figure 3.7b shows the angular dependence of c_eff.

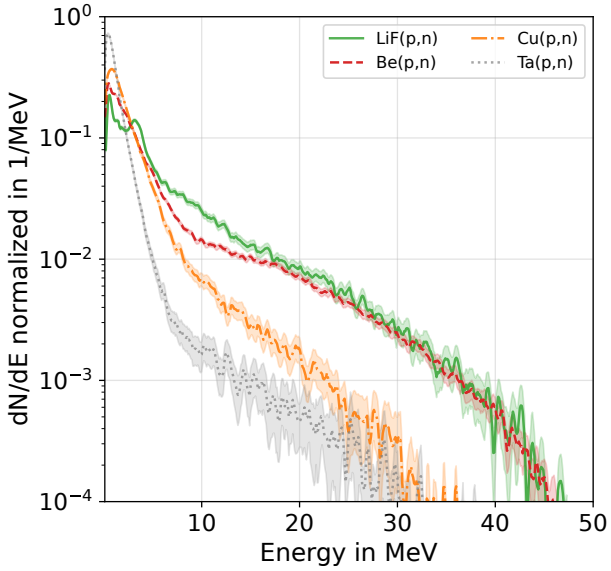

Figure 3.6.: Neutron spectra obtained from PHITS simulations utilizing a TNSA proton spectrum measured at the DRACO laser facility. Neutrons are scored at $0°$. See chapter 4 for more details on the input spectrum.

Material	c_eff in b · cm^2/neutron
LiF	$(3.9 \pm 0.2) \times 10^{-5}$
Be	$(4.0 \pm 0.2) \times 10^{-5}$
Cu	$(4.2 \pm 0.2) \times 10^{-5}$
Ta	$(4.6 \pm 0.3) \times 10^{-5}$

Table 3.1.: Calculated values for c_eff for different catcher materials, based on the spectra shown to the left. Only the converter material was changed in the Monte Carlo simulation.

The difference between the effective response value calculated by the new method in comparison to the value used by (Kleinschmidt et al. 2018) ranges from $30\,\%$ to $53\,\%$ at $0°$, depending on the converter material. Thus, simply substituting $\bar{c}$ by c_eff can change the measured neutron fluence by up to $53\,\%$, for the converter materials tested. As a rough rule of thumb, the lower the average neutron energy emitted from the target, the greater the value for c_eff. Conversely, projectile-converter combinations that produce higher energetic neutrons have smaller c_eff. This is also reflected in spectra shown in Figure 3.6.

At LDNS, neutrons are often generated from a mix of protons and deuterium ions, due to the usage of

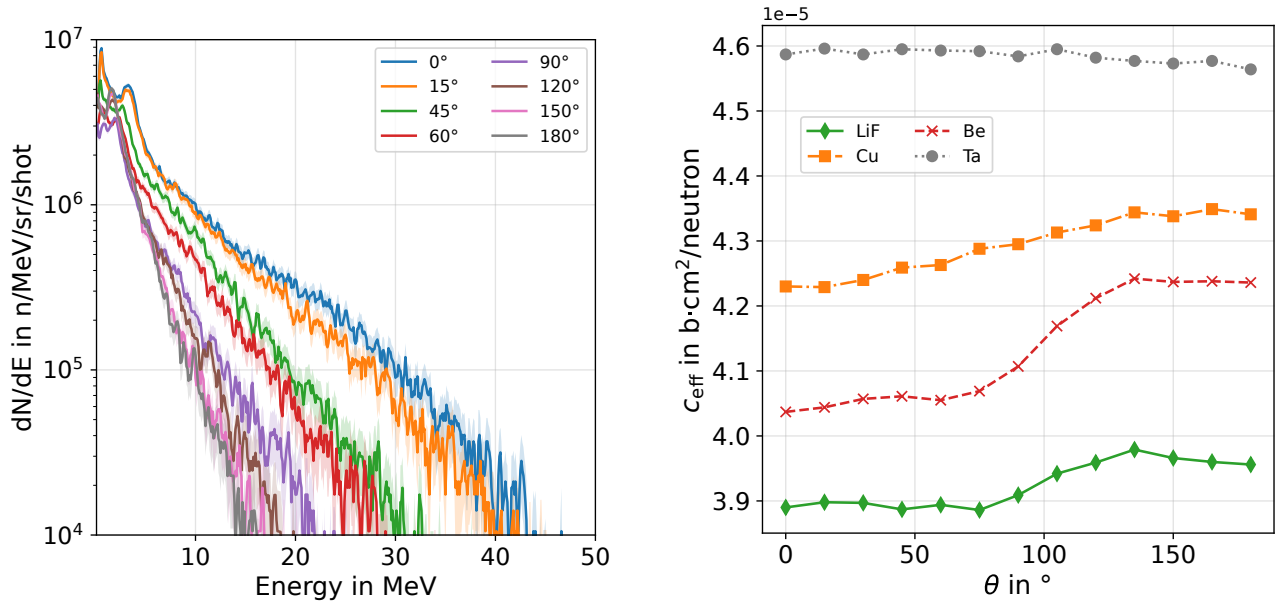

(a) Neutron spectrum emitted by LiF at different angles. (b) Angular dependency of c_{eff}.

Figure 3.7.: (a) shows neutron spectra from PHITS simulations using a LiF converter scored at different angles. (b) show the angular dependence of c_{eff} for a LiF catcher, based on the spectra shown in (a). Also included is the angular dependency using a Cu catcher.

deuterated targets, see (Roth, D. Jung, et al. 2013; Kleinschmidt et al. 2018). These ”mixed” sources can also be treated by this new approach, as long as the relative contributions from each projectile to the overall neutron yield is known. The neutron spectrum can then be expressed as a linear combination of both source terms

$$\Phi_{\text{tot}}(E_{\text{n}}) = \sum_i \alpha_i \Phi_i(E_{\text{n}}), \tag{3.20}$$

with $\sum_i \alpha_i = 1$. α_i represent the relative contribution of projectile i to the total yield, whereas $\Phi_i(E_{\text{n}})$ is the differential neutron spectrum. Practically, this means that the absolute spectra for all projectile species of interest must be measured at LDNS. In the majority of cases, the projectiles of interest are limited to protons and deuterons.

In the case of deuterated targets, generating both proton and deuterium beams, a lower boundary for the neutron fluence can be determined by only using the neutron spectrum from (p,n) reactions to calculate c_{eff}. Deuteron induced (d,n) reactions commonly have large positive Q-values (depending on the converter material), meaning emitted neutrons have higher energies. Recalling that higher average neutron energies lead to lower values for c_{eff}, thus increasing the neutron number per solid angle as calculated by Equation 3.11.

Determination of s_{eff}

The temperature dependency of the sensitivity $s(T)$ was investigated by BTI and published in (Ing et al. 1997). Based on the published data, the effective sensitivity can be expressed as

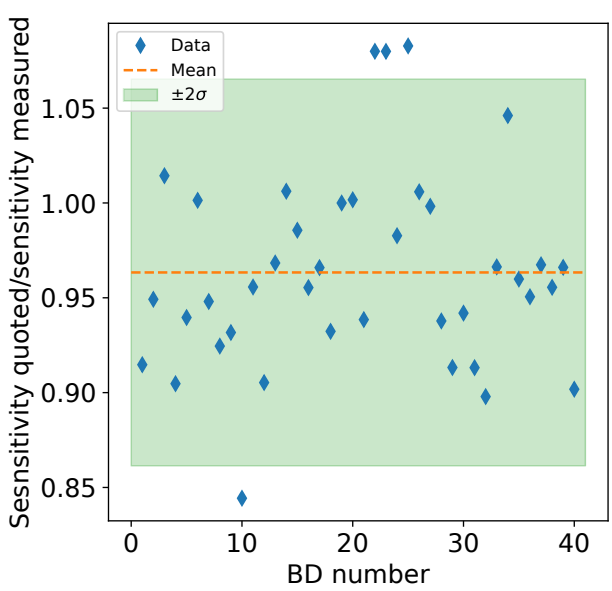

(a) Variance of the quoted sensitivity.

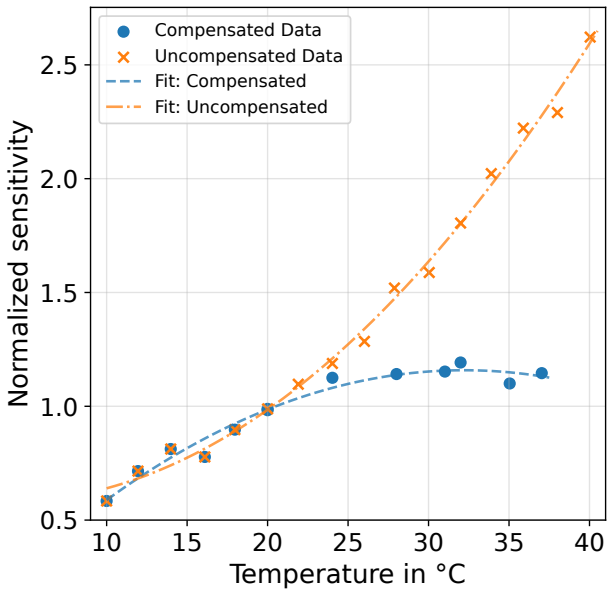

(b) Temperature dependency of BDs.

Figure 3.8.: (a) shows variations of the quoted vs. measured sensitivity of 40 different bubble detectors. The data is obtained from BTI and is published in (Ing 2001). (b) published data of the temperature dependence for two kinds bubble detectors. In this work only detectors of the compensated type are used. The lines are fits to the corresponding data points.

$$s_{\text{eff}}(T) = \frac{s_0}{k_{\text{dev}}} \cdot f(T) \tag{3.21}$$

$$= \hat{s}_0 \cdot f(T), \tag{3.22}$$

where s_0 is supplied by BTI and is the reference sensitivity at $20\,^{\circ}\text{C}$. k_{dev} is a correction factor taking the deviation between quoted and measured sensitivity of the detectors into account and is based on a data set published in (Ing 2001). The data compares the sensitivity given by BTI, referred to as quoted sensitivity, to measured sensitivity by dividing the quoted by the measured sensitivity, see Figure 3.8a. k_{dev} is defined as the mean of the data points and results in $k_{\text{dev}} = 0.963$. The uncertainty of $\hat{s}_0$ is determined from the standard deviation of the published data set and defined as $\Delta\hat{s}_0/\hat{s}_0 = 0.102$.

The temperature dependence is obtained by fitting a quadratic function to the data provided in (Ing et al. 1997), displayed in Figure 3.8b and is given by

$$f(T) = a_0 \cdot T^2 + a_1 \cdot T + a_2, \tag{3.23}$$

with a_i representing the fit parameters listed in Table 3.2. At $T = 20\,^{\circ}\text{C}$ the correction that is applied to s_0 is $f(T)/k_{\text{dev}} = 1.024$, leading to a difference of about $2.4\,\%$ compared to the previously used method. At the reference temperature of $20\,^{\circ}\text{C}$, the influence of the corrections is mostly negligible, but for deviation from the reference temperature, the correction becomes more significant. For example, at $16\,^{\circ}\text{C}$ the difference is greater than $10\,\%$.

Table 3.2.: Coefficients for Equation 3.23 fit to data published in (Ing et al. 1997).

BD kind	a_0 in 10^{-3} 1/°C^2	a_1 in 10^{-2} 1/°C	a_2
Compensated	-1.2 ± 0.2	7.4 ± 0.9	-0.04 ± 0.1
Uncompensated	1.5 ± 0.2	-1.1 ± 0.8	0.6 ± 0.1

Uncertainty contributions and limitations

This section investigates the precision of the method discussed above. Precision in the context of this section is defined as the relative uncertainty $\Delta N/N$, with the total uncertainty ΔN calculated according to Equation 3.12. For the discussion, results that were measured during an experimental campaign at the DRACO laser system are utilized. The experimental campaign will be discussed in detail in the next chapter. The focus in this section is on the dependence of the precision on the number of recorded bubbles for commonly used distances between the source and the bubble detector. Since c_{eff} and Δc_{eff} are needed for the discussion, the values presented for LiF in Table 3.1 are used. $\Delta d = 3\,\text{cm}$ is given by the dimensions of the detector, the source and the flight path. The value used here is based on the DRACO experimental campaign and is the smallest possible value for the uncertainty of the distance, determined by the size of the bubble detectors and catcher. Furthermore, $T = (20 \pm 1)\,°\text{C}$ is assumed for the analysis. $\Delta E_{\text{n}} = 0.05\,\text{MeV}$ is defined by the energy mesh used in the Monte Carlo simulation and a value $s_0 = 25\,\text{bubbles/mrem}$ is used.

The final contribution to the total uncertainty is the uncertainty in the number of recorded bubbles Δb. This uncertainty consists of two parts; first, the uncertainty due to Poisson statistics. The second contribution is related to the visual readout of the bubble detectors. During the experiment the bubble detectors are readout by the Bubble Reader III (Bubble Technology Industries 2024) manufactured by BTI. Readout using the Bubble Reader is based on counting the bubbles in two images taken from opposite sides of the detector. Due to the 3D distribution of bubbles inside the detector, the obtained bubble number is subject to uncertainty, as bubbles can overlap or two bubbles can be mistaken for one by the software. To estimate the uncertainty associated with the readout process, each bubble detector is readout at four different random positions. Afterwards, the standard deviation of the four readouts is calculated and defined as the uncertainty/error of the readout δb. Figure 3.9a shows the correlation between the number of bubbles b and the readout uncertainty δb, for data recorded at the DRACO laser system. Thus, the uncertainty Δb for a number of bubbles b is defined as:

$$\Delta b = \sqrt{b} + \delta b. \tag{3.24}$$

Using the fit shown in Figure 3.9a, the precision of the method can be estimated, using Equation 3.13. This is done for distances ranging from 0.5 to $3\,\text{m}$, which contains the most commonly used distances. The results can be seen in Figure 3.9b. Concerning the number of bubbles b, the maximum is set to 1000 bubbles. It can be seen that in a best-case scenario a relative uncertainty of around $14\,\%$ can be achieved, at a distance of $3\,\text{m}$ from the source and $b = 1000$ bubbles. When positioning the detector at a distance of $0.5\,\text{m}$, the lowest achievable relative uncertainty is around $19\,\%$.

Taking Equation 3.13 into account in combination with the results of Figure 3.9a, it can be seen that for $b \lesssim 20$ to 30 bubbles, the precision is dominated by the influence uncertainty uncertainty contribution Δb. In contrast, going to large values of $b \gtrsim 200$ bubbles shows a much slower decrease in the uncertainty, meaning that in this range, the dominant contribution does not originate from Δb. Again, using Equation 3.13 shows that the contribution from Δd is dominant in this range. Since $\Delta d \approx 3\,\text{cm}$ is limited by the dimension of the

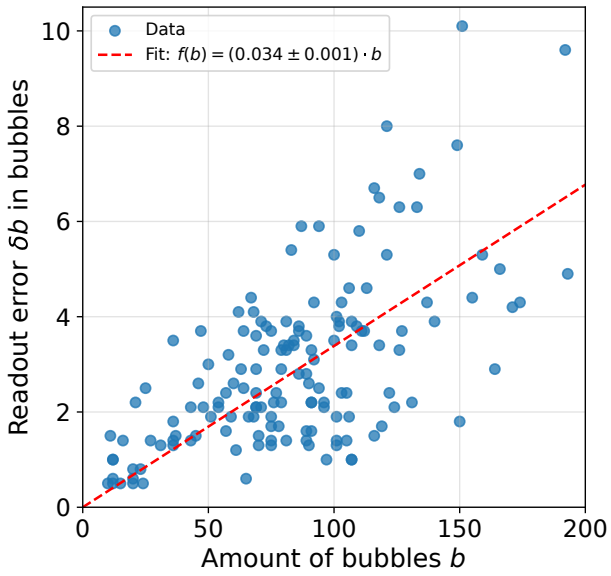

(a) Readout error vs. number of counted bubbles.

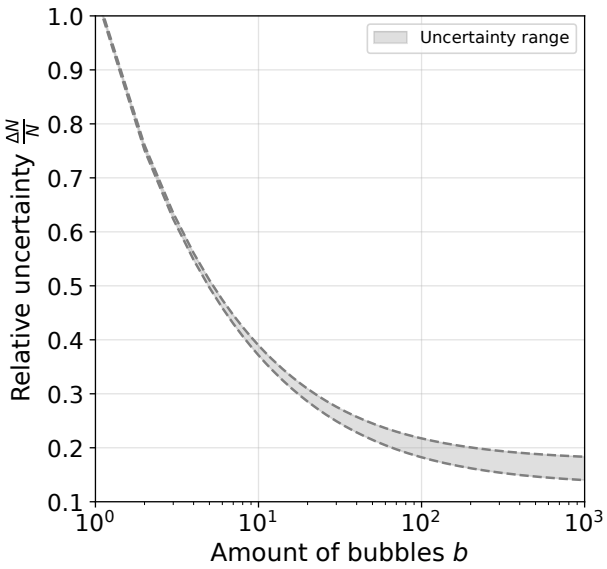

(b) Relative uncertainty of the method.

Figure 3.9.: (a) shows the correlation between the number of bubbles and readout error based on experimental data obtained at the DRACO laser. A correlation coefficient of 0.62 is found. (b) shows the relative uncertainty of the calculated neutron flux in dependency on the amount of bubbles b. A sensitivity of $s_0 = 25\,\text{bubbles/mrem}$ is assumed and values δb are based on the fit shown in (a).

bubble detector and the neutron source, this figure cannot be improved and thus represents the limit of the achievable precision.

In Figure 3.10 the contribution of each term of Equation 3.13 is shown, for a selected measurement using the LiF converter during the DRACO campaign. The number of bubbles for most detectors ranges from 25 to 130 bubbles per detector for the results shown in the figure. Thus, based on Figure 3.9b, that for most detectors Δb should be the dominant contribution. This assumption is confirmed by the data presented in the plot, except for the bubble detector labeled with "Jumper". This detector contained around 190 bubbles and therefore the influence of Δb becomes smaller and it can be seen that the contribution of Δd starts to play a more prominent role, as expected from Figure 3.9b.

From Figure 3.10 it can also be seen that $\Delta \hat{s}_0$ can contribute significantly to the overall uncertainty. This is due to the large variation of the quoted versus measured sensitivity shown in Figure 3.8a. However, in contrast to the contributions from Δd, the influence of this term can be reduced by conducting calibration measurements for each bubble detector. Thereby, the sensitivity can be determined for each detector individually, which will be more accurate than the correction term calculated here.

From the considerations presented above, a minimum relative uncertainty of $0.14 \leq \Delta N/N \leq 0.2$ under realistic experimental conditions is established based on results presented in Figure 3.9b. In the regime of small values for b, the precision is limited by the contribution of Δb to the relative uncertainty and for large values of b, it is limited by the dimension of the detectors and neutron source.

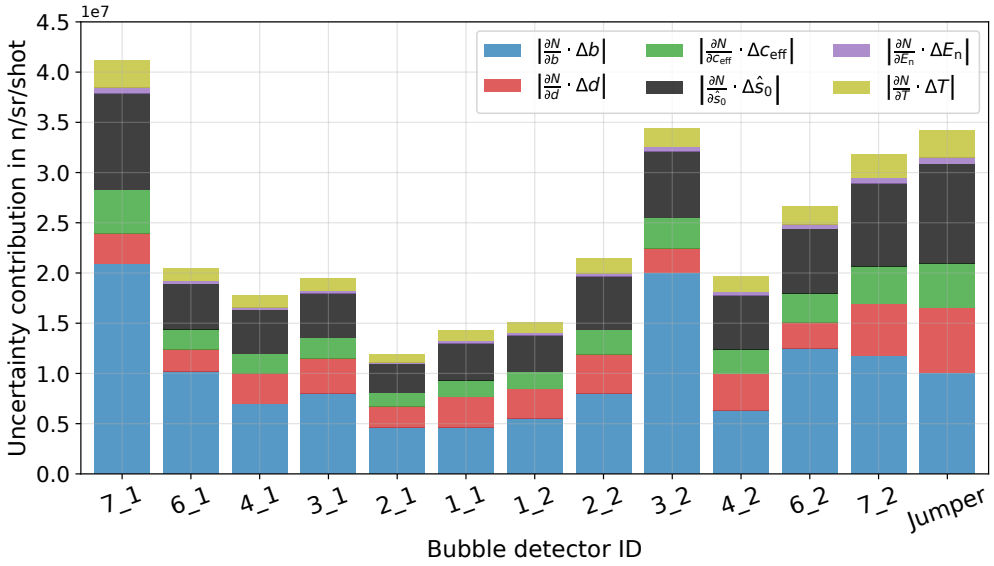

Figure 3.10.: Values for the individual uncertainty terms of Equation 3.13. The presented results are based on data recorded during an experimental campaign at the DRACO laser system, which will be discussed in detail in the next chapter. It can be seen that the contribution for Δb is dominant for the recorded data set. Secondary contributions originate from $\Delta \hat{s}_0$ and Δd. The contribution of $\Delta \hat{s}_0$ can be minimized by calibrating the bubble detectors with a known neutron source before an experiment.

4. Comprehensive characterization of a LDNS at the DRACO laser system

The experiment detailed in this chapter took place at the Helmholtz Zentrum Dresden Rossendorf (HZDR) and was carried out in collaboration with the University of Seville and the HZDR. The campaign had two main goals. The first goal was to demonstrate the capability of LDNS sources to function as a platform for nuclear physics experiments, such as neutron cross section measurements in the fast neutron regime. To achieve this goal, semiconductor-based diamond detectors were used and analyzed by the University of Seville as part of another doctoral thesis (Millán-Callado 2023). The second goal was to comprehensively characterize the neutron source by investigating the generated neutron fields, where they originate, the neutron generation stability, and the performance of the detectors (beamlines). This characterization was conducted as part of the presented thesis and is the topic of this chapter.

During the campaign neutrons were generated by employing the pitcher-catcher scheme, directing laser accelerated protons on a catcher, either made from lithium-fluoride (LiF) or copper (Cu). The dominant mechanism of neutron production inside the catcher is (p,n) reactions. Neutrons generated by (p,n) reactions in the catcher are referred to as primary neutrons and constitute the ”true” neutron signal of the measurements. At LDNS, secondary radiation sources originating from the acceleration process (here TNSA) can interfere with measurements or cause secondary neutron generation outside the catcher. These secondary radiation sources cause a harsh background radiation environment that complicates measurements at LDNS. Therefore, a firm understanding of the contributions arising from secondary sources is vital to understanding and designing LDNS and experiments.

The results presented in this chapter are currently being prepared for publication.

4.1. Experimental setup

The DRACO laser is a Ti:Sa based CPA system capable of delivering $30\,\mathrm{J}$ of laser pulse energy with pulse durations in the range of $30\,\mathrm{fs}$, resulting in a peak power of $1\,\mathrm{PW}$ (Ziegler, Albach, et al. 2021). Repetition rates range from shot on demand to the Hz regime, with up to $10\,\mathrm{Hz}$ operation successfully demonstrated (P. L. Poole et al. 2018; Rehwald, Assenbaum, Bernert, Curry, et al. 2023). During the experimental campaign, which took place between October 18th to 29th 2021, laser pulses were delivered on demand with a usual time between shots of 60 to $120\,\mathrm{s}$ (Ziegler, Albach, et al. 2021). More than 1200 laser shots were taken, with a daily average of around 165.

The p-polarized laser pulse is directed into a target chamber made of stainless steel and aluminum, where it was focused to a full-width at half maximum (FWHM) spot size of $2.6\,\mu\mathrm{m}$ using a $f/2.3$ glass-based off-axis parabola (OAP). Peak intensity in the focus reached up to $5 \times 10^{21}\,\mathrm{W/cm^2}$. A plasma mirror was used to achieve the best possible proton acceleration performance by improving the temporal contrast of the laser pulse (Obst, Metzkes, et al. 2018; Speicher et al. 2018). The improved contrast opens up the possibility of using thinner targets, which results in better performance of the TNSA mechanism (Speicher et al. 2018; Zimmer, Scheuren, Ebert, et al. 2021). Utilizing a plasma mirror resulted in a reduction of the laser energy that was delivered on the target, from $30\,\mathrm{J}$ down to 17 to $20\,\mathrm{J}$. Targets made from polystyrene

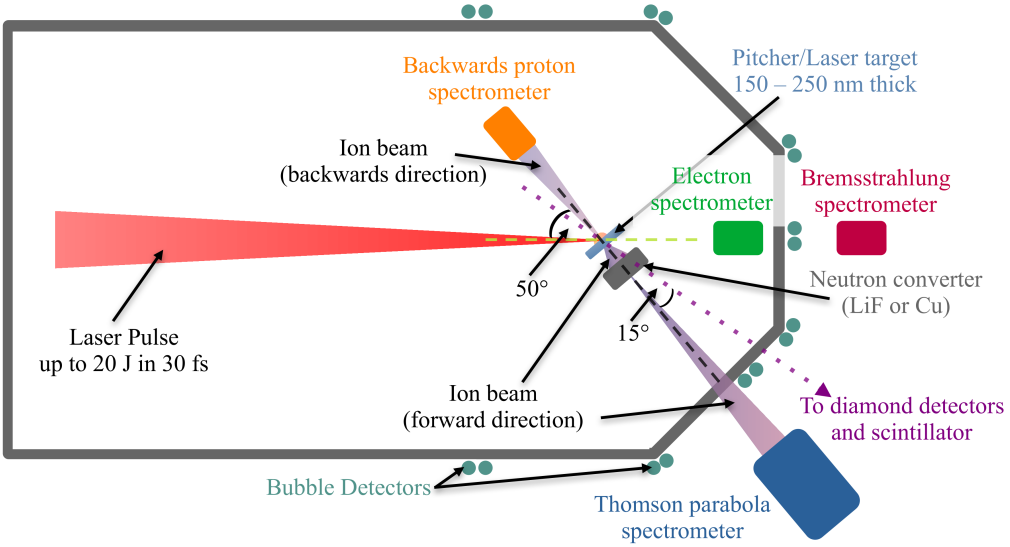

Figure 4.1.: Schematic drawing of the experimental setup (not to scale). The angle between the laser and the target normal (black dashed line) was $50°$ to enable the measurement of the backward ion beam. Up to three electron and two bremsstrahlung spectrometer, placed at different positions, were used at the same time. Here only the most relevant electron and bremsstrahlung spectrometer positions are shown. Neutron detectors were placed under an angle of $15°$ indicated by the purple dotted line, relative to the target normal. Bubble detectors were placed around the target chamber.

with a thickness ranging from 150 to 250 nm were used, manufactured by the HZDR and TU Darmstadt. Two different types of targets were deployed, one made from regular polystyrene and one made from deuterated polystyrene, for which the hydrogen was replaced by deuterium. These different types will be referred to as non-deuterated and deuterated targets, respectively. The laser pulse had an incidence angle of $50°$ relative to the target normal. A schematic drawing of the setup and the detectors can be found in Figure 4.1. In this setup, the target normal is considered to be $0°$ (dashed black line). The incidence angle was chosen to avoid collision of the backward propagating ion beam with the OAP, which allows for the analysis of the backward ion beam, as it can be measured by an ion spectrometer.

Ions propagating in the forward direction (see Figure 4.1) were recorded by a Thomson parabola (Alejo, Gwynne, et al. 2016), in which the ions are deflected by an electric and magnetic field, separating them according to their energy and charge-to-mass ratio. Figure 4.4 shows an example of the data recorded by the Thomson parabola. The deflected ion beam is directed onto a calibrated LANEX (scintillating) screen/microchannel plate (MCP), which is recorded by a camera (D. Jung, Hörlein, et al. 2011). A proton spectrometer based on the deflection of protons in a magnetic field was placed in backward direction and was again readout by a camera. Inside the target chamber electron spectrometers were placed at different positions (Figure 4.1 only shows the position of the spectrometer used in further analysis). The working principle is similar to the backward proton spectrometer, where the charged particles (electrons) are deflected by a magnetic field, with subsequent scintillation signal generation in a LANEX screen. Finally, bremsstrahlung spectrometers were placed outside the target chamber. Each spectrometer consists of different absorber materials from which the photon spectrum can be reconstructed. These detectors are part of the standard ion acceleration setup at DRACO.

Neutron production took place in the pitcher-catcher scheme, with the polystyrene targets constituting

the pitcher and the catcher, responsible for neutron generation, being either a copper (Cu) plate or a lithium-fluoride (LiF) cylinder. Each catcher had a centrally drilled hole with a diameter of 4 mm to allow ions to be passed through to the Thomson parabola for on-shot evaluation of the ion beam. The dimensions of the Cu plate were 5 cm by 5 cm with a thickness of 3 mm. The LiF cylinder had a cylinder radius of 1.9 cm and a thickness of 1 cm. These materials were chosen for their high (p,n) reaction cross section and due to their ease of handling. The catchers were placed 7.4 cm behind the (laser) target. Notably, when using the LiF converter, debris generation from the impact of the plasma/ion beam in the catcher caused damage to unused targets, rendering them unusable. To counteract debris generation, a steel foil with a thickness of around 30 µm was placed over the LiF converter disc, which solved the debris issue but reduced the neutron conversion efficiency for the LiF catcher (see section 4.6). The steel foil did not need to be changed throughout the campaign. No such issues were encountered using the Cu catcher.

Neutron diagnostics were placed outside the target chamber at different positions and distances from the catcher. Different diagnostics were used, such as bubble detectors (BDs), a fast plastic scintillator coupled to a PMT and a diamond-based semiconductor detector. Bubble detectors were placed in pairs around the outside of the target chamber under different angles. The most commonly used setup placed BDs at $0°$, $60°$ and $120°$ relative to the target normal (dashed black line). BDs were placed at up to 12 positions on selected shots to investigate the angular distribution of the neutron emission. In this configuration, only a single detector was placed at each position.

Diamond detectors and the scintillator were placed under $15°$, relative to the target normal (black dashed line), indicated by the purple dotted line, relative to the target normal at a distance of 1.448 m and 3.752 m from the center of the catcher, respectively. A fast plastic scintillator of the EJ-232Q(0.5) type, manufactured by Eljen Technology (Eljen Technology 2021), was used. According to the manufacturer, the fast decay component of the scintillator has a decay time of 700 ps. The scintillator is cylindrical with a radius of 7.5 cm and a thickness of 2.5 cm; it is coupled to a Hamamatsu R2083 photomultiplier tube and readout by a fast oscilloscope (sampling rate 25 GS/s). From the traces recorded by the oscilloscope, the neutron spectrum is reconstructed according to the procedure described in section 3.2. Each trace is synchronized in time according to a reference time given by the rising edge of the γ-flash that arrives at the scintillator before the neutrons. The setup used for the diamond detector and its analysis is discussed in detail in (Millán-Callado 2023) and not further elaborated here.

4.2. Analysis of the laser-plasma accelerator's performance

One central concern regarding laser-driven neutron sources is the stability of the source performance. Because the neutron performance of a source is directly tied to the properties of the accelerated particle beam that is used to generate the neutrons, the ion acceleration performance is the first point of investigation. Of interest is the cut-off energy that can be achieved and the number of ions that are accelerated per laser pulse. Significant variations in either of these parameters translate directly to variations in the neutron output of the source. For the characterization, the proton acceleration performance of the laser-plasma accelerator (LPA) is the primary point of interest. A summary of the performance of the laser-plasma accelerator (LPA) is given in Figure 4.2.

The University of Seville and the HZDR reconstructed the proton spectra and proton number from the Thomson parabola data; details of the reconstruction can be found in (Millán-Callado 2023). Figure 4.3 a-c shows the proton cut-off energy for the three exemplary days (October 22nd, 28th and 29th). Over these days a mean proton cut-off energy of (49.8 ± 4.1) MeV is achieved with the mean proton number reaching $(4.6 \pm 1.3) \times 10^{12}$ p/sr/shot. The proton number for each shot can be found in Figure 4.3 d-f. Ion acceleration is mostly stable over the course of the experimental campaign, as long as the laser parameters were unchanged, which was the case for the 22nd and 29th. In contrast, the overall performance is more

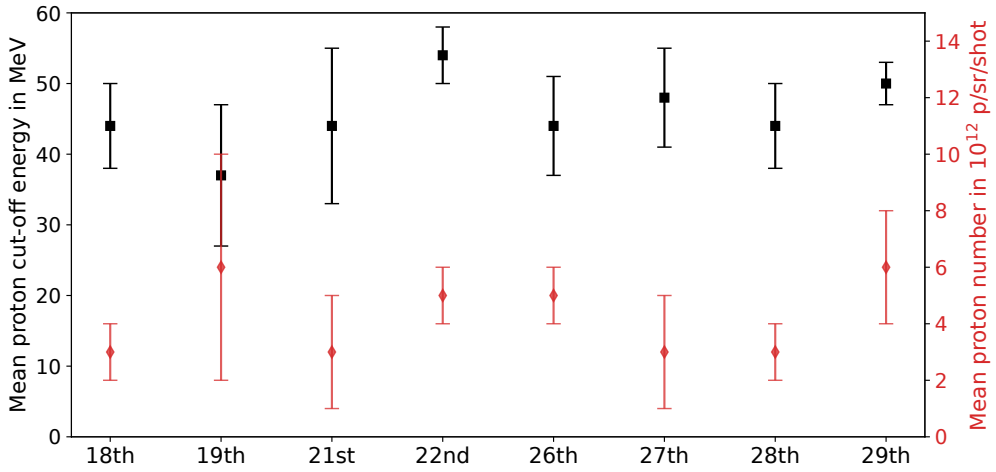

Figure 4.2.: Summary of the proton acceleration performance of DRACO for all days. Data for the 22nd, 28th and 29th are discussed in more detail in the text and are also displayed in Figure 4.3. Proton energies and numbers displayed are mean values. The uncertainty is calculated from the standard deviation of the data sets. Shots where the laser parameters deviated significantly from the optimum settings are excluded when calculating the mean, see for example Figure 4.3b and 4.3e. For most days, the excluded shots are limited to the first shots of the days, which were used to tune the LPA and can be considered warm-up shots.

unstable for the 28th as the laser parameters varied throughout the day, leading to a less optimized setup, which is reflected in the data. For the 28th, the mean cut-off energy is reduced by 13 to 22 %, while the variance is increased by 55 to 88 %. Similarly, the mean proton number is also reduced by up to 55 %. The 28th also exhibits the largest relative variance in the number of accelerated protons at 37 %.

In the case where the optimal laser parameters are used, with regard to ion production, stable operation could be observed over the entire day, which was the case for the 22nd and 29th (see Figure 4.3a and 4.3d for example). The mean cut-off energy spread of these two days is 6.7 %, while the proton number varies by 27.8 % from the mean value. Concerning neutron production, the proton energy can be considered stable, and the variation in cut-off energy should only minimally affect the overall neutron yield. However, the variation in the proton number is significant with almost 30 %. Since the neutron yield is linearly proportional to the proton number (see subsection 2.3.2), the neutron yield per shot can also fluctuate by up to 30 % or more.

In addition to the acceleration of ions in the forward direction, an energetic ion beam propagating in the backward direction is also observed. Mean cut-off energies of (35 ± 6) MeV are measured, with proton numbers reaching about 30 % of the forward proton beam numbers. The shape of the spectrum and absolute proton numbers for the forward and backward ion beam are determined from RCF measurements of a previous beamtime using the same setup. The RCF data is cross-referenced and validated with the data recorded by the ion spectrometers. The RCF measurement determines the proton number to 5.6×10^{11} protons/shot and 1.7×10^{11} protons/shot for the forwards and backward propagating beam, respectively. A conversion efficiency of 3 to 3.5 % is calculated from laser energy to forward proton beam. A comparison between the forward and backward propagating proton beam is displayed in Figure 4.5a.

Looking at the data from the Thomson parabola, of which Figure 4.4 shows an example, it can be seen that protons are not the only ion species accelerated by the laser. Multiple traces are visible, corresponding to

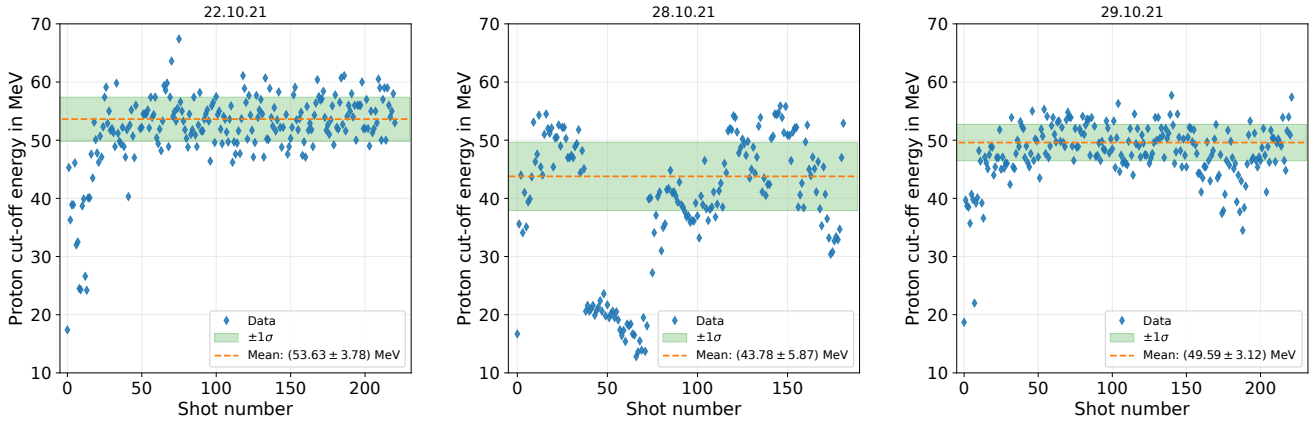

(a) Proton energies for the 22nd. (b) Proton energies for the 28th. (c) Proton energies for the 29th.

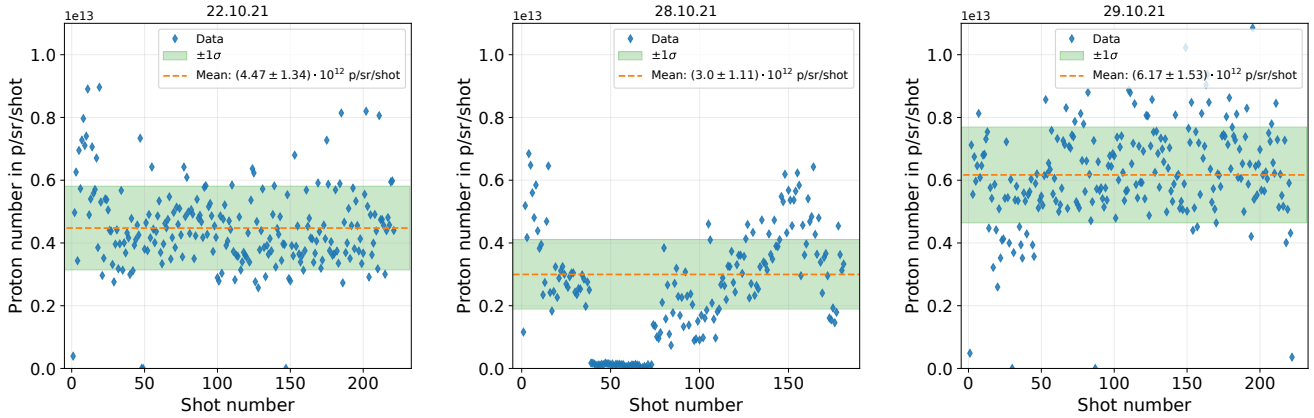

(d) Proton numbers for the 22nd. (e) Proton numbers for the 28th. (f) Proton numbers for the 29th.

Figure 4.3.: (a)-(c) shows proton cut-off energies of the forward propagating proton beam. The first shots of the day are warm-up shots to determine optimal settings for the laser, this reflected by the below average proton energy. In figure (b), starting from shot 38 to shot 72 the laser energy on target was reduced to 2 to $3\,\mathrm{J}$ to investigate the neutron production for a low energy laser systems discussed in section 4.8. These shots were excluded when calculating the mean. The low energy shots can be further subdivided by target type. Shots 38 to 57 were taken on non-deuterated target, with shots 58 to 72 using deuterated targets. Figures (d)-(f) show the proton numbers recorded by the Thomson parabola for the same shots. A linear scale was used to better highlight shot-to-shot fluctuations. The overall proton production was stable within a day. However, larger differences between days of up to $50\,\%$ can be observed when comparing (d) and (f).

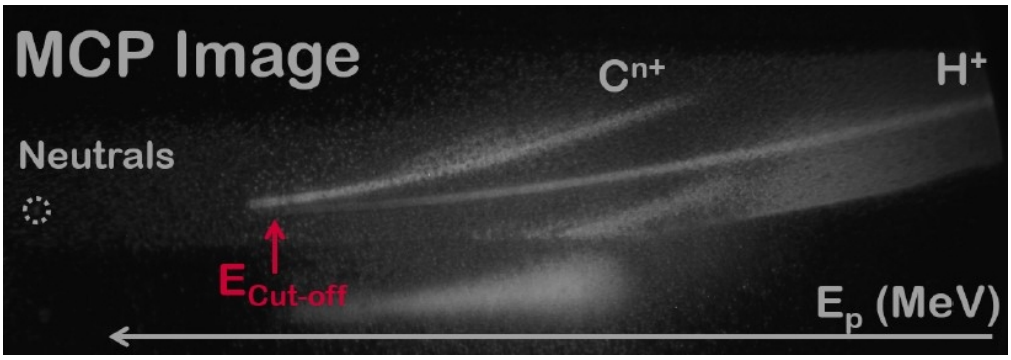

Figure 4.4.: Exemplary image of the data recorded by the Thomson parabola. Multiple traces are clearly visible, with the top trace belonging to carbon ions and the bottom trace to protons. Image courtesy of the HZDR and University of Seville.

carbon ions with different charge states. Using the deuterated targets shows the same behavior, but the traces for C^{6+} and deuterium overlap due to their equal mass-to-charge ratio. The presented discussion is limited to non-deuterated targets for the most part, as the used setup did not allow for absolute measurements of the deuterium spectra. Using the non-deuterated targets mean cut-off energies for carbon of (15.4 ± 1.8) MeV/u on the 22nd and (14.7 ± 1.7) MeV/u on the 29th are measured. The number of carbon ions is lower by a factor of ~ 218 (Cu) and ~ 146 (LiF) compared to the proton numbers of the forward proton beam for these days.

Electrons and x-rays/γ-rays accompanying the ion acceleration can cause secondary neutron generation inside the target chamber and lead shielding, affecting the performance of the neutron source. In this context, performance means both neutron production per shot, the spatial and temporal resolution for applications and the scattering background. The production of neutrons from electrons and photons has been introduced in subsection 2.3.2. In Figure 4.5c, the averaged electron spectra for the 22nd and the 29th, respectively, are displayed. Figure 4.5d shows a photon spectrum extracted from the bremsstrahlung spectrometer (by the HZDR), where the data was accumulated over ten shots. Both the γ-ray and electron spectra exhibit an exponential decay toward higher energies. The figures show that the photon spectrum reaches a cut-off energy of 4 MeV and is therefore well below the neutron production threshold of 6 to 9 MeV for the materials found in the DRACO target area. The integrated photon fluence is 3.1×10^{11} photons/shot. Beyond 4 MeV the photon signal was below the detection threshold and could not be reconstructed.

Observed electron spectra exhibit mean electron cut-off energies of 38 MeV and 28 MeV, containing up to 1.6×10^{11} electrons. Electrons exceeding 8 to 10 MeV can generate bremsstrahlung with energies sufficient for neutron generation via (γ,n) reactions.

Concerning neutron production, on the 22nd, only the Cu catcher was in use for neutron production and is referred to as ”Cu day” for the rest of this chapter, whereas LiF was the only used catcher on the 29th and is therefore labeled as the ”LiF day”.

4.3. Neutron production and source stability

This section discusses the neutron production and source stability measured by bubble detectors (BDs) and the fast plastic scintillator. As previously mentioned the fast plastic scintillator was placed under $15°$ with respect to the target normal and the BDs are placed at $0°$, $60°$ and $120°$, unless stated otherwise. The BDs were analyzed using the methodology developed as part of this work, detailed above in section 3.3. Analysis

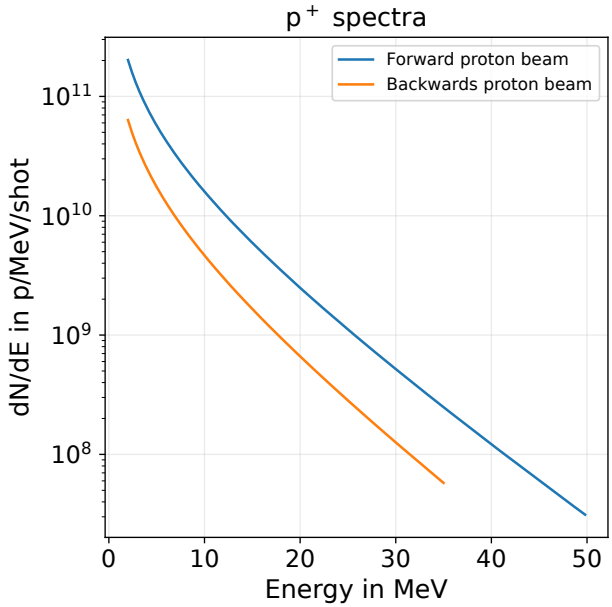

(a) Proton spectra.

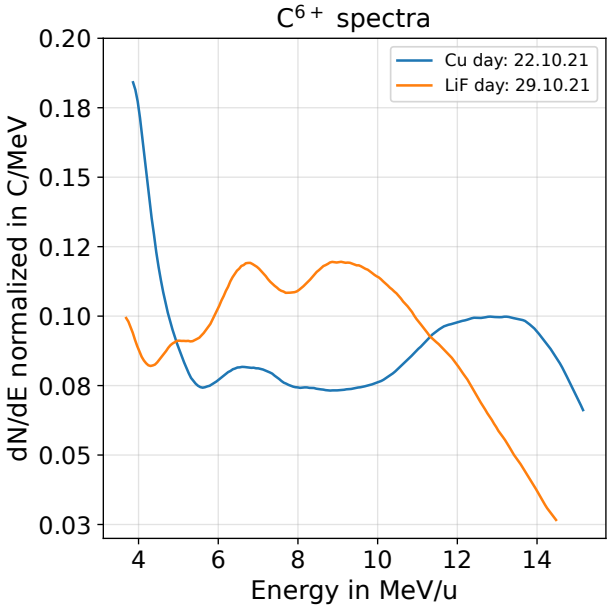

(b) Carbon ion spectra.

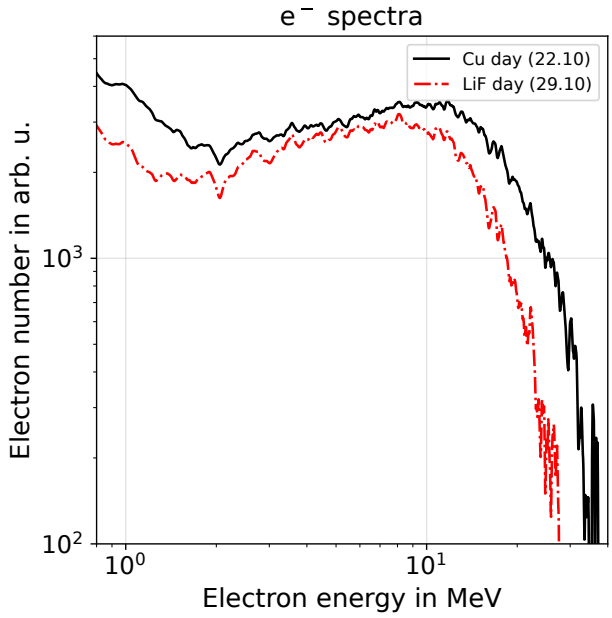

(c) Electron spectra.

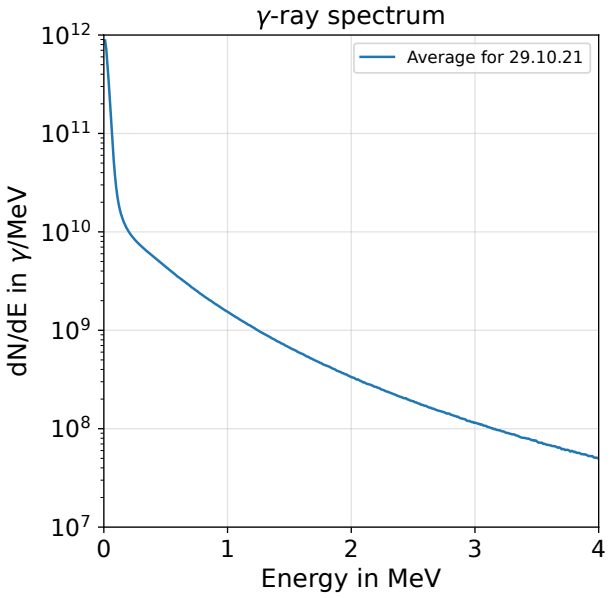

(d) Photon spectra.

Figure 4.5.: Figure (a) shows the proton spectra in forward and backward direction, obtained from RCF measurements previously conducted by the HZDR. The integrated proton number of the backwards beam is equal to $30.4\,\%$ of the proton number contained in the forward propagating beam. (b) shows the normalized carbon spectra measured by the Thomson parabola for different days. (c) displays the mean electron spectra for different days. (d) shows the γ-ray spectrum unfolded from the bremsstrahlung spectrometer data. The spectrometer was only deployed during the last day of the campaign. Thus, only data from the 29th can be used. The spectra were provided by the University of Seville and the HZDR.

of the diamond semiconductor detectors was part of another doctoral thesis and the methodology can be found in (Millán-Callado 2023), with the results used as a point of comparison. First neutron numbers obtained from Bubble Detector measurements are presented, followed by measurements of the neutron spectrum from the scintillator.

Bubble detectors placed in pairs of two in forward direction under $0°$ (Figure 4.1) were irradiated for 10 to 15 shots. The irradiation cycle of 10 to 15 shots is referred to as a shot set. Afterwards, they were readout by a BDR-III Bubble detector reader produced by BTI (Bubble Technology Industries 2024). The number of shots was selected so that each detector contained roughly 70 to 120 bubbles after irradiation. Figure 4.6a shows neutron numbers obtained from BDs and compares them to the average proton number and cut-off energy for the corresponding shots.

Average neutron production based on bubble detector measurements are calculated using weighted averaged, with the individual shot set weighted according to their uncertainty. For Cu the average neutron production is calculated to $\bar{n}_{\mathrm{Cu},0°} = (4.0 \pm 0.3) \times 10^7$ n/sr/shot. Switching to the LiF catcher results in an increase of approximately 22.5 % in the measured neutron number at $\bar{n}_{\mathrm{LiF},0°} = (4.9 \pm 0.5) \times 10^7$ n/sr/shot. From Figure 4.6a it can be seen that the proton cut-off energy was more stable during the time the LiF catcher was in use, resulting in a mean standard deviation of 2.8 MeV compared to 3.9 MeV for the Cu catcher shot sets. Furthermore, the mean cut-off energy reached is about 14 % higher during the LiF shots, at 50.4 MeV, compared to 44.2 MeV in the case of the shots utilizing the Cu catcher. Shot sets 4 and 6 notably fall out of line with regard to proton energy/number and neutron number due to changing laser parameters. For example, for shot set 6, the position of the laser focus relative to the target was changed, resulting in less efficient proton acceleration.

Excluding sets, where the average cut-off energy is below 40 MeV, the mean neutron number detected for Cu increases to $\bar{n}_{\mathrm{Cu},0°} = (4.3 \pm 0.3) \times 10^7$ n/sr/shot, bringing the difference in neutron production down to 14 % in favor of the LiF catcher. In future references $\bar{n}_{\mathrm{Cu},0°}$ always refers to a value of $(4.3 \pm 0.3) \times 10^7$ n/sr/shot. A standard deviation of 1.3×10^7 n/sr/shot for the reduced Cu data set is obtained, resulting in an observed relative variation between different shot sets of 30 %. This variation is in line with the expected variation of 28.1 % resulting from fluctuations in the number of accelerated protons, as discussed in section 4.2. Overall, the mean neutron production form LiF and Cu are comparable and within the uncertainty of the measurement.

What is interesting to see is the strong variation in the neutron fluence measured by the BDs. For example, when comparing shot sets 3 and 13 the neutron yield measured for shot set 3 is 2.1 times higher than that of set 13. Meanwhile, both the proton cut-off energy and the proton number recorded during these sets show higher values for shot set 13. The mean proton cut-off energy was 4.2 % higher for shot set 13 while also showing a reduction in standard deviation. The same hold true for the proton number, which is almost twice as high, albeit at a larger standard deviation. From theory discussed in subsection 2.3.2, BDs should measure similar or more neutrons for shot set 13 when compared to set 3. Two possibilities are likely responsible for this behavior. The first is the intrinsic accuracy of the bubble detectors, with the second being related to the proton beam detection. Since the on-shot proton beam parameters are measured by a Thomson parabola, only a small portion of the ion beam can pass through the pinhole and be measured. If the ion beam impinges the catcher at an angle, only the edges of the proton beam can be measured. Since the highest proton energies are located close to the center of the beam (Obst, Göde, et al. 2017; Brack et al. 2020), this causes the measured cut-off energy to be lower than it actually is. Judging from the rest of the data, the second explanations is more likely to be accurate.

Investigation of the angular dependency of neutron production is conducted in two different ways. Two additional pairs of BDs are present at $60°$ and $120°$ during (most of) the shot sets discussed for the bubbles

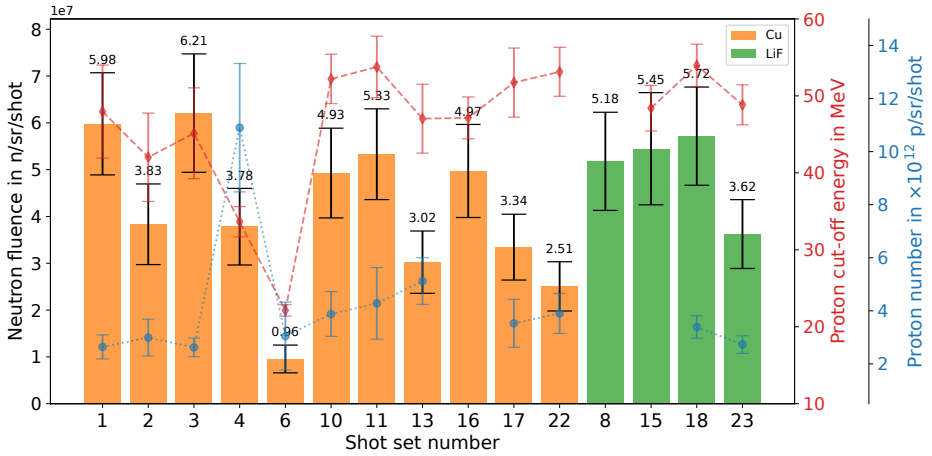

(a) Bubble Detector at $0°$

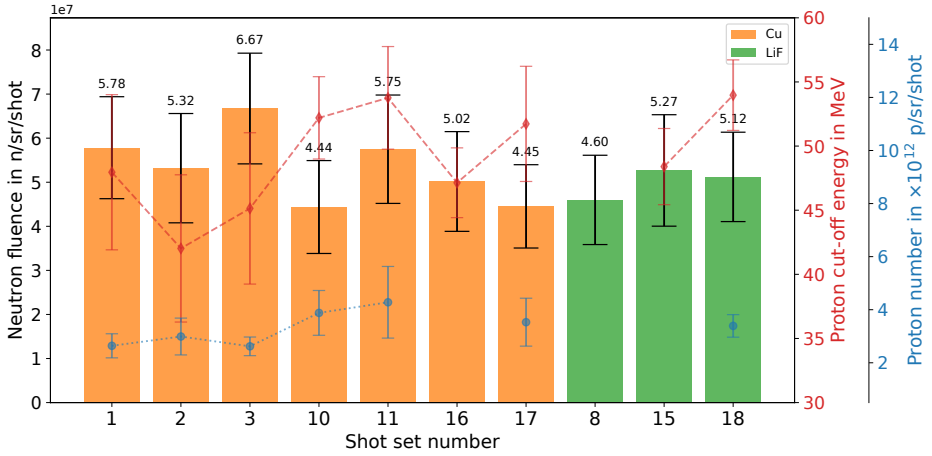

(b) Bubble Detector at $60°$

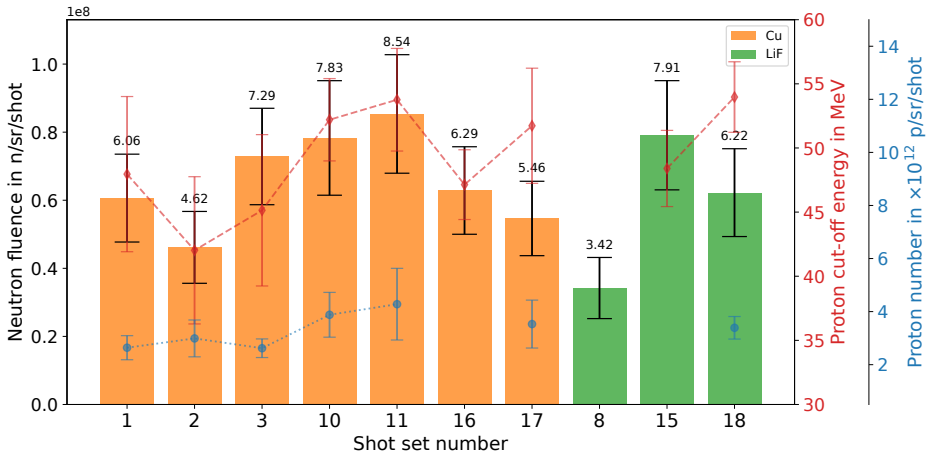

(c) Bubble Detector at $120°$

Figure 4.6.: (a) Neutron fluence measured by BDs placed at $0°$ relative to the target normal. Each shot set averaged over 10 to 15 shots. Also displayed is the measured mean proton cut-off energy (red) and proton number (blue) for the corresponding shots and their standard deviation. (b) and (c) show the neutron fluences measured at $60°$ and $120°$.

in $0°$. The results are displayed in Figure 4.6b and 4.6c. The mean calculated neutron number for the Cu catcher is $n_{\mathrm{Cu},60°} = (5.3 \pm 0.5) \times 10^7$ n/sr/shot and $\bar{n}_{\mathrm{Cu},120°} = (6.5 \pm 0.7) \times 10^7$ n/sr/shot. An increase in measured neutron number of up to $33\,\%$ compared to the mean at $0°$ for the same shot sets. In the case of the LiF catcher, the mean calculated neutron number is $n_{\mathrm{LiF},60°} = (5.0 \pm 0.6) \times 10^7$ n/sr/shot and $n_{\mathrm{LiF},120°} = (5.9 \pm 0.8) \times 10^7$ n/sr/shot. Comparing again with the mean yield at $0°$ for the same shot sets shows an increase of up to $10\,\%$. From the characteristics of (p,n) reactions and Monte Carlo simulations shown later in this chapter, it is expected that the neutron yield should be increased in the forward direction compared to larger angles. Since the BDs measure an increased neutron fluence at large angles, this indicates that the bubble detector measurement is affected by either neutron scattering or the presence of a secondary neutron source.

Additionally, three shot sets, consisting of 15 shots each, are dedicated investigating the neutron fluence for a wide range of angles around the target chamber. Two sets were recorded for Cu and one for LiF, the results of which are displayed in Figure 4.7. For these shot sets, only a single bubble detector was used at each position, except for the forward direction at $0°$, where two BDs were placed. A tendency for the neutron number to increase in backward direction can be observed by up to a factor of 3.2, which is even higher than what was observed from the data shown in Figure 4.6.

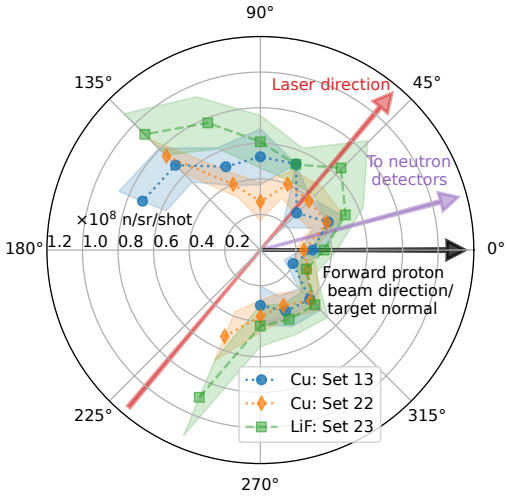

Figure 4.7.: Neutron yield in dependence of the angle relative to the target normal. For each shot set and both catchers the data was acquired over 15 shots each. No distinct angular dependency could be observed.

Deviations from the expected emission behavior can result from neutrons scattering inside the target area or from the influence of a secondary neutron source near the BDs placed at large angles. At this stage, it is difficult to assess the scattering contribution without the help of Monte Carlo simulations. However, due to the experimental setup, it can be assumed that neutron production from the backward proton beam caused neutron generation in the proton spectrometer. Since the spectrometer is located near the BDs that were placed at 120 to $135°$, it can influence the measured neutron fluences. The distance from the spectrometer to the BDs is comparable to their distance to the catcher. In general, the target chamber was surrounded by many bulk objects such as vacuum chambers and other equipment, which can increase the scattering background.

The peak in neutron fluence close to the laser axis could originate from hot/energetic electrons generated by the laser during its interaction with the target, see subsubsection 2.2. The electrons travel along the laser axis and impinge on the target chamber walls made of stainless steel and aluminum. The electrons are decelerated in the walls, emitting bremsstrahlung, which can lead to (γ,n) reactions, if sufficiently energetic photons are generated. In this case, neutron generation would occur only a few centimeters away from the BDs on the laser axis, resulting in an increased measured neutron fluence.

Based on the presented measurements, directed neutron emission, as reported in (Kleinschmidt et al. 2018), could not be observed during the DRACO campaign. Within the measurement uncertainty, the observed neutrons are emitted isotropically.

The neutron production can also be monitored using the fast scintillator, by integrating the neutron signal it measures. To do so, the γ-flash must be subtracted from the raw data first (see section 3.2), leaving just

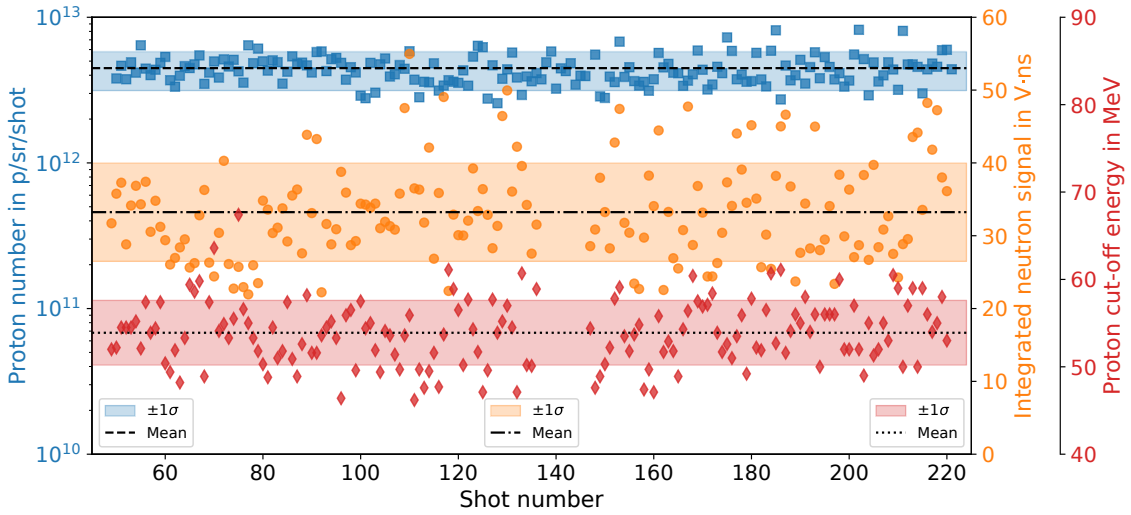

(a) Stability monitoring for the Cu day (22nd).

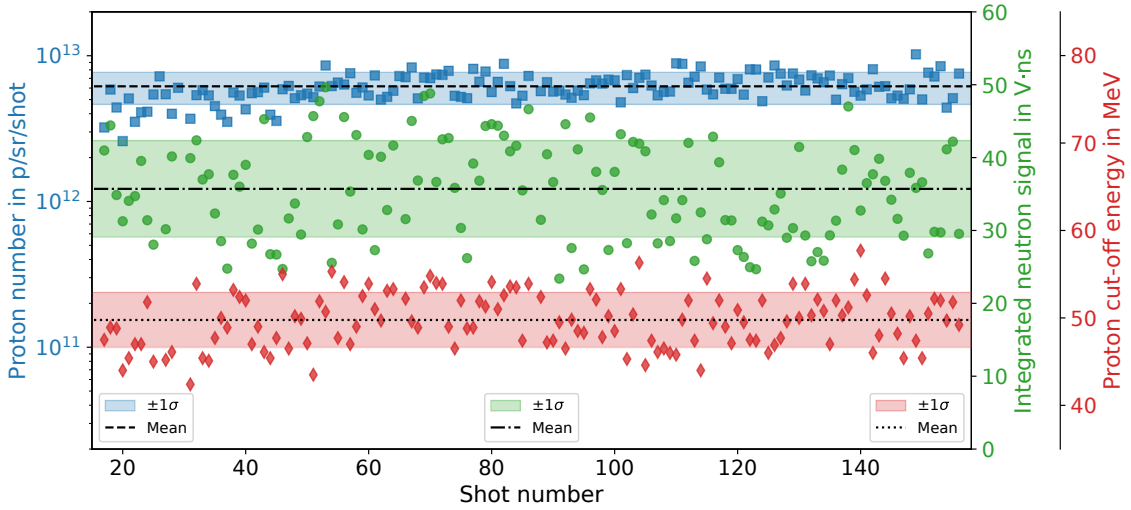

(b) Stability monitoring for the LiF day (29th).

Figure 4.8.: In this figure the proton number (blue) and cut-off energy (red) are displayed. Also shown is the integral neutron production (orange/green) as obtained from the fast plastic scintillator. In figure (a) Cu (orange) was used as converter material, whereas LiF (green) was utilized in figure (b). The data was acquired on the 22nd (a) and 29th (b), respectively.

the neutron signal, which is then (numerically) integrated. The results are displayed in Figure 4.8a for the 22nd (Cu day) and Figure 4.8b for the 29th (LiF day). The data shows a relative variation in neutron production of $20.3\,\%$ for the Cu day and $18.5\,\%$ for the LiF day. This variation in neutron production primarily originates from variations in the LPA's performance, where the number of accelerated protons can vary by up to $30\,\%$. Based on bubble detector measurements (at $0°$), it could be seen that at the position of the detectors, the mean neutron fluence generated by LiF is $14\,\%$ increased over the Cu results. This trend is also observed in the integral scintillator signals, showing a mean increase of $8\,\%$ for the LiF catcher over the Cu catcher. Overall, the results from the scintillator are in good agreement with results obtained by the BDs.

In conclusion, the neutron production exhibits relative variations in neutron production of 18 to $30\,\%$, depending on the converter used. Cu exhibits a slightly larger variation in neutron production compared to LiF when looking at data recorded by the fast scintillator. However, neutron numbers obtained from the BDs indicated a larger relative variation ($30\,\%$) for Cu than was measured by the scintillator ($20\,\%$). The variation for the BDs was obtained by taking the data of five different days, whereas the scintillator data was only analyzed for the 22nd. From Figure 4.6a it is visible that the neutron production in Cu was subject to large variations between different days, resulting in overall larger relative variations for the Cu catcher. The results obtained from the BDs, as well as from the scintillator confirm stable neutron production over a single day, with larger deviations observed between different days, resulting from the laser-plasma accelerator performance (see Figure 4.3). Demonstrating the stability of the source over many successive shots is an important step for the adoption of LDNS. The behavior of the angular neutron distribution does not match the expected behavior or previously published data (Kleinschmidt et al. 2018) and needs to be further investigated with the help of Monte Carlo simulations, described in section 4.5.

4.4. Reconstruction of neutron spectra from plastic scintillator data

Besides the neutron number, it is also essential to know the spectral distribution of the generated neutrons in order to conduct neutron measurements. The spectrum is reconstructed from the fast scintillator measurements, using the method described in section 3.2. One advantage of employing scintillator-based detectors is that a (rough) spectrum can theoretically be obtained from a single shot due to its high efficiency and size. However, the statistics obtained from a single shot are often very limited. Thus, to obtain a smooth spectrum the data of multiple shots needs to be averaged, returning the mean neutron spectrum. This way, shot-to-shot fluctuations of the LPA's performance can be compensated. Therefore, averaging over as many shots as possible is desirable to sample the mean neutron spectrum more accurately.

After reconstructing the neutron spectra, the integral neutron fluence is calculated and compared to the previous section's bubble detector (at $0°$) measurements. In order to ensure comparability between the detectors, the same shot sets as shown in Figure 4.6a are used, which are displayed in Figure 4.9a for Cu and Figure 4.9b for LiF. In addition, scintillator data recorded over 101 shots (Cu, 22nd) and 122 shots (LiF, 29th) is analyzed and shown in Figure 4.9c. These results are referred to as full day (Cu/LiF day) data sets.

Figure 4.9a and 4.9b show that the reconstructed spectra closely resemble each other within their uncertainty, which is again indicative of reproducible neutron production, even over different days. Furthermore, it can be seen (in Figure 4.9c, for example) that the LiF spectra exhibit higher neutron fluence at higher energies and achieve higher maximum neutron energies. Due to the materials involved in the (p,n) reactions, a maximum neutron energy of $47.9\,\mathrm{MeV}$ (LiF) and $47.6\,\mathrm{MeV}$ (Cu) is expected. However, the measured mean maximum neutron energy for LiF is $(31 \pm 6)\,\mathrm{MeV}$ and $(19 \pm 2)\,\mathrm{MeV}$ for Cu, well below the expected value from theory. This discrepancy is due to the influence of the γ-flash on the measured signal, the low production

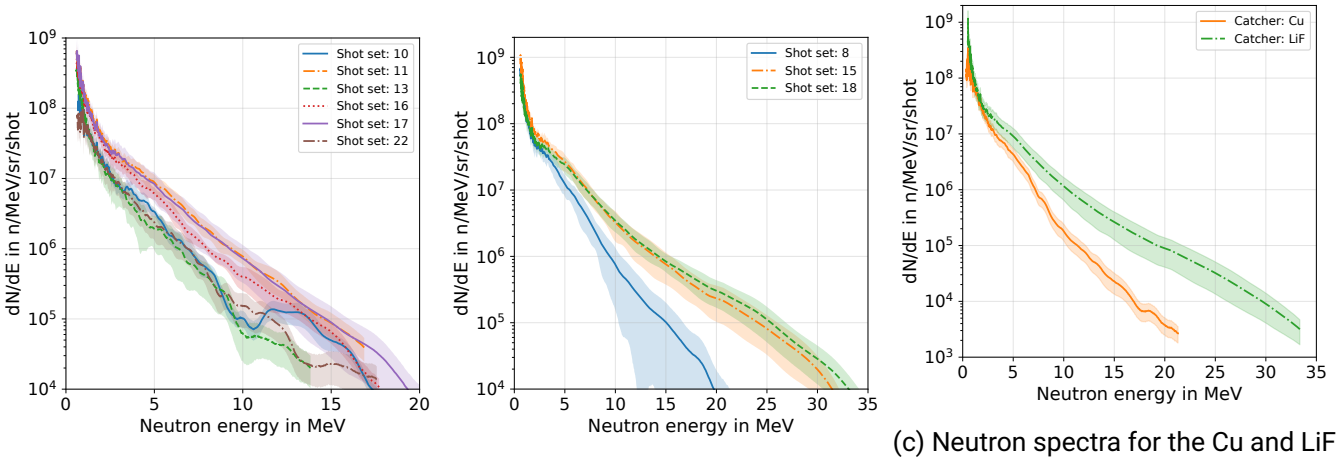

(a) Neutron spectra for the Cu catcher. (b) Neutron spectra for the LiF catcher. (c) Neutron spectra for the Cu and LiF day.

Figure 4.9.: Neutron spectra reconstructed from traces recorded by the fast plastic scintillator for Cu (a) and LiF (b) catcher. Shots used for the reconstruction of these spectra correspond to the shot sets in the legend and are the same sets as used for the bubble detector measurements, which consist of 10 to 15 shots each. (c) shows the mean neutron spectra averaged over all shots taken in the same configuration on the 22nd (Cu) and 29th (LiF). Up to 122 shots were averaged.

rate of neutrons with the highest energies and their low detection efficiency at less than $3\,\%$. Therefore, during the subtraction of the γ-flash, the limited signal generated by the highest energetic neutrons is lost.

Based on the spectra displayed in Figure 4.9, neutron numbers are obtained by numerical integration. Using the numbered shot sets, a mean neutron fluence of $(43 \pm 9) \times 10^7\,\mathrm{n/sr/shot}$ is calculated for LiF, with a yield of $(19 \pm 8) \times 10^7\,\mathrm{n/sr/shot}$ obtained for Cu. The individual results are summarized in Table 4.1. Comparing the integral fluence of scintillator measurements to the BDs shows an increase of factor 8.8 for the LiF catcher and factor 4.4 using the Cu catcher. The full day shot sets displayed in figure Figure 4.9c return slightly lower integral neutron numbers compared to the individual shot sets of (a) and (b). For LiF, the reduction from the mean neutron number is around $37\,\%$, whereas for Cu, it is around $11\,\%$. None of the calculated integral neutron numbers agree with the bubble detector measurements.

To conclude, neutron spectra reconstructed from traces measured using a fast plastic scintillator are incompatible with neutron fluences recorded by the other detectors. The neutron fluence measured by the scintillator is elevated by up to a factor of 12 compared to the BDs, suggesting a systematic error in the measurement and/or reconstruction that has yet to be considered. One cause could be improper fitting and subtraction of the γ-flash can further increase a potential offset, which can cause an overestimation of the neutron fluence. Furthermore, the contribution of scattered neutrons was not included in the analysis so far. To quantify these contributions, Monte Carlo simulations of the experimental setup need to be conducted, which will be introduced in the next section.

4.5. Simulation of the experimental setup

Extensive Monte Carlo simulations are conducted to verify and analyze the measurement results presented above, allowing for further insight into the individual contributions to the measured signals and their origin. The influence of scattered neutrons on each detector is investigated and compared to the direct neutron signal. Thanks to the elaborate detection setup used to characterize the laser-plasma accelerator of the

Table 4.1.: Maximum neutron energies and integrated neutron fluence Φ_{Scint} calculated from scintillator data displayed in Figure 4.9. An average fluence of $(1.9 \pm 0.8) \times 10^8$ n/sr/shot is obtained for Cu and $(4.3 \pm 0.9) \times 10^8$ n/sr/shot for LiF, when excluding the full day data.

Catcher	Shot set	Φ_{Scint} in 10^7 n/sr/shot	Max. energy in MeV
Cu	10	10 ± 2	21.6
	11	28 ± 5	16.9
	13	13 ± 5	13.8
	16	23 ± 5	17.7
	17	28 ± 12	20.1
	22	9 ± 3	17.6
	Cu full day (22nd)	17 ± 4	21.1
LiF	8	35 ± 11	21.4
	15	55 ± 13	32.4
	18	39 ± 11	35.6
	LiF full day (29th)	27 ± 9	33.4

neutron source, detailed simulations can be carried out, which investigate the contribution of each particle species.

First, the DRACO target chamber's geometry and target area are modeled in PHITS, including the BDs, diamond detectors and the fast plastic scintillator. Furthermore, the vacuum chambers for the Thomson parabola spectrometer, including the spectrometer are also included. The lead shielding surrounding the detectors, the backward proton spectrometer, and the lead shielding and parabola inside the target chamber are also included. The geometry implemented in PHITS can be seen in Figure 4.10. The room's walls are made from concrete, and a thin epoxy layer covers the floor plate.

The large orange-green structure in the center is the target chamber and breadboard, with the green boxes outside the target chamber housing magnets for the Thomson parabola and electron spectrometer. Purple blocks represent the lead shielding of the diamond (closest to the target chamber) detectors and the fast plastic scintillator (in the corner). The active detector volume with its corresponding material is placed inside their respective shielding setup. Neutrons entering the volume of these detectors are tallied directly.

Lines visible to the left and top of the target chamber in Figure 4.10 are particle termination planes. Particles passing through the boundary of these planes are terminated and not further transported. This is done to keep the simulation times within a reasonable level and should not affect the tally results at the detector position in any meaningful way due to the distance from the detectors. During the experiment, the target area was filled with various other equipment, such as tables, benches, detectors, cabinets holding equipment etc. To keep the complexity of the Monte Carlo geometry at a reasonable level, only the most relevant structures are included in the simulation model.

Seven different source terms are used in total for the Monte Carlo simulation. Two source terms were used for protons: one for the forward-propagating proton beam and one for the protons in the backward direction. The proton source terms are based on the RCF measurements displayed in Figure 4.5a. The cut-off energy was adjusted to 49.8 MeV, based on the mean cut-off energy determined from data presented in Figure 4.3a-c, with a total proton number of 5.6×10^{11} p/shot entering the catcher. For the proton beam in backward direction, the cut-off energy is set to 35 MeV, with 1.7×10^{11} p/shot contained within the beam. The lower energy limit of the protons was set to 2 MeV in both cases. This limit was chosen due to the

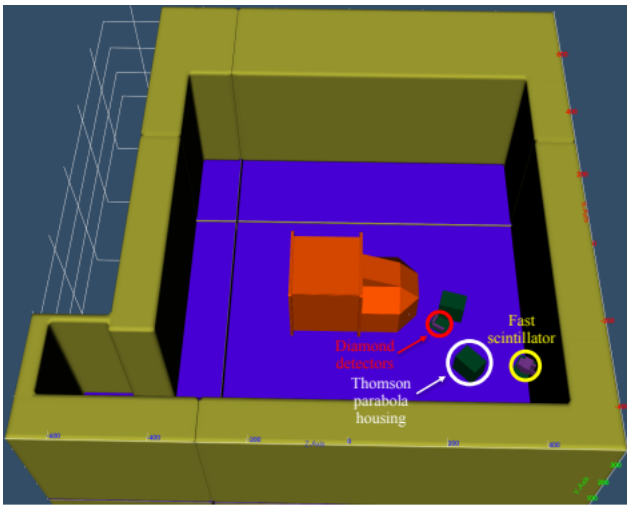

(a) PHITS model of the target area.

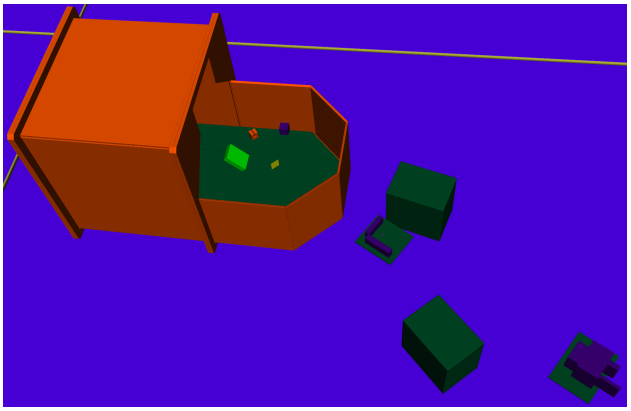

(b) Zoomed in view on the relevant parts of the setup.

Figure 4.10.: (a) PHITS model of the DRACO target chamber and target area. Not shown here is the ceiling also made from concrete. Different colors represent different materials, with green representing aluminum, orange is used for stainless steel and purple for lead. The lines to the top and left of the target chamber are termination planes at which the particle transport is terminated, this is done to minimize the simulation time.

energetic threshold for (p,n) reactions of the used catcher materials. The half-opening angle of the proton beam is set to $15°$ in the simulations.

Next, two source terms were used to investigate the neutron yield from the simultaneously accelerated carbon beam impinging on the catcher. The spectra were reconstructed from Thomson parabola data by the HZDR and are displayed in Figure 4.5b. Expected neutron yields from (^{12}C,n) reactions in the catcher are compared to yields expected from (p,n) reactions to determine the significance of the carbon-based neutron production and the influence on the neutron fluence at the detector positions.

For the electron spectra, data recorded on the 22nd and 29th is averaged for each day and analyzed by the HZDR to obtain electron spectra, displayed in Figure 4.5c. The spectra are measured along the laser propagation axis at an angle of $50°$ relative to the target normal, see Figure 4.1. For the simulations it is assumed that this spectrum is emitted isotropically in 4π. The electron number measured by the electron spectrometer is then extrapolated to isotropic emission. Again, due to the energetic threshold of neutron production from electron beams, the lower energy limit is set to $10\,$MeV. On the 22nd (Cu day), the mean electron cut-off energy is measured at $38\,$MeV and the 29th (LiF day) recording $28\,$MeV. The total electron number in 4π calculated from the averaged spectra resulted in 1.6×10^{11} el/shot for both days.

Lastly, the γ-ray spectrum displayed in Figure 4.5d is reconstructed by the HZDR from bremsstrahlung spectrometer data of the 29th. Only data for the 29th is available for the bremsstrahlung spectrometer and is thus used as an approximation for all days. The maximum photon energy recorded with reasonable uncertainty is $4\,$MeV, well below the neutron production threshold. Possible signals from photons above $4\,$MeV could not be distinguished from the background. Therefore, the maximum photon energy is below the threshold of (γ,n) reactions and no neutron production is expected. However, the photon fluence at the position of the detectors is still of importance since it can overlap in time with the neutron signal, leading to distortions of the neutron signal.

A sufficient number of source particles must be transported to ensure reasonable statistical accuracy of the

Table 4.2.: Summary of the particles, materials and geometric shapes used for source strength assessment. Catcher in the context of Cu refers to a plate with dimensions of $10\,\mathrm{cm}$ x $10\,\mathrm{cm}$ and thickness of $3\,\mathrm{mm}$. The LiF catcher is of cylindrical shape with a thickness of $1\,\mathrm{cm}$ and radius of $1.9\,\mathrm{cm}$. For stainless steel a plate of $10\,\mathrm{cm}$ x $10\,\mathrm{cm}$ with a thickness of $2\,\mathrm{cm}$ is used and for lead the dissensions are $10\,\mathrm{cm}$ x $10\,\mathrm{cm}$ x $10\,\mathrm{cm}$.

Particle	Material	Geometric shapes
Proton	Cu, LiF, Stainless steel	Catcher, Catcher, Plate
Carbon	Cu, LiF	Catcher, Catcher
Electron	Cu, LiF, Stainless steel, lead	Catcher, Catcher, Plate, Block

Monte Carlo simulation results. In the case of protons, 4×10^{10} protons were used for each simulation. In the case of carbon 10^{10} particles are used per run. The number of carbon ions used in the simulation can be reduced compared to the protons due to the higher neutron production rate (discussed in the next section). The photon simulation utilized 5×10^{9} particles and the simulations conducted for the electrons employed a total of 2.5×10^{9} particles for each run. Since the computational cost of electron and photon transport is greater than that of ions/neutrons, fewer particles are transported in order to keep the simulation times reasonable. Variance reduction techniques such as importance sampling are applied to the electron and photon simulations to ensure statistical significance.

4.6. Results of PHITS Monte Carlo simulations

The Monte Carlo simulations are subdivided into two parts. The first part thoroughly investigates neutron production at the source for the two catchers, using the various source terms displayed in Figure 4.5. The second part investigates and compares the detector results, using the source terms of Figure 4.5 in conjunction with the full geometry of the experimental setup shown in Figure 4.10.

4.6.1. Simulation of the simplified neutron source setup

The neutron source strength is simulated for all relevant particle and material combinations found in the experiment. A simplified geometry is used, as seen in Figure 4.11, as only the neutron spectra and conversion efficiencies are of interest here. The source is defined as a pencil beam consisting of either protons, carbon ions or electrons, using the spectral distributions introduced in the previous sections. The photon source term is not evaluated in the context of neutron production as the maximum photon energy is below the threshold for neutron production.

Catchers in the simulations have the same dimensions as those used during the experiment. The backward proton spectrometer was approximated by a $10\,\mathrm{cm}$ by $10\,\mathrm{cm}$ stainless steel plate with a thickness of $2\,\mathrm{cm}$, sufficient for stopping the backward proton beam. The same stainless steel plate is also used to estimate the neutron production from the target chamber walls, with the thickness determined by the strength of the target chamber wall. In the pitcher-catcher setup, the forward propagating proton beam is completely stopped by the catcher and for this reason, only the converter geometry is simulated for the forward proton beam. Table 4.2 summarizes the used particle and material combinations. Like the proton beam, the carbon beam is stopped by the catcher and the neutron production is thus only scored for the different catchers. In contrast, due to the assumed isotropic emission of the electrons in later simulations, they can interact

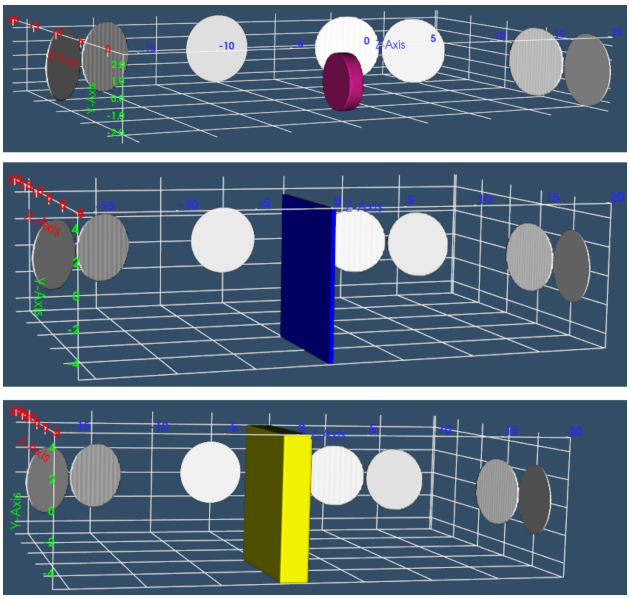

(a) Target and tally setup for the source simulations.

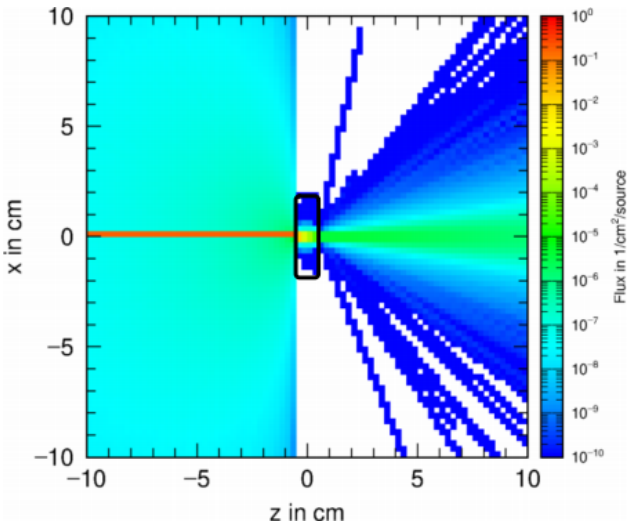

(b) Exemplary PHITS output showing the proton beam.

Figure 4.11.: (a) Depiction of the simplified PHITS geometry used to investigate neutron generation from different material and projectile combinations summarized in Table 4.2. The colored geometries are the LiF/Cu catcher (top/middle) and the stainless steel plate is displayed at the bottom. The gray circles represent tally surfaces for the angular scan displayed in Figure 4.12c and 4.12d. The particle beam travels along the z-axis from left to right. (b) shows the incoming proton beam (red) impinging on a LiF catcher (black outlines). The color scale indicated the proton fluence of a given pixel. Protons exit the catcher on the right side, as the thickness was slightly lower than the stopping range.

with the catcher, the target chamber and lead shielding placed inside the target chamber. As a result, the neutron production from all available geometries is tested using electrons.

Neutron production is scored in 4π to evaluate the conversion efficiency from source particles to neutrons and the results are displayed in Figure 4.12a and 4.12b. For the forward proton, the angular emission is scored at angles relevant to the positions of the detectors in the experiment. The main emission angles of interest are $0°$ (BD), $15°$ (diamond detectors and scintillator), and $60°/120°$ (BD). The results are displayed in Figure 4.12c and 4.12d.

Starting with the forward propagating proton beam impinging on either the LiF or Cu catcher. A conversion efficiency of $\eta_{\mathrm{LiF,p^+}} = (2.3 \pm 0.1) \times 10^{-4}\,\mathrm{n/p}$ and $\eta_{\mathrm{Cu,p^+}} = (4.5 \pm 0.1) \times 10^{-4}\,\mathrm{n/p}$ is obtained. With the forward proton beam containing $5.6 \times 10^{11}\,\mathrm{p/shot}$ this leads to a total expected neutron production of $(1.3 \pm 0.1) \times 10^{8}\,\mathrm{n/shot}$ and $(2.5 \pm 0.1) \times 10^{8}\,\mathrm{n/shot}$. According to the simulation results, the expected neutron production at the source is almost twice as high for the Cu catcher compared to LiF. The conversion efficiency for the LiF catcher is significantly influenced by the $30\,\mu\mathrm{m}$ thick steel foil that was needed due to excessive debris generation. Without the steel foil, the expected neutron production at the source would be around $70\,\%$ higher, putting it in the same range as the neutron production from Cu. Figure 4.12a shows the normalized neutron spectra (emitted in 4π) for all tested combinations. In Figure 4.12b the corresponding total conversion efficiencies per incoming source particle is displayed. The spectra were truncated in the y-axis for better readability. Simulations suggest a maximum neutron energy of $47\,\mathrm{MeV}$ for LiF and $44.6\,\mathrm{MeV}$

for Cu, which aligns with the expectation for these reactions.

As discussed in section 4.2, the proton beam in the forward direction has a standard deviation of ± 4.1 MeV in its cut-off energy of 49.8 MeV. Additional simulations are carried out using the upper and lower limit of the uncertainty range to estimate the influence of the fluctuating proton cut-off energy. Using the lower energy limit (45.7 MeV) the neutron production in LiF is reduced by 1 % and increase by 2 % for the upper limit (54 MeV). Running simulations for Cu yielded a decrease/increase of 3 %/4 %. Based on these findings the fluctuation of the proton cut-off energy is not deemed relevant to the overall stability of neutron production, especially when compared to the fluctuation in proton number, as discussed in section 4.2. Thus, the fluctuations in the cut-off energy are not considered in further simulations.

In Figure 4.12c and 4.12d the angular dependence of the neutron spectrum generated by the forward proton beam is displayed. Neutron production at angles close to $0°$ is increased compared to larger angles, as is expected. Moreover, the maximum neutron energy close to $0°$ is also increased. Comparing the spectra at $0°$ and $15°$ shows that the expected neutron fluence and spectra are almost identical for these positions. This means that the BDs placed at $0°$ and the diamond detectors/scintillator placed at $15°$ should be exposed to an almost identical number of neutrons with comparable spectral distribution.

The expected mean neutron fluence for these angles is $(2.5 \pm 0.1) \times 10^7$ n/sr/shot for Cu and $(3.3 \pm 0.4) \times 10^7$ n/sr/shot for LiF. The expected fluences also highlight the dependence of the angular neutron distribution on the catcher material. Compared to Figure 4.6, the neutron fluence obtained from the simulation is reduced compared to the mean fluence measured by the bubble detectors. For LiF, the experimentally measured mean fluence is almost 49 % higher than the simulation results. For Cu, the measured increase is even larger at 72 %. These increases suggest significant contributions from the secondary source terms and neutron scattering.

Neutron production from the backward propagating proton beam impinging the stainless steel plate resulted in a conversion efficiency of $\eta_{\text{Fe},^{12}\text{p}^+} = (2.4 \pm 0.1) \times 10^{-4}$ n/p, which is around 1.9 times lower than the efficiency achieved by Cu. In the case of the LiF, catcher the conversion efficiencies are equal within their uncertainty. Thus, the neutron yield from the backward propagating proton beam can significantly contribute to the overall neutron generation. Taking the number of accelerated protons in forward and backward direction into account, up to 25 % of the neutron production could originate from the (backward) proton beam impinging on the backwards proton spectrometer. The influence of these neutrons increases further if the detector is placed at a position where the distance between the detector and the spectrometer is similar to or shorter than the distance between the detector and the catcher. This is the case for the BDs placed at large angles ($\gtrsim 110$ to $120°$).

Next, the neutron conversion efficiency for carbon ions interacting with the catcher is investigated. The total neutron conversion efficiency from LiF(^{12}C,n) reactions is determined to $\eta_{\text{LiF},^{12}\text{C}} = (1.8 \pm 0.1) \times 10^{-3}$ n/^{12}C and $\eta_{\text{Cu},^{12}\text{C}} = (2.6 \pm 0.1) \times 10^{-3}$ n/^{12}C for Cu(^{12}C,n) reactions. Again, the efficiency of LiF is influenced by the steel foil, resulting in a 42 % reduction in conversion efficiency. Notably, the carbon induced neutron production efficiency is 5.8 to 7.8 times higher than the efficiency of (p,n) reactions. However, recalling the significantly reduced number of accelerated carbon ions compared to protons from section 4.2, the expected overall contribution of (^{12}C,n) reactions to the neutron production inside the catcher should only be around 2.5 % for Cu and up to 5.1 % for LiF. Neutrons generated by carbon ions can influence the accuracy of a measurement, since their time-of-flight correlation with energy does not fully match that of the neutrons generated by protons. Since carbon ions have a lower velocity than protons, they require more time to move from the pitcher to the catcher, thus stretching the primary neutron beam in time and reducing the energy resolution. Measurements that are very sensitive to deviations from the ideal time-of-flight therefore, require the distance between the pitcher and catcher to be as small as possible.

Lastly, the neutron production of electron-induced reactions is investigated. As discussed in subsec-

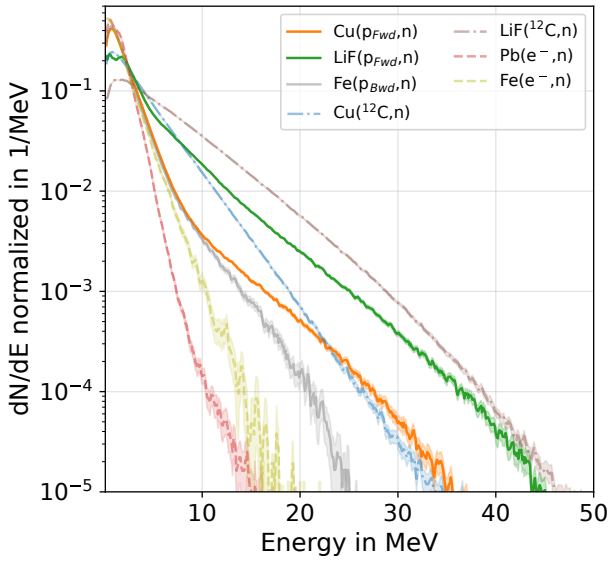

(a) Neutron spectra emitted in 4π.

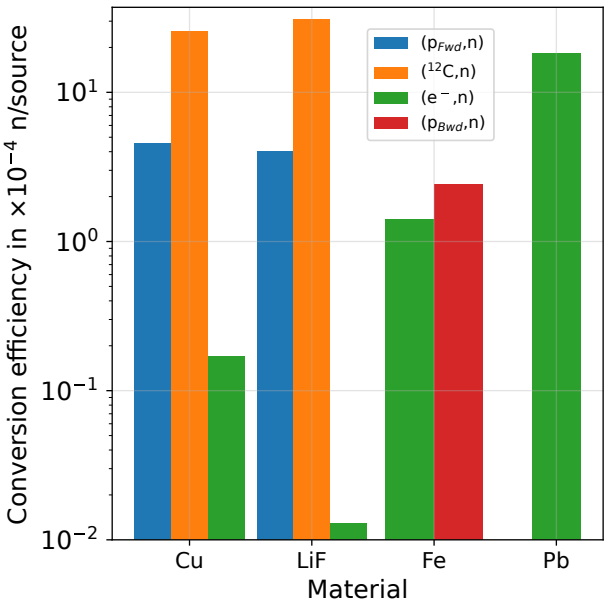

(b) Neutron conversion efficiencies.

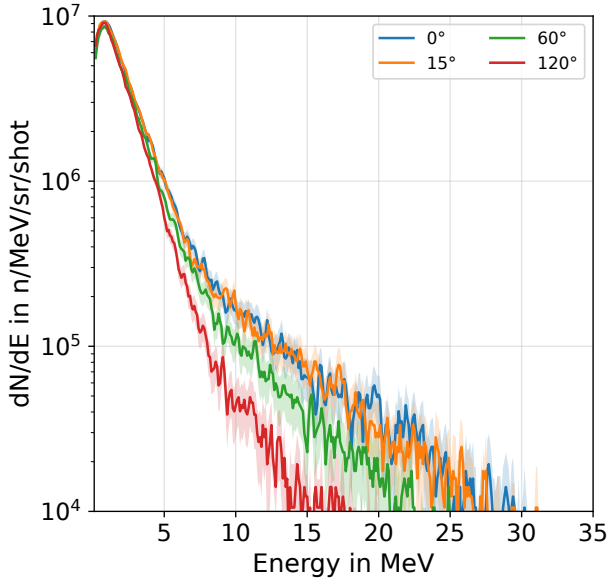

(c) Angular neutron distribution.

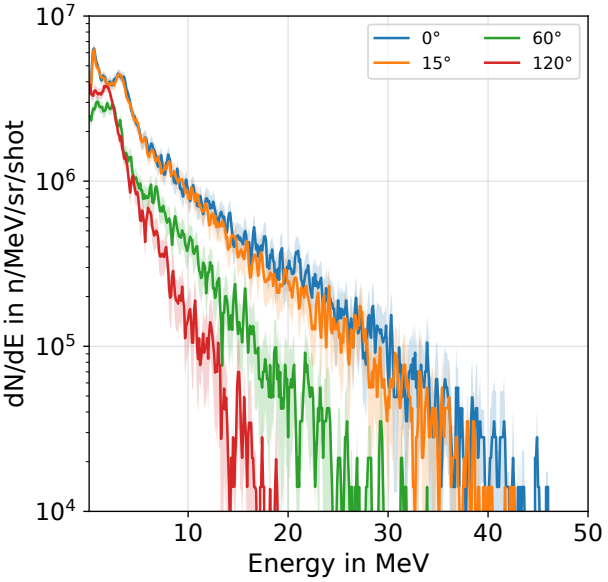

(d) Angular neutron distribution.

Figure 4.12.: (a) compares the neutron spectra emitted in 4π of all tested combinations mentioned in Table 4.2. (b) displays the conversion efficiency for all combinations. Stainless steel is referred to as "Fe" in the legend and labels. Simulations for electrons impinging on Fe or Pb use the electron spectrum recorded on the 22nd, which is a worst case approximation due to its higher energies. Figure (c) and (d) show the angular dependence of the emitted neutron spectrum for the forward proton beam impinging on Cu (c) and LiF (d). The neutron number is calculated using the experimentally determined proton number of 5.6×10^{11} p/shot. Shaded areas display the uncertainty of the simulations.

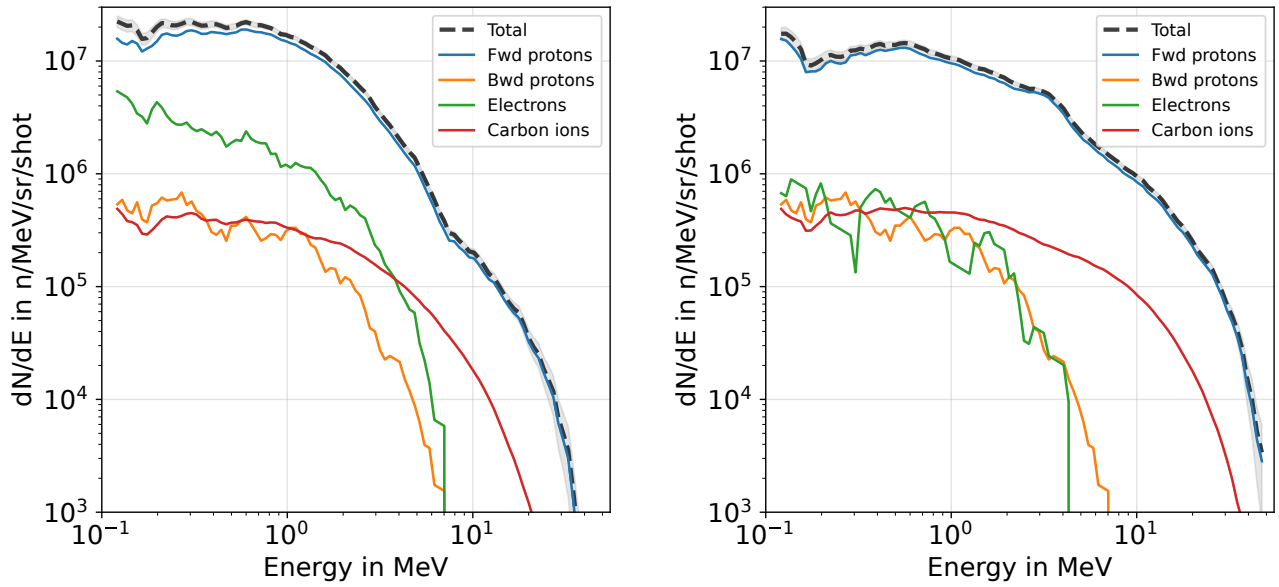

(a) Cu catcher: Individual source term contribution.

(b) LiF catcher: Individual source term contribution.

Figure 4.13.: Contribution of each source term at the position of the bubble detector placed at $0°$ for the Cu catcher (a) and LiF catcher (b). Fwd and Bwd refer to the forward and backward proton beam, respectively. It is visible that the secondary neutron production is dominated by electrons when using the Cu catcher. For the LiF catcher, secondary neutron production mostly originates from the carbon beam impinging on the catcher. The uncertainty is only included for the total spectrum for better readability and is represented by the gray shaded area.

tion 2.3.2, neutron production from electron beams is based on the conversion to bremsstrahlung photons and their interaction with the material. The neutron conversion efficiency for electrons impinging the LiF or Cu catcher is $\eta_{\mathrm{LiF,e^-}} = (1.3 \pm 0.2) \times 10^{-6}\,\mathrm{n/e^-}$ and $\eta_{\mathrm{Cu,e^-}} = (1.7 \pm 0.1) \times 10^{-5}\,\mathrm{n/e^-}$, respectively. Similarly to the case of the carbon ions, the contribution from electrons to the overall neutron production in the catcher is limited to less than $1\,\%$. Contrary to the case of the catcher, significant neutron production can be expected from electrons impinging on the stainless steel walls of the target chamber and lead shielding inside the target chamber at conversion efficiencies of $\eta_{\mathrm{Fe,e^-}} = (1.4 \pm 0.1) \times 10^{-4}\,\mathrm{n/e^-}$ and $\eta_{\mathrm{Pb,e^-}} = (1.8 \pm 0.1) \times 10^{-3}\,\mathrm{n/e^-}$, respectively. Neutrons generated by electrons inside the target chamber walls or shielding are especially relevant for detectors close to these geometries, such as the BDs, which are typically fixed directly to the target chamber during experiments. In Figure 4.12b a summary of the conversion efficiencies for all combinations discussed is presented.

4.6.2. Results of the full geometry simulations and comparisons

In this part of the thesis, the full geometry displayed in Figure 4.10 is used to further investigate the neutron fluence at the position of the detectors. The individual contributions from each source term are analyzed and compared, starting with the bubble detectors. The simulation results are then compared to the experimental results obtained from the scintillator and the diamond detector. Since the scintillator shows the largest deviation from the simulation results presented so far and is incompatible with the results of the other detectors, the radiation fields at its position are investigated further.

In total, eight different simulations are conducted using the full geometry. Three simulations are carried

out for protons, one for each converter using the forward propagating proton beam and one using the backward propagating proton beam. Two simulations for each catcher material using the respective electron and carbon source terms. The last simulation is conducted using the γ-ray spectrum, which is used to investigate the overlap of the neutron and photon signals in time at the position of the scintillator. All source terms are discussed in section 4.2 and displayed in Figure 4.3. The forward proton beam is considered the main source term, with the other source terms also referred to as secondary source terms.

At the position of the detectors, neutron energies and arrival times are scored for neutrons entering the detector volume. Furthermore, the counter function of PHITS is leveraged to investigate the interactions that neutrons undergo on their way to the detector. The counter functions allows one to distinguish between neutrons that interacted with the walls of the room or shielding and neutrons that arrived without any interactions. Results from the simulations are references by the word ”tally” or the phrase ”at the position of the detector”. This is done to avoid confusion between experimentally measured results and simulation results.

The first point of investigation is the contribution of each source term, i.e. protons, electrons and carbons, to the total neutron tally at the detector position of the bubble detector placed at 0°. Starting with the Cu catcher, neutrons arriving at the position predominately originate from (p,n) reactions in the catcher, induced by the forward proton beam. These neutrons make up $87.1\,\%$ of all arriving neutrons. Figure 4.13a shows the contribution of each source term to the overall signal. Neutrons generated by the electron source term contribute $8.4\,\%$ of the total fluence at the detector position, with an additional $3\,\%$ from carbon ions and $1.5\,\%$ from the backward proton beam. The significant contribution from the electrons is due to the large (γ,n) cross section of around $100\,\mathrm{mb}$ (Soppera et al. 2014). Utilizing the LiF catcher shows that $91.4\,\%$ of the arriving neutrons originate from (p,n) reactions inside the catcher. Of the secondary source terms, the contribution from the carbon ions is the largest at $5.7\,\%$, with about equal contributions from the electrons and backward proton beam, at $1.6\,\%$ and $1.4\,\%$, respectively. The disassembled neutron spectrum for LiF is shown in Figure 4.13b. The relative contributions of the individual source terms at the position of the bubble detector are in agreement with the conversion efficiencies presented in Figure 4.12b. In the case of the Cu catcher, the carbon contribution is lower than expected from the conversion efficiency. This is due to the amount of carbon ions accelerated on the Cu day during the experiment, which was only $67\,\%$ of the carbon ions accelerated for the LiF day.

In Figure 4.14, the tallied neutron spectrum for the bubble detector (0°) is compared to the spectra at the position of the scintillator and the diamond detectors for both the Cu (Figure 4.14a) and LiF (Figure 4.14b) catcher. From the presented spectra it can be seen that the neutron spectra are different at each detector position. For example the neutron fluence below $1\,\mathrm{MeV}$ is significantly reduced at the position of the diamond detector compared to the bubble detector and scintillator positions. Furthermore, it can be seen that the tallied spectrum for the scintillator falls off much faster for neutron energies above $2\,\mathrm{MeV}$. In contrast, the spectral shape at the bubble and diamond detector position above $2\,\mathrm{MeV}$ resemble each other closely, with the diamond detector showing a reduced neutron fluence. The fast fall-off for the scintillator is a consequence of the bulk lead shielding placed between the catcher and the detector to shield it from the γ-flash.

Besides the relative contribution of each source term to the total neutron spectrum, the integral neutron fluence at the detector is also relevant when characterizing a source, especially in the context of applications. Therefore, the neutron number obtained at the position of the detectors in the simulation is compared to the experimentally measured fluence. The simulation results are obtained by counting the neutrons arriving at the source, with subsequent normalization to the solid angle spanned by the detector. Starting with the BDs, the integrated neutron fluence obtained from the simulations $(4.4 \pm 0.2) \times 10^7\,\mathrm{n/sr/shot}$ (Cu) and $(4.9 \pm 0.2) \times 10^7\,\mathrm{n/sr/shot}$ (LiF), respectively. The neutron fluence obtained from the simulations

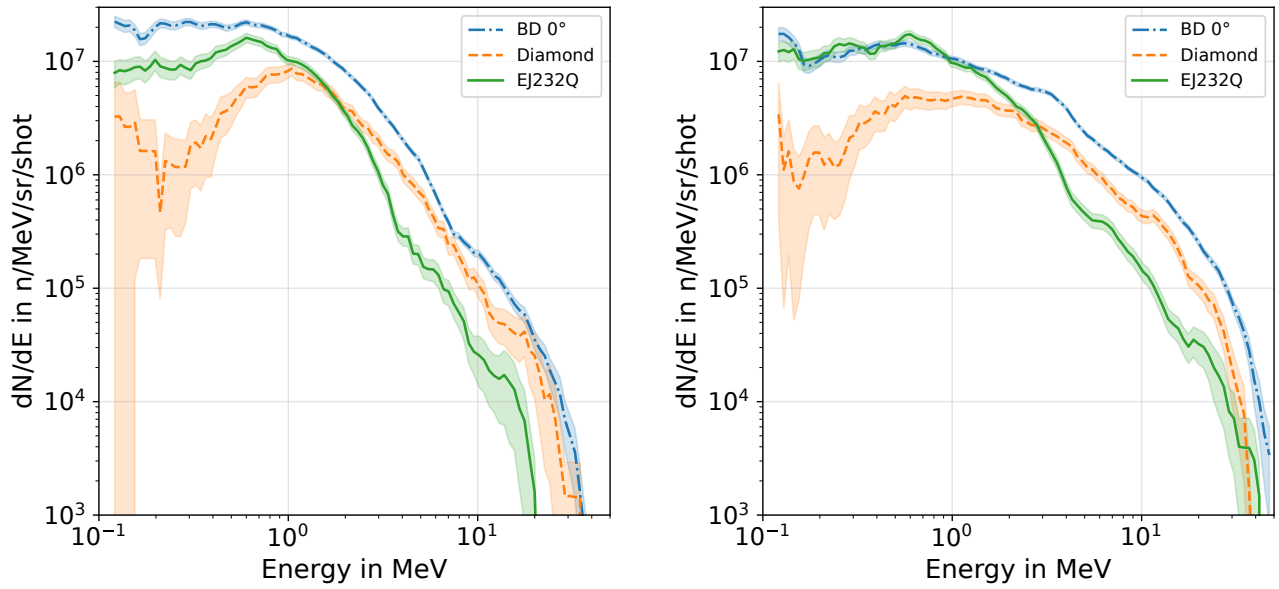

(a) Cu catcher generated neutron spectrum.

(b) LiF catcher generated neutron spectrum.

Figure 4.14.: (a) shows the neutron spectrum determined from PHITS simulations at the position of the bubble detector under $0°$, diamond detector and the fast scintillator. The spectra are generated considering neutron production from all source terms. (b) shows the results for the LiF disc. Shaded areas represent the uncertainty of the simulation.

for the bubble detector at $0°$ is in excellent agreement with the experimentally measured mean values of $n_{\mathrm{Cu},0°} = (4.3 \pm 0.3) \times 10^7$ n/sr/shot and $n_{\mathrm{LiF},0°} = (4.9 \pm 0.5) \times 10^7$ n/sr/shot. The difference between simulations and measurements is less than $3\,\%$, within the uncertainty of the simulation results and the methodology used to analyze the detectors (see section 3.3). Interestingly, simulation results presented in Figure 4.12b suggest that the total conversion efficiency for Cu is twice as high than that of LiF. However, both experimental (bubble detector) measurements and the full geometry simulation results return a higher neutron fluence for the LiF catcher. This is a result of the emission characteristics of LiF, which has an emission that more strongly peaked around $0°$. Figure 4.15 compares the measured neutron fluence using BDs and the neutron fluence obtained from Monte Carlo simulations for all tested angles.

Comparing simulation results for the BDs placed at 60 and $120°$ to the experimental results shows reasonable agreement, see Figure 4.15. In the case of the Cu catcher the deviation from simulation to experimental results is $6\,\%$ for the BDs placed under $60°$. The simulations also reproduce the increase in neutron fluence at the $60°$ relative to the $0°$ position, as was observed in the experimental data. At $120°$ the difference between simulation and experiment increases to $44\,\%$, with the neutron fluence obtained from simulations decreasing relative to the fluence at the $60°$ position. This is contrary to experimental observations, where the highest neutron fluence is recorded by the BDs at $120°$. Possible causes for the large deviations at $120°$ are the particle termination planes, which are shown in Figure 4.10, and auxiliary equipment placed close to the $120°$ bubble detector position, such as tables, drawers etc. These objects are not included in the simulations. Omitting bulk objects in close proximity to the detector position can influence the scattering contributions, which, in the absence of the scatterer, leads to a reduction in neutron fluence. While great care is taken to ensure minimal impact on the results, as a consequence of simplifying the geometry, the results suggest that the simulations might have been affected and further investigation into the matter is warranted.

Table 4.3.: Integrated neutron fluence arriving at the diamond detector and the plastic scintillator, calculated from simulation data. The corresponding neutron spectra are displayed in Figure 4.14. For the scintillator the spectrum is integrated for neutron time-of-flight corresponding to $E_{\mathrm{n}} \geq 0.9\,\mathrm{MeV}$, whereas for the diamond detector only neutron with energy $\geq 2\,\mathrm{MeV}$ are included. The restriction to the time-of-flight is applied to minimize the influence of source overlap. For the diamond detector the energetic threshold is a consequence of the reaction threshold.

Detector	Cu catcher fluence in n/sr/shot	LiF catcher fluence in n/sr/shot
BD $0°$	$(4.4 \pm 0.2) \times 10^7$	$(4.9 \pm 0.2) \times 10^7$
Diamonds	$(6.9 \pm 1.1) \times 10^6$	$(1.3 \pm 0.2) \times 10^7$
Scintillator	$(1.0 \pm 0.2) \times 10^7$	$(1.7 \pm 0.2) \times 10^7$

For the LiF catcher (shown on the right) at $60°$ the deviation between simulation and experiment is around $20\,\%$. The difference at $120°$ is close to $100\,\%$. Therefore, the simulations did not capture the characteristics of the measurement. Furthermore, while the shortcoming in the case of Cu is likely due to a oversimplification of the experimental geometry, this explanation seems unlikely for LiF, as the simulations fail to capture the general trend of higher neutron fluence at larger angles. Instead, the simulations show a continuous decrease in neutron fluence at larger angles. This deviation warrants further investigation in the future to determine the cause of the discrepancy. Different nuclear data libraries for LiF should be used as a first point of investigation to validate the initial angular neutron distribution emitted by the catcher.

Looking at the contribution of neutrons generated by the forward proton beam to the scintillator and diamond detector tallies reveals that for the scintillator, $75.5\,\%$ (Cu)/$86.4\,\%$ (LiF) and for the diamond detector, $86.5\,\%$ (Cu)/$90.7\,\%$ (LiF) of arriving neutrons are generated by the primary source term. As in the case of the bubble detectors, the electron source term has the second largest contribution for Cu, whereas it is the carbon beam for LiF. This shows that up to $25\,\%$ of neutrons can originate from secondary source terms, which can negatively impact the performance of the detection system.

The simulation results are further cross-referenced with the neutron spectra experimentally measured by the diamond detector. Results for the diamond detectors were provided by and obtained from (Millán-Callado 2023). Comparing the integral neutron fluence at the position of the diamond detector to the experimentally measured value shows good agreement within the uncertainty. The comparisons can be seen in Figure 4.16. During the experiment, a fluence of $(7 \pm 2) \times 10^6\,\mathrm{n/sr/shot}$ is measured for the Cu catcher by the diamond detector, with $(9 \pm 3) \times 10^6\,\mathrm{n/sr/shot}$ measured for the LiF catcher (Millán-Callado 2023).

Due to the detection reaction, the diamond detector has an energetic threshold of $2\,\mathrm{MeV}$, below which neutrons cannot be detected (Millán-Callado 2023). Thus, neutrons tallied at the position of the bubble detector are only considered in the analysis if their energy is greater or equal to this threshold. The simulations obtained an integral fluence of $(6.9 \pm 1.1) \times 10^6\,\mathrm{n/sr/shot}$ for the Cu catcher, corresponding to a deviation of less than $2\,\%$ between the experiment and the simulation. Furthermore, the spectral shape shows good agreement between the measurement and the simulation, as seen in Figure 4.16a. The measured fluence closely matches the simulation, up to energies of $(22 \pm 1)\,\mathrm{MeV}$. Above $22\,\mathrm{MeV}$ the experimentally measured spectrum is elevated compared to the simulations results. However, the difference can be explained by the limited statistics of the simulations for neutrons exceeding $20\,\mathrm{MeV}$ due to the low generation efficiency for high energy neutrons. This reduction is visible in Figure 4.12c, where neutron production above 7 to $8\,\mathrm{MeV}$ is almost two orders of magnitude lower than the yield between 1 to $2\,\mathrm{MeV}$.

In contrast, the results for the LiF catcher do not show agreement to the same level. The integral neutron

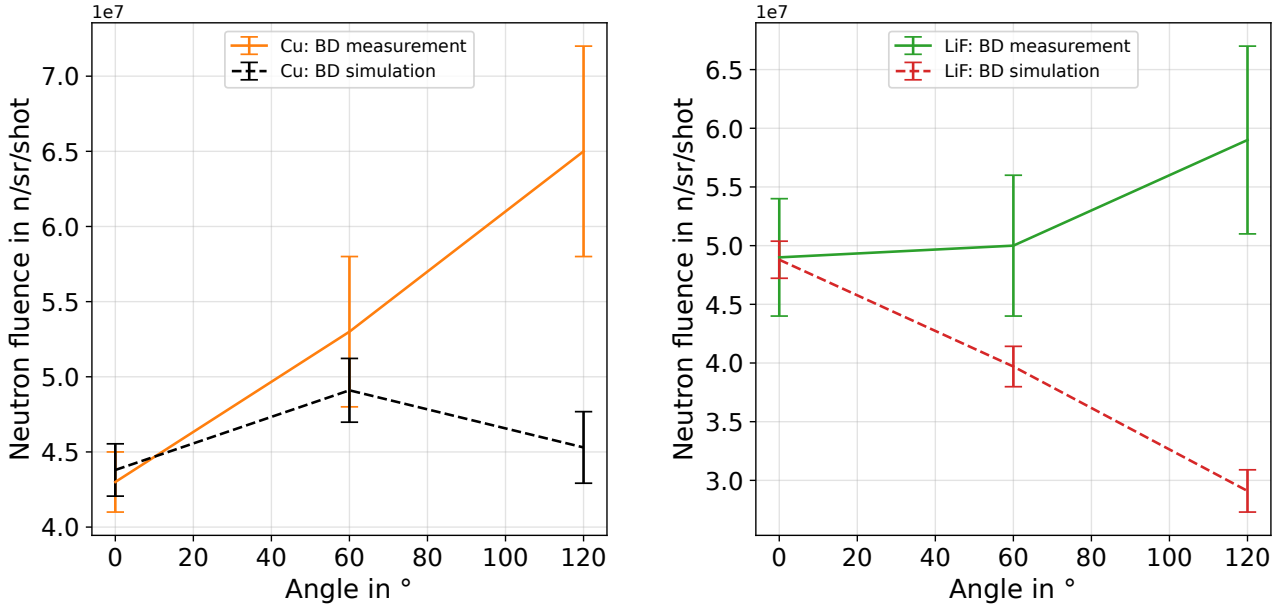

(a) Cu catcher: Comparison between measurements and simulations.

(b) LiF catcher: Comparison between measurements and simulations.

Figure 4.15.: Comparison of the neutron fluence obtained experimentally from bubble detector measurements (solid line) and from PHITS simulations (dashed line). The fluence for the BDs is calculated from the mean of the data shown in Figure 4.6. The lines are meant to guide the eye.

fluence obtained from the simulation is $45\,\%$ higher than that recorded during the experimental campaign at $(1.3 \pm 0.2) \times 10^7\,\mathrm{n/sr/shot}$. Nonetheless, the spectral shapes are in good agreement, as seen in Figure 4.16c, but the simulation results are offset towards higher fluences. Unlike in the case of Cu, limited statistics of the simulation cannot explain the differences and further investigation into the LiF simulations is required.

At the position of the scintillator, the neutron spectra obtained from the simulation show a substantially lower fluence compared to the spectra shown in Figure 4.9 and the corresponding integral fluences listed in Table 4.1. For the Cu catcher, the simulations return a total neutron fluence of $(2.1 \pm 0.2) \times 10^7\,\mathrm{n/sr/shot}$ at the position of the scintillator, which is a factor of 4 to 14 lower compared to the fluences measured during the experiment. Similarly, the measurement for LiF exceeds the simulation results of $(2.7 \pm 0.3) \times 10^7\,\mathrm{n/sr/shot}$ by a factor of about 10 to 20. The findings suggest a systematic issue with the reconstruction algorithm.

In Figure 4.16, the tallied spectra from the simulations are compared to the reconstructed spectra (figures (b) and (d), respectively). For the comparison, only the Cu and LiF full day data sets shown in Figure 4.9c are used. A multiplicative scaling factor is applied to the reconstructed scintillator spectra to compensate for the overestimation introduced during the reconstruction. This allows for better comparability of the spectral shapes. The scaling factor is calculated based on the integral neutron fluence of the simulation and experimental data and is defined as

$$k_{\mathrm{scale}} = \frac{\int \phi_{\mathrm{sim}}\,\mathrm{d}E}{\int \phi_{\mathrm{exp}}\,\mathrm{d}E}.$$

In this equation, ϕ_{sim} is the neutron spectrum at the position of the scintillator obtained from the simulation and ϕ_{exp} is the reconstructed, measured neutron spectrum. For both spectra, only neutrons $\geq 0.9\,\mathrm{MeV}$ are

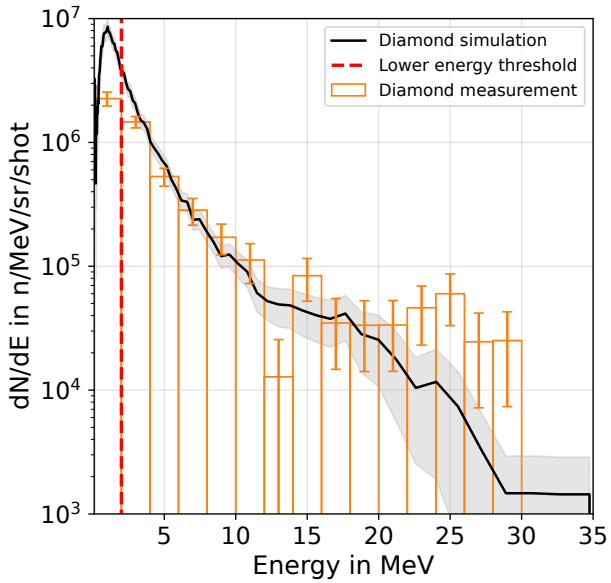

(a) Cu catcher: Diamond detector.

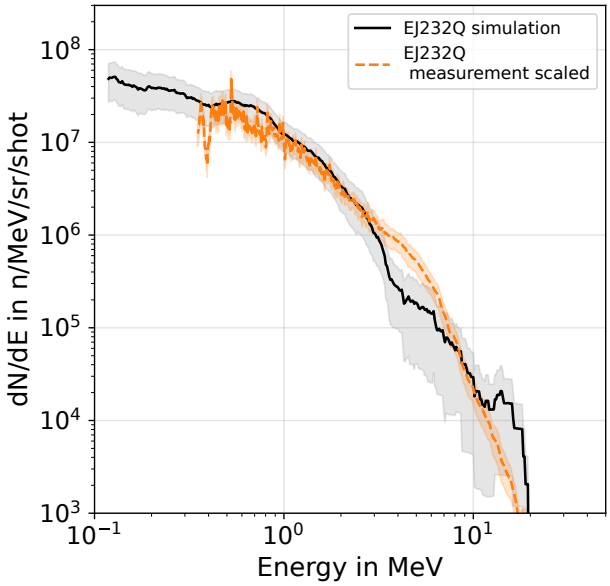

(b) Cu catcher: Scintillator.

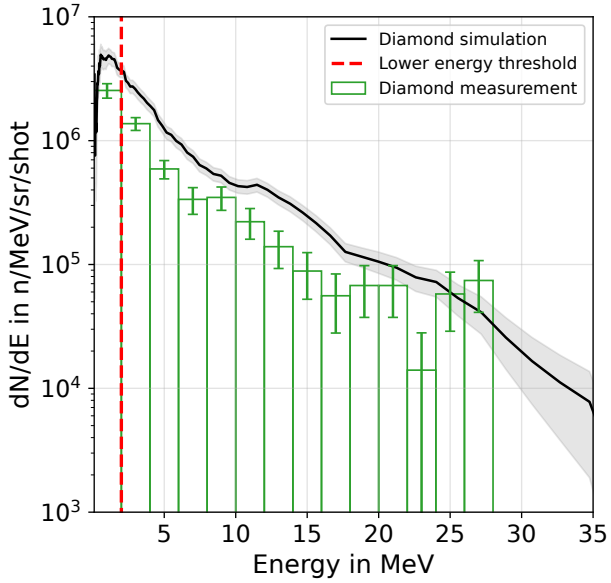

(c) LiF catcher: Diamond detector.

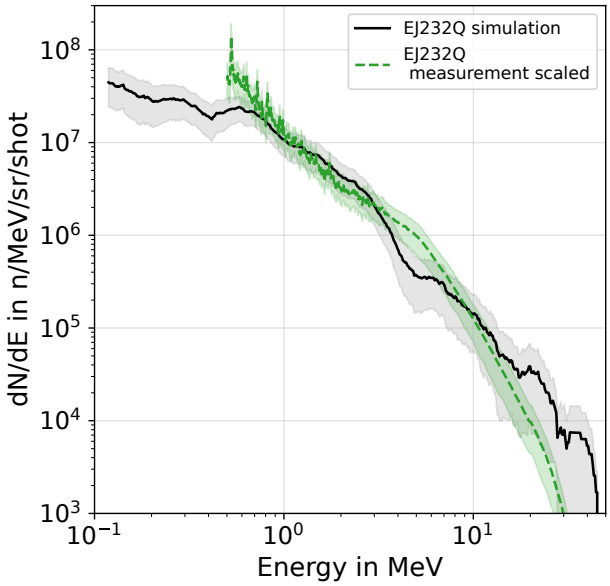

(d) LiF catcher: Scintillator.

Figure 4.16.: Neutron spectra obtained from scintillator and diamond detector measurements. (a) and (c) compare the spectral shape obtained from the diamond detectors to the simulation results and show good agreement. (b) and (d) compares the (scaled) neutron spectrum reconstructed from scintillator data to the simulation results. After scaling the scintillator spectra, they agree with the simulation results.

used for determining k_{scale}. This energy threshold will be elaborated on and justified later in this section. Afterwards, the scintillator spectrum is multiplied by k_{scale}. For the Cu converter, a value of $k_{\text{scale}} = 0.122$ is obtained and for LiF, a value of $k_{\text{scale}} = 0.109$. After scaling the spectra, good agreement can be observed between the simulated and measured spectral shapes. In both cases, the reconstructed spectra closely resemble the spectra obtained from simulations. Only below 1 MeV does the spectrum start to deviate significantly from the simulation results in the case of LiF. No definitive explanation can be given, but since a similar overestimation is not observed in Cu, it needs to be specific to the neutron spectrum generated by LiF. It could be due to the more abundant (relative to the Cu catcher) high energy neutrons inducing (n,xn) reactions inside the lead shielding.

The measured neutron cut-off energy for the LiF catcher of (34 ± 1) MeV is in reasonable agreement with the value obtained from the simulation (41 ± 3) MeV. Figure 4.16d compares reconstructed and simulated neutron spectra at the scintillator position, where the y-axis is truncated at 10^3 n/MeV/sr/shot for better visibility. After scaling, the spectral shapes of the simulated and reconstructed neutron spectrum for the Cu catcher are in good agreement over the entire energy range displayed in Figure 4.16b. In addition, the maximum neutron energy is also in good agreement, with a measured maximum of (22 ± 1) MeV and (23 ± 2) MeV obtained from the simulations.

The results show that the neutron spectra measured by the diamond detector reproduce the neutron spectra expected from simulations, while the scintillator fails to do the same. The deviation between simulated and measured spectra is less than $5\,\%$ (Cu) and $45\,\%$ (LiF) for the diamond detectors. Spectra retrieved from scintillator data overestimate the neutron fluence by up to a factor of ~ 20. Nonetheless, it is still possible to retrieve the shape of the neutron spectrum from the scintillator data. Since converting the measured scintillator signal to neutron spectra is quite involved and depends strongly on assumptions made and Monte Carlo simulations for modeling its response, minor errors can result in significant deviations.

Further investigation into the scintillator results

Due to the significant discrepancies between the simulated and measured data for the scintillator, the simulation results are further investigated to narrow down the origin of the deviation and potentially compensate for them. Potential causes for deviations originating from the experiment are overlapping γ-flash and neutron signals (in time), leading to an increased photon generation in the scintillator. Further causes can be scattering contributions, which could result in high energy neutrons overlapping in time with neutrons of lower energy, thus increasing the amount of light generated by the scintillator. Similarly, contributions from neutrons generated by the secondary source terms can also play a role since the neutrons are not correlated with the assumed time-of-flight times. Especially for lower neutron energies $\lesssim 1$ to 3 MeV, this can cause significant overestimation of the neutron fluence, due to the non-linearity between neutron energy and light yield.

The first point of investigation is the overlap between photons and neutrons in time. Because neutron energies are determined via time-of-flight measurements, an overlap in time can lead to overestimation of the neutron fluence. Figure 4.17 displays both catchers' time-of-flight signal for neutrons (black line) and photons (red dashed line). The contribution from the γ-flash is visible, arriving after about 13 ns (first peak). The second, more prominent peak arriving after 17 ns is caused by scattered photons near the detector. The time difference between the first and second peak of around 4 ns suggests that a reflection from the wall behind the detector, see Figure 4.10, is most likely responsible, since the distance to the wall is between 0.5 to 1 m. The reflected peak increases in intensity, as no shielding facing the wall was present during the experiment.

Also visible is a significant overlap of photons and neutrons from 55 to 200 ns, corresponding to neutron energies of 2 to 25 MeV. This range covers most of the energy range measured by the scintillator. Based on

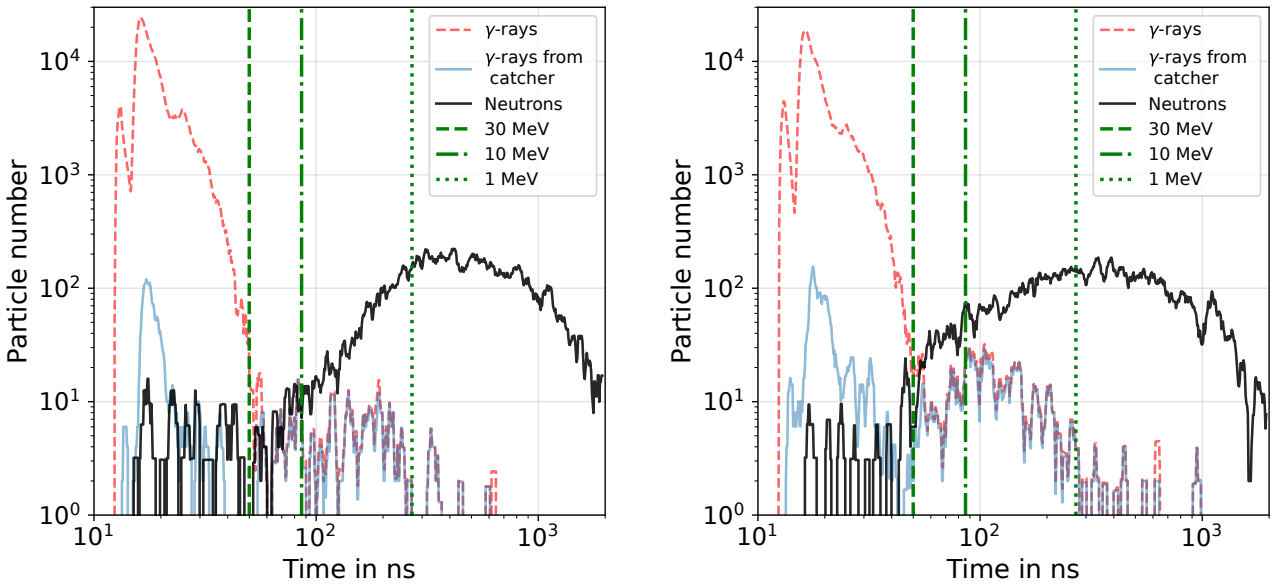

(a) Cu catcher time-of-flight signals.

(b) LiF catcher time-of-flight signals.

Figure 4.17.: Results obtained from Monte Carlo simulations. (a) Time distribution of γ-rays (red) and neutrons (black) reaching the scintillator for the Cu catcher. The vertical green lines indicate ToF for selected energies. Considerable overlap between photons and neutrons can be seen for neutron energies between 2 to $25\,\mathrm{MeV}$. As indicated by the blue line these photons mostly originate from the simulation run utilizing the forward proton beam. (b) show the time distribution of photons and neutrons arriving at the scintillator for the LiF catcher. Again significant overlap between the neutrons above $2\,\mathrm{MeV}$ and photons is visible.

the energy spectrum of these photons, it is likely that they either originate in the catcher and arrive at the detector via scattering or are generated from inelastic neutron collisions in the lead shielding. The significant time difference between the time of the proton beam impinging on the catcher and the arrival time of the photons at the detector suggests that this component is dominated by photons from inelastic (n,n') neutron scattering in the shielding and room scattering. Of these arriving photons, $26\,\%$ have energies above $1\,\mathrm{MeV}$ and a maximum energy of around $7\,\mathrm{MeV}$. The energies are sufficiently large to generate a signal inside the scintillator, but do not dominate over the neutron contribution at the same times. Nonetheless, the photon contribution plays a role in the overestimation of the neutron fluence by the scintillators, especially for the highest neutron energies. However, the neutrons of the highest energies have the lowest influence on the integral neutron fluences.

Following up on the initial assessment of Figure 4.17, it is also visible that the neutrons become dominant around $100\,\mathrm{ns}$ after the laser-target interaction. This is despite the fact, that the photon time-of-flight to the detector is $t_\gamma = 3.752\,\mathrm{m/c_0} \approx 13\,\mathrm{ns}$ and up to $15\,\mathrm{cm}$ of lead were used to shield the detector from the photons. Consequently, in the setup used at DRACO, measurements relying on a plastic scintillator-based detector are only really suited for use at LDNS, where distances of $\gtrsim 4\,\mathrm{m}$ are achievable to avoid significant overlap with the photon signal. The overlap is worsened during an experiment due to the slow decay of the scintillator in the ns range, which was not considered in the results presented here. Furthermore, bulk shielding material is also detrimental to the measurement due to photon generation via inelastic neutron scattering inside the shielding material. Additionally, recalling the structure of the γ-flash consisting of the direct and the reflected components suggests that placing detectors in close proximity to walls should be

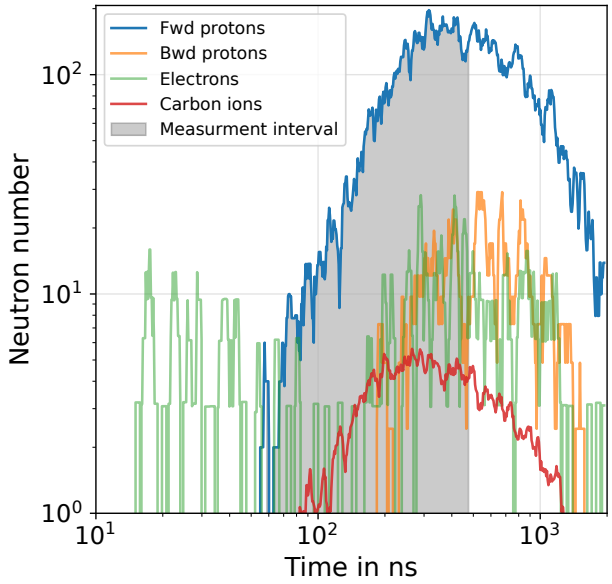

(a) Cu catcher: Arrival times.

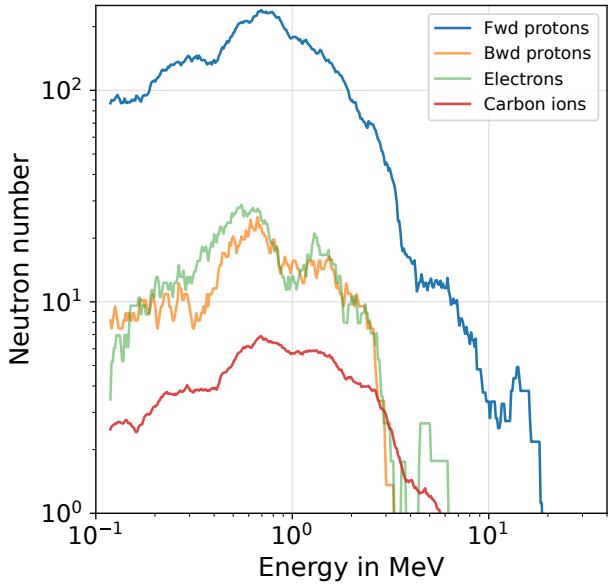

(b) Cu catcher: Energy.

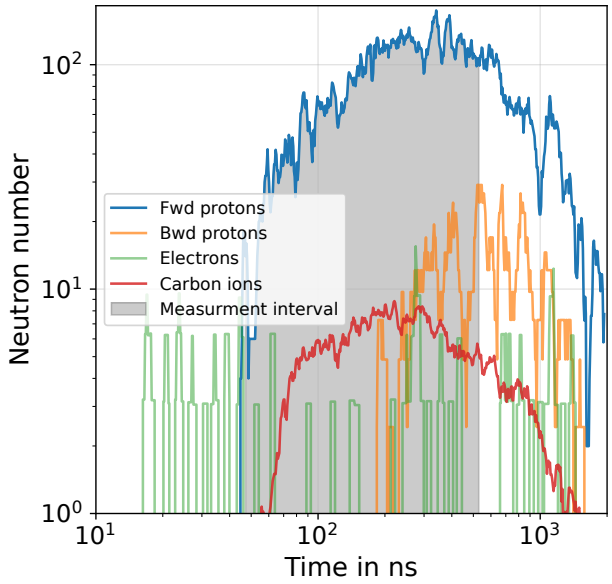

(c) LiF catcher: Arrival times.

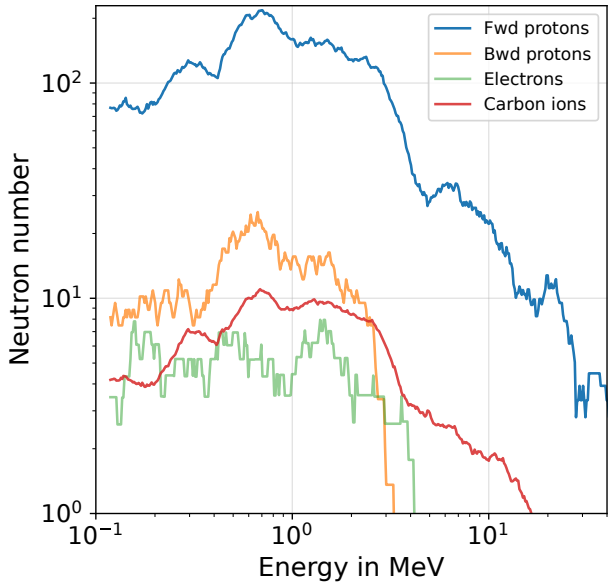

(d) LiF catcher: Energy.

Figure 4.18.: Contribution of each source term at the position of the scintillator scored versus arrival times (a), (c) and energy (b), (d). Displayed are absolute neutron numbers that arrive at the detector position per shot. The gray area indicates the time interval used for the reconstruction of the experimentally measured scintillator traces.

avoided. During the experiment the detector was placed at a distance of 0.5 to 1 m from the wall. The results imply that a greater distance to the wall benefits the detector setup, as the influence of the γ-flash can be reduced. Furthermore, the shielding setup needs to be optimized beforehand using Monte Carlo simulations to determine sources of noise and minimize their influence. Such an optimization is highly location-specific and thus needs to be done for every detector and setup individually.

Figure 4.18 shows neutron numbers arriving at the scintillator position for each source term with respect to energy and time. As can be seen from figures (a) and (c), neutrons generated by the electron source term arrive at the scintillator first. These neutrons do not contribute to the signal since they overlap with the γ-flash and are thus obscured (see Figure 4.17) and removed during the γ-flash subtraction.

The time interval used for the spectral reconstruction of the neutron beam is indicated by the gray-shaded area in Figure 4.18. The bounds of the gray area are obtained from the mean scintillator trace (after subtracting the γ-flash) for the Cu/ LiF day that was used to reconstruct the neutron spectra shown in Figure 4.16b and 4.16d. Within this interval, neutrons generated by the forward proton beam are the dominant contribution, the "desired" neutrons. Within the total time frame of interest, around 85 % (Cu) and 87 % (LiF) of the neutrons originate from (p,n) reactions inside the catcher. However, for both catcher and within the gray area, it can be seen that for times later than 270 ns, 10 % of neutrons arriving at the scintillator originate from the backward proton beam, with the total contribution from the secondary source term adding up to 15 to 18 %. This is troublesome for a couple of reasons. The highest energetic neutrons generated by the backward proton beam that reach the scintillator position have energies of 2 to 4 MeV. These neutrons overlap in time with 0.25 to 1 MeV neutrons generated in the catcher by the forward proton beam. The light yield inside the scintillator for 2 to 4 MeV neutrons is on average is about 3 to 5 times higher than that of 300 to 800 keV neutrons, this can be seen in Figure 3.3a. This increase leads to an overestimation of the neutron number below 0.9 to 1 MeV and is partly responsible for the overestimation in the reconstructed spectra. More precisely the overestimation affects neutrons with flight times that correspond to 0.9 to 1 MeV.

From Figure 4.18a and 4.18c it can also be seen that the pulse stretches over 1 µs, a clear indication of contributions from scattered neutrons. While the tail of the neutron distribution does not affect the scintillator measurement, since it is outside the measurement time interval, scattered neutrons can also arrive within the interval, thus affecting the scintillator signal and the reconstruction.

Neutrons generated by carbon-induced reactions only have a limited influence on the measured time distribution of the neutron spectrum, both in the case of Cu and LiF catchers. This is due to the neutrons originating inside the catcher and the shape of the emitted spectrum, which closely matches that of the proton-induced reactions, see Figure 4.18b and 4.18d. Furthermore, the time-of-flight of the neutrons closely match that or fall within the uncertainty of the ToF for neutrons generated by the forward proton beam inside the catcher. Moreover, the overall contribution to the total neutron number is limited at less than 6 % of the total signal for both catchers.

Overall, the neutrons arriving at the scintillator originate mainly from the catcher, with other contributions only playing a minor role over most of the energetic and time ranges of interest. Nonetheless, the contributions of secondary neutron sources significantly impact the neutron signal below 0.9 to 1 MeV. Thus, a cut-off in time, corresponding to neutron energies below 0.9 MeV, is applied to the scintillator traces. This correction reduces the measured neutron fluence by the scintillator, which is more compatible with results obtained from the BDs and the simulations. Table 4.4 shows the updated values for the different shot sets. Comparing the results to bubble detector measurements still shows an overestimation of factor 1.4 to 7. However, the overall deviation is reduced compared to the data presented in Table 4.1, where the deviations reached up to a factor of 12. Thus, the overestimation is likely caused by assumptions and simplifications made in the reconstruction method, highlighting the need for the method to be revised. An in-depth conclusion,

Table 4.4.: Updated integral neutron fluence Φ_{scint} calculated from scintillator data, after applying the cut-off in time, excluding neutrons below $0.9\,\text{MeV}$. The results are compared to mean neutron fluence measured by the BDs displayed in Figure 4.6a.

Catcher	Shot set	Φ_{Scint} in 10^7 n/sr/shot	$\Phi_{\text{Scint}}/\Phi_{\text{BDs}}$
Cu	10	6 ± 1	1.4
	11	16 ± 3	3.7
	13	6 ± 3	1.4
	16	13 ± 3	3.0
	17	15 ± 7	3.5
	22	6 ± 2	1.4
	Full day (22.10)	9 ± 1	2.1
LiF	8	21 ± 6	4.3
	15	35 ± 8	7.1
	18	28 ± 7	5.7
	Full day (29.10)	13 ± 2	2.7

summarizing and discussing all findings of the DRACO experimental campaign is given in section 4.9.

4.6.3. Assessment of background levels and resolution functions

Since neutron measurements rely on the time-of-flight (ToF) technique, it is crucial that the recorded flight time actually corresponds to the appropriate energy. Energy and flight time can deviate when neutrons undergo scattering events before reaching the detector or if the primary neutron pulse length is comparable to the ToF. Using Monte Carlo simulations, the correlation between these two quantities can be investigated and summarized in what is referred to as a resolution function (RF). In these simulations, the full geometry, including all source terms, is used. From the RF, beamline-dependent correction can be calculated and the feasibility of applications for a given setup/beamline can be assessed (Sabate Gilarte 2017).

To obtain the resolution function, both the actual neutron time-of-flight t_{n}, which is the time at which the neutron enters the detector and the energy of the neutron E_{n} as it enters the detector volume are needed. The data can then be binned in energy and time, yielding the resolution function. Comparing the value for t_{n} to the ideal flight time, calculated from the distance l to the detector and the relativistic kinetic energy, shows if neutrons arriving at the detector used the shortest path possible. The ideal flight time corresponds to the direct and, therefore, shortest flight path, containing the direct or ”true” neutron signal.

In Figure 4.19a and 4.19c, the time of flight distribution versus the energy of the neutrons is shown, using the copper catcher. The dashed red line is the energy-time correlation for the ideal case. The top figure shows the result for the bubble detector placed at $0°$, whereas the bottom shows the scintillator. The inset shows a zoomed in view of the data. The two resolution functions show a different distribution for the neutrons at each detector position. While most neutrons are situated tightly around the dashed red line for the bubble detector, neutrons at the scintillator show a broad distribution around the ideal ToF. This means that the neutron signal at the scintillator is more strongly affected by scattered neutrons than the bubble detector. However, a significant contribution besides the ideal ToF for the bubble detector can also be observed. From the plots, it is already visible that the experimental setup does not allow for precision measurements, such as cross section measurements, especially below $5\,\text{MeV}$. Furthermore, it shows that neutron fluences obtained from the detector are influenced by contributions from scattered neutrons, which

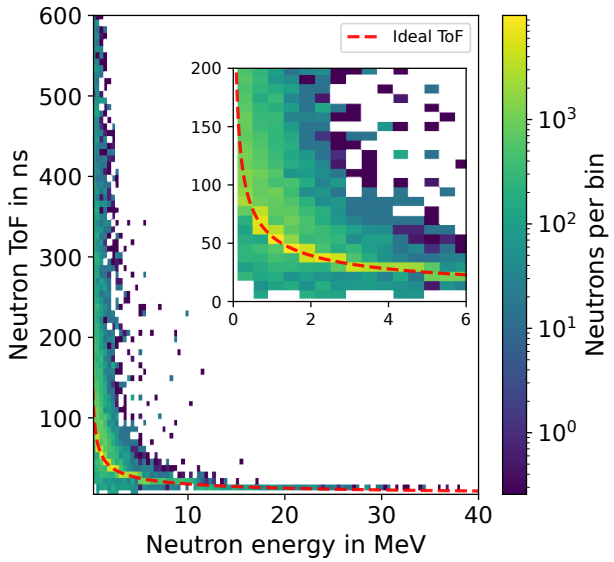

(a) 2D resolution function for the bubble detector.

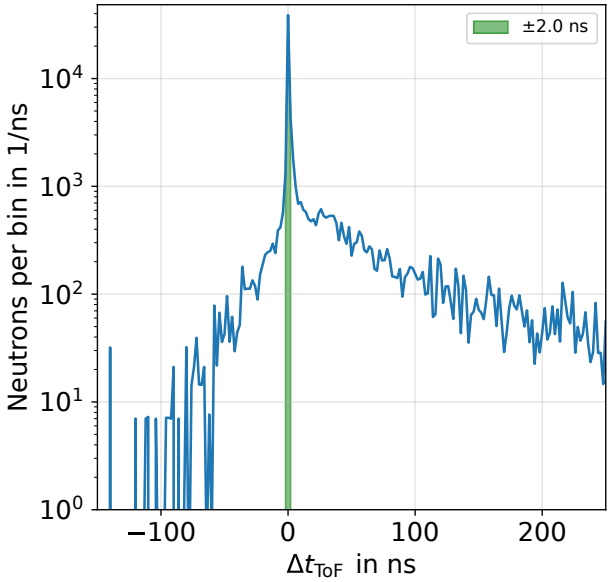

(b) Neutron distribution n_{ToF} based on (a).

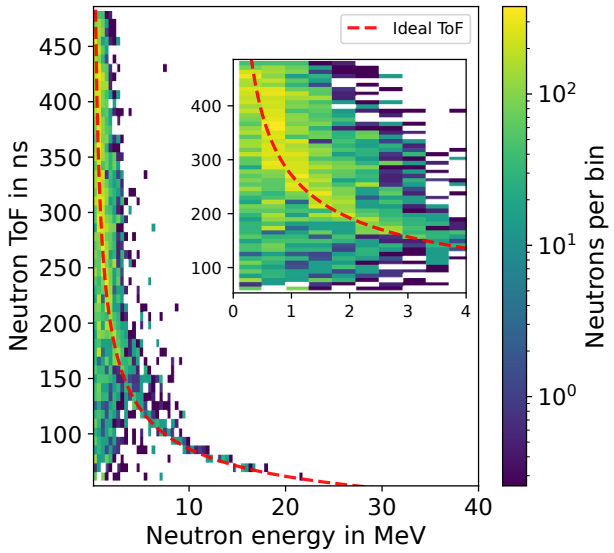

(c) 2D resolution function for the scintillator.

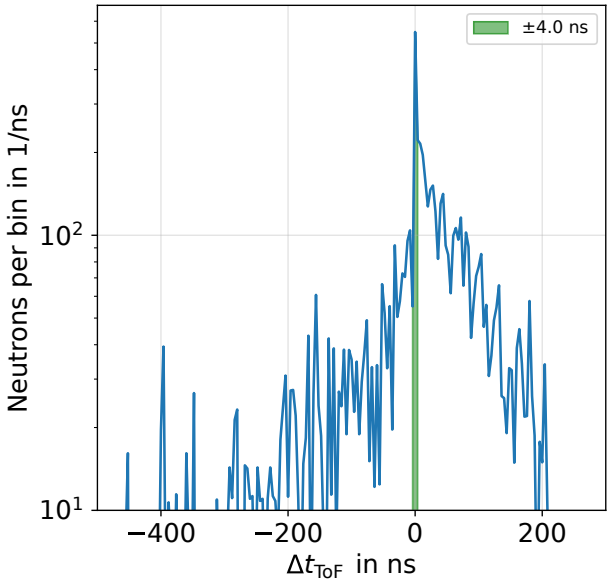

(d) Neutron distribution n_{ToF} based on (c).

Figure 4.19.: Results from PHITS simulations using a Cu catcher. Resolution functions for the bubble detector placed at $0°$ (a) and (b), as well as the scintillator (c) and (d) are shown. For the scintillator only neutrons arriving in the time interval indicated by the gray shaded area in Figure 4.18a are considered. (a) and (c) show the relation between arrival time and energy of the neutrons at the position of the detectors. The red dashed line indicated the ideal time-of-flight. The insets show a zoomed in view. (b) and (d) show the results of Equation 4.2. The green shaded area indicates the direct signal component of the scored neutrons listed in Table 4.5.

Table 4.5.: Percentage of direct neutrons arriving at each detector for a given catcher used during the experiment. Up to $59\,\%$ of the neutron at the detector arrive via scattering in the case of the Cu catcher, excluding the scintillator. For LiF up to $62\,\%$ of neutrons do not fall within $\pm\,\mathrm{d}t$.

Detector	Cu catcher	LiF catcher
Diamond	$71.3\,\%$	$80.0\,\%$
Scintillator	$10.3\,\%$	$11.2\,\%$
BD $0°$	$52.5\,\%$	$64.9\,\%$
BD $60°$	$49.4\,\%$	$53.8\,\%$
BD $120°$	$41.4\,\%$	$38.4\,\%$

can lead to overestimating the fluence at the detector position.

To more easily distinguish and quantify the contribution of scattered neutrons to the total amount of neutrons arriving at the position of the detector, the RF can be expressed in terms of a single variable Δt_{ToF}. Calculating Δt_{ToF} also requires t_{n} and E_{n}. Note again that t_{n} is the actual time the neutron needed to arrive at the detector and E_{n} is the energy with which the neutron enters the detector volume. These two quantities do not have to be correlated, as is demonstrated in Figure 4.19 (a) and (c). The energy E_{n} can be used to calculate the time-of-flight $t(E_{\mathrm{n}})$ that actually corresponds to E_{n} using

$$t(E_{\mathrm{n}}) = t_{\gamma} \cdot \left[1 - \left(\frac{\mathrm{m_n c^2}}{E_{\mathrm{n}} + \mathrm{m_n c^2}}\right)\right]^{-0.5}, \tag{4.1}$$

where $t_{\gamma} = l/\mathrm{c}$ is the time of flight for photons from the source to the detector. Note that $t(E_{\mathrm{n}})$ does not have to equal t_{n}. Then Δt_{ToF} is defined as

$$\Delta t_{\mathrm{ToF}} = t_{\mathrm{n}} - t(E_{\mathrm{n}}). \tag{4.2}$$

For neutrons where $\Delta t_{\mathrm{ToF}} = 0 \pm \mathrm{d}t$, the tallied ToF t_{n} matches the calculated time $t(E_{\mathrm{n}})$ within an uncertainty $\mathrm{d}t$. This means that t_{n} and E_{n} are actually correlated. Thus, these neutrons are not affected by scattering events (mostly) taking the direct path and are the desired signal, which will be referred to as direct signal/neutrons. An uncertainty of $\mathrm{d}t$ is present die to the geometry of both the catcher and the detector, in addition to the primary temporal neutron pulse structure and the temporal resolution of the detector. Neutrons that do not fall within $\mathrm{d}t$ are affected by neutron scattering and do not take the shortest path from the catcher to the detector. These neutrons are referred to as the indirect/noise signal. Figure 4.19b and 4.19d display the neutron number n_{ToF} per Δt_{ToF} bin, based on the data in Figure 4.19a and 4.19c. The green-shaded area corresponds to the $\pm\,\mathrm{d}t$ time interval.

Positive values for Δt_{ToF} mainly originate from three sources. First, neutrons that initially do not travel in the direction of the detector are scattered towards the detector, thus taking longer to arrive. Second, neutrons taking the direct path are scattered multiple times within the shielding surrounding the detector before entering the detector. Third, the neutrons do not originate from (p,n) reactions inside the catcher. For example neutrons generated by the backward proton beam arrive at later times as a consequence of the increased distance between the generation location and the detector. Negative values can be caused by secondary sources that are closer to the detector than the catcher, for example, neutrons generated via (γ,n) reactions inside the target chamber walls or lead shielding of the detector. Additionally, neutrons that down-scatter close to the detector result in negative times since the neutron traveled most of the distance

at a higher energy. Moreover, neutron multiplication via (n,xn) reactions has a similar effect as neutron down-scattering has on Δt_{ToF}.

Using the distribution for n_{ToF} from Figure 4.19b and 4.19d, the fraction f of the unscattered (direct) neutrons to the overall neutron number at the position of the detector can be calculated by integration, resulting in

$$f = \frac{\int_{-\,\mathrm{d}t}^{\mathrm{d}t} n_{\mathrm{ToF}}(\Delta t_{\mathrm{ToF}})\,\mathrm{d}\Delta t_{\mathrm{ToF}}}{\int_{-\infty}^{\infty} n_{\mathrm{ToF}}(\Delta t_{\mathrm{ToF}})\,\mathrm{d}\Delta t_{\mathrm{ToF}}}. \tag{4.3}$$

In this definition, $f = 1$ means a perfect correlation between time-of-flight and energy for every neutron entering the detector. Thus, for experimental measurements, a beamline with $f = 1$ is desired. Otherwise, corrections based on the RF are necessary. Table 4.5 summarizes the values for f for the different detectors and catchers used during the experimental campaign. The method reveals that the ToF-energy correlation only holds for around half the neutrons arriving at most detectors, indicating large scattering contributions. The only exception is the diamond detector, where the correlation holds for at least $71\,\%$ of the arriving neutrons ($f = 0.71$).

Experimentally, this can be tested by conducting a shadow bar measurement, in which a thick block of polyethylene blocks the direct path between the catcher and detector. The block scatters the direct neutrons, leaving only the indirect contribution. Shadow bar measurements conducted during the beamtime, reveal an f of 0.5 to 0.6 for the diamond detector, meaning that $50\,\%$ to $60\,\%$ of neutrons take the direct path from source to detector (Millán-Callado 2023). The value is in reasonable agreement with the simulation results presented in Table 4.5, with the deviations most likely resulting from the limited statistics of the shadow bar measurements. In the following the results for the scintillator and the bubble detector placed at $0°$ are further investigated. Only the results for the Cu catcher are discussed, with the LiF results shown in section A.1.

Investigating the resolution function of the bubble detector placed at $0°$ more closely reveals that $52.5\,\%$ percent of the neutrons measured arrive within the expected time window $\pm\,\mathrm{d}t$. With no shielding in the vicinity of the BDs, only the target chamber and the target area's floor can cause the observed scattering contribution. Nonetheless, comparing Figure 4.19a to 4.19c shows that the tallied neutrons adhere more closely to the ideal ToF for the bubble detector than is the case for the scintillator, as indicated by the colormap. From Figure 4.19b, it can be seen that the distribution is strongly biased towards positive values for Δt_{ToF}, meaning neutrons arrive later than their energy suggests. Calculating the number of neutrons for $\Delta t_{\mathrm{ToF}} < -2\,\mathrm{ns}$ and comparing it to the number of neutrons arriving with $\Delta t_{\mathrm{ToF}} > 2\,\mathrm{ns}$ reveals that the number of neutrons arriving too late is 6 times higher than that of neutrons arriving too soon. This means that the indirect neutron signal is strongly influenced by contributions from neutron scattering and neutrons generated by secondary source terms in a location further away from the detector than the catcher. Compared to the neutron spectrum at the source position, the number of neutrons below $\sim 1\,\mathrm{MeV}$ should be elevated at the position of the bubble detector. Curiously, the direct component for the bubble detector is increased when using the LiF catcher compared to the copper catcher, which is also observed for the diamond detectors. The difference could be caused by differences in spectral distribution between the two catchers. LiF generates a higher average neutron energy ($6.7\,\mathrm{MeV}$ vs. $5.3\,\mathrm{MeV}$), resulting in an increased mean free path inside matter. Furthermore, the emission of neutrons in a forward direction close to 0° is favored in LiF compared to Cu.

From the RF of the scintillator, the direct component arriving within $\pm\,\mathrm{d}t$ is calculated to be $10.3\,\%$, with the remaining $89.7\,\%$ arriving at times not corresponding to their energy. Looking at the data in Figure 4.19d and the indirect signal, it can be seen that, in contrast to the bubble detector, the indirect signal is more

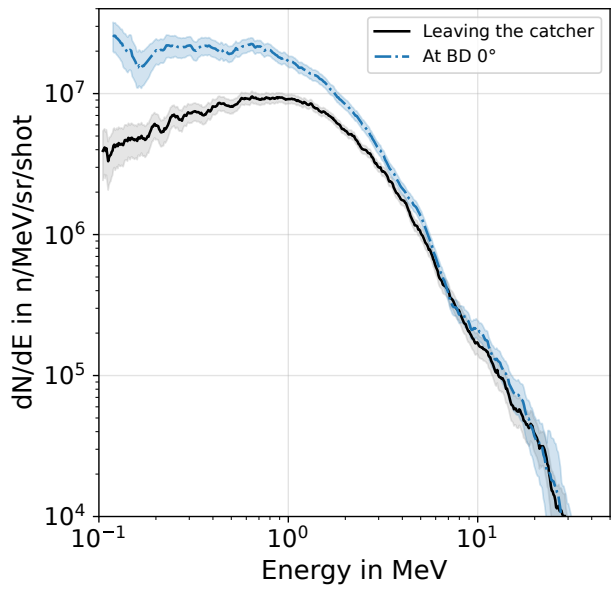

(a) Cu catcher: Bubble detector results.

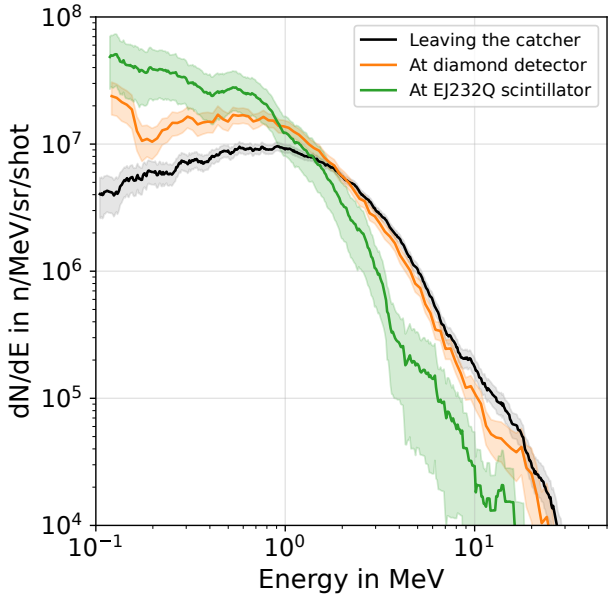

(b) Cu catcher: Scintillator and diamond detector results.

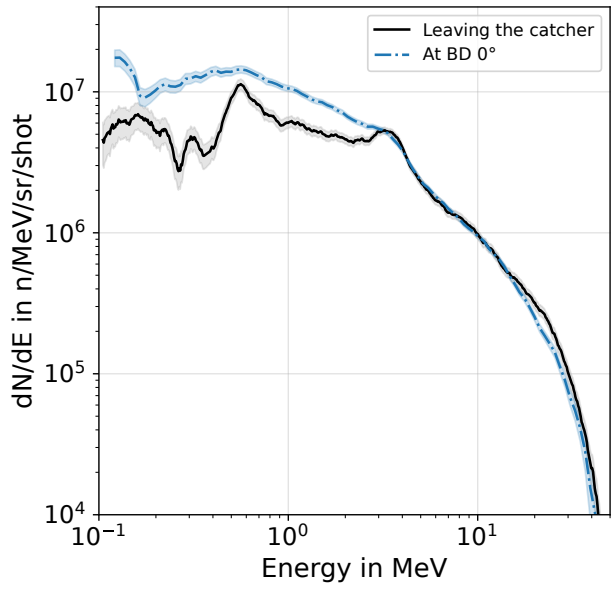

(c) LiF catcher: Bubble detector results.

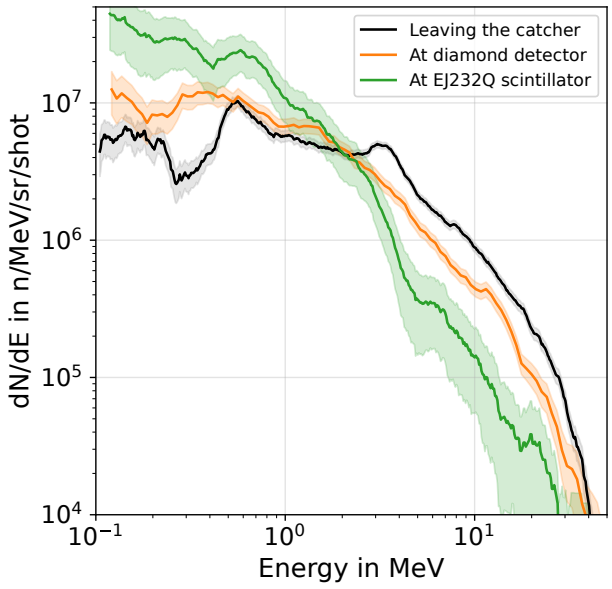

(d) LiF catcher: Scintillator and diamond detector results.

Figure 4.20.: Comparison between the neutron spectrum emitted at the source and the spectrum arriving at the detector position. (a) and (c) show the results for the bubble detector position at $0°$. (b) and (d) show the results for the scintillator and diamond detector position.

evenly distributed between neutrons arriving too soon and too late. For the scintillator, the amount of neutrons arriving with $\Delta t_{\mathrm{ToF}} > 4\,\mathrm{ns}$ is 1.6 times larger than that of neutrons corresponding to $\Delta t_{\mathrm{ToF}} < -4\,\mathrm{ns}$ (for the bubble detector, this number was 6). A significant amount of neutrons arrive sooner than they should, according to their tallied energy, indicating significant moderation and neutron multiplication inside the lead shield. In the neutron spectrum, these effects should be visible by increasing lower energy neutrons ($E_{\mathrm{n}} \leq 1$ to $2\,\mathrm{MeV}$) and reducing neutron fluence above 5 to $7\,\mathrm{MeV}$.

The neutron spectrum obtained from the full geometry simulations at the position of the bubble detector and scintillator is compared to the simulated neutron spectrum that leaves the catcher, discussed in subsection 4.6.1 and displayed in Figure 4.12c and 4.12d. Note that these spectra are generated using only the forward proton beam source term, whereas the full geometry simulation utilizes all source terms. The results for the bubble detector are presented inFigure 4.20a and 4.20c. For energies above 3 to $4\,\mathrm{MeV}$ the neutron spectrum closely matches the spectrum emitted from (p,n) reactions inside the catcher. This part of the spectrum is almost unaffected by scattering and originates from (p,n) reactions inside the catcher. The most significant deviation occurs for neutrons below $1\,\mathrm{MeV}$ as a result of neutrons generated from the electron source term and moderation by the room. Since most of the neutrons arrive for $\Delta t_{\mathrm{ToF}} > 2\,\mathrm{ns}$ (too late) and since the high energy part of the spectrum is almost unchanged, neutrons must be scattered by nuclei with much greater mass than the neutron. Consequently, it is likely that most of the neutrons are scattered by the target chamber.

Results for the scintillator are presented in Figure 4.20b and 4.20d, showing that the neutron spectrum arriving at the detector position exhibits large deviations from the spectrum emitted by the catcher. The neutron fluence below 1 to $2\,\mathrm{MeV}$ is elevated compared to the spectrum at the catcher, whereas larger energies are suppressed. The suppression at larger energies indicates strong neutron moderation either inside the lead shielding or the wall of the target area. Furthermore it can indicate neutron multiplication via (n,2n) reactions inside the lead, which have a threshold energy of around $7.4\,\mathrm{MeV}$. This is aligns with conclusions drawn from the RF presented in Figure 4.19d. For reference, the spectrum at the position of the diamond closely resembles the spectrum emitted by the catcher. The main difference between the scintillator and diamond detector setup is the significantly reduced lead shielding, highlighting the influence of the lead shielding surrounding the scintillator.

The counter function of PHITS is leveraged to verify the results obtained from the RF and the spectral comparison of the previous paragraphs.Using the counter function, neutrons can be tagged every time they undergo a scattering event in a specified region of the experimental setup. Afterward, a mask can be applied to the data in post-processing, which can be used to exclude neutrons that were scattered in a specific region. The results for different masks can be seen in Figure 4.21, where the top row shows the RFs for the bubble detector and the bottom for the scintillator.

As before, the bubble detector is investigated first. Figure 4.21a displays the resolution function when excluding neutrons that arrive at the bubble detector after being scattered by the walls of the target area. Comparing this RF to the one including neutrons scattered by the target area (Figure 4.19a) shows only marginal differences, with only a slight reduction of neutrons detected at very long flight times (> 200 to $300\,\mathrm{ns}$). In contrast, excluding neutrons that are scattered by the target chamber results in a completely different RF, as shown in Figure 4.21b. In this case, almost all contributions not corresponding to the ideal ToF vanish and only a few contributions at mostly large ToFs ($> 200\,\mathrm{ns}$) remain, originating from room scattering. In fact, 40 to $50\,\%$ of the total number of neutrons at the position of the detector are excluded by this mask. In the figure's inset, a contribution sitting just above the ideal ToF is visible for energies ranging from approximately 1 to $5\,\mathrm{MeV}$. These neutrons are generated from the secondary source term. Contributions situated below the ideal ToF in Figure 4.21b originate from the electron source term. This can be confirmed when excluding all neutrons that underwent at least one scattering, leaving

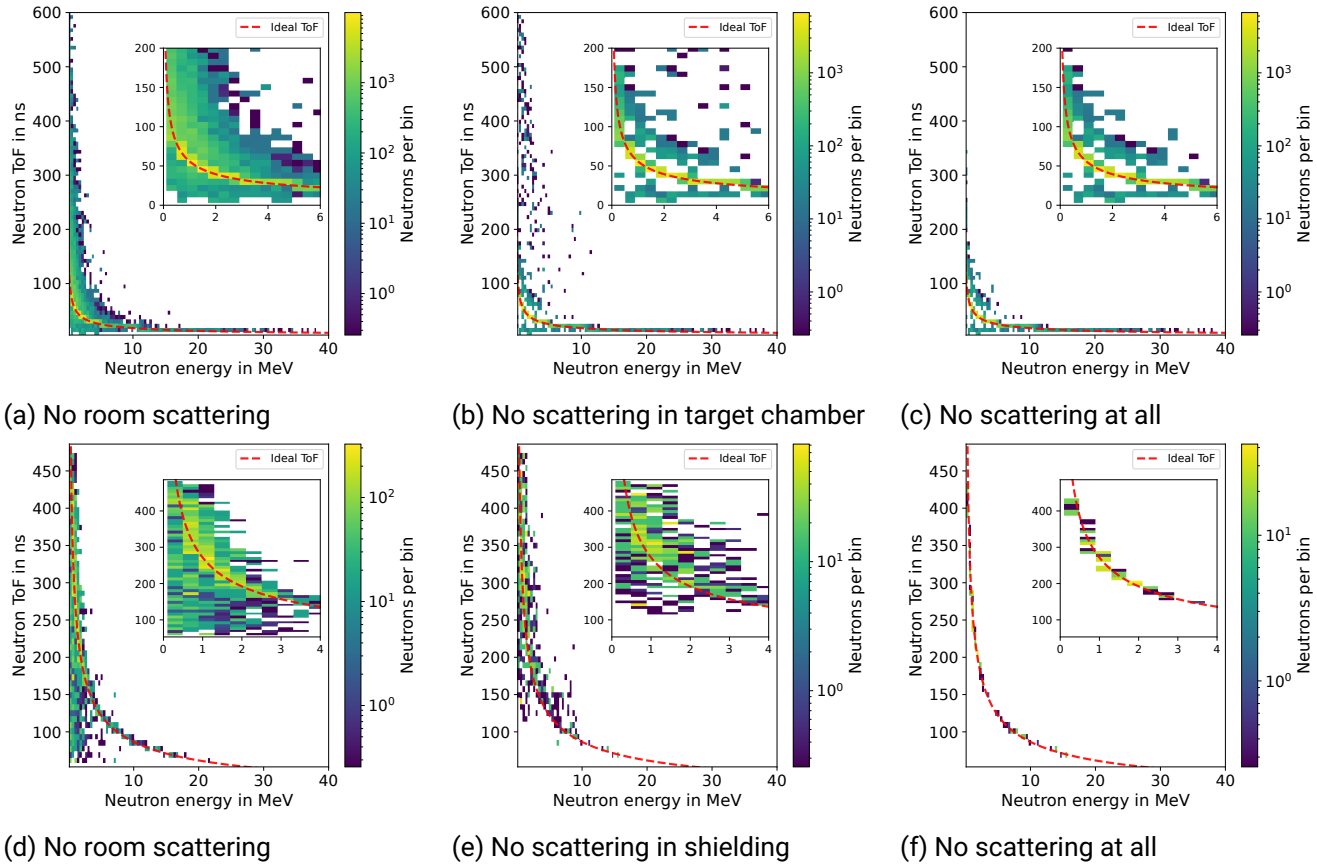

(a) No room scattering (b) No scattering in target chamber (c) No scattering at all

(d) No room scattering (e) No scattering in shielding (f) No scattering at all

Figure 4.21.: Results are obtained from PHITS simulations using the Cu catcher. The top row shows results for the bubble detector at $0°$ with the bottoms row showing results for the scintillator. (a)/(d) 2D resolution function when excluding neutrons that are scattered by the room before reaching the detector. (b)/(e) shows the resolution function of the detectors excluding neutrons that underwent scattering in either the target chamber and/or the lead shielding. (c)/(f) shows neutrons that have not interacted with anything before entering the bubble detector or scintillator. Neutrons deviating from the ideal ToF in (c) and (f) cannot be generated by the forward proton beam inside the catcher.

only unscattered neutrons to contribute, as depicted in Figure 4.21c. Using the data of this figure and Equation 4.3 to calculate the direct neutron component, falling within $\pm \mathrm{d}t$, reveals that around $95\,\%$ of neutrons fall within this range. Therefore, in an ideal case, without neutron scattering, the contribution of the secondary source terms to the bubble detector measurement is around $5\,\%$.

Switching to the scintillator shows that room-scattered neutrons play a more significant role compared to the bubble detector results, as indicated by Figure 4.21d. Here, only $48\,\%$ of all neutrons arriving at the scintillator have not undergone at least one scattering, even with the walls of the target area. The high percentage can partly be explained by the proximity of the room's walls to the detector and the lack of shielding at the backside of the detector, facing the wall. However, the bulk lead shielding surrounding the detector is even more influential. Only about $13\,\%$ of the neutrons entering the scintillator have not interacted with the lead shielding. This can be readily seen in Figure 4.21e. Finally, only scoring unscattered neutrons (Figure 4.21f) shows that $> 99\,\%$ of the arriving neutrons fall within $\pm \mathrm{d}t$.

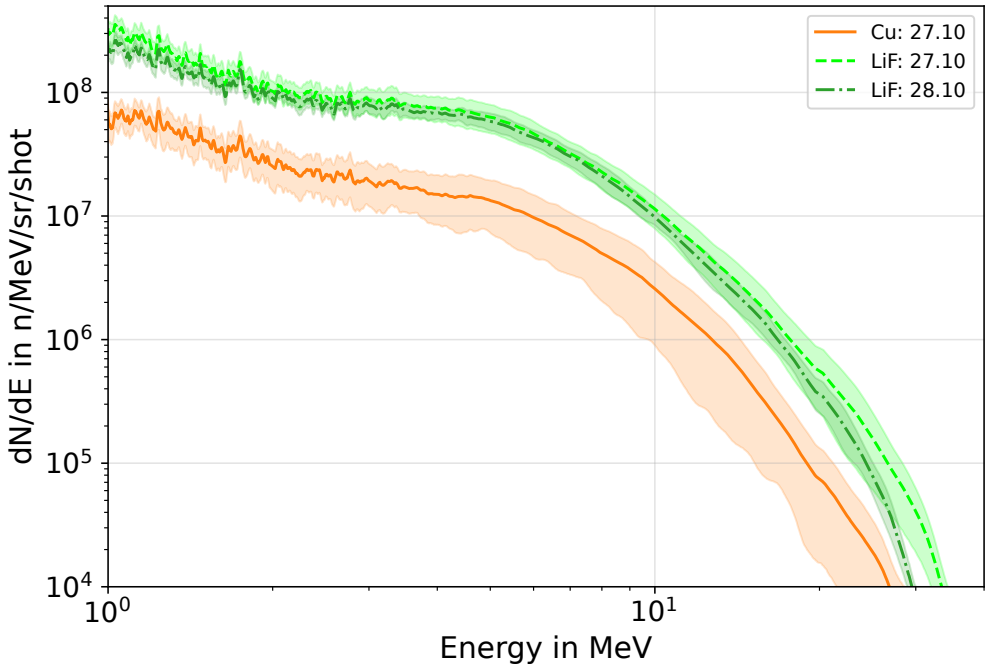

Figure 4.22.: Reconstructed neutron spectra for the different catchers using deuterated targets.

To summarize, the RF allows for an in-depth assessment of the performance of a detection system and the beamline. In the context of LDNS, massive shielding assemblies surrounding fast neutron detectors significantly influence the distribution of the measured signal. Furthermore, proximity to the target area's walls increases contributions from scattered neutrons. Regarding BDs, only 38 % to 65 % of the measured neutrons arrive at the detector unscattered; the rest do not take a direct path from the source to the detector. Scattered neutrons arriving at the bubble detector that might have otherwise not been directed towards the bubble detector lead to an overestimation of the true neutron fluence. This overestimation in the available fluence can lead to erroneous assumptions regarding measurement times and achievable precision for a given irradiation time. Moreover, as neutron scattering is sensitive to the geometry and materials used in the experimental setup the contribution of scattered neutrons to the overall fluence is unique for each setup. This significantly complicates comparisons of the neutron fluences measured at different laser facilities based on measurements that did not take this scattering component into account and correct for it.

4.7. Neutron production from deuterated targets

During the beamtime, deuterated targets were used to boost the neutron production. Neutron production from these targets will only briefly be discussed, as not many shots could be taken using these due to limited target supply. Furthermore, obtaining absolute deuterium spectra from the Thomson parabola was impossible, as the setup is not calibrated for absolute measurements of deuterium ions. Here, the integral neutron fluence obtained from the scintillator is analyzed, taking the findings of previous sections into account.

In Figure 4.22, the mean reconstructed neutron spectra for the LiF and Cu converter are shown, recorded over 15 shots, with the shaded area corresponding to the uncertainty due to shot-to-shot variations. Calcula-

tions of the neutron fluence include the mean overestimation factor from Table 4.4. For Cu this factor is 2.4 and for LiF it is 5.0.

For the Cu catcher, the neutron fluence is $(6 \pm 1) \times 10^7$ n/sr/shot, corresponding to an increase of 30 to 40 % over the fluence achieved by non-deuterated targets. Using the LiF catcher, the calculated neutron fluence at the detector is $(1.2 \pm 0.3) \times 10^8$ n/sr/shot, which is an increase of 140 % compared to the non-deuterated targets. An increase in maximum neutron energy is also observed. The increase is much larger for the copper catcher going from a mean of 18 MeV to 31 MeV, whereas for LiF the increase was more modest going from 29 MeV to 34 MeV.

A significant increase in the neutron number can be observed, more than doubling the measured fluence of the LiF catcher by using deuterated targets instead of non-deuterated ones. The findings align with data published in (Roth, D. Jung, et al. 2013; Kleinschmidt 2017; Zimmer, Scheuren, Kleinschmidt, et al. 2022). Boosting neutron production by employing deuterated targets is especially attractive when laser parameters otherwise limit the source performance or if an application requires the highest fluences possible.

4.8. Neutron production from shots with low laser pulse energy

One of the laser parameters of interest when it comes to shrinking laser-driven neutron sources with regard to size and cost is the laser energy delivered with each pulse. The influence of lower laser energy per pulse on neutron production was investigated on the 28th, where the laser energy is reduced to 2 to 3 J on target for 35 shots. Of these shots, non-deuterated targets were used for 20 shots and deuterated targets for 15 shots. Both BDs (only for deuterated shots) and the scintillator are used to assess the generated neutron fluence. LiF is the only catcher material used during these low energy shots due to the high neutron production cross sections of Li at low energies and lower energetic threshold for (p,n) reactions.

In Figure 4.23a, the reconstructed neutron spectra for both target types are displayed. Juxtaposed is the neutron production obtained from BDs in 0°, 60° and 120°, when using the deuterated targets.

With the reduction in laser pulse energy and using non-deuterated targets, the mean proton cut-off energy is reduced to (20 ± 1) MeV with a mean proton fluence of $(1.3 \pm 0.3) \times 10^{11}$ p/sr/shot. Compared to the full energy (~ 20 J on target) shots discussed in section 4.2, the proton cut-off energy is reduced by a factor of 2 to 3, with the proton fluence reduced by factor ~ 35. This reduction in proton fluence translates directly to neutron production. Thus, a reduction by at least a factor of 35 is expected. Truncating the forward proton spectrum of Figure 4.5a at 20 MeV and simulating the total neutron conversion efficiency results in $(1.3 \pm 0.1) \times 10^{-4}$ n/p$^+$. The neutron conversion efficiency from the low energy laser shots is 57 % of the efficiency achieved by the full laser energy shots (50 MeV cut-off). Combining the expected conversion efficiency from the simulation with the reduced proton production, one expects a reduction in neutron fluence of at least factor 61 compared to the full energy shots. Note that in this estimation, the influence of shielding is not included.

In Figure 4.23a, the blue line displays the neutron spectrum obtained from the non-deuterated targets. The spectrum is obtained by averaging over all 20 laser shots, with the shaded area corresponding to the uncertainty. To evaluate the integral neutron fluence, the mean overestimation factor of 5.0, based on Table 4.4, is applied to the spectrum. An integral neutron fluence of $\sim (4 \pm 3) \times 10^5$ n/sr/shot is obtained. Compared to the full laser energy shots, the fluence is reduced by a factor of 72, which agrees with the expected reduction.

Due to multi-species effects, switching to deuterated targets further reduces the proton cut-off energy and number (Huebl et al. 2020). The mean proton cut-off energy is reduced to (16 ± 2) MeV with a mean proton number of $(8 \pm 4) \times 10^{10}$ p/sr/shot. Unfortunately, the chosen experimental setup could not

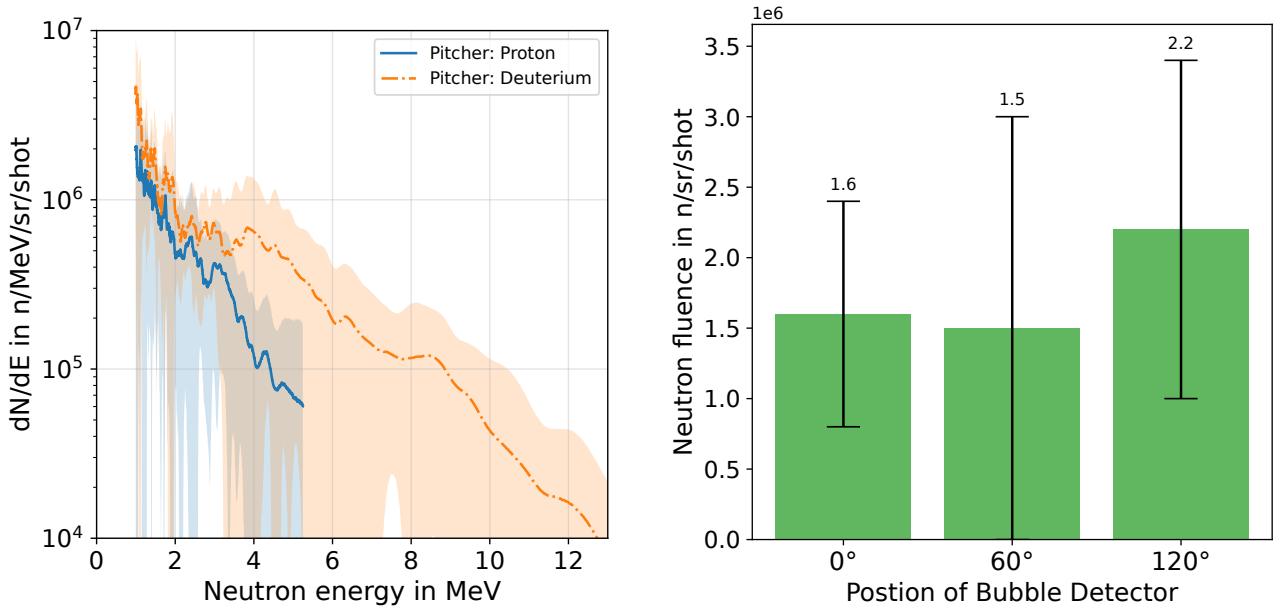

(a) Reconstructed neutron spectra for low laser energy shots.

(b) Bubble detector measurements for the deuterated targets.

Figure 4.23.: (a) shows neutron spectra reconstructed from scintillator data. The blue spectrum is generated by using a non-deuterated pitcher, whereas orange shows the neutron spectrum obtained when using deuterated targets. (b) shows the neutron fluence obtained from BDs at different angular positions for deuterated targets. Limitations discussed in section 3.3 apply to the analysis of the Bubble Detector data shown here.

measure the deuterium spectrum. As measured by the scintillator (orange, dashed line in Figure 4.23a), the neutron fluence doubles to $(1.0 \pm 0.9) \times 10^6$ n/sr/shot, compared to the non-deuterated targets. The mean overestimation factor of 5.0 for the scintillator is again applied during the analysis. This value is confirmed by the integral fluence obtained from the BDs, placed at $0°$, with $(1.6 \pm 0.8) \times 10^6$ n/sr/shot. Similar to the full energy shots, an increase in neutron fluence at larger angles is observed. The results of the bubble detector measurement are displayed in Figure 4.23b.

To put the obtained results into context, they are compared to values published by (Zulick et al. 2013), where a neutron fluence of $(1.0 \pm 0.5) \times 10^7$ n/sr/shot is reported for deuterated targets. The laser system used by Zulick *et al.* delivered (1.1 ± 0.4) J of laser energy on target, around a factor of 2 to 3 lower than what was used during the low energy shots described above. Neutrons were measured using BDs, but no information on how they were evaluated is given. A mix of deuterium and proton-based neutron generating reactions was used in the reported results. In comparison to the results of this work, the reported fluence is one (compared to results from deuterated targets) to two (non-deuterated targets) orders of magnitude larger and approaches the fluence measured during full energy shots of the DRACO campaign ($\sim 5 \times 10^7$ n/sr/shot). In (Lelièvre et al. 2023) (pre-print), a neutron fluence of $(5 \pm 2) \times 10^6$ n/sr/shot, solely from (p,n) reactions, is reported, with 10 J of laser energy on target. Results presented in this work and (Lelièvre et al. 2023) suggest that the neutron fluence might be overestimated by (Zulick et al. 2013). Thus, neutron fluence estimations for LDNS using low laser energies, based on Zulick's results, should be cautiously considered, as they may be overly optimistic.

4.9. Conclusions drawn from the DRACO experiment for the next steps in LDNS development

To conclude this chapter on the characterization of a laser-driven neutron source, the most important takeaways from the DRACO campaign will be summarized and briefly discussed.

First and foremost, it needs to be emphasized that over the course of this analysis, it could be demonstrated that state-of-the-art Monte Carlo codes such as PHITS are capable of modeling laser-driven neutron sources with reasonable accuracy, if the experimental setup is carefully transferred to the simulation space. Requirements for successful simulations of a LDNS includes the access to nuclear data libraries for the relevant neutron generating reaction channels, such as (p,n) or (γ,n), for example. Furthermore, knowledge of the individual particle source terms found at LDNS is necessary to replicate the experiment faithfully. The last point is especially challenging, as many particle species are accelerated simultaneously and travel together in bunches, such as electrons, protons and carbon ions, as a result of the TNSA mechanism (Roth and Schollmeier 2017).

Combined contributions from secondary source terms reached up to 10 to $25\,\%$ of the overall neutron signal, depending on the detector's location and setup. This contribution can play a significant role during measurements that require high precision. Which of the secondary source term contributions is dominant depends on the setup. For example, for the LiF catcher, it could be demonstrated that the largest contribution originates from the carbon ions with up to $8\,\%$. The contribution is reduced to a maximum of $5\,\%$ for the Cu catcher. The experimental setup used during the beamtime did not allow for measurement of the backward propagating carbon beam and its influence can therefore not be assessed. However, due to the high conversion efficiency from ^{12}C to neutrons, one must assume that its contribution rivals or exceeds that of the backward propagating proton beam. These findings highlight the importance of ion acceleration in the backward direction, which can generate neutron numbers comparable to the catcher. Thus, it is recommended to utilize large laser incidence angles ($>= 40°$) for LDNS to allow for the placement of a beam dump in the backward direction. Borated polyethylene is a suitable material for the beam dump.

Assessing the influence of the electron source term is not as straightforward as in the case of the carbon beam. This is because the neutron conversion efficiency depends strongly on the geometry and materials that are located closest to the laser-target interaction point. For the shots using the Cu catcher, the contribution of the electron source term reaches up to $17\,\%$, while it played no important role for the LiF catcher.

The same holds true for the backward propagating proton beam. During this experimental campaign, the material closest to the laser-target interaction point in the backward direction was the steel magnet yoke of the ion spectrometer. Within the steel, the conversion efficiency reached up to 50 to $100\,\%$ of the conversion efficiency for the catcher. Its contribution during the experiment is reduced due to the much greater distance from the neutron detectors to the backwards ion spectrometer. Not properly accounting for these protons can lead to difficulties during neutron measurements, as will be seen in the next chapter. Depending on the location of the secondary source and the detector, this secondary source could potentially dominate the signal the at detector position. Therefore, all particle contributions should be considered when designing a LDNS, starting with electrons, protons, carbon and other heavy ions as well as photons.

From the simulations presented in this chapter it can also be seen that neutron scattering has a significant influence on the overall signals measured by different detectors, with 20 to $90\,\%$ of the signal being influenced by scattered neutrons. To address this issue, the neutron source and the detector should ideally be located in different rooms, with each room optimized to the specific requirements. The rooms should then be connected via a collimation/beam transport system. A properly collimated neutron beam can reduce the contribution of scattered neutrons at the position of the detector, as most of the neutron scattering is limited to the source room. Furthermore, the measurement room where the detectors are located should also

minimize the contribution of scattered neutrons. This can be achieved by allowing a distance of 2 to 3 m from the detector to the walls, ceiling and floor in all directions (Khabaz 2015; Al Qaaod et al. 2024) and installing an appropriate beam dump behind the detector. Having separate source and measurement rooms also eliminates the need for shielding directly in front of the detector, which is shown to have a large influence on the detected neutrons. Using separated rooms approach, absorbers can be placed inside the source room or in the beam transport system, resulting in scattering taking place outside the measurement room, far away from the detector.

Moreover, placement plays a vital role in bubble detector measurements. If BDs are to be used at LDNS, they should be placed away from the target chamber and, if possible, free-standing in the room. As shown by Monte Carlo simulations above, up to 62 % of the detected neutrons are influenced by scattering, which can lead to an overestimation of the neutron fluence. Additionally, the amount of scattered neutrons reaching the detector depends on the room's geometry and the setup, thus resulting in a location-specific contribution. This location-specific contribution makes a comparison of neutron fluences derived from bubble detector measurements taken at different facilities challenging without proper corrections. Placing BDs in close proximity to bulk objects such as radiation shielding made from metal or plastic, as well as the target chamber itself, should be avoided, as this only increases the contribution from scattered neutrons.

For stability assessment of the source, measuring the different particle spectra for each shot is crucial. Especially in the case of the forward proton beam the data can later be used to normalize measurements to the neutron production. Of all the source terms, it is most important to be able to measure the forward proton beam on-shot. However, being able to measure the secondary source terms help in the analysis and modeling of the experiment in post processing. Measuring each source term can be a challenge at LDNS as the neutron generation process "destroys" the ion beams and many conventional methods for determining the beam charge, i.e. beam pick-ups, cannot be applied to laser-plasma accelerator as easily, due to the harsh noise environment. In this work on-shot ion beam analysis has been achieved by drilling a small hole in the center of the catcher, allowing protons to pass through for analysis downstream. In this way the accelerator performance could be monitored. However, the aperture of the small hole can lead to complications if the ion beam does not impinge the catcher centrally, as could be seen in the bubble detector measurement.

The results presented in this chapter make it clear that detailed Monte Carlo simulations are essential to analyzing measurements conducted at laser-driven neutron sources. They are needed to determine correction factors and establish the origin of the detected neutrons. Without these simulations the significance of results can be diminished, if not otherwise compensated by experimental techniques.

When combining corrections derived from Monte Carlo simulations, knowledge of individual source terms and their contributions, and well-characterized neutron detectors, LDNS are a promising alternative to currently available neutron sources. The next step in the evolution of LDNS should be the construction of a laser system dedicated to neutron production, with beamlines designed to take advantage of the characteristics of LDNS. With a dedicated laser-based neutron source, the focus can shift from source design, optimization, and characterization to applications that leverage the unique characteristics of LDNS (Alvarez et al. 2014; Alejo, Ahmed, et al. 2015; Yogo, Arikawa, et al. 2023). The dedicated facility should incorporate results presented within this chapter and should adopt a design where the neutron generation is separated from the experimental hall.

5. Neutron imaging at the PHELIX laser system

While the DRACO campaign is used to fully characterize a laser-driven neutron source concerning its stability and the influence of different source terms on the generated neutron fields, experimental campaigns conducted at the PHELIX laser system (Bagnoud et al. 2010) at the GSI in Darmstadt are used to demonstrate the feasibility of different neutron applications. The PHELIX laser system can provide laser pulses with energies of up to $150\,\mathrm{J}$ with a pulse duration of 500 to $600\,\mathrm{fs}$. The beam is focused using a $f/1.5$ copper off-axis parabola, resulting in a spot size of around $4\,\mu\mathrm{m}$ (FWHM) and achieving a maximum intensity of $\sim 10^{20}\,\mathrm{W/cm^2}$. The laser targets used were either deuterated or non-deuterated polystyrene foils with a thickness of $1\,\mu\mathrm{m}$, allowing for the acceleration of protons and deuterons in the TNSA regime. PHELIX can deliver one shot every $90\,\mathrm{min}$, which severely limits the number of available shots and statistics that can be accumulated during an experimental campaign.

This part of the work focuses on the demonstration of neutron imagining; see section 2.5 for more details on the method and references. Both thermal and fast neutron imaging were investigated at the PHELIX laser, with results discussed in this chapter.

5.1. Thermal neutron resonance imaging

The spatial distribution of isotopes inside a sample can be obtained by employing (thermal) neutron resonance imaging (NRI). This is achieved by matching the viewed neutron energy window to the cross section of the isotope of interest.

To demonstrate the feasibility of NRI at LDNS, a thermal resonance imaging station was set up during an experimental campaign in 2020, which was conducted at the PHELIX laser system. During the experiment a proof of principle measurement of a simplified variant of NRI could be demonstrated and is published as part of (Zimmer, Scheuren, Kleinschmidt, et al. 2022). Figure 5.1a shows the experimental setup, including the imaging station on the lower left side. The detector for the resonance imaging system was provided by Surface Concept GmbH (Surface Concept 2024). It consists of a borated (^{10}B) MCP with a diameter of $40\,\mathrm{mm}$, which detects neutrons by means of delayline anode and is readout in event mode. In event mode, the x-/y- coordinates where neutrons interacted with the detector and its timestamp are measured. The detector is placed at a distance of $l = 1.45\,\mathrm{m}$ from the moderator/source. For thermal neutrons at $25.3\,\mathrm{meV}$, the detector achieves a temporal resolution of $\Delta t_{\mathrm{MCP}} = 380\,\mathrm{ns}$, with a detection efficiency of $50\,\%$ and a pixel size of $36\,\mu\mathrm{m} \times 48\,\mu\mathrm{m}$, according to the manufacturer. An uncertainty of $\Delta t_{\mathrm{Mod}} \approx 200\,\mu\mathrm{s}$ is assumed for the moderation time of thermal neutrons based on Monte Carlo simulations. From these values $\Delta t \approx 200.38\,\mu\mathrm{s}$ is obtained. The energy resolution of the setup can be calculated via

$$\frac{\Delta E}{E} = 2 \cdot \sqrt{\left(\frac{\Delta l}{l}\right)^2 + \left(\frac{\Delta t}{t}\right)^2}. \tag{5.1}$$

Δl is the uncertainty in the distance from the moderator to the detector. Due to the size of the moderator and the detector the uncertainty is $\Delta l \approx 8\,\mathrm{cm}$, which results in an energy resolution of $\Delta E/E = 0.62$. The

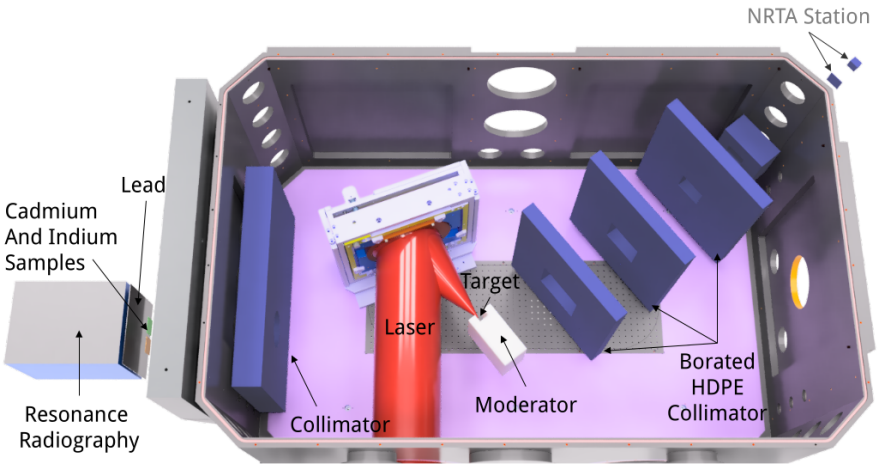

(a) CAD drawing of the experimental setup.

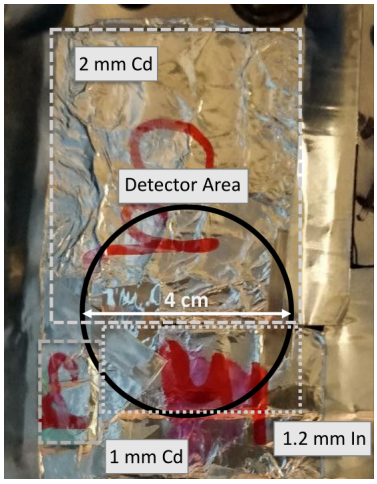

(b) Image of the NRI sample.

Figure 5.1.: (a) shows the experimental setup of the campaign conducted at PHELIX in 2020. The blue pieces inside the target chamber form the collimation system. In the context of this work only the resonance imaging station is of relevance. (b) shows the NRI sample to be investigated, with the black circle indicating the active detector area. Images shown are obtained from (Zimmer, Scheuren, Kleinschmidt, et al. 2022), courtesy of Marc Zimmer.

uncertainty in time Δt is the dominant factor limiting the resolution. The contribution from Δt is 5.5 times as high as that of Δl.

The moderator facing side of the detector is shielded against low energy γ-rays by $2\,\mathrm{mm}$ of lead and is housed inside 10 cm of borated polyethylene shielding to minimize the neutron background. To further minimize the influence of fast neutrons and γ-rays, the detector trigger is set to $100\,\mu\mathrm{s}$ after the laser-target interaction, and neutron events are recorded for a total of $3\,\mathrm{ms}$.

The sample under investigation consists of one large $5\,\mathrm{cm} \times 5\,\mathrm{cm}$ cadmium (Cd) plate with a thickness of $2\,\mathrm{mm}$ covering the top half of the active detector area. A smaller $1\,\mathrm{cm} \times 2\,\mathrm{cm}$ cadmium plate with a thickness of $1\,\mathrm{mm}$ and a $4\,\mathrm{cm} \times 4\,\mathrm{cm}$ indium sample with a thickness of $0.8\,\mathrm{mm}$ and $1.2\,\mathrm{mm}$ are placed in front of the bottom half of the detector. A picture of the sample in relation to the detector area can be seen in Figure 5.1b. In total, 17 shots are used for the investigation of the sample.

Converting the neutron arrival time to energy, using the time-of-flight technique, allows one to reconstruct the thermal neutron spectrum at the detector position, with the detector sensitivity adjusted for each energy according to the (n,α) reaction cross section of ^{10}B. Due to the trigger setting of $100\,\mu\mathrm{s}$ after the laser shot, the maximum neutron energy that can be measured is $1.1\,\mathrm{eV}$. In Figure 5.2a, the measured neutron spectrum is displayed (black line), with a 10-point moving average applied to reduce the impact of statistical fluctuations. Clearly visible is the thermal neutron peak at $25.3\,\mathrm{meV}$. The second visible peak at around $0.1\,\mathrm{eV}$ is caused by a combination of neutrons at that specific energy and scattered neutrons that thermalize in the polyethylene shielding. The neutron fluence drops sharply above $0.2\,\mathrm{eV}$ (arrival time of around $210\,\mu\mathrm{s}$ after the shot). This drop-off is likely caused by the influence of the γ-flash, which (at least) partially depletes the MCP and reduces the sensitivity for some $100\,\mu\mathrm{s}$.

Due to the detectors capability of spatially resolving neutron events, the spectrum can also be obtained for the top half of the detector, covered by Cd and the bottom half. The respective spectra are displayed by the blue (dash-dotted) and orange (dashed) lines in Figure 5.2a. For the portion of the detector that

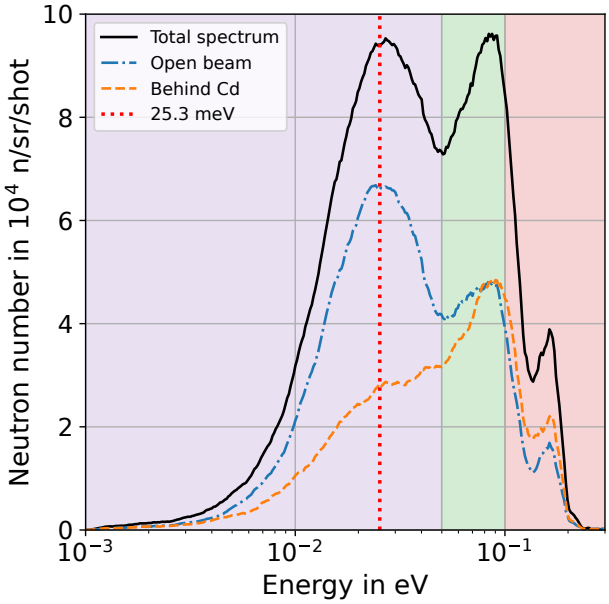

(a) Measured thermal neutron spectrum.

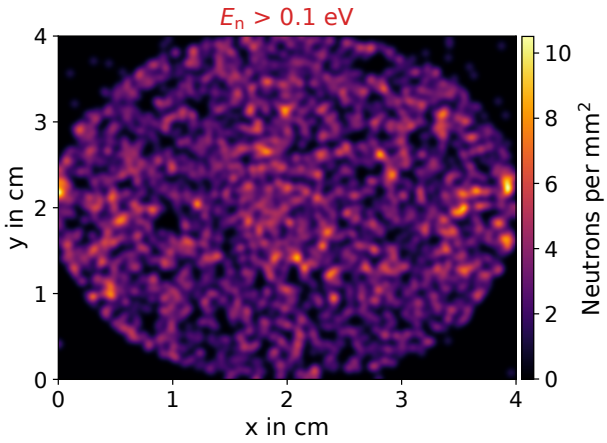

(b) Image corresponding to the red energy range.

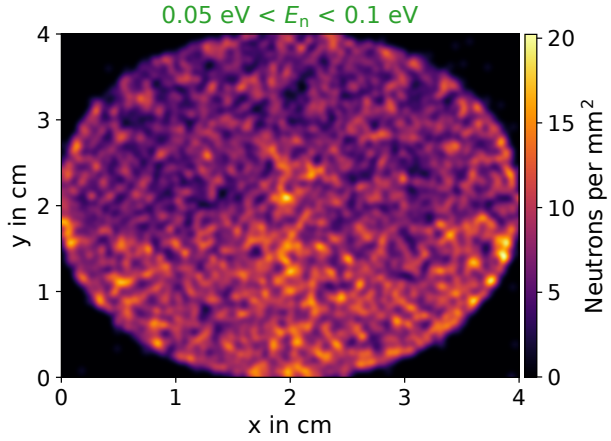

(c) Image corresponding to green energy range.

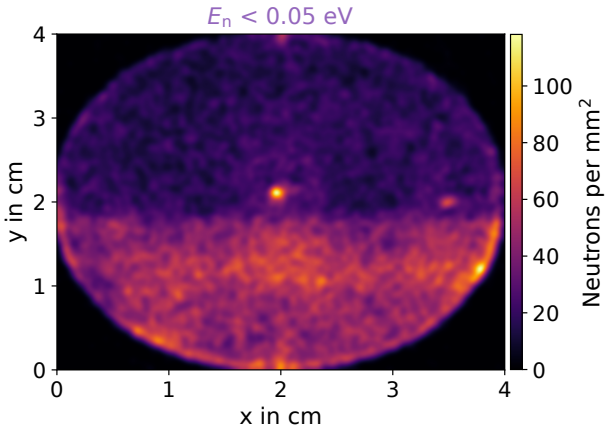

(d) Image corresponding to the purple energy range.

Figure 5.2.: (a) Neutron spectrum recorded by the detector, with the top half covered fully by a $2\,\mathrm{mm}$ thick Cd plate. The bottom half was only partially covered by an indium sample with a thickness of up to $1.2\,\mathrm{mm}$. (b)-(d) shows the measured spatial neutron distribution for three different energy ranges, corresponding to the colored areas of (a). The neutron fluence clearly changes going from one energy range to another.

is covered by the Cd plate, the thermal neutron peak disappears due to the high (n,γ) absorption cross section of ^{113}Cd, reaching up to 2×10^4 b. The remaining neutrons are the noise floor and originate from the room and the shielding setup. The dashed blue line shows that thermal neutrons can still be detected in the absence of Cd. Comparing the blue to the orange curve, a signal-to-noise ratio of $2.2 : 1$ is obtained for thermal neutrons. In order to investigate more complex samples or isotopes with narrower resonances, the signal-to-noise ratio of the setup needs to be improved. In (Zimmer, Scheuren, Kleinschmidt, et al. 2022), it is shown that a ratio of around $15 : 1$ is needed to detect the presence of a resonance with a FWHM of 0.55 eV. The signal-to-noise ratio can be boosted by improving the beamline's collimation system, adapting the detector's shielding setup, and improving statistics by accumulating more laser shots. In particular, the collimation system and the shielding setup needs to be adapted to the specific experimental setup and should be designed with the help of Monte Carlo simulations. The results reinforce the conclusions from the comprehensive source characterization presented in the previous chapter.

To demonstrate NRI, a clear change in the spatial distribution of the neutrons needs to be visible when looking at different energy ranges, which are indicated by the colored areas in Figure 5.2a. Images corresponding to the energy windows of the shaded area are displayed in Figure 5.2b-5.2d. The images are reconstructed from the x-/y-coordinate data recorded by the detector, with a 9-pixel radius Gaussian-blur filter applied to each image to smooth out the intensity distribution. A Gaussian-blur filter is necessary due to the low counting statistics. The bright spot in the middle of images (c) and (d) is a known detector artifact as a result of high count rates, according to Surface Concept GmbH (private communications). Going from the energy window with the highest energies (b) to the lowest (d) shows a clear difference in the neutron distribution. The average neutron fluence of the top and bottom half is almost identical in (b), which corresponds to the red area in Figure 5.2a, at $(2.6 \pm 1.2)\,\mathrm{n/mm^2}$ (top) and $(2.4 \pm 1.2)\,\mathrm{n/mm^2}$ (bottom). Thus, the Cd sample cannot be resolved. In (c), corresponding to the green area, the average neutron fluence is still comparable at $(6.6 \pm 2.2)\,\mathrm{n/mm^2}$ and $(9.0 \pm 2.3)\,\mathrm{n/mm^2}$ for the top and bottom, respectively. In the low energy window shown in (d), corresponding to the purple area, the Cd sample can be resolved and a significant difference in neutron fluence between the top at $(18.7 \pm 6.3)\,\mathrm{n/mm^2}$ and the bottom with $(51.9 \pm 8.2)\,\mathrm{n/mm^2}$ can be observed. The difference in neutron fluence results from the large (n,γ) neutron absorption cross section of ^{113}Cd. The thick part of the indium sample might also faintly be visible towards the bottom right of the figure. In this area, an average neutron count of $(48.5 \pm 7.3)\,\mathrm{n/mm^2}$ is obtained, a reduction of up to $8.2\,\%$ in neutrons per mm^2. However, unlike in the case of Cd, the decrease in neutron fluence is within the uncertainty of the measurement. Thus, no claim can be made that the presence of indium causes this decrease. The measurement's findings are corroborated by Monte Carlo simulations included in (Zimmer, Scheuren, Kleinschmidt, et al. 2022).

In summary, laser-driven neutron sources are a suitable neutron generation platform for NRI. While the proof-of-principle demonstration in this work is relatively simple, more complex samples can be investigated with appropriate adjustments to the experimental setup. TThe first area that needs to be addressed is the collimation system to improve the signal-to-noise ratio. Due to geometric constraints, an elaborate collimation system could not be implemented during the experiment, as it would have interfered with the laser pulse. In future campaigns, a collimation system similar to the one used for the neutron resonance transmission analysis (NRTA) station in Figure 5.1a (top right) should be implemented. Furthermore, the direct line of sight from the detector to the laser-matter interaction point should be shielded by lead to limit the influence of the γ-flash on the detector, which blinded the detector for neutrons above 1 eV. The shielding needs to be placed as close as possible to the laser-matter interaction point so that it does not interfere with the neutron beam. Additionally, the shielding in which the detector is housed needs to be optimized, which would further improve the signal-to-noise ratio. This can be achieved lining the inside of the detector housing with a 1 to 2 mm thick Cd layer. The Cd layer absorbs neutrons that are moderated but

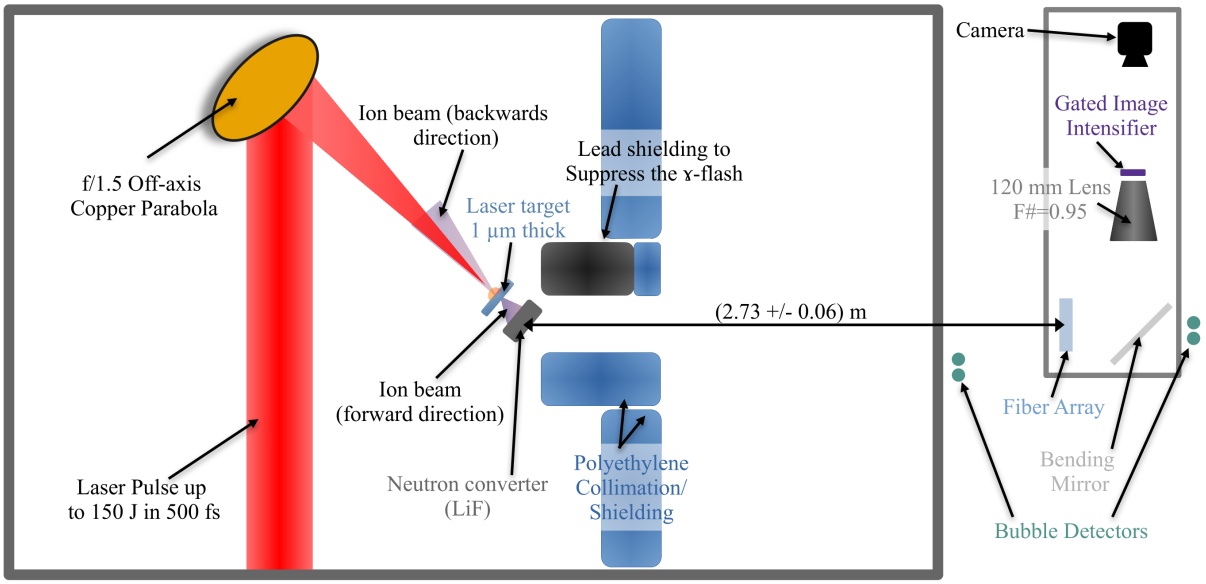

Figure 5.3.: Fast neutron imaging setup at PHELIX, during the 2023 beamtime, showing the inside of the target chamber and the FNI detector, not to scale. The detector is an evolution of the TRION detector first build and deployed by the PTB in Braunschweig (Mor, Vartsky, et al. 2009).

not captured by the shielding assembly.

The large uncertainty in moderation time Δt_{Mod} for thermal neutrons severely limits the energy resolution of the employed experimental setup. This is a consequence of the moderator design, which was optimized for epi-thermal neutron generation (Zimmer, Scheuren, Kleinschmidt, et al. 2022). The resolution of the setup does not limit measurements presented in this work due to the broad resonance of ^{113}Cd. However, in the case of narrower resonances, the energy resolution can become a problem. For example, the resonance of ^{115}In at $1.45\,\text{eV}$ has a FWHM of $0.11\,\text{eV}$. Using the experimental setup as described, neutrons with an energy of $1.45\,\text{eV}$ have an associated uncertainty of $0.17\,\text{eV}$, which is larger than the FWHM of the resonance. Thus, the energy resolution needs to be improved for more complex samples and narrower resonances. This can be achieved by optimizing (shrinking) the moderator or increasing the flight path length. Going from $1.45\,\text{m}$ to $2.5\,\text{m}$ would result in a resolution of $\Delta E/E = 0.067$ and an uncertainty of $0.1\,\text{eV}$ for $1.45\,\text{eV}$ neutrons.

Finally, to enable the investigation of samples within a reasonable time frame, a PHELIX-like laser system operating in the 1 to $100\,\text{Hz}$ range is needed (Zimmer, Scheuren, Kleinschmidt, et al. 2022).

5.2. Fast neutron imaging

Over the course of this work, two experimental campaigns were conducted at the PHELIX laser in 2021 and 2023 to demonstrate the feasibility of energy-selective fast neutron imaging (FNI). Although variations in the neutron cross section are much more subtle compared to the epi-thermal region, choosing a suitable energy window can help to highlight the distribution of elements of interest in a sample by improving the contrast for these. This has been demonstrated before in (Mor, Vartsky, et al. 2009; Mor, Dangendorf, et al. 2015).

The experimental setup for the FNI campaign can be seen in Figure 5.3. In the disc-shaped LiF converter, neutron generation occurs via (p,n) and (d,n) reactions, which are induced by the forward propagating TNSA

ion beam. The backward ion beam propagates to the back of the target chamber, where it impinges on the copper parabola, which can also result in the generation of neutrons via the previously mentioned reaction channels. As neutrons originating from the parabola are considered noise, the parabola is shielded by up to 20 cm of borated polyethylene, depicted by blue blocks in Figure 5.3. The neutron beam originating in the LiF converter is shaped using a collimation system consisting mainly of borated polyethylene. Additionally, 20 cm of lead (black block in Figure 5.3) is used to block the direct line of sight from the detector to the laser-target interaction point. This is done to suppress the γ-flash signal as much as possible to obtain a "pure" neutron image.

Also displayed is the fast neutron imaging detector, which is an evolution of the TRION detector (Mor, Vartsky, et al. 2009) developed originally at the Physikalisch-Technische Bundesanstallt (PTB) in Braunschweig. It is based on an array of BCF-10 scintillating plastic fibers (Luxium Solutions 2024), where each fiber has a cross section of 1 mm $\times$ 1 mm and a length of 3 cm. The individual fibers are stacked in an array to achieve a total active detector area of 10 cm $\times$ 10 cm. The detection principle is the same as that of the fast plastic scintillator used in the DRACO campaign. Light generated in the fibers is imaged onto a gated image intensifier. By utilizing the gating capabilities of the image intensifier, specific neutron energies can be selected, according to their time-of-flight. The back of the image intensifier is then recorded by a CCD camera, which generates the final image.

The detector setup was slightly adjusted between the 2021 and 2023 campaigns, based on the findings of the previous experiment. The original image intensifier used for the 2021 experiment exhibited age-related defects and was therefore replaced. The new image intensifier exhibits a higher quantum efficiency in the emission range of the fibers, while delivering the same amplification. Furthermore, the readout camera was also replaced by a so-called ProxiKit (Proxi Vision 2024), which is a combination of a camera and an image intensifier. Thus, the detector system for the 2023 campaign has a total of two image intensifiers. Nonetheless, the detector's operating principle remains unchanged. The reasons for implementing these changes are discussed below in the context of the obtained results.

Neutron generation at PHELIX is achieved by employing the pitcher-catcher setup. Again, a mix of deuterated and non-deuterated plastic foils was used as laser targets, with a thickness of 0.8 to 1 µm. Here, the incidence angle of the laser pulse on the target is $10°$, due to geometric constraints imposed by the setup and radiation protection. An average laser pulse energy of (133 ± 16) J is achieved over the course of the two beamtimes. Ions are accelerated by the laser pulse in the TNSA regime to a cut-off energy of (52 ± 12) MeV, according to RCF measurements. The ions were then directed into a LiF converter target, with a thickness of 2 cm. Based on bubble detector measurements, the mean neutron fluence measured during both campaigns is $(2.0 \pm 0.5) \times 10^9$ n/sr/shot. Results could be averaged over the beamtimes as the neutron production of the LDNS was stable between the two campaigns.

The FNI detector was placed at a distance of (4.02 ± 0.06) m during the first PHELIX campaign (2021) and the image intensifier was gated in such a way that neutrons with energies of 0.1 to 8.5 MeV fall within the gate window. This energy window comprises around 70 to 75 % of the generated neutrons. The time separation between the arrival of the γ-flash and 8.5 MeV neutrons is around (86 ± 1) ns. Based on bubble detector measurements, the neutron fluence on the fiber array is calculated to be $(1.2 \pm 0.3) \times 10^4$ n/cm^2/shot. Due to the setup, the maximum incident angle at which neutrons can enter the detector is calculated to be around $1.3°$. Figure 5.4a shows the recorded signal after averaging over eight shots and subtracting the camera readout noise. The large, illuminated circular spot in the center of the image is the signal generated by the image intensifier as captured by the readout camera. This is the region of interest (ROI) in the context of the 2021 beamtime. The image is recorded using the open beam, meaning no object is placed between the source and detector. While the signal from the image intensifier can be, due to the selection of color scale and range, the strength of the signal is too low compared to the background. The average pixel value

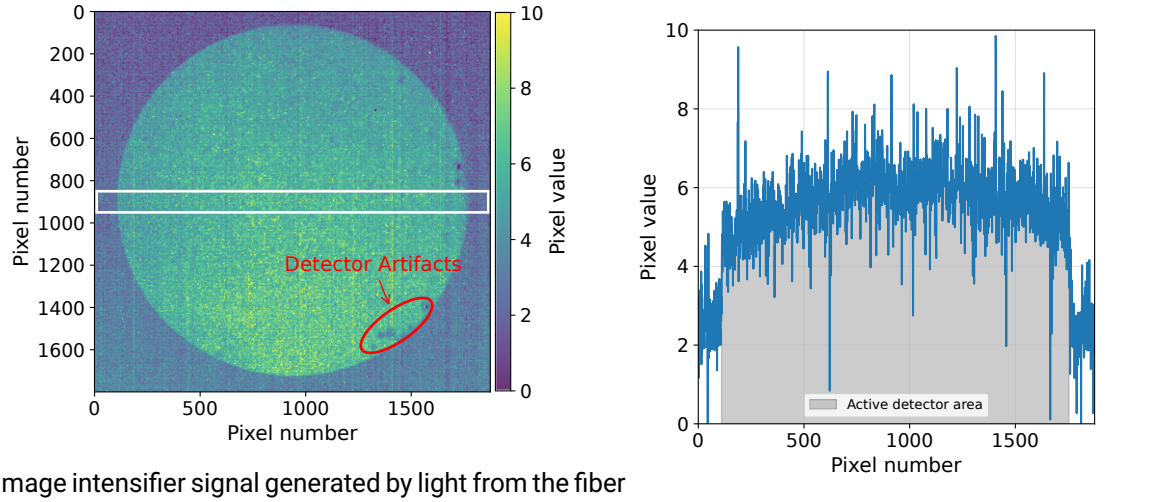

(a) Image intensifier signal generated by light from the fiber array.

(b) Horizontal pixel lineout for the white box.

Figure 5.4.: (a) shows the signal captured by the readout camera. The glow is caused by neutrons depositing energy inside the scintillating fiber array. Stripes running from top to bottom in the image are caused by the readout of the camera. Examples of detector artifacts mentioned in the text are highlighted by a red ellipse. (b) shows a horizontal lineout by averaging over 100 rows, corresponding to the area indicated by the white box in (a). The gray-shaded area corresponds to the active detector area of (a).

outside the ROI is 4 ± 5 and 7 ± 6 inside the ROI. Also shown in Figure 5.4b is a pixel value lineout of the area indicated by the white rectangle in (a). Analysis of an imaging phantom was not possible during this campaign as a consequence of the very low signal-to-noise ratio of around $1.8 : 1$. Stripes visible in Figure 5.4a are caused by the readout of the camera and are also visible as the large spikes in Figure 5.4b.

As a result of the low signal strength, modifications to the experimental setup were carried out for the 2023 campaign at PHELIX, as mentioned before. Additionally, to increase the neutron fluence and thus the signal strength, the distance to the source is reduced to $(2.73 \pm 0.06)\,\mathrm{m}$, which approximately doubles the neutron fluence at the detector position. The signal-to-noise ratio is addressed by changing the image intensifier to a new model with an increased sensitivity and replacing the readout camera. Crucially, the new camera is also equipped with an image intensifier and is therefore capable of single photon detection, thereby reducing the effects of camera-induces readout noise.

The neutron fluence at the position of the detector is again monitored by BDs and is calculated to $(2.7 \pm 0.8) \times 10^4\,\mathrm{n/cm^2/shot}$, an increase of $125\,\%$ compared to the 2021 campaign, as expected. The downside of moving the detector to the source is that the separation in time between the γ-flash and the highest neutron energy of interest ($10\,\mathrm{MeV}$) reduces to about $50\,\mathrm{ns}$. Signals generated by the fibers are comparable to that of the plastic scintillator shown in section 3.2. Reducing the time separation between the neutron and γ-flash signal is problematic, as it can lead to overlapping signals. The resulting image is not a pure neutron image but also contains information generated by the interaction of the γ-flash with the phantom. This significantly influences the measured absorption of the imaging phantom. Therefore, to avoid this overlap, the image intensifier gate is set to $t_\gamma + 130\,\mathrm{ns}$, where t_γ is the ToF of the γ-flash. The gate is then open for $300\,\mathrm{ns}$, corresponding to a neutron energy range of 0.2 to $2\,\mathrm{MeV}$. Due to the limited energy window, only 30 to $40\,\%$ of the generated neutrons are usable. Furthermore, the maximum incidence angle at which the neutrons can enter the detector increases to $2°$.

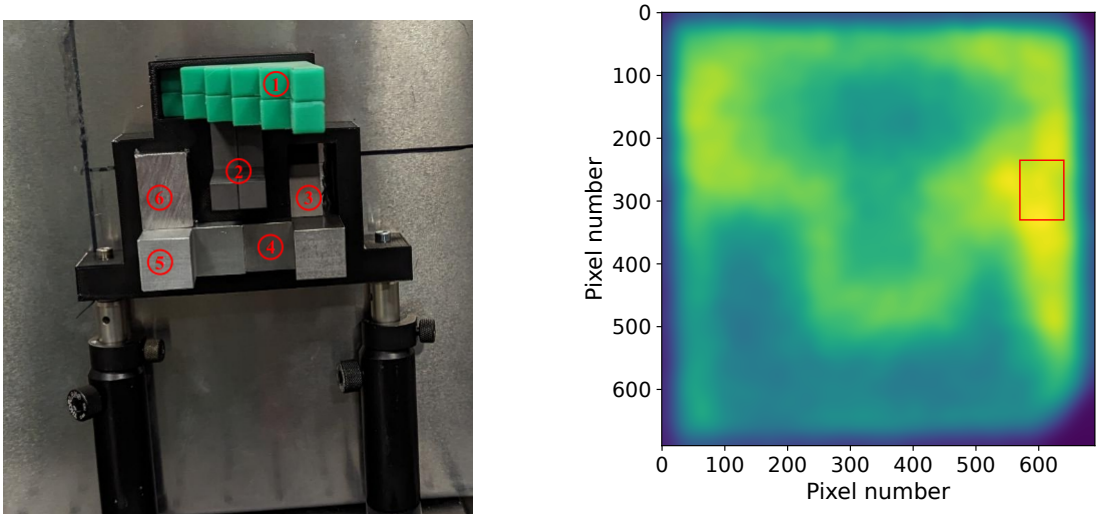

(a) Imaging phantom.

(b) Measured neutron radiography.

Figure 5.5.: (a) shows the imaging phantom and its holder used during the 2023 beamtime at PHELIX. The phantom spells the letters ”T” and ”U”. Materials used for the phantom are 1) polyethylene (PE, $1\,\mathrm{cm} \leq d \leq 6\,\mathrm{cm}$), 2) graphite ($d = 2\,\mathrm{cm}$ and $4\,\mathrm{cm}$), 3) tungsten ($0\,\mathrm{cm} \leq d \leq 3\,\mathrm{cm}$), 4) steel ($d = 3\,\mathrm{cm}$ and $5\,\mathrm{cm}$), 5) aluminum ($d = 3\,\mathrm{cm}$ and $5\,\mathrm{cm}$) and 6) lead ($d = 3\,\mathrm{cm}$). (b) shows the neutron radiography image of the phantom, average over $17\,\mathrm{shots}$ and applying a $13\,\mathrm{pixel}$ Gaussian blur filter. The red box is the area used for dose normalization in the following post-processing steps.

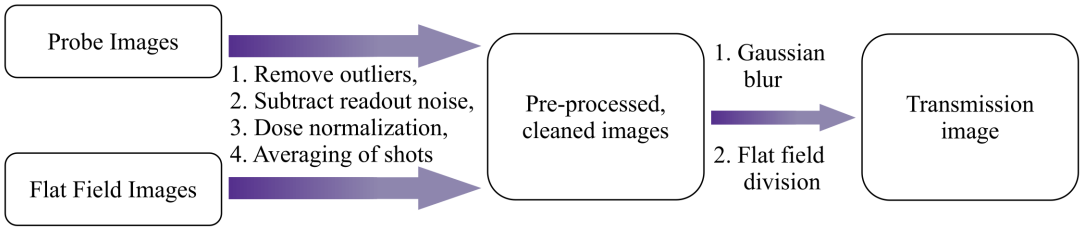

Figure 5.6.: Flow chart detailing the image processing workflow to go from raw images to the transmission image shown in Figure 5.7a. The transmission image reconstructed from the nELBE data in Figure 5.10b follows the same workflow, but in the last step the Gaussian blur was omitted as it was not necessary.

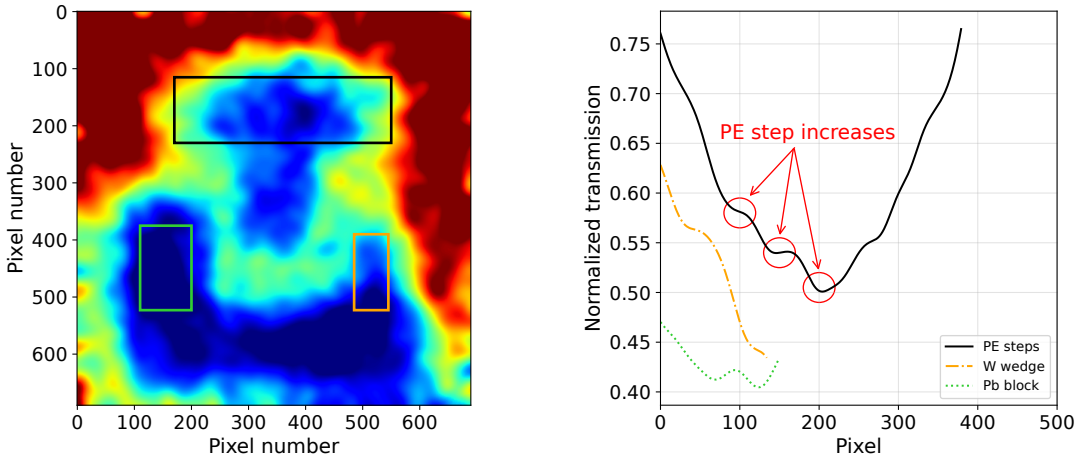

(a) Normalized transmission image of the phantom.

(b) Calculated outlines for the colored boxes.

Figure 5.7.: (a) shows the transmission radiography of the imaging phantom shown in Figure 5.5a. Areas marked in red correspond to high transmission, whereas blue symbolized areas of low transmission. (b) shows the normalized transmission I_T for the boxes in (a). The lineouts average pixel values going from top to bottom for vertical and left to right for horizontal ones.

Figure 5.5 shows the imaging phantom and neutron image obtained during the 2023 beamtime. The phantom consists of six materials in various geometries and thicknesses d. The neutron radiography shown is the average of 17 images (shots), after subtracting the camera readout noise. A clear improvement compared to the 2021 beamtime is visible as a result of the discussed changes. However, the image still suffers from low statistics and distortion, making it difficult to recognize the shape of the phantom. Due to the limited statistics, a 13-pixel Gaussian-blur filter is applied to smooth out the pixel distribution.

In order to gain insight into the makeup of a device under test, the normalized transmission image is needed, as the transmission/absorption can be related to the properties of materials (see chapter 2). The raw radiography image needs to be further processed to obtain the transmission image. Figure 5.6 shows a flow chart of the processing steps applied to obtain the transmission image. In the first step, bright outlier pixels are removed by applying a median filter that replaces a pixel's value with the median of the surrounding pixels, but only if the pixel value exceeds the median value of the neighboring pixels by a set threshold. As multiple images taken over many shots are used to increase statistics, the individual images need to be dose rate normalized before averaging to account for shot-to-shot fluctuations in neutron generation and detection. To achieve this, a dose normalization factor D_{corr} is calculated for each image according to

$$D_{\text{corr}} = \frac{D_{\text{FF}}}{D_{\text{Probe}}}, \tag{5.2}$$

where D_{FF} and D_{Probe} are the average pixel value contained within the red rectangle, displayed in Figure 5.5b, for both the flat field image (I_{FF}) and images including the phantom (I_{Phantom}), respectively. Afterwards, each image is multiplied by its corresponding correction factor. The dose-normalized shots are then averaged, returning the pre-processed, cleaned images. Finally, by dividing the averaged phantom images by the flat field image, the phantom's transmission image (I_T) can be obtained, i.e. $I_T = I_{\text{Phantom}}/I_{\text{FF}}$.

Figure 5.7 shows the transmission image and lineouts for the marked areas. The general shape of the imaging phantom can be seen in the transmission image, although the extent of the horizontal top bar of the letter "T" is much shorter than in the image shown in Figure 5.5a. Both the thinnest part (left side,

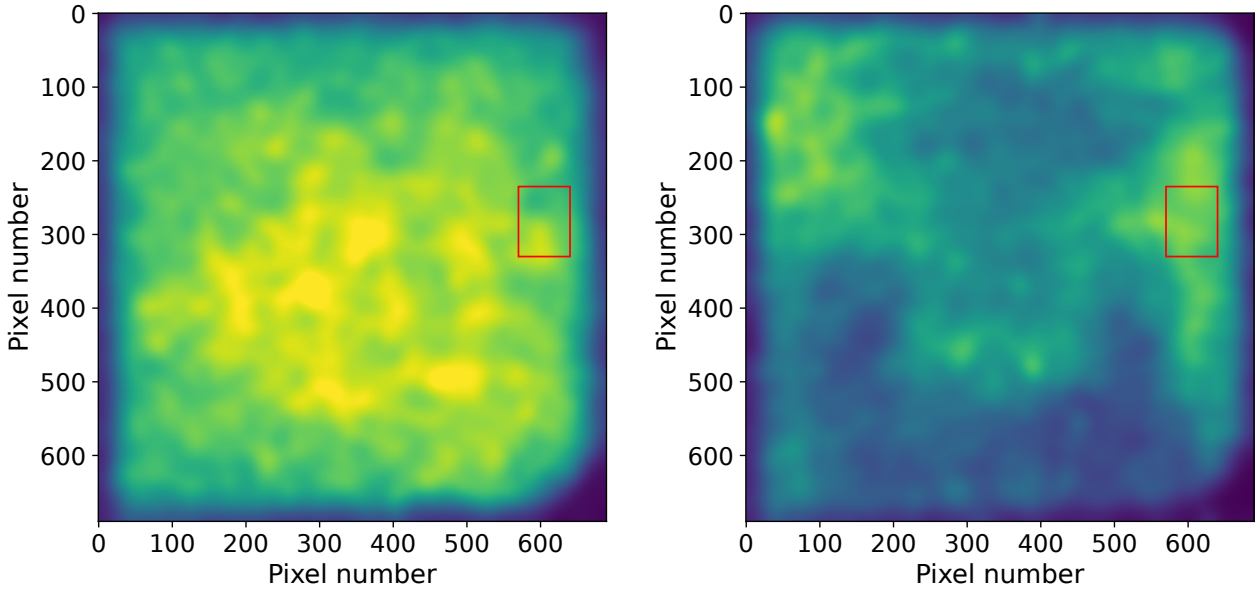

(a) Flat field beam dump image.

(b) Beam dump image with imaging phantom.

Figure 5.8.: (a) shows the open beam imaged recorded when switching the LiF catcher for a plastic beam dump. (b) shows the image generated when using the plastic beam dump, but here the phantom is placed in front of the detector.

thickness 1 cm) and the thickest part (right side, thickness 6 cm) of the top bar are missing, which is also reflected in the lineout in (b).

Starting with the tungsten wedge (orange box) and looking at the transmission lineout, the expected trend for the transmission is correctly reproduced, with the top showing the highest transmission and the bottom the lowest, with a continuous decrease in transmission. In the case of the polyethylene (black box), four of the six steps are visible going from left to right. However, the transmission increases again for the thickest part of the steps, which should not be the case.

For the lead portion of the phantom (green box), a constant transmission is expected since no variation in thickness is present. However, the transmission varies by more than $10\,\%$, which could be the result of inhomogeneous irradiation of the array and low statistics.

In theory, the recorded transmissions could be used to calculate the thickness of each shape. However, in the case of the polyethylene the transmission does not follow the expected behavior and using the transmissions to calculate the thickness returns values between 3 cm ($I_T = 0.75$) and 8 cm ($I_T = 0.5$), which do not match the actual thickness of 1 to 6 cm going from left to right in Figure 5.5a. The same is true for the tungsten wedge, where the calculated thickness ranges from 3.1 to 5.5 cm, whereas the actual thickness ranges from 0 to 3 cm.

Since the calculated values do not match the actual thickness of the used phantom and because the thickest PE part is not visible, different factors affecting the measurement are briefly investigated and discussed. Among those is the influence of secondary neutron sources and other radiation sources, such as x-rays and the afterglow of the fiber array. Since the γ-rays generated by the laser target interaction arrive at the detector first, they can excite the fiber array, resulting in light emission. The intensity of the light emission decays with a scintillator specific decay time; for the fibers used here, the fast component has a decay time of 2.7 ns. If the signal caused by the γ-rays is much larger than the neutron signal, then the decaying signal

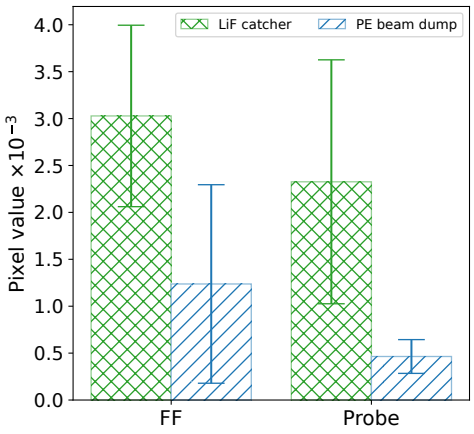

(a) Brightness comparison between the LiF and PE catcher.

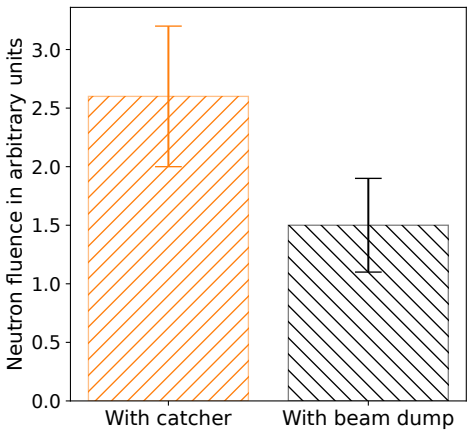

(b) Measured neutron fluence behind the Cu parabola.

Figure 5.9.: (a) Comparison of the recorded pixel values presented in Figure 5.5b and 5.8. When using the beam dump the image still reaches 20 to $40\,\%$ of the recorded brightness compared to the results where the LiF catcher is present. This means that a large fraction of the recorded signal is not generated by neutrons from the catcher. (b) shows the neutron fluence behind the parabola for shots using the catcher and the beam dump, highlighting the neutron generation by the parabola.

can be comparable in strength to the neutron signal. The recorded signal is now comprised of both photon and neutron caused signals. Thus, the measured transmission does not correspond solely to neutrons.

To investigate the contribution from secondary sources and scattered neutrons, the LiF catcher is replaced by a polyethylene (PE) block that acts as a beam dump for the forward propagating ion beam. Thereby, neutron generation by the catcher is suppressed and any recorded signal must originate (mainly) from outside the catcher.

Figure 5.8 shows the recorded images after switching out the LiF converter for PE. Both the flat field images and the image containing the phantom are shown. Even though no neutron converter is present, the imaging phantom is still visible in Figure 5.8b. Using the normalization area marked in red, the brightness of the shots with the LiF converter is compared to results obtained using the PE block. Beginning with the flat field images (FF), the intensity when using the PE beam dump is $41\,\%$ of the intensity when using the LiF converter. When the phantom is placed in front of the detector, this value is reduced to around $20\,\%$, as summarized in Figure 5.9a.

These measurements show that significant contributions to the recorded signals originate outside the catcher. This has a significant influence on the calculated transmissions of Figure 5.7a. Investigating the neutron fluence at the detector position for the beam dump shots returns a value of $(0.2 \pm 0.1) \times 10^9$ n/sr/shot, around $15\,\%$ of the fluence recorded with the LiF converter present. While the statistics for the images shown in Figure 5.8 are quite limiting, the relative change in brightness generally agrees with the change in neutron fluence measured by the BDs. With the LiF converter not present, neutron generation can only occur from the backward proton beam impinging on the copper parabola, with copper having a comparable neutron conversion to LiF, as shown in Figure 4.12b. BDs are placed at the target chamber behind the parabola to verify this further. The results of these measurements are shown in Figure 5.9b. The neutron fluence behind the parabola retains $60\,\%$ of the neutron fluence in the absence of the LiF catcher compared to shots where the catcher is present, making it a significant source of neutrons in the used setup.

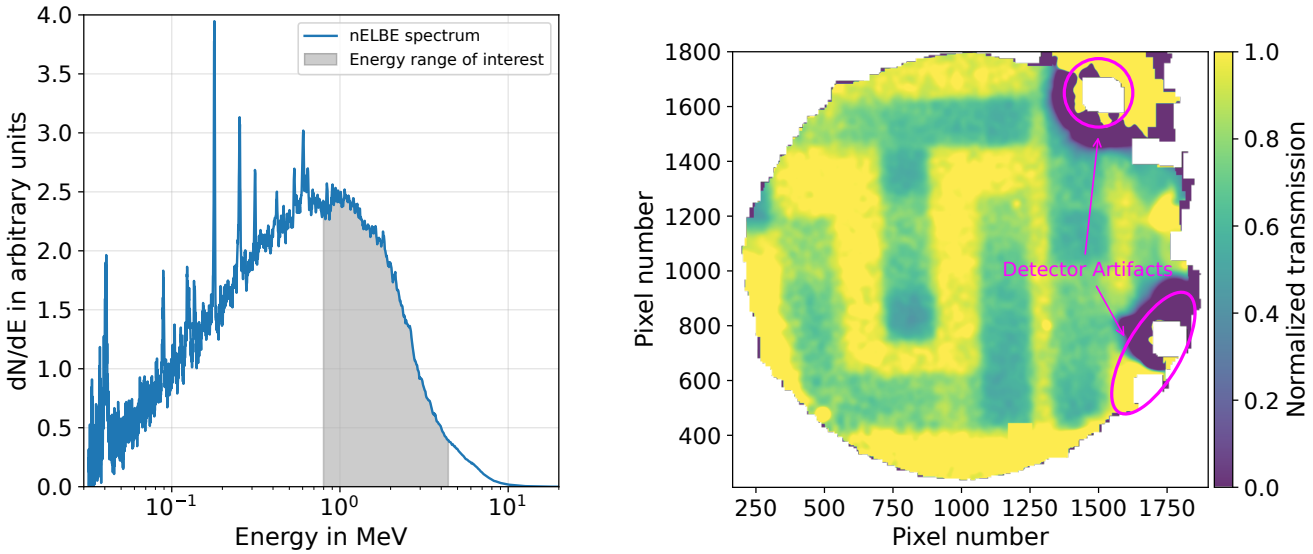

(a) Neutron spectrum of nELBE.

(b) Neuron radiography obtained after an exposure of $300\,\mathrm{s}$.

Figure 5.10.: (a) shows the neutron spectrum of nELBE at the position of the detector, courtesy of Roland Beyer and Arnd Junghans. The total flux at the position is $6.6 \times 10^4\,\mathrm{n/cm^s/s}$ (Beyer et al. 2013). (b) shows a radiography image generated by neutrons with energies from 0.8 to $2.65\,\mathrm{MeV}$, corresponding to the gray area in (a). The neutron statistics of this image are the basis of the results shown in Figure 5.11. The imaging phantom used here is slightly different than the one displayed in Figure 5.5a.

It needs to be noted that it is still possible, that some of the recorded signal during the beam dump shots originates from the interaction of the γ-flash with the detector. However, this contribution can only be investigated by Monte Carlo simulations of the experimental setup, comparable to the ones presented in chapter 4. In order to conduct these simulations, the source terms need to be measured, which was not possible in the setup used during the experiment.

In conclusion, the FNI results obtained at PHELIX show that proper collimation is critical to FNI experiments at LDNS. Furthermore, it can be seen that secondary radiation sources can influence the measured signal, as demonstrated by switching the neutron converter for a plastic beam dump. In the described experimental setup, the two most likely secondary sources influencing the measurement are neutrons, which originate from the Cu parabola and the afterglow of the fiber array, caused by the γ-flash. The influence of the parabola can be reduced by increasing the incidence angle of the laser pulse on the target in such a way that the backward proton beam clears the parabola and is stopped by a proper beam dump. Limiting the influence of the γ-flash can only be achieved by increasing the difference in arrival times for neutrons and photons or using fibers with shorter decay times.

The following section compares the results obtained at PHELIX to those obtained at the nELBE neutron facility. The comparison is used to estimate the minimum required number of PHELIX pulses to obtain a radiography that can be used to analyze an imaging phantom. Additionally, the neutron fluences measured at DRACO are used to approximate the number of shots required from a laser system that delivers less energy per pulse.

Comparison to nELBE results and first optimizations

Based on data recorded during an additional neutron radiography campaign at the (conventional) neutron source nELBE (Beyer et al. 2013), an approximation of the required neutron flux for neutron imaging can be found. Note that this approximation is only valid for the detection system used in this work and assumes a well-collimated neutron beam. nELBE is a neutron source based on a superconducting electron accelerator, generating neutrons through (γ,n) reactions by impinging a $35\,$MeV electron beam on a liquid lead target. At the source, a neutron current of $1.6 \times 10^{11}\,\mathrm{n/s}$ (Beyer et al. 2013) is obtained, passing through a collimation system before entering the measurement area where the imaging detector is located. At the position of the detector, a neutron flux of $6.6 \times 10^{3}\,\mathrm{n/s/cm^2}$ is obtained, with a maximum divergence angle of $0.3°$. Again, by properly gating the image intensifier, an energy region of interest can be selected, which in this case is 0.8 to $2.65\,$MeV and contains $51\,\%$ of the generated neutrons. The neutron spectrum in the measurement area is shown in Figure 5.10a. The detector is placed at a distance of $(10.24 \pm 0.05)\,$m from the source.

In Figure 5.10b, the result of a single $300\,$s long exposure is shown, corresponding to an integral neutron fluence of $10^6\,\mathrm{n/cm^2}$ reaching the fiber array. To achieve an image of this quality, $\hat{n} = 10^4$ neutrons have to enter each fiber of the array in a comparable energy window. This number can be used as a baseline to calculate the number of laser shots required to obtain an image of similar quality, assuming a well-collimated neutron beam. The measured mean neutrons fluences ϕ_n recorded at DRACO, which is $4.9 \times 10^7\,\mathrm{n/sr/shot}$ for the LiF catcher and at PHELIX (2023) with $2 \times 10^9\,\mathrm{n/sr/shot}$ are used. Calculating the fraction f of neutrons that fall within the same 0.8 to $2.65\,$MeV energy range used at nELBE returns a value of $f = 0.25$ for the LDNS. The calculation is based on the $15°$ neutron spectra shown in Figure 4.12d. Additionally, a distance of $d = 3\,$m from the source to the detector is assumed. The number of needed shots n_shot can then be calculated by

$$n_\mathrm{shots} = \frac{\hat{n}}{\phi_\mathrm{n} \cdot f \cdot \Omega}, \tag{5.3}$$

where $\Omega = A/d^2$ is the average solid angle of a fiber with area A. f is defined as $f = \frac{\int_{E_0}^{E_1} \phi_\mathrm{n}\,\mathrm{d}E}{\int_0^\infty \phi_\mathrm{n}\,\mathrm{d}E}$, with E_0 and E_1 denoting the boundaries of the energy interval.

Starting with the DRACO neutron fluence, one obtains, on average, $1.3\,\mathrm{n/fiber/shot}$ within the specified energy window. Thus, at least 7827 shots are needed to achieve the same neutron statistics per fiber as obtained during the nELBE beamtime. If the image is to be acquired within $5\,$min, a repetition rate of $26\,$Hz is needed. This number is close to the capabilities of current laser systems, with DRACO having demonstrated proton acceleration at $10\,$Hz already (P. L. Poole et al. 2018; Rehwald, Assenbaum, Bernert, Brack, et al. 2023). Using the neutron fluence generated by PHELIX results in $56\,\mathrm{n/fiber/shot}$ on average. This translates to a total of 180 shots that are required to achieve the same statistics as at nELBE. As a point of reference, 50 to 70 shots can be obtained during a typical two-week-long PHELIX campaign, meaning that three to four beamtimes are needed to generate a single high-quality image at PHELIX. If the measurement should be conducted within 5 min, a repetition rate of $0.6\,$Hz is required, which is just outside of the range what state-of-the-art, PHELIX class, high-energy laser systems can deliver. However, planned future laser systems, such as the SHARC laser (Siders 2018), should be capable of achieving these repetition rates.

By increasing the distance d from the detector to the source, the usable energy window can be increased, which results in a higher utilization factor of the generated neutron spectrum. Care needs to be taken to ensure that the separation in time between the photon and neutron signal is sufficient to avoid significant overlap. The time separation $\Delta\tau$ is defined as:

$$\Delta\tau = t_\mathrm{n}(E_\mathrm{n}) - t_\gamma$$

with $t_\mathrm{n}(E_\mathrm{n})$ the neutron time-of-flight for a given distance d and energy E_n. In this equation t_γ is the photon time-of-flight to cover the distance d. Assuming $\Delta\tau \geq 130\,\mathrm{ns}$, which was the time separation used during the 2023 PHELIX campaign, the upper limit for the energy window can be calculated using the relativistic kinetic energy. With the energy window defined, the number of shots required to obtain 10^4 neutrons in each fiber can be calculated in dependence on the distance d according to Equation 5.3. The results of this calculation for both the neutron fluences generated by DRACO and PHELIX can be found in Figure 5.11. The plot shows that a minimum exists for a distance of $3.25\,\mathrm{m}$, which corresponds to an energy range of 0.8 to $3.9\,\mathrm{MeV}$. At this distance, the number of required shots is reduced to 122 for PHELIX and 5302 for DRACO, a reduction of $32\,\%$.

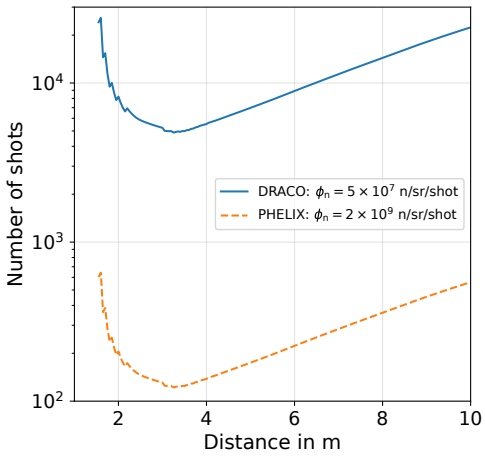

Figure 5.11.: Number of required shots to obtain 10^4 neutrons per fiber for different distances from source to the detector. At $3.25\,\mathrm{m}$ the number of required shots has a minimum.

In summary, energy-selective fast neutron imaging could be successfully demonstrated using the PHELIX laser system. However, the quality of the obtained neutron images is lower than needed to assess a complex sample. The results are limited by contributions from scattered background neutrons and secondary neutron sources inside the target chamber, contributing 20 to $40\,\%$ of the total signal strength. Therefore, it is advisable to separate the source from the detection area by a wall and guide the neutron beam to the detector via a suitable collimation system.

Further limiting the results is the low repetition rate and the resulting low neutron flux that can be obtained from PHELIX as a result of its laser architecture. Using results obtained from the conventional neutron source nELBE reveals that at least 180 shots at PHELIX are needed to obtain high enough image quality for quantitative analysis. By optimizing the distance between the detector and the source, the number of shots can be decreased to 122 at a distance of $3.25\,\mathrm{m}$.

The results presented here are encouraging for upcoming laser systems that can operate at higher repetition rates as drivers of neutron sources for fast neutron imaging if the surrounding experimental area is designed according to its specific needs.

6. Scaling and performance of laboratory scale Laser-Driven Neutron Source

In Chapter 4, it could be demonstrated that high-intensity ultra-short pulse laser systems are capable drivers of stable, reproducible, and well-controlled neutron sources, with adequate preparation, setup, and monitoring of the laser plasma accelerator's performance. However, it was also shown that the neutron generation strongly correlates with the laser pulse energy, which was also found through simulations (Zimmer, 2020) and measurements (Yogo, Lan, et al. 2023). The strong correlation presents a challenge to the field of LDNS regarding the scalability and miniaturization of these sources. Both of these characteristics are important aspects concerning the adoption of these sources.

Laser systems delivering high energy pulses ($\gtrsim 20$ to $30\,\mathrm{J}$), which can deliver adequate neutron fluence per shot, commonly suffer from lower than practical repetition rates due to heat buildup effects inside the laser system, which can negatively affect the beam quality, acceleration performance (Patrizio 2020) and thus also neutron production. Furthermore, higher laser pulse energies also require larger optics (to prevent damage), which drives up both the cost and size of these systems. Consequently, LDNS utilizing high laser pulse energies would be mostly restricted to research facilities/centers, similar to conventional sources such as research reactors or spallation sources, albeit at a reduced cost and size. Limited access to laser-based neutron sources hinders their development and adoption, while increased costs hinders the commissioning of a laser system solely dedicated to producing neutrons.

Due to these consideration and the potential of mobile neutron sources, the miniaturization of these sources to a laboratory scale and demonstrating the viability of low laser pulse energy LDNS has been an ongoing effort in the community (Zulick et al. 2013; Papp et al. 2022). The miniaturization should not negatively affect conversion efficiency. In this context, miniaturization means both physical miniaturization and a reduction in laser pulse energy while simultaneously increasing the repetition rate of the laser system. However, as previously mentioned and shown in section 4.8, pitcher-catcher schemes utilizing (p,n) reaction for neutron production are not well suited to operate at low laser pulse energies.

However, there is a promising solution to the challenges of laboratory-scale LDNS. Electron-based LDNS, utilizing LWFA, can meet all the necessary requirements. These sources are ideal for driving compact, laboratory scale neutron sources, as they can generate high energy electron beams with low laser pulse energies. For instance, in (S. P. Mangles et al. 2006), a quasi mono-energetic electron beam peaked around $\sim 150\,\mathrm{MeV}$ is obtained from a $0.6\,\mathrm{J}$ laser pulse. In a pitcher-catcher scheme, this electron beam can efficiently drive a neutron source via (γ,n) reactions. By enabling efficient neutron generation at lower laser pulse energies, this approach allows for the miniaturization of the laser driver, offering a promising path forward for the miniaturization of these sources.

Switching from laser-accelerated ion beams to electron beams comes with key advantages. As stated, electrons can be accelerated efficiently at laser energies $< 1\,\mathrm{J}$. This energy range is not far from what commercial short-pulse laser systems can deliver, resulting in a high technological readiness level. Commercial laser systems based on thin Yb:YAG discs can deliver an average laser power of $200\,\mathrm{W}$ at a repetition rate of $1\,\mathrm{kHz}$, with pulse durations of $500\,\mathrm{fs}$ (Trumpf Scientific 2024) and below. Systems delivering up to $1\,\mathrm{kW}$ of average laser power, with increased pulse energy and shorter pulses, are currently being developed and have recently been demonstrated (Barbiero et al. 2023; Mans et al. 2023; Pfaff et al. 2023). Concerning

their compactness, the laser system discussed in (Pfaff et al. 2023) had a footprint of $\sim 30\,\mathrm{m}^2$, which would fit inside a standard 40-foot shipping container (ISO 2020), making it highly mobile in addition to its other features.

Another significant advantage of LWFA is the generation of quasi mono-energetic electron beams, which are peaked around a mean energy E_{mean} with an certain energy spread. The energy spread, defined as the full width at half maximum (FWHM), around E_{mean} is typically in the order of 10 to $25\,\%$ of E_{mean} (Osterhoff et al. 2008; Banerjee et al. 2012; Maier et al. 2020), but narrower spectra can also be obtained (Jalas et al. 2023). The electron beams also exhibit a much lower beam divergence $< 1^\circ$ compared to ion beams generated via TNSA ~ 20 to 30°.

The final key advantage originates from the targetry systems used to generate LWFA electron beams. Recalling from subsection 2.2.1 that the most common target systems for LWFA are self-replenishing targets, such as gas jets/nozzles and gas cells, it becomes clear that LWFA sources are already compatible with high laser repetition rates. Using low laser energies $< 50\,\mathrm{mJ}$, LWFA electron acceleration has been demonstrated at the kHz repetition rate level over extended periods (Z.-H. He et al. 2013; Faure et al. 2018; Rovige et al. 2020; Salehi et al. 2021; Monzac et al. 2024), obtaining up to $15\,\mathrm{MeV}$ quasi mono-energetic electron beams. In contrast, the field of high repetition rate targetry for laser-ion acceleration is still an active field of research and development (A. S. Tebartz 2018; Treffert 2023). Although high repetition rate capabilities of these target systems has been demonstrated (Morrison et al. 2018), the generated ion energies were not suitable for driving a neutron source. Furthermore, the long-term stability of the source, Maier *et al.* (Maier et al. 2020) demonstrated that stable operation at $1\,\mathrm{Hz}$ over $24\,\mathrm{hours}$ can be achieved.

All these factors make LDNS based on laser-accelerated electrons an intriguing alternative to ion-based sources. It needs to be emphasized that LDNS based on ion- and electron-induced reactions are not mutually exclusive; rather, each has its own advantages and disadvantages, which need to be considered in the context of the desired applications when deciding on a generation mechanism. While LWFA of electrons can produce continuous electron spectra (see, for example (Shaw et al. 2021))) that are similar in shape to the proton spectra generated via TNSA, here the focus is on the quasi mono-energetic electron beams that can be obtained when driving LWFA in the bubble/blowout regime (Wenz and S. Karsch 2020). In this chapter, neutron sources based on laser-accelerated electrons are referred to as LENS (Laser Electron Neutron Source[s]), whereas sources relying on laser-accelerated ions are referred to as LIoNS (Laser Ion Neutron Source[s]). The results presented in this chapter have been accepted for publication in the European Physical Journal Plus (Scheuren, Jäger, et al. 2024).

6.1. Optimization of neutron generation at a LENS

This section investigates and optimizes the neutron conversion efficiency for a LENS for a given electron energy E_{mean}. Monte Carlo simulations are utilized to calculate the expected neutron conversion efficiency η_{n}. The optimization comprises the primary neutron production target (catcher/converter) and gives recommendations on the required electron beam parameters to drive an electron-based LDNS most efficiently. For a general overview of the parameters, nuclear data libraries and models used in the simulations presented below, the reader is referred to section 3.1. The conversion efficiency is defined as the amount of neutrons generated per incoming electron $[\eta_{\mathrm{n}}] = \mathrm{n/e^-}$, emitted in 4π. Optimization of the conversion efficiency for a given quasi mono-energetic electron beam energy E_{mean} is essential to ensure that the source works to its fullest potential. From the conversion efficiency the neutron source strength Y can be calculated by

$$Y = \eta_{\mathrm{n}}(E_{\mathrm{mean}}) \cdot Q_{\mathrm{beam}}, \tag{6.1}$$

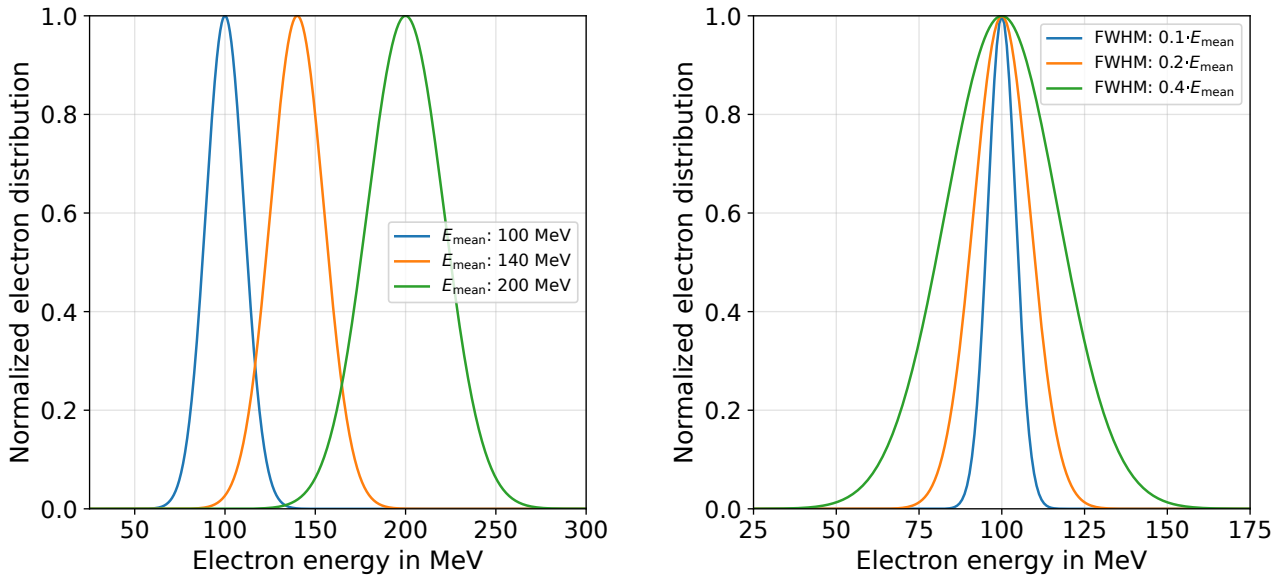

(a) Electron spectra for different E_{mean}.

(b) Electron spectra for different E_{FWHM}.

Figure 6.1.: (a) Initial electron distribution used in simulations for three different E_{mean} energies. The FWHM of each spectrum corresponds to $0.25 \cdot E_{\text{mean}}$. (b) shows example spectra for $E_{\text{mean}} = 100\,\text{MeV}$ with varying FWHM.

where Q_{beam} is the charge contained within the electron beam. Therefore, the two most important factors concerning neutron production are the conversion efficiency η_{n} and the beam charge. Before the conversion efficiency can be optimized, the source term input for the Monte Carlo simulation needs to be introduced.

6.1.1. Source term definitions

The electron spectrum used as input for the simulations is characterized by the central energy of its quasi mono-energetic peak, E_{mean}, and its FWHM (E_{FWHM}). The shape of the spectrum used in the simulations follows a Gaussian distribution. In the first step, the value for E_{mean} is varied to find the most effective electron energy to drive a neutron source. Ten different values for E_{mean} are investigated, which will cover the electron acceleration capabilities of a broad range of laser systems. The following energies are selected $E_{\text{mean}}[\text{MeV}] \in \{35, 50, 75, 100, 125, 140, 200, 250, 300, 350\}$. The highest energy of $350\,\text{MeV}$ is chosen to keep muon production at a reasonable level with regard to radiation safety. The lower limit of $35\,\text{MeV}$ is chosen as it includes the giant dipole resonance (GDR) of most catcher materials of interest. It thus results in higher neutron conversion efficiencies (η_{n}), as excitation of the GDR is the dominant neutron production channel (Swanson 1979).

The second point of investigation is the dependence of the neutron yield on the width (E_{FWHM}) of the quasi mono-energetic peak, where the width is defined as a percentage of the central energy,

$$E_{\text{FWHM}} = p \cdot E_{\text{mean}}. \tag{6.2}$$

As a commonly found value for the FWHM is $p \approx 0.25$ (Osterhoff et al. 2008; Banerjee et al. 2012), $p = 0.25$ is adopted as the default value for the simulations. When investigating the influence of the peak's width on the neutron production, p is varied (while keeping E_{mean} constant), with $p \in \{0.05, 0.1, 0.15, 0.2, 0.25, 0.3, 0.35, 0.4\}$.

Figure 6.1a and 6.1b show examples of the used input spectra. In (a) the value for E_{mean} is varied, with $p = 0.25$, whereas in (b), $E_{\text{mean}} = 100\,\text{MeV}$ is constant and p is varied.

6.1.2. Neutron conversion efficiency optimization

To maximize the neutron fluxes at LENS, a suitable catcher needs to be selected. Parameters of interest for the catcher are its shape and material composition. For a final target design, other important secondary aspects need to be considered as well, such as converter heating and heat conduction or changes in chemistry due to heating/cooling. However, these secondary factors are not the main focus of the investigation.

Due to the fact that electron based sources generate neutrons in a two-step process, the optimization of the converter target's geometry can be of great importance, as several in-depth studies have indicated (Jallu et al. 1999; Huang et al. 2005; Petwal et al. 2007; Sari et al. 2013). Therefore, different converter geometries are investigated, including spheres, hemi-spheres, cubes and cylinders all made of tungsten. This is done to determine the geometric shape which maximized the neutron conversion efficiency η_{n} per volume.

The neutron yield from a spherical tungsten converter in dependence on the radius is displayed in Figure 6.2a, the statistical uncertainty is contained within the markers of the plot. The neutron flux increases steeply for all energies until it starts to saturate at values between 2.5 to $3.5\,\text{cm}$. A further increase of the radius results in less neutrons leaving the converter, as saturation sets in and absorption of neutrons becomes a noticeable factor. Conversion efficiencies in excess of $0.1\,\text{n/e}^-$ can be achieved with electron energies above $300\,\text{MeV}$. Figure 6.2b shows the conversion efficiency for a hemi-spherical converter target, with the flat side facing the incoming electron beam. The maximum conversion efficiency is achieved for radii between 5 to $6\,\text{cm}$, with saturation setting in around $5\,\text{cm}$ for electron beams below $250\,\text{MeV}$, while beams with higher energy saturate around $6\,\text{cm}$. Noticeably, no discernible difference in the maximum achievable conversion efficiency between the spherical and hemi-spherical target is observed for the tested electron energies. The main differentiating factor is the volume required to achieve the maximum conversion efficiency. In Figure 6.2c the results for a cubic conversion target are shown, where saturation starts to set in at a side-length around 5 to $6\,\text{cm}$ and the highest recorded conversion efficiency is again comparable to the previous geometries. Lastly, in (d) the results for a selected energy using a cylindrical catcher are shown, in dependence on the radius and its height. For the shown example of $E_{\text{mean}} = 200\,\text{MeV}$ the conversion efficiency starts to saturate for radii greater than $2\,\text{cm}$ and heights exceeding $5\,\text{cm}$. Table 6.1 shows a comparison of the highest conversion efficiency that is achieved by each geometry for $E_{\text{mean}} = 200\,\text{MeV}$ electron beams.

Table 6.1.: Comparison of the maximum conversion efficiency for different converter geometries for a $200\,\text{MeV}$ electron beam. The achieved conversion efficiencies are comparable, but the volumes of the converters differ by up to a factor of 2.3. Spherical and cylindrical converters delivered the highest conversion efficiency while also being most compact.

Geometry	η_{n} in $\times 10^{-2}$ n/e$^-$	V in cm^3
Sphere	(6.760 ± 0.003)	113.1
Cylinder	(6.774 ± 0.003)	125.7
Cube	(6.729 ± 0.003)	216.0
Hemi-Sphere	(6.640 ± 0.003)	261.8

Of the tested geometries, the spherical and cylindrical converter targets provide high neutron conversion efficiencies, while also being compact. However, simulations show that the volume of the cylindrical target can increase significantly for higher electron energies. In contrast, the required volume remains constant for the spherical converter across all energies tested, making it the more flexible option of the two. For this reason, all further simulations are conducted using a spherical converter.

Besides the converter geometry, the choice of material can significantly influence the expected neutron

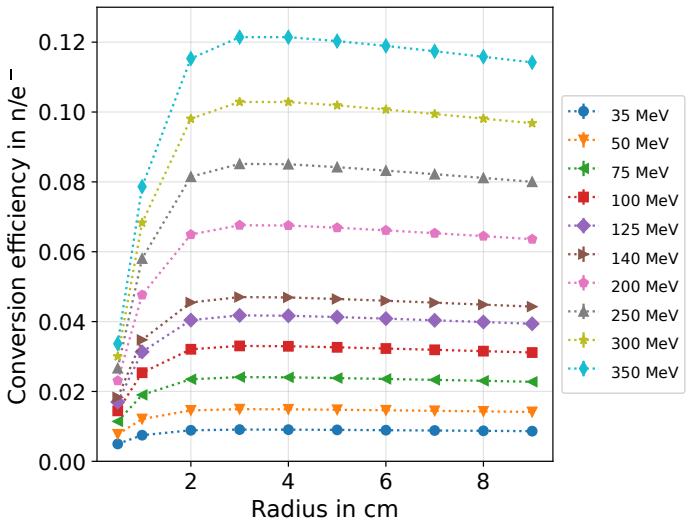

(a) Conversion efficiencies for a spherical catcher.

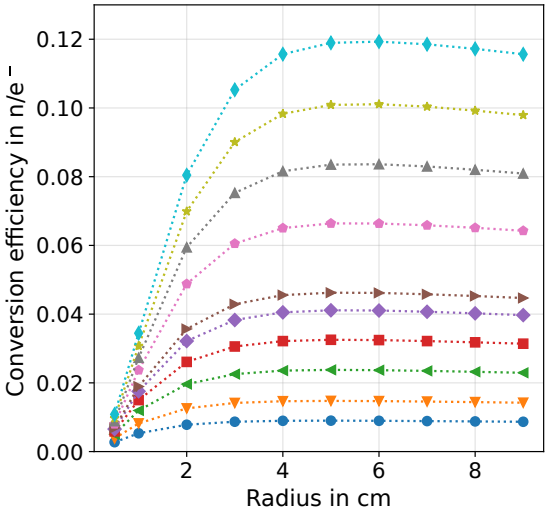

(b) Conversion efficiencies for a hemi-spherical catcher.

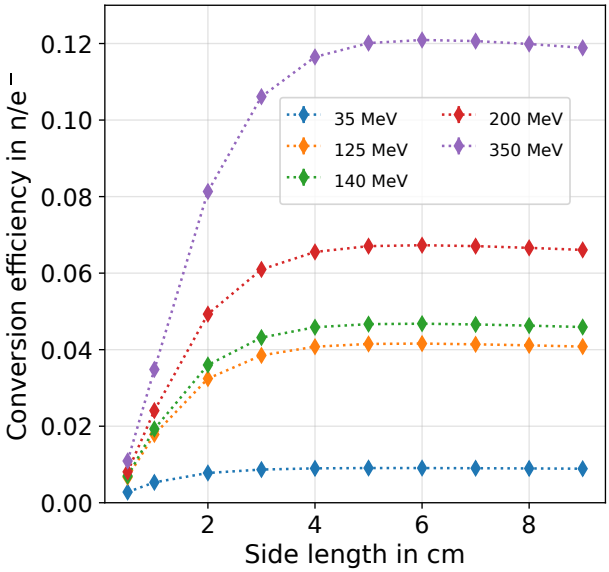

(c) Conversion efficiencies for a cubic catcher.

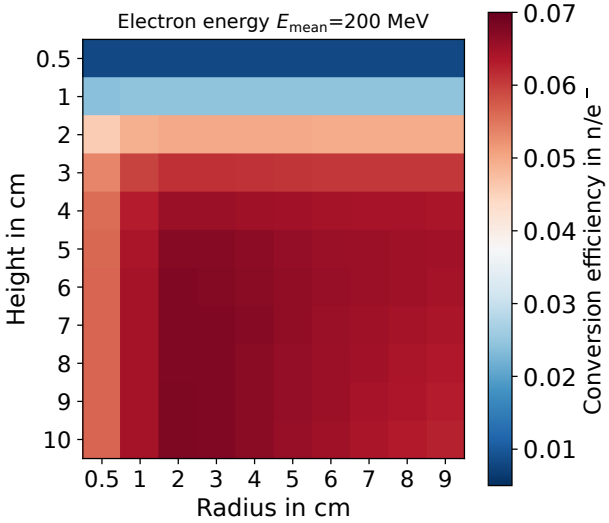

(d) Conversion efficiencies for a cylindrical catcher.

Figure 6.2.: Neutron conversion efficiency for a spherical tungsten converter (a) for different E_{mean}. (b) shows the conversion efficiency for a hemi-spherical converter. The two top figures share the legend. (c) shows the conversion efficiency for a cubic conversion target in dependence on its side length. (d) shows the conversion efficiency matrix for a cylindrical converter in dependence on its radius and height. This example shows the conversion efficiency for a $200\,\text{MeV}$ electron beam.

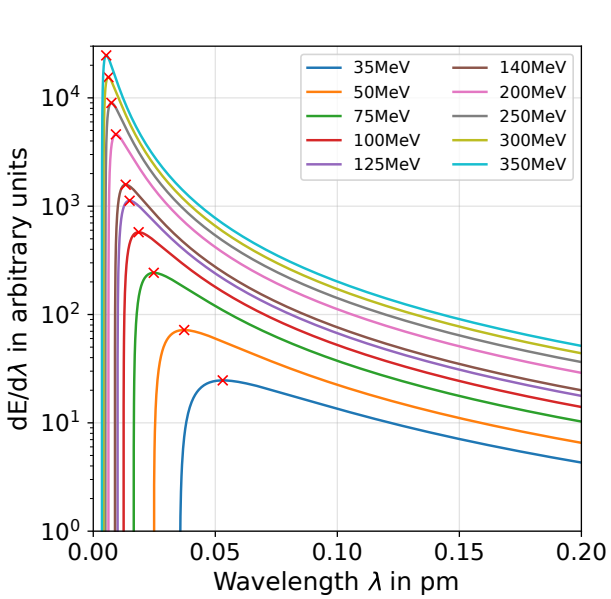

(a) Expected bremsstrahlung emission spectrum.

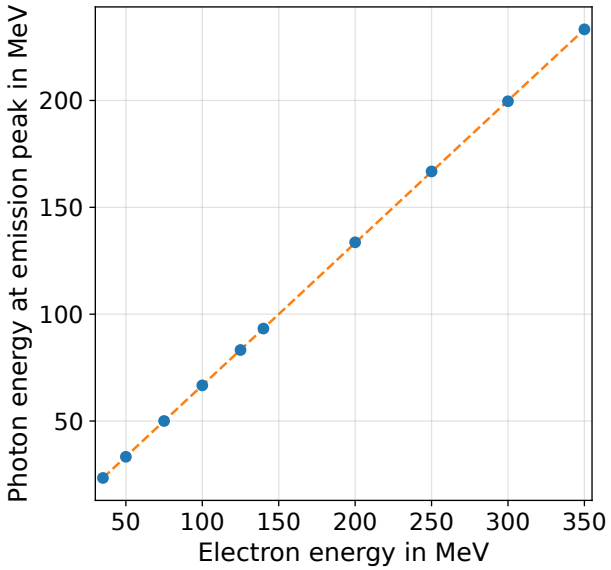

(b) Comparison between the photon and electron energy where the photon emission peaks.

Figure 6.3.: (a) shows the expected energetic distribution of photons from electrons impinging on the converter, based on Equation 2.56. (b) displays the dependence of the photon energy, where the emission peaks, on the electron energy. The peaks for each energy are marked by red crosses in (a). The dashed line serves to guide the eye.

conversion efficiency. Materials need to fulfill certain criteria to be suitable as converter target. The material needs to have a high density in order to increase the chance of a photon interacting with a nucleus and it needs to have large cross sections for (γ,xn) reactions. Furthermore, it needs to have a high atomic number, as the generation of bremsstrahlung photons is proportional to it, according to Equation 2.56. This equation is typically used to calculate the emission spectrum of a mono-energetic electron beam with energy E_{el}. In the case of the quasi mono-energetic electron beams generated by LWFA, E_{el} can be replaced by E_{mean} in a first approximation if the shape of the spectrum is symmetric around E_{mean}. Figure 6.3a shows the expected photon emission spectrum based on Equation 2.56, with Figure 6.3b showing the correlation between the electron energy E_{mean} and the photon energy at which the emission peaks. The dashed line between the points serves to guide the eye and a linear trend can be observed.

From these considerations, lead (Pb), tungsten (W), uranium (U) and tantalum (Ta) are selected for further investigation. In Figure 6.4a the conversion efficiencies for the different materials are displayed. In this figure only the best performing converter at each energy is shown. Starting with the lead-based converters, a radius of $9\,\mathrm{cm}$ (saturation starts to set in around $r = 4$ to $6\,\mathrm{cm}$) is needed to achieve the maximum neutron yield, whereas uranium only requires a sphere with a $5\,\mathrm{cm}$ radius. In the case of U, saturation starts to set in around $r = 2$ to $4\,\mathrm{cm}$, depending on the energy. Tungsten and tantalum achieve their highest conversion efficiency at radii of $3\,\mathrm{cm}$ and $4\,\mathrm{cm}$, respectively.

Pb, Ta and W all achieve similar conversion efficiencies, ranging from 0.01 to $0.13\,\mathrm{n/e^-}$ depending on the energy. However, the lead converter requires a volume 11 to 27 times larger than the other two materials, making it the least desirable material for a compact neutron source. Additionally, lead possesses the lowest melting point of all tested materials at $327\,^{\circ}\mathrm{C}$, resulting in (partial) melting of the converter under continuous load. To combat this, a liquid lead catcher would need to be implement, making the experimental setup

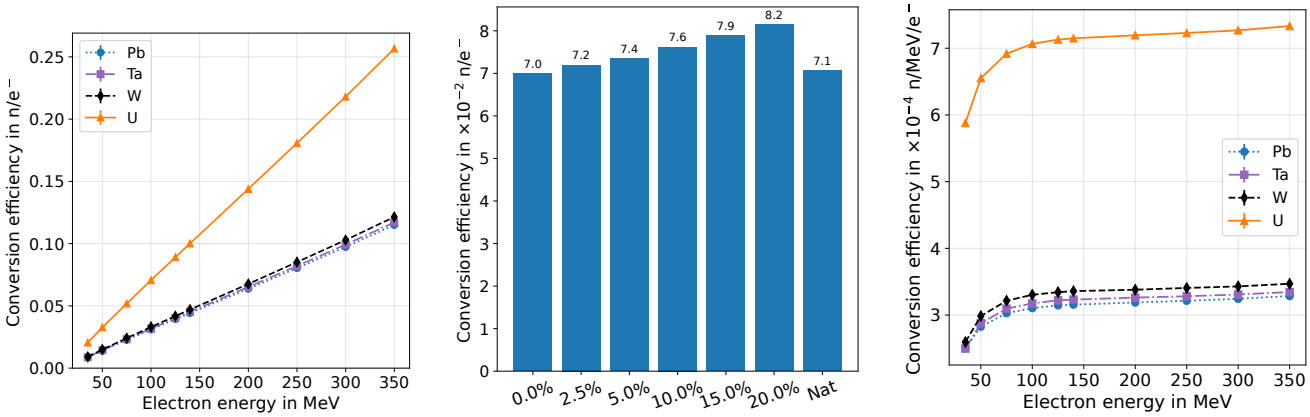

(a) Conversion efficiency for different materials.

(b) Conversion efficiency for varying enrichment levels.

(c) Conversion efficiency per MeV of electron energy.

Figure 6.4.: (a) displays the maximum conversion efficiency achieved for each material simulated at a given E_{mean}. Uranium exhibits the biggest relative increase in efficiency for $E_{\text{mean}} \lesssim 100\,\text{MeV}$. The dashed line is a linear fit to the corresponding data points, see Table 6.2. (b) Neutron conversion efficiency in dependence on the amount of ^{235}U present in the converter, given in mass percentage. A sphere with $5\,\text{cm}$ radius was used. (c) Maximum achievable conversion efficiency for a spherical target per MeV of electron energy. The point of diminishing returns is reached between 100 and $150\,\text{MeV}$. Here solid lines are only used to guide the eye. Statistical uncertainties for (a) and (c) are contained within the markers.

much more complex. Thus, lead-based converters are only relevant if the activation of the converter after irradiation is important, as lead generates less long-lived isotopes, making disposal easier to facilitate (Swanson 1979).

The highest absolute efficiency is achieved by uranium, exceeding the other tested materials by an average factor of 2.2. Even at low electron energies of $35\,\text{MeV}$, the conversion efficiency exceeds $0.02\,\text{n/e}^-$, ranging up to $0.25\,\text{n/e}^-$ for $E_{\text{mean}} = 350\,\text{MeV}$ electron beams. Figure 6.5 shows the full data set for the uranium-based conversion target. The lowest performing converter material is lead, underperforming tungsten by 3.5 to 6.5% (at $35\,\text{MeV}$ and $100\,\text{MeV}$) and tantalum by 0 to 2.5% (at $35\,\text{MeV}$ and $125\,\text{MeV}$). A correlation between the value of E_{mean} and the maximum neutron conversion efficiency can be seen in Figure 6.4a. A function of the form

$$\eta_{\text{fit}}(E_{\text{mean}}) = a \cdot (E_{\text{mean}} - \delta) \tag{6.3}$$

is fitted to the data points, where a is the free fit parameter and δ is the weighted energy threshold for (γ,n) reactions. δ is determined by the weighted energy threshold for (γ,n) reactions for each isotope contained by the converter material (natural composition). The resulting fit parameters for the tested catcher materials are displayed in Table 6.2. This fit can be used to approximate the neutron production for an arbitrary electron energy, withing the displayed energy range.

Although the converter volume to achieve the highest conversion efficiency for uranium ($r = 5\,\text{cm}$) is 4.6 times larger than that of tungsten ($r = 3\,\text{cm}$), the much higher conversion efficiency allows for the usage of smaller uranium spheres, which would still result in a higher conversion efficiency compared to tungsten. For example, at $E_{\text{mean}} = 100\,\text{MeV}$ a uranium sphere with $r = 1\,\text{cm}$ outperforms the tungsten converter ($r = 3\,\text{cm}$) by at least a factor of 1.6 (see Figure 6.5). The conversion efficiency can be increased by up

Table 6.2.: Fit parameters for fits presented in Figure 6.4, based on Equation 6.3 (a). From th fit the conversion efficiency at a given electron energy E_{mean} can be estimated.

Material	a in $10^{-4}\,\text{n/e}^-/\text{MeV}$	δ in MeV
Lead	3.33 ± 0.01	7.4
Tantalum	3.41 ± 0.01	7.6
Tungsten	3.60 ± 0.02	7.3
Uranium	7.44 ± 0.01	6.1

to $15\,\%$, if the ^{235}U content of the converter is increased. Figure 6.4 (b) shows conversion efficiencies for a $E_{\text{mean}} = 100\,\text{MeV}$ electron beam and varying ^{235}U enrichment levels. An upper limit of $20\,\%$ is chosen for the target to be considered a low-enrichment target. While an increase in conversion efficiency can be obtained by increasing the ^{235}U content, from the same figure it can also be seen that using depleted uranium ($0\,\%$ enrichment) does not meaningfully affect the conversion efficiency. However, a sphere with a diameter of $10\,\text{cm}$ and $20\,\%$ enriched uranium poses a significant proliferation risk. Thus, using enriched uranium catchers does not significantly increase the conversion efficiency and should only be considered if the boost is required.

To put the obtained conversion efficiencies into context, the results are compared to the efficiency obtained from a LIoNS. As a point of comparison, data presented in Figure 4.12b is used. The comparison shows that electron-based sources posses a much higher conversion efficiency than ion-based sources. Simulated conversion efficiencies for the measured DRACO proton beam presented in the previous chapter returned efficiencies between 2.3 to $4.5 \times 10^{-4}\,\text{n/p}^+$. Using a $35\,\text{MeV}$ electron beam and the worst performing geometry displayed in Figure 6.2a returns a conversion efficiency of $5 \times 10^{-3}\,\text{n/e}^-$, an increase exceeding one order of magnitude. This advantage for electron-based sources results from the indirect neutron generation process, in which the electrons need to generate γ-rays first. A high energy electron generates more than one photon on average when emitting bremsstrahlung. Therefore, this intermediate process boosts the conversion efficiency. Monte Carlo simulations suggest that around 1.2 to 40 photons are generated per electron, depending on E_{mean}, the converter geometry and choice of material.

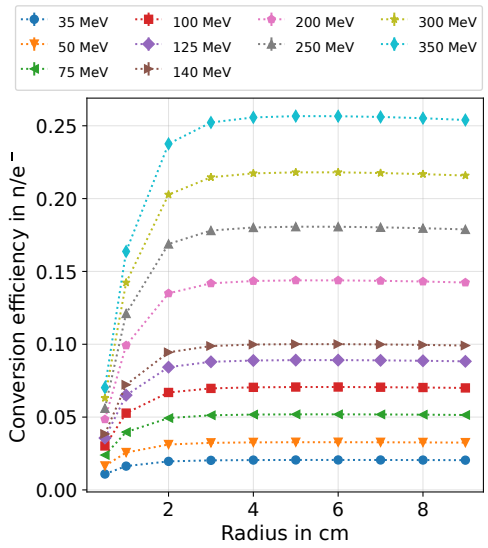

Figure 6.5.: Neutron conversion efficiencies for the spherical uranium converter. Natural isotopic composition is assumed for the simulations.

While Figure 6.4a shows a linear increase in the conversion efficiency with E_{mean}, it does not include the "cost" of generating higher electron energies. Therefore, to determine the optimal working point regarding the electron energy, the conversion efficiency per MeV of electron energy is reviewed and displayed in Figure 6.4c. For each material, a point of diminishing return is achieved between 100 to $150\,\text{MeV}$, which is consistent with values reported in (Papp et al. 2022). Thus, a further increase of the electron energy only results in increased requirements for the laser system, i.e. higher pulse energy, without resulting in

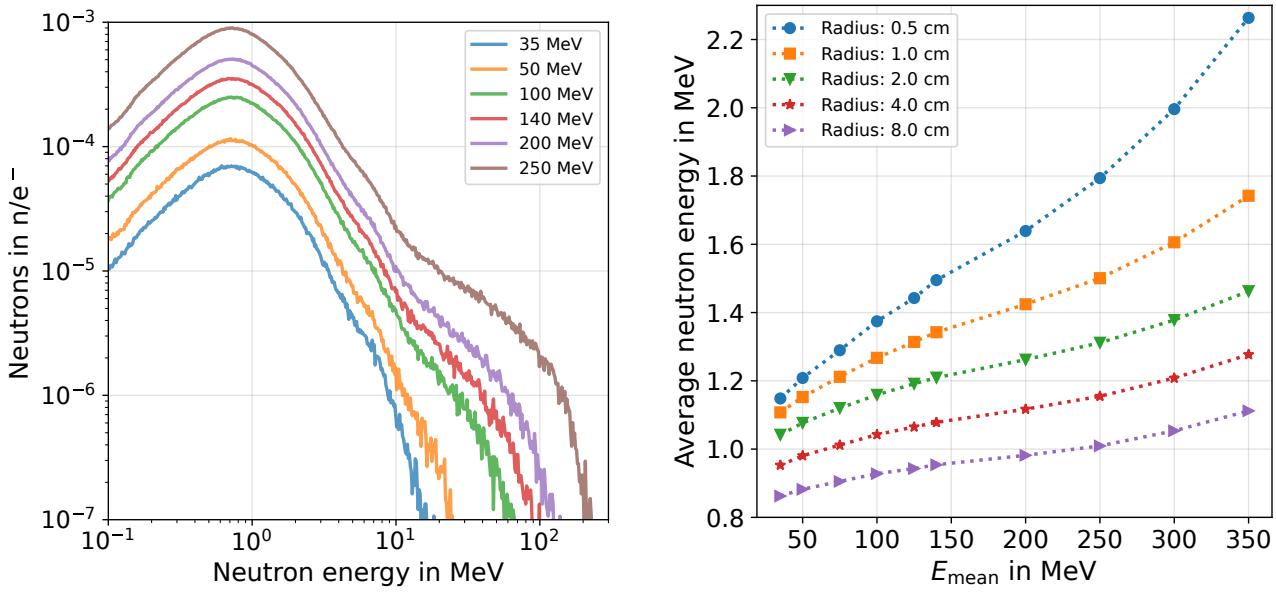

(a) Emitted neutron spectra for for different E_{mean}.

(b) Average energy of the emitted neutrons.

Figure 6.6.: (a) Neutron spectra for different electron energies using a tungsten converter, $r = 3\,\text{cm}$. (b) Average neutron energy for different converter radii and electron energies. Moderation inside the converter can be observed for increased radii. The dotted line is to guide the eye.

significantly higher conversion efficiencies. Additionally, higher electron energies also mean more energy deposition increasing the thermal load on the converter. Another benefit of keeping the electron energy at $\lesssim 140\,\text{MeV}$ is that muon production cannot occur below this energy (Swanson 1979), relaxing the radiation protection requirements of such a source. For reference, a source deploying a $350\,\text{MeV}$ electron beam generates around 10^{-6} to $10^{-5}\,\mu/\text{e}^-$, according to Monte Carlo simulations. For these reasons, an electron-based LDNS should utilize electrons energies between 100 to $150\,\text{MeV}$ and focus on maximizing the electron beam's charge per pulse to further increase the neutron flux.

Looking at the generated neutron spectra displayed in Figure 6.6a, using a tungsten catcher, one notable feature is that the neutron spectrum peaks slightly below $1\,\text{MeV}$ but can extend up to $200\,\text{MeV}$. The neutron fluence above $1\,\text{MeV}$ rapidly falls off towards higher energies, decreasing more than one order of magnitude from 1 to $10\,\text{MeV}$. Above $10\,\text{MeV}$, the formation of a high energy tail is caused by the the quasi-deuteron effect (Swanson 1979). In Figure 6.6b, the average neutron energy for tungsten converters of different radii is displayed. As expected the neutron energy decreases with increasing radius due to moderation inside the converter. Low average neutron energies make these sources especially interesting for beamlines that provide moderated neutron beams. The low average energies are helpful, as they increase the moderation efficiency of the neutron spectrum by the catcher.

6.1.3. Dependence of the neutron conversion efficiency on E_{FWHM}

The simulations so far assumed a Gaussian distribution of the electron energies around E_{mean} and a FWHM corresponding to $25\,\%$ ($p = 0.25$) of E_{mean}. Under experimental conditions, shot-to-shot fluctuations can cause the distribution to widen/narrow or experience an asymmetry towards higher or lower energies (Osterhoff et al. 2008; Maier et al. 2020). These fluctuations can affect the neutron production. Therefore, the influence of such fluctuations is characterized in this section. For this, two cases are studied separately.

The first case only considers symmetric broadening/narrowing around E_{mean}, whereas the second case considers a truncated distribution favoring lower energy electrons. Only the case of favoring lower electron energies is considered, as decreasing the electron energy results in a lower conversion efficiency, as indicated by Figure 6.4a.

Implementing these constraints in the simulation requires parameterizing the lower and upper energy limits that the underlying Gaussian distribution should sample. These bounds are then used to limit the energy range in which the electrons are sampled during the source generation step of the simulation. The subsequent electron transport is unaffected by these boundaries. In the case of symmetrical broadening the upper and lower energy bounds are given by

$$E_{\text{bounds}} = (1 \pm 2 \cdot p) \cdot E_{\text{mean}},$$

with p varying from 0.05 to 0.4. In case of asymmetrical broadening two different definitions for the upper and lower boundaries are used in order to obtain the truncated distribution. They are defined as:

$$\begin{aligned} E_{\text{upper}} &= (1 + 0.5 \cdot p) \cdot E_{\text{mean}} \\ E_{\text{lower}} &= (1 - 2 \cdot p) \cdot E_{\text{mean}}. \end{aligned}$$

A comparison between these definitions for $E_{\text{mean}} = 200\,\text{MeV}$ and different values for p can be seen in Figure 6.7a. The simulations were conducted using a tungsten converter with a radius of $3\,\text{cm}$, with electron energies varying from 100 to $200\,\text{MeV}$. The energies were selected based on the results of the previous section.

The results can be seen in Figure 6.7b. For the symmetrically broadened spectra, neutron conversion efficiencies are stable over a wide range of spectral widths and no meaningful variation in the conversion efficiency can be observed. This is due to the linearity in neutron production discussed above. The maximum recorded difference is $< 0.5\,\%$ for all energies displayed and the conversion efficiency can be considered stable. However, the situation differs when the spectrum widens asymmetrically in favor of lower electron energies. Here, the efficiency decreases more noticeably, with a decrease of around $4\,\%$ in case of $E_{\text{mean}} = 200\,\text{MeV}$ and $4.4\,\%$ for $E_{\text{mean}} = 100\,\text{MeV}$, which are the highest recorded decreases.

From Equation 6.1, it can be seen that the neutron yield depends linearly on both the conversion efficiency and beam charge. With a maximum decrease of $4.4\,\%$ in the conversion efficiency due to the asymmetrical broadening of the electron spectrum, the neutron yield only changes by the same percentage. In contrast, in (Maier et al. 2020), a fluctuation in beam charge of $\pm 11\,\%$ rms is reported over a total of 100k shots. Therefore, fluctuations of the beam charge play a bigger role in stable neutron production. Furthermore, due to $\eta_{\text{n}} \propto E_{\text{mean}}$, fluctuations in E_{mean} are likely more influential on the source performance than fluctuations in E_{FWHM}.

6.2. Estimating neutron yields from a set of laser parameters

The previous section showed that a hypothetical LENS can achieve much higher conversion efficiency than what is typically achieved at a LIoNS. The results from the optimization are used to calculate the expected neutron flux that can be provided from a real laser system that is currently under development (Pfaff et al. 2023; Mans et al. 2023; Barbiero et al. 2023) and should become available within the next 1 to $2\,\text{years}$. The laser parameters of the system are summarized in Table 6.3.

To use the results of the catcher optimization, the expected electron beam parameters for the laser system need to be calculated. Lu's (W. Lu et al. 2007) framework introduced in subsection 2.2.1 is used

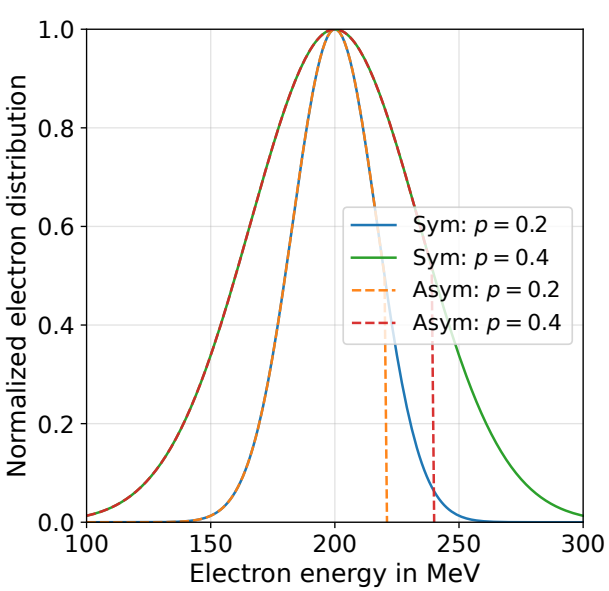

(a) Exemplary electron input spectrum.

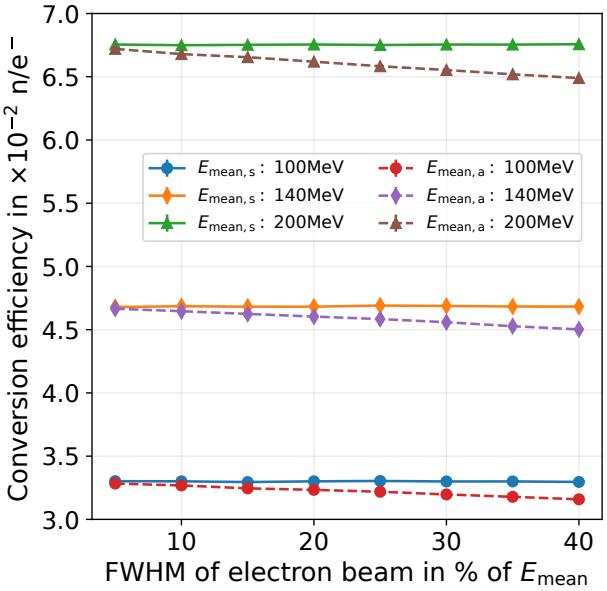

(b) Effect of E_{FWHM} on the conversion efficiency.

Figure 6.7.: (a) Comparison between a symmetrical (Sym) and asymmetrical (Asym) broadening of the electron input spectrum. (b) Neutron yield for a spherical tungsten target with $r = 3\,\mathrm{cm}$ for varying values of FWHM of the underlying electron beam. The line connecting the marker is to guide the eye of the reader. The solid line is for symmetrical broadening of the electron spectrum (subscript s), while the dashed line represents the asymmetrical broadening (subscript a). For the symmetrically broadened spectra neutron conversion efficiencies are stable over a wide range of spectral widths. Statistical uncertainties are contained within the markers.

Table 6.3.: Laser parameters for a kW laser-driven neutron source. The system is based on the Yb:YAG thin disc amplified laser systems as reported in (Pfaff et al. 2023; Mans et al. 2023; Barbiero et al. 2023). A q-factor of 0.35 is assumed. The converter material consists of a tungsten sphere with a radius of $r = 3\,\mathrm{cm}$. The fit function displayed in Figure 6.4a is used to estimate the neutron conversion efficiency per electron. The results presented in the LIoNS tab are based on the results obtained from the full laser energy shots of the DRACO campaign (see section 4.3). The neutron fluence obtained using the LiF catcher $(4.9 \pm 0.5) \times 10^7\,\mathrm{n/sr/shot}$ is used as the basis and extrapolated to 4π for the comparison. The shot repetition rate during the experiment was one shot every 1 to $2\,\mathrm{min}$ and this value is used to scale the results. The average neutron energy for the LIoNS system is based on the spectra shown in Figure 6.8a. The low energy LIoNS data is based on the data presented in section 4.8, where the neutron fluence of $(1.6 \pm 0.8) \times 10^6\,\mathrm{n/sr/shot}$ (measured by BDs) is extrapolated to 4π.

Parameter	**LENS**	**LIoNS**	**Low energy LIoNS**
Laser energy in J	0.4	17	2 to 3
Laser pulse length in fs	35	30	30
Wavelength in nm	1030	800	800
Focus FWHM in µm	8	2.6	2.6
Repetition rate in Hz	2500	$(0.8 - 2) \times 10^{-2}$	n.a.
Normalized vector potential a_0	2	48	15 to 20
E_{mean} in MeV	145	n.a.	n.a.
Q_{beam} in pC	96	n.a.	n.a.
Neutron yield in $10^7\,\mathrm{n/shot}$	3.0	62.8	2.0
Neutron yield in $10^{10}\,\mathrm{n/s}$	7.3	$(0.5 - 1.1) \times 10^{-3}$	n.a.
Average neutron energy in MeV	1.1	4.0	n.a.

(see Equation 2.49-2.51) to calculate the electron beam parameters, which are used as an input for Equation 6.3 and additional Monte Carlo simulations. From Monte Carlo simulations, the expected neutron spectrum is tallied, using a $r = 3\,\mathrm{cm}$ spherical tungsten converter. For these simulation the FWHM of the electron beam is set to $0.25 \cdot E_{\mathrm{mean}}$. The calculated neutron performance is shown in Table 6.3, where it is compared to the results of a LIoNS, obtained from the DRACO experimental campaign discussed in chapter 4.

In Table 6.3 the label LIoNS corresponds to the full energy DRACO shots, with low energy LIoNS referring to the low laser energy shots. For the low energy LIoNS the neutron fluence obtained from the deuterated targets is used for the comparison, whereas the LIoNS results are based on fluences generated by the non-deuterated targets. The set using the deuterated targets is selected, as it is the only low laser energy shot set where bubble detectors were used to measure the fluence.

The results in Table 6.3 show that the LENS cannot match the neutron fluence generated by the full energy DRACO shots on a per shot basis. The neutron fluence from the LIoNS exceeds the expected LENS neutron fluence by factor a of ~ 20. Comparing the expected LENS neutron yield to the results of LIoNS published in (Kleinschmidt et al. 2018; Zimmer 2020; Yogo, Arikawa, et al. 2023) confirms this result. In these publications, laser shots with energies in excess of $100\,\mathrm{J}$ were used to drive the neutron source, with the reported per shot yields exceeding the expected LENS yields by three to almost four orders of magnitude. However, the situation changes when looking at the low energy shots from DRACO. Here, the measured and expected neutron fluences are about equal despite the fact that the LENS only required 15 to $20\,\%$ of the

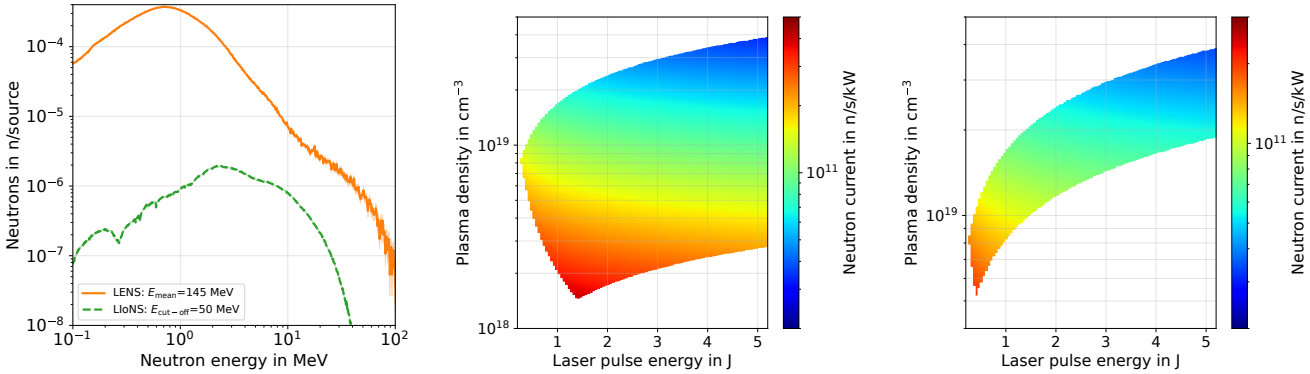

(a) Emitted neutron spectra in 4π. (b) Max. E_{mean}: 500 MeV. (c) Max. E_{mean}: 140 MeV.

Figure 6.8.: (a) Neutron spectra obtained from Monte Carlo simulations for the laser system detailed in Table 6.3. The LIoNS spectrum is based on Monte Carlo simulations presented in the chapter on the DRACO beamtime (full energy shots), using the LiF catcher. The term "source" in the y-axis label refers to either electrons (LENS) or protons (LIoNS). (b) shows the expected neutron yield for a 1 kW average power laser system with a pulse length of 35 fs and a wavelength of 1030 nm. A tungsten converter is assumed and the neutron yield is based on the fit shown in Figure 6.4a (black dashed line). The maximum electron energy is limited to 500 MeV. (c) shows the expected yield for a maximum electron energy of 140 MeV. The value was chosen in order to prevent muon generation.

laser energy of the low energy LIoNS. This again highlights the expected advantage that a LENS has over LIoNS for low laser energies.

When taking the repetition rates of these systems into account and comparing the average neutron flux, the LENS outperforms the other systems. In this case, the LENS exceeds the yield obtained at DRACO by up to four orders of magnitude. The required laser energy to drive the LENS is only 2 % of the laser pulse energy delivered by DRACO, which would allow for a more portable, compact and cheaper laser system. The neutron spectrum generated by the LENS can be seen in Figure 6.8a. The maximum recorded neutron energy is around 100 MeV, with the peak current situated at around 0.8 MeV. Even when scaling the DRACO results to 10 Hz, which is at the cutting edge of current laser technology (Mourou et al. 2011; Rus et al. 2013), the neutron flux only reaches around 10 % of the expected yield of the LENS. Furthermore, the neutron yield can be further increased for the electron-based sources by switching from tungsten to a uranium converter. This change would double the expected neutron flux, as a result of the higher conversion efficiency.

To better understand the scalability of electron-based LDNS, the above introduced method is used to estimate the expected neutron flux per kW of average short pulse laser power for different laser pulse energies. The results are displayed in Figure 6.8b. The yield is calculated in dependence on the plasma density and laser pulse energy while assuming a laser pulse duration (FWHM) of 35 fs at a wavelength of 1030 nm. In the figure, the maximum electron energy is limited to 500 MeV, as this is the upper limit for which the neutron conversion efficiency fit of Table 6.2 is valid. The highest expected neutron flux is around 4×10^{11} n/s, comparable to currents obtained at nELBE (Beyer et al. 2013) and RANS/RANS-II (Kobayashi et al. 2021). From this simple model, the optimal laser energy for such a laser system is expected to be between 1 to 2 J, with higher energies performing worse as a consequence of the reduced repetition rate and the 500 MeV energy limit imposed on the electron beam. If muon production is to be avoided, the maximum electron energy should not exceed 140 to 150 MeV. Expected neutron yields for combinations not exceeding this energy are displayed in Figure 6.8c. When the energy is limited to 140 MeV, the model suggests an

optimum in the required laser energy between 0.5 to $1\,\mathrm{J}$, which is close to the laser systems under development (Pfaff et al. 2023; Mans et al. 2023; Barbiero et al. 2023). This means that compact LDNS, which are competitive to existing conventional neutron sources, should become available within the next 1 to 2 years.

One relevant aspect neglected so far is the expected amount of heat introduced to the catcher, which can potentially damage the it. The heat load is estimated by scoring the energy deposition per incoming electron in the Monte Carlo simulations. For the $145\,\mathrm{MeV}$, an average of $135\,\mathrm{MeV/e^-}$ is deposited. At a repetition rate of $2.5\,\mathrm{kHz}$ and a charge of $96\,\mathrm{pC/shot}$, this corresponds to a heat load of $\dot{Q}_{\mathrm{heat}} \approx 35\,\mathrm{W}$. Due to the high melting point of tungsten, this heat load should not be problematic under experimental conditions. Since electron acceleration takes place in a vacuum chamber, the catcher is also placed in vacuum. Thus, thermal radiation constitutes the dominant form of heat transfer away from the catcher. The loss via thermal radiation can be calculated through

$$\dot{Q} = \epsilon \sigma A \cdot (T_{\mathrm{W}}^4 - T_{\mathrm{env}}^4), \tag{6.4}$$

where A is the surface area of the converter, σ the Stefan-Boltzmann constant, ϵ the emissivity and T_{W} the temperature of the tungsten catcher and T_{env} the temperature of the environment, respectively (Cengel 2011). For ϵ values between 0.05 and 0.2 are assumed (Schweizer 2024). If $\dot{Q}$ matches the introduced heat load, steady state operation is obtained and no further heating should occur. The final temperature at which the losses match the introduced heat can be calculated by

$$T_{\mathrm{W}} = \sqrt[4]{T_{\mathrm{env}}^4 + \frac{\dot{Q}_{\mathrm{heat}}}{\epsilon \sigma A}}, \tag{6.5}$$

with a temperate of $20\,^{\circ}\mathrm{C}$ for the environment. Using this equation, a maximum steady state temperature of around 450 to $750\,^{\circ}\mathrm{C}$ is obtained, depending on the value for ϵ. This is well below the melting point of $3400\,^{\circ}\mathrm{C}$ of tungsten. Thus in this first approximation, the heat load introduced should not pose too much of a hindrance.

6.3. Further increasing the neutron source strength

One central result of section 6.1 is that a LENS should aim for electron energies (E_{mean}) between 100 to $150\,\mathrm{MeV}$. Staying within this energy range promises a reasonable trade off-between the conversion efficiency per MeV electron energy, the required laser system to drive the source and the heat load imparted on the converter, in addition to radiation safety aspects (Swanson 1979). Therefore, with the energy limited in this way, according to Equation 6.1, the neutron production per shot can only be increased by increasing each electron beam's charge.

This section provides an outlook on a promising method for increasing the beam charge in the blow-out/bubble regime of LWFA. During the acceleration, the electrons occupy a small sub-volume within the bubble. While the electrons are trapped and accelerated with the bubble, they can emit so-called betatron radiation (Corde et al. 2013). The betatron radiation's source size can be used to estimate the sub-volume occupied by the electrons in the bubble, typically in the order of $2\,\mu\mathrm{m}$ (Wenz, Schleede, et al. 2015; Schnell et al. 2015). By increasing this volume, the charge of the electron beam can potentially be increased. Using a donut-shaped focus profile can be a way to increase this volume, as the sub-volume goes from a point-like volume to a ring-like volume.

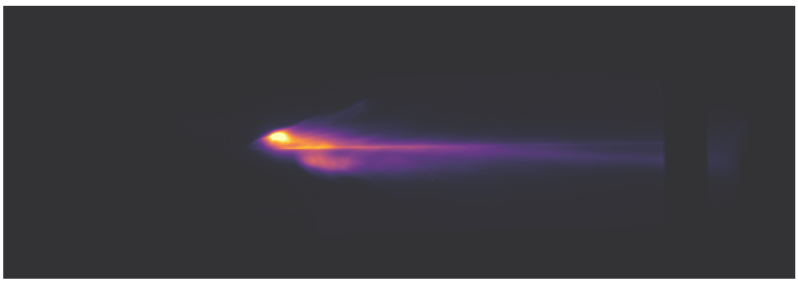

Figure 6.9.: Electron beam profile obtained when using a donut shaped laser focus profile. For this shot the electrons were deflected by the magnet.

This idea was tested by Stephan Kuschel during a proof-of-principle experimental campaign in 2021 at the **Je**naer **Ti**tanium:Sapphire (JETI) laser. The data was supplied by him for analysis during the course of this thesis. The campaign's main goal was to demonstrate the capability of accelerating electrons using a donut-shaped focus profile and investigate whether or not these beams tend to increase the electron beam charge. In this section, the donut focus profile is also referred to as vortex beam. Furthermore, during the experiment, the laser pulse energy was kept constant for both the Gaussian and vortex beam, meaning that the vortex beam had a lower a_0 than the Gaussian beam.

The electron beam is probed using a scintillating screen that is viewed by a camera. The distance from the laser target to the scintillator is $(2355 \pm 5)\,\mathrm{mm}$. Additionally, a magnet can be inserted, resulting in an energy-dependent deflection of the electrons. Using the vortex beam, electrons were successfully accelerated. Figure 6.9 shows a measured electron profile, for a shot where the electrons were deflected by the magnet. It needs to be emphasized that the experimental setup does not allow for a quantitative comparison between vortex and Gaussian beam results. Instead, the data is analyzed to show trends between the two beams where possible. For this, two parameters are investigated, the first being the pointing stability, followed by the beam charge.

Figure 6.10a shows a comparison of the pointing stability for both the Gaussian (orange "x" markers) and vortex beam (green "+" markers). An electron beam propagating in a straight line from the interaction point to the scintillator would land on the red diamond, referred to as the center position. The pointing of the electron beam is always given in reference to this point. The marker positions are obtained by analyzing the image of each shot and determining the x- and y-coordinates of the center of mass of the pixel distribution within the image. Afterwards, the coordinates of the reference point are subtracted from the center of mass coordinates, with the result displayed in Figure 6.10a.

The center of mass for the pointing of the electron beams generated by the Gaussian and vortex beams is also shown. It can be seen that the center of mass for both beams is close to the reference point, although a larger spread is visible for the vortex beam. The shaded area around the center of mass marker indicated the standard deviation of the individual shots to the center of mass result. Here, the tighter grouping of the results for the Gaussian beam becomes apparent. Nonetheless, in the context of LENS, the pointing of both beams is sufficiently stable since the distance that the beam needs to travel from the target to the converter is typically less than $10\,\mathrm{cm}$.

In Figure 6.10b a comparison between the Gaussian and vortex beams is given. The plot shows a trend that for the same laser energy, the vortex beam is capable of accelerating equal or higher charges. Note, according to Equation 2.51, the beam charge Q_{beam} is probational to $a_0^{(3/2)}$. Thus, the difference in charge

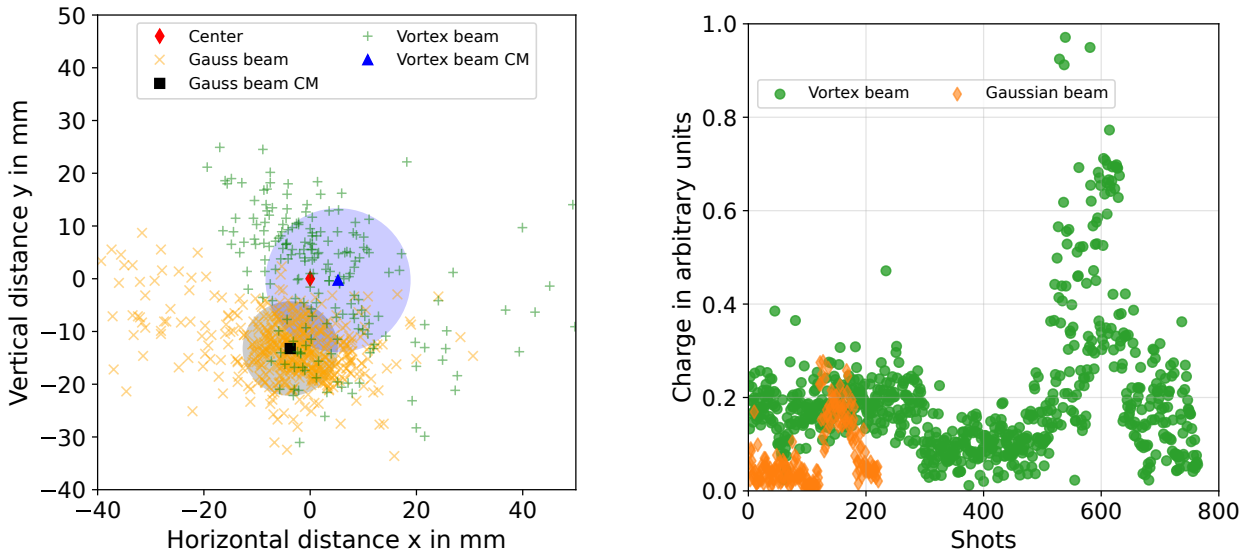

(a) Pointing stability of the electron beam.

(b) Charge of the electron beam.

Figure 6.10.: Resulting pointing and charge of electron beams generated by a Gaussian and donut shaped focus profile. (a) shows the position distribution where the electron beam's center of mass (CM) intersected the scintillator in relation to a defined, central reference position, after propagating over a distance of $235.5\,\mathrm{cm}$. (b) shows the charge of the electron beams, based on the total signal strength generated by the scintillating screen.

might be even higher when matching the values for a_0 for both the Gaussian and vortex beam instead of the pulse energy, as was the case during the experimental measurement. If the electron energy E_{mean} is not significantly reduced for the vortex beam, this method can be used to boost the neutron source strength. A recent study suggests that a vortex beam should not negatively impact the electron energy (Ghasemi et al. 2024). However, more research into this area is needed to draw definitive conclusions and quantify the influence of the vortex beam on electron acceleration.

6.4. LENS as a source of (epi-) thermal neutron beams

One promising prospect for laser-accelerated electron-based neutron sources is the generation of thermal and epi-thermal neutron beams. Neutrons generated via photo-nuclear reactions have a lower average energy compared to LIoNS, as is demonstrated in Table 6.3. With lower average energies, neutrons need to undergo less scattering events to thermalize. Additionally, neutrons with lower energy have shorter mean free path lengths inside matter, which increases the chance of scattering. In combination with the high conversion efficiency per electron, a LENS can serve as the foundation of a compact thermal and epi-thermal neutron source. This section compares moderation efficiency between a LENS and a LIoNS, utilizing the moderator design used during the experimental campaign at PHELIX. Details on the moderator can be found in (Zimmer 2020; Zimmer, Scheuren, Kleinschmidt, et al. 2022) and the target-moderator assembly is displayed in Figure 6.11a. The converter (purple geometry) is placed inside the moderator (light blue geometry) to more efficiently couple the generated neutrons to the moderator.

The electron spectrum for the LENS is based on Table 6.3 and the shape of the proton spectrum generated by the PHELIX laser is obtained from (Wagner 2014, Figure 5.15), with the proton cut-off energy adjusted

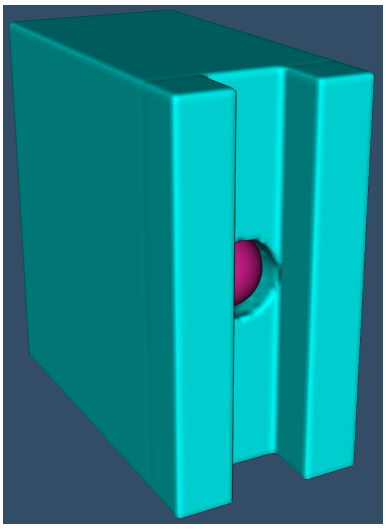

(a) Moderator design.

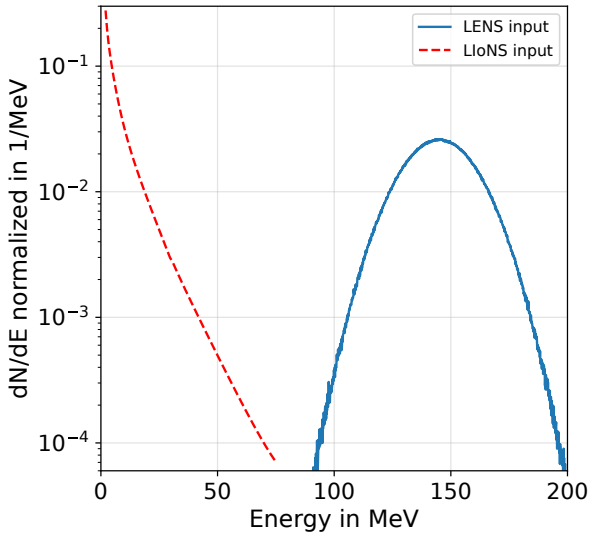

(b) Input source spectra.

Figure 6.11.: (a) Moderator design employed during the 2020 PHELIX experimental campaign discussed in section 5.1. The image shows the geometric implementation in the Monte Carlo simulations for evaluating the LENS performance. Light blue represents areas made from polyethylene, whereas magenta represents tungsten. (b) Input spectra for both protons (red, dashed line) and electrons (blue line) used to generate neutrons in their respective conversion targets, as discussed in the text.

to 70 MeV. The respective input spectra are shown in Figure 6.11b. The converter used for the proton beam is a LiF disc with a radius of 2 cm and a thickness of 2 cm. A tungsten sphere with a radius of 2 cm is used for the electron beam.

The primary generated neutron spectra that leave the catcher can be seen in Figure 6.12a. The LENS spectrum peaks around 0.8 MeV and has an average neutron energy of 1.1 eV. In contrast, the LIoNS spectrum "peaks" around 4 MeV and has an average energy of 6.4 MeV. The large difference in conversion efficiency per source particle is apparent, reaching up to two orders of magnitude between 0.5 and 2 MeV. This difference in conversion efficiency needs to be taken into account for a proper comparison between the moderation efficiency achieved by the LENS and LIoNS. To do so the results of the LIoNS are scaled to the same primary neutron conversion efficiency using a scaling factor k_{scale}. The factor is calculated via $k_{\text{scale}} = \eta_{\text{LENS}}/\eta_{\text{LIoNS}}$, where η_i is the respective conversion efficiency per incoming source particle. Afterwards, the moderated neutron spectrum for the LIoNS is multiplied by k_{scale}. In Figure 6.12b the scaled moderated neutron spectra, tallied at $90°$ relative to the incoming electron/proton beam, is displayed. A clear increase in the neutron number for both the thermal and epi-thermal energy region can be seen for LENS compared to LIoNS. Calculating the amount of neutrons contained in the fast (n_f) and thermal (n_t) neutron peaks and taking the quotient n_t/n_f shows an increase in thermalized neutrons of factor 2.6 when using a LENS instead of a LIoNS. This means that for the LENS, a higher percentage of neutrons thermalize for the same moderator, i.e. the moderation efficiency is increased for the electron-based source. In a similar way, the epi-thermal neutron flux between 1 and 100 eV is increased by a factor of 2.5 for the LENS. The mean free path inside PE for 1.1 MeV neutrons is 2.4 cm, whereas it is 6.9 cm for 6.4 MeV. The reduction in mean free path is the dominant cause of the increased moderation efficiency. The average number of collisions needed for a

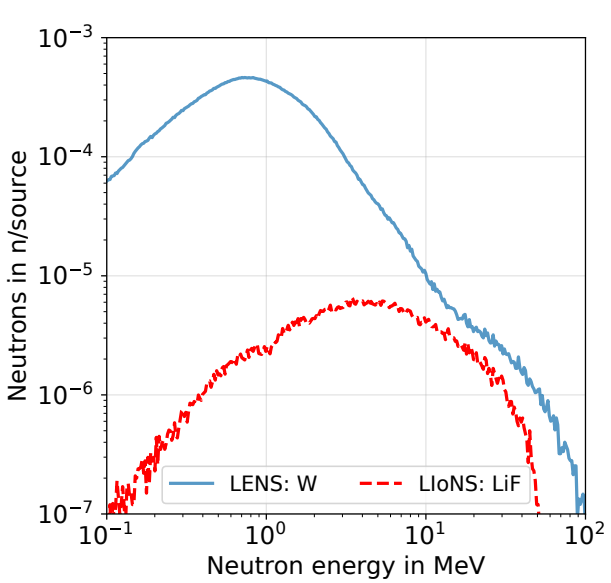

(a) Primary neutron spectra.

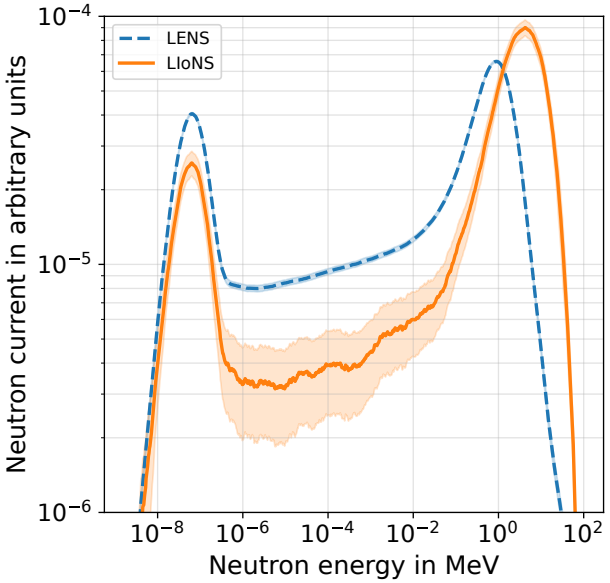

(b) Moderated neutron spectra.

Figure 6.12.: (a) Neutron spectra leaving the catcher. (b) Moderated neutron spectra using the moderator design shown in (a). The spectrum generated by the LIoNS is normalized to the conversion efficiency of the LENS to allow for better comparability. The shaded areas represent the statistical uncertainty of the Monte Carlo simulations.

neutron to thermalize also plays a minor role with regard to the moderation efficiency. Utilizing the average neutron energies, an average of approximately 13 to 16 collisions are required to reach the 1 to $10\,\mathrm{eV}$ range from $1.1\,\mathrm{MeV}$. For comparison, the spectrum generated by the LIoNS with an average neutron energy of $6.4\,\mathrm{MeV}$ requires an average of 15 to 18 collisions to reach the same energies. For the LENS, the efficiency to obtain neutrons with energies between 1 and $100\,\mathrm{eV}$ is $(1.52 \pm 0.01) \times 10^{-3}\,\mathrm{n/e^-}$. In contrast, the efficiency per proton is $(1.24 \pm 0.04) \times 10^{-5}\,\mathrm{n/p^+}$, decreasing two orders of magnitude per source particle. Using the electron beam charge from Table 6.3, a total neutron source strength between 1 and $100\,\mathrm{eV}$ of $10^8\,\mathrm{n/s}$ can be achieved by the LENS.

The simulation results presented above highlight the potential of a LENS as a source of moderated neutrons. The neutron moderator used in the above simulations was optimized for an experimental campaign at a LIoNS (see section 5.1). Therefore, the moderated neutron flux can be further increased by optimizing the moderator to the specific characteristics of a LENS, which should be the topic of future research. This section also shows that LENS and LIoNS are not mutually exclusive. While LENS have an advantage with respect to average neutron fluxes, LIoNS provide much higher instantaneous fluxes. Furthermore, differences in the emitted neutron spectra demonstrate that LENS are more suitable for applications requiring moderated neutron beams, whereas LIoNS should be used when requiring fast neutrons.

7. Summary and Conclusion

The goal of this thesis was to comprehensively characterize a laser-driven neutron sources, based on the results of an experimental campaign conducted at the DRACO laser system. Insight gained from the characterization can be used to aid the design of neutron beamlines at a (future) laser facility that is solely dedicated to neutron production. Using in-depth Monte Carlo simulations, the influence of secondary radiation source terms, which originate as a by-product of the TNSA mechanism, on the neutron production and the performance of the detectors was quantified. Furthermore, a mix of measurements and simulations investigated the viability of laser-driven neutron sources based on laser systems that deliver less than $5\,\mathrm{J}$ per pulse. It could be shown that electron beam accelerated via LWFA are highly promising, as the acceleration requires low laser energies, while still providing high neutron conversion efficiencies.

Additionally, a method for analyzing the results of bubble detector measurements was developed, which results in more accurate neutron fluence measurements at laser-driven neutron sources. Finally, energy-selective neutron imaging utilizing fast and thermal neutrons was investigated at the PHELIX laser system. Using thermal neutron beams, a proof-of-principle demonstration of neutron resonance imaging could be achieved for the first time at a laser-driven neutron source. Energy-selective fast neutron imaging was also successfully demonstrated, although the quality of the results were somewhat limited. Based on these results, a set of recommendations was given that should improve future experiments' results.

During the analysis of the DRACO campaign, a thorough examination of the neutron fluences measured by bubble detectors was conducted. It became apparent that these measurements did not match the neutron fluences observed by other detectors and Monte Carlo simulations. This discrepancy led to the development of an adapted analysis method, which resulted in reduced neutron fluences by 15 to $40\,\%$, compared to methods presented in (D. Jung, Falk, et al. 2013; Kleinschmidt et al. 2018). The results of the developed method are in good agreement with Monte Carlo simulations conducted for the DRACO campaign, where deviations of less than 10 to $20\,\%$ were observed for most cases. However, due to this thesis being close to finalization at the time of conceptualization of this method, extensive validation measurements could not be conducted yet. A comprehensive comparison and validation campaign is planned for the future. This includes using different neutron sources, such as ^{252}Cf and AmBe (americium beryllium) for calibration. The method has been submitted for publication and is currently under review at Review of Scientific Instruments (Scheuren, Millan-Callado, et al. 2024).

The DRACO experimental campaign served as the basis for the comprehensive characterization of an (ion-based) laser-driven neutron source. This required an elaborate experimental setup, which allowed for measuring all relevant source terms for each shot. Namely, these source terms were the forward and backward propagating proton beam, the forward propagating carbon beam, as well as the emitted electrons and γ-rays. Of the listed source terms, only the forward proton beam is the desired primary source term, with the rest being secondary terms that introduce background noise to measurements. Based on detailed Monte Carlo simulations, it could be determined that up to 10 to $25\,\%$ of the neutrons arriving at the detectors originated from secondary source terms, such as the backward proton or carbon beam. Which secondary source term is dominant depends on the catcher that was used. Neutron generated from the carbon beam

was the dominant secondary contribution for LiF, whereas it was neutron generation from the electron source term for the Cu catcher.

Furthermore, the corresponding resolution functions quantified and summarized the influence of neutron scattering for the detectors/neutron beamlines of the experiment. The resolution functions indicated that up to 20 to $90\,\%$ of neutrons that arrive at the detector position are influenced by scattering. For these neutrons, the correlation between time-of-flight and their energy is at least partially lost, making it challenging to conduct neutron measurements that require energy determination. Monte Carlo simulations showed that the detector shielding significantly influences the measured neutron signals at the detector position. The commonly used method of fixing bubble detectors directly to the target chamber is responsible for the dominant scattering contribution to bubble detector measurements. Therefore, from now on, bubble detectors should be placed free-standing within the target area, thereby improving the accuracy and comparability of neutron fluence measurements. The significant scattering contribution found for the bubble detector measurements raises questions on the comparability of neutron fluences measured by bubble detectors at different facilities, as the scattering background is highly geometry dependent.

The last point of interest investigated during the DRACO campaigns concerned the scalability of laser-driven neutron sources. This investigation was conducted for laser pulses utilizing the full energy that DRACO can deliver (17 to $20\,$J on target) and pulses that delivered around one-tenth of the maximum possible energy (2 to $3\,$J) on target. From these results, questions arose concerning the competitiveness of LDNS with respect to achievable neutron fluxes. Using the fluence of $(4.9 \pm 0.5) \times 10^7\,\mathrm{n/sr/shot}$ obtained from the LiF catcher for the full laser energy shots and assuming isotropic neutron emission, a total neutron fluence around $\sim 6 \times 10^8\,\mathrm{n/shot}$ is obtained. In order to achieve the same source flux as other compact, conventional neutron sources, such as RANS and RANS-II (Otake 2020; Kobayashi et al. 2021), a repetition of around 0.1 to $1\,$kHz is required. Moreover, it was shown that the required repetition rate can be approximately halved when using deuterated targets due to the additional neutron production from deuterium. Reducing the laser energy resulted in neutron fluences of $(1.6 \pm 0.8) \times 10^6\,\mathrm{n/sr/shot}$ for deuterated targets, resulting in a total neutron production of around $2 \times 10^7\,\mathrm{n/shot}$. Thus requiring a repetition rate of around 1 to $10\,$kHz to be competitive with RANS-II. These energy and repetition rate requirements correspond to an average laser power of approximately 3 to $30\,$kW, which is beyond the capabilities of current-day ultra-short pulse laser technologies for the required pulse energies. Additionally, the high repetition rate in itself brings a lot of challenges with it in regard to targetry, see for example (Treffert 2023), while not all neutron applications are compatible with high repetition rates.

The PHELIX laser system was used to conduct measurements to determine the feasibility of energy-resolved neutron imaging. The measurements were conducted using both thermal and fast neutron beams. A moderator was used to reduce the energy of the generated neutrons to obtain thermal neutron beams. Utilizing this thermal neutron beam, the feasibility of neutron resonance imaging could be demonstrated for the first time at a laser-driven neutron source. This was done by measuring the neutron fluence's energy dependency for a detector partially covered by ^{113}Cd. Depending on the neutron energy, the Cd sample could be resolved due to its large absorption cross section. The results were published as part of (Zimmer, Scheuren, Kleinschmidt, et al. 2022). The signal-to-noise ratio and the energy resolution limited the resolution of the measurements. These issues can be addressed by optimizing the experimental setup to the requirements of (resonance) imaging, for example, by using an appropriate collimation system. Energy-selective fast neutron imaging could also be demonstrated during a separate beamtime at the PHELIX laser. However, the results are limited due to inadequate collimation of the neutron beam, disruptive contributions from secondary sources (most likely neutron production by the focusing parabola) and low neutron statistics.

To final chapter of this thesis discussed a potential pathway to the miniaturization of laser-driven neutron

sources. The miniaturization can be achieved by reducing the laser energy to $\lesssim 1\,\mathrm{J}$ while achieving high conversion efficiencies. The best way to achieve these goals is by employing electron beams using LWFA. Depending on the energy of the electron beam, conversion efficiencies up to $0.25\,\mathrm{n/e^-}$ can be achieved. Using the phenomenological description of LWFA provided by (W. Lu et al. 2007), the neutron flux of a $1\,\mathrm{kW}$ laser system could be calculated. The results show that such a source should be competitive with RANS, generating an expected source strength of around $7 \times 10^{10}\,\mathrm{n/s}$.

For future works, it is important that the presented method for converting bubble detector measurements to neutron fluences is validated and, if needed, adjusted. Furthermore, LDNS must be investigated thoroughly regarding radiation protection requirements and activation expected from their operation. Concerning the characterization of LDNS, it is important to investigate the influence of the backward carbon ion beam on the neutron source, following the methods discussed in this work. Additionally, the influence of deuterium ions on the resolution function needs to be investigated. Lastly, the community should focus their effort on these sources, considering their respective strengths. For example, for generating a moderated neutron beam, it makes sense to utilize electron-based LDNS as long as the measurement does not require high instantaneous fluxes. Ion-based LDNS should primarily be used for applications that require fast neutrons, as the neutron spectrum generated by ion-induced reactions is more suitable for these applications.

Bibliography

Bouguer, P. (1729). *Essai d'optique sur la gradation de la lumière*. Claude Jombert.

Lambert, J. H. (1760). *Photometria sive de mensura et gradibus luminis, colorum et umbrae*. sumptibus vidvae E. Klett, typis CP Detleffsen.

Beer (1852). "Bestimmung der Absorption des rothen Lichts in farbigen Flüssigkeiten". In: *Annalen der Physik* 162.5, pp. 78–88.

Bohr, N. (1913). "II. On the theory of the decrease of velocity of moving electrified particles on passing through matter". In: *The London, Edinburgh, and Dublin Philosophical Magazine and Journal of Science* 25.145, pp. 10–31.

Duane, W. (1915). "Proceedings of the American Physical Society. On X-ray Wave-Lengths". In: *Phys. Rev.* 6, p. 166.

Debye, P. and E. Hückel (1923). "The theory of electrolytes. I. Freezing point depres-sion and related phenomena [Zur Theorie der Elektrolyte. I. Gefrierpunktserniedrigung und verwandte Erscheinungen]". In: *Physikalische Zeitschrift* 24, pp. 185–206.

Kramers, H. A. (1923). "XCIII. On the theory of X-ray absorption and of the continuous X-ray spectrum". In: *The London, Edinburgh, and Dublin Philosophical Magazine and Journal of Science* 46.275, pp. 836–871.

Bethe, H. (1930). "Zur Theorie des durchgangs schneller korpuskularstrahlen durch Materie". In: *Annalen der Physik* 397.3, pp. 325–400.

Sommerfeld, A. (1931). "Über die beugung und bremsung der elektronen". In: *Annalen der Physik* 403.3, pp. 257–330.

Chadwick, J. (1932a). "Possible existence of a neutron". In: *Nature* 129.3252, pp. 312–312.

– (1932b). "The existence of a neutron". In: *Proceedings of the Royal Society of London. Series A, Containing Papers of a Mathematical and Physical Character* 136.830, pp. 692–708.

Bloch, F. (1933). "Zur Bremsung rasch bewegter Teilchen beim Durchgang durch Materie". In: *Annalen der Physik* 408.3, pp. 285–320.

Haxby, R., W. Shoupp, W. Stephens, and W. Wells (1941). "Photo-fission of uranium and thorium". In: *Physical Review* 59.1, p. 57.

Baldwin, G. and G. Klaiber (1947). "Photo-fission in heavy elements". In: *Physical Review* 71.1, p. 3.

Serber, R. (1947). "The production of high energy neutrons by stripping". In: *Physical Review* 72.11, p. 1008.

Birks, J. (1951). "The specific fluorescence of anthracene and other organic materials". In: *Physical Review* 84.2, p. 364.

Birks, J. B. (1951). "Scintillations from organic crystals: specific fluorescence and relative response to different radiations". In: *Proceedings of the Physical Society. Section A* 64.10, p. 874.

Chou, C. (1952a). "Saturation effect of plastic scintillators". In: *Physical Review* 87.5, p. 903.

– (1952b). "The nature of the saturation effect of fluorescent scintillators". In: *Physical Review* 87.5, p. 904.

Watt, B. (1952). "Energy spectrum of neutrons from thermal fission of U 235". In: *Physical Review* 87.6, p. 1037.

Akhiezer, A. I. and R. Polovin (1956). "Theory of wave motion of an electron plasma". In: *Soviet Phys. JETP* 3.

Butler, S. (1957). "Direct nuclear reactions". In: *Physical Review* 106.2, p. 272.

Levinger, J. (1957). “Migdal’s and Khokhlov’s Calculations of the Nuclear Photoeffect”. In: *Physical Review* 107.2, p. 554.
Barber, W. and W. George (1959). “Neutron yields from targets bombarded by electrons”. In: *Physical review* 116.6, p. 1551.
Gooding, T. and H. Pugh (1960). “The response of plastic scintillators to high-energy particles”. In: *Nuclear Instruments and Methods* 7.2, pp. 189–192.
Levinger, J. S. (1960). “Nuclear photo-disintegration”. In: *(No Title)*.
Hamburger, E., B. Cohen, and R. Price (1961). “Low-Energy Protons Produced in the Deuteron Bombardment of Nuclei”. In: *Physical Review* 121.4, p. 1143.
Kazi, A. H., N. C. Rasmussen, and H. Mark (1961). “Measurement of the Deuteron Binding Energy using a Bent-Crystal Spectrograph”. In: *Physical Review* 123.4, p. 1310.
Dawson, J. and C. Oberman (1962). “High-frequency conductivity and the emission and absorption coefficients of a fully ionized plasma”. In: *The Physics of Fluids* 5.5, pp. 517–524.
Griffin, J. J. (1966). “Statistical model of intermediate structure”. In: *Physical review letters* 17.9, p. 478.
Alsmiller Jr, R. and H. Moran (1967). “Photoneutron production from 34-and 100-Mev electrons in thick uranium targets”. In: *Nuclear Instruments and Methods* 51.2, pp. 339–340.
Gayther, D. and P. Goode (1967). “Neutron energy spectra and angular distributions from targets bombarded by 45 MeV electrons”. In: *Journal of Nuclear Energy* 21.9, pp. 733–747.
Smith, D., R. Polk, and T. Miller (1968). “Measurement of the response of several organic scintillators to electrons, protons and deuterons”. In: *Nuclear Instruments and Methods* 64.2, pp. 157–166.
Ingle, R., F. Gillespie, and L. Weston (1970). “Fast Fission Chamber Amplifier-Discriminator System”. In: *Review of Scientific Instruments* 41.11, pp. 1539–1543.
Litvak, A. (1970). “Finite-amplitude wave beams in a magnetoactive plasma”. In: *Sov. Phys. JETP* 30.344, p. 166.
Coffey, T. (1971). “Breaking of large amplitude plasma oscillations”. In: *The Physics of Fluids* 14.7, pp. 1402–1406.
Lapp, R. and A. Howard (1972). *Nuclear Radiation Physics*. Prentice-Hall.
Madey, R. and F. Waterman (1972). “The response of NE-228 liquid scintillator to 3.5, 5.8 and 10.5 MeV protons”. In: *Nuclear Instruments and Methods* 104.2, pp. 253–256.
Max, C. E., J. Arons, and A. B. Langdon (1974). “Self-modulation and self-focusing of electromagnetic waves in plasmas”. In: *Physical Review Letters* 33.4, p. 209.
Carter, L. L. and E. D. Cashwell (1975). *Particle-transport simulation with the Monte Carlo method*. Tech. rep. Los Alamos National Lab.(LANL), Los Alamos, NM (United States).
Catto, P. and R. M. More (1977). “Sheath inverse bremsstrahlung in laser produced plasmas”. In: *The Physics of Fluids* 20.4, pp. 704–705.
Bondarenko, L., V. Kurguzov, Y. A. Prokof’ev, E. Rogov, and P. Spivak (1978). “Measurement of the neutron half-life”. In: *JETP Lett.(USSR)(Engl. Transl.);(United States)* 28.5.
Decoster, A. (1978). “Nonlinear travelling waves in a homogeneous cold collisionless plasma”. In: *Physics Reports* 47.5, pp. 285–422.
Madey, R., F. M. Waterman, A. R. Baldwin, J. N. Knudson, J. Carlson, and J. Rapaport (1978). “The response of NE-228A, NE-228, NE-224, and NE-102 scintillators to protons from 2.43 to 19.55 MeV”. In: *Nuclear Instruments and Methods* 151.3, pp. 445–450.
Del Pizzo, V. and B. Luther-Davies (1979). “Evidence of filamentation (self-focusing) of a laser beam propagating in a laser-produced aluminium plasma”. In: *Journal of Physics D: Applied Physics* 12.8, p. 1261.
Swanson, W. P. (1979). “Radiological safety aspects of the operation of electron linear accelerators”. In: *IAEA Technical Report Series No. 188*.
Tajima, T. and J. M. Dawson (1979). “Laser electron accelerator”. In: *Physical review letters* 43.4, p. 267.

Wiza, J. L. et al. (1979). “Microchannel plate detectors”. In: *Nucl. Instrum. Methods* 162.1-3, pp. 587–601.
Zankl, G., J. Strachan, R. Lewis, W. Pettus, and J. Schmotzer (1981). “Neutron flux measurements around the Princeton large tokamak”. In: *Nuclear Instruments and Methods in Physics Research* 185.1-3, pp. 321–329.
Dietze, G. and H. Klein (1982). *NRESP4 and NEFF4-Monte Carlo codes for the calculation of neutron response functions and detection efficiencies for NE 213 scintillation detectors*. Tech. rep. Physikalisch-Technische Bundesanstalt.
Lamb, B. and G. Morales (1983). “Ponderomotive effects in nonneutral plasmas”. In: *The Physics of fluids* 26.12, pp. 3488–3496.
Booth, T. E. (1985). *Sample problem for variance reduction in MCNP*. Tech. rep. Los Alamos National Lab.(LANL), NM (USA).
Kruer, W. L. and K. Estabrook (1985). “J× B heating by very intense laser light”. In: *The Physics of fluids* 28.1, pp. 430–432.
Noble, R. J. (1985). “Plasma-wave generation in the beat-wave accelerator”. In: *Physical Review A* 32.1, p. 460.
Brunel, F. (1987). “Not-so-resonant, resonant absorption”. In: *Physical review letters* 59.1, p. 52.
Sprangle, P., C.-M. Tang, and E. Esarey (1987). “Relativistic self-focusing of short-pulse radiation beams in plasmas”. In: *IEEE transactions on plasma science* 15.2, pp. 145–153.
Sun, G.-Z., E. Ott, Y. Lee, and P. Guzdar (1987). “Self-focusing of short intense pulses in plasmas”. In: *The Physics of fluids* 30.2, pp. 526–532.
Dickens, J. (1988). *SCINFUL: A Monte Carlo based computer program to determine a scintillator full energy response to neutron detection for E/sub n/between 0. 1 and 80 MeV: Program development and comparisons of program predictions with experimental data*. Tech. rep. Oak Ridge National Lab.(ORNL), Oak Ridge, TN (United States).
Katsouleas, T. and W. Mori (1988). “Wave-breaking amplitude of relativistic oscillations in a thermal plasma”. In: *Physical review letters* 61.1, p. 90.
Sprangle, P., G. Joyce, E. Esarey, and A. Ting (1988). “Laser wakefield acceleration and relativstic optical guiding”. In: *AIP Conference Proceedings*. Vol. 175. American Institute of Physics, pp. 231–239.
Wilks, S., W. Kruer, M. Tabak, and A. Langdon (1992). “Absorption of ultra-intense laser pulses”. In: *Physical review letters* 69.9, p. 1383.
Buckner, M., R. Noulty, and T. Cousins (Aug. 1994). “The Effect of Temperature on the Neutron Energy Thresholds of Bubble Technology Industries’ Bubble Detector Spectrometer”. In: *Radiation Protection Dosimetry* 55.1, pp. 23–30. ISSN: 0144-8420. DOI: 10.1093/oxfordjournals.rpd.a082371.
Bauer, D., P. Mulser, and W.-H. Steeb (1995). “Relativistic ponderomotive force, uphill acceleration, and transition to chaos”. In: *Physical review letters* 75.25, p. 4622.
Modena, A., Z. Najmudin, A. Dangor, C. Clayton, K. Marsh, C. Joshi, V. Malka, C. Darrow, C. Danson, D. Neely, et al. (1995). “Electron acceleration from the breaking of relativistic plasma waves”. In: *nature* 377.6550, pp. 606–608.
Bertsch, G., P.-G. Reinhard, and E. Suraud (1996). “Particle evaporation from semiclassical dynamics”. In: *Physical Review C* 53.3, p. 1440.
O’Rielly, G., N. Kolb, and R. Pywell (1996). “The response of plastic scintillator to protons and deuterons”. In: *Nuclear Instruments and Methods in Physics Research Section A: Accelerators, Spectrometers, Detectors and Associated Equipment* 368.3, pp. 745–749.
Balashov, V. V. and G. Pontecorvo (1997). *Interaction of particles and radiation with matter*. Vol. 68. Springer.
Ing, H., R. Noulty, and T. McLean (1997). “Bubble detectors—A maturing technology”. In: *Radiation Measurements* 27.1, pp. 1–11. ISSN: 1350-4487. DOI: 10.1016/s1350-4487(96)00156-4.
Mori, W. (1997). “The physics of the nonlinear optics of plasmas at relativistic intensities for short-pulse lasers”. In: *IEEE Journal of Quantum Electronics* 33.11, pp. 1942–1953.

Startsev, E. and C. McKinstrie (1997). “Multiple scale derivation of the relativistic ponderomotive force”. In: *Physical Review E* 55.6, p. 7527.
Key, M., M. Cable, T. Cowan, K. Estabrook, B. Hammel, S. Hatchett, E. Henry, D. Hinkel, J. Kilkenny, J. Koch, et al. (1998). “Hot electron production and heating by hot electrons in fast ignitor research”. In: *Physics of plasmas* 5.5, pp. 1966–1972.
Vshivkov, V. A., N. M. Naumova, F. Pegoraro, and S. Bulanov (1998). “Nonlinear electrodynamics of the interaction of ultra-intense laser pulses with a thin foil”. In: *Physics of Plasmas* 5.7, pp. 2727–2741.
Disdier, L., J. Garconnet, G. Malka, and J. Miquel (1999). “Fast neutron emission from a high-energy ion beam produced by a high-intensity subpicosecond laser pulse”. In: *Physical review letters* 82.7, p. 1454.
Jallu, F., A. Lyoussi, E. Payan, H. Recroix, A. Mariani, G. Nurdin, A. Buisson, and J. Allano (1999). “Photoneutron production in tungsten, praseodymium, copper and beryllium by using high energy electron linear accelerator”. In: *Nuclear Instruments and Methods in Physics Research Section B: Beam Interactions with Materials and Atoms* 155.4, pp. 373–381.
Koning, A., J. Akkermans, and A. Gandini (1999). “Pre-equilibrium nuclear reactions: an introduction to classical and quantum-mechanical models”. In: *Proceedings of the Workshop: Nuclear reaction data and nuclear reactors*. World Scientific Singapore, pp. 143–158.
Snavely, R., M. Key, S. Hatchett, T. Cowan, M. Roth, T. Phillips, M. Stoyer, E. Henry, T. Sangster, M. Singh, et al. (2000). “Intense high-energy proton beams from petawatt-laser irradiation of solids”. In: *Physical review letters* 85.14, p. 2945.
Ing, H. (2001). “Neutron measurements using bubble detectors — terrestrial and space”. In: *Radiation Measurements* 33.3, pp. 275–286. ISSN: 1350-4487. DOI: 10.1016/s1350-4487(00)00154-2.
Lamarsh, J. R., A. J. Baratta, et al. (2001). *Introduction to nuclear engineering*. Vol. 3. Prentice hall Upper Saddle River, NJ.
Parfenova, Y. L. and M. Zhukov (2001). “Study of deuteron breakup in light targets at intermediate energies”. In: *The European Physical Journal A-Hadrons and Nuclei* 12.2, pp. 191–197.
Wilks, S., A. Langdon, T. Cowan, M. Roth, M. Singh, S. Hatchett, M. Key, D. Pennington, A. MacKinnon, and R. Snavely (2001). “Energetic proton generation in ultra-intense laser–solid interactions”. In: *Physics of plasmas* 8.2, pp. 542–549.
Eliezer, S. (2002). *The interaction of high-power lasers with plasmas*. CRC press.
Gläser, W. (2002). “The new neutron source FRM II”. In: *Applied Physics A* 74, s23–s29.
Malka, V., S. Fritzler, E. Lefebvre, M.-M. Aleonard, F. Burgy, J.-P. Chambaret, J.-F. Chemin, K. Krushelnick, G. Malka, S. Mangles, et al. (2002). “Electron acceleration by a wake field forced by an intense ultrashort laser pulse”. In: *Science* 298.5598, pp. 1596–1600.
Pukhov, A. and J. Meyer-ter-Vehn (2002). “Laser wake field acceleration: the highly non-linear broken-wave regime”. In: *Applied Physics B* 74, pp. 355–361.
Pukhov, A. (2002). “Strong field interaction of laser radiation”. In: *Reports on progress in Physics* 66.1, p. 47.
Buffler, A. (2004). “Contraband detection with fast neutrons”. In: *Radiation Physics and Chemistry* 71.3-4, pp. 853–861.
Kostyukov, I., A. Pukhov, and S. Kiselev (2004). “Phenomenological theory of laser-plasma interaction in “bubble” regime”. In: *Physics of Plasmas* 11.11, pp. 5256–5264.
Lancaster, K., S. Karsch, H. Habara, F. Beg, E. Clark, R. Freeman, M. Key, J. King, R. Kodama, K. Krushelnick, et al. (2004). “Characterization of Li 7 (p, n) 7 Be neutron yields from laser produced ion beams for fast neutron radiography”. In: *Physics of plasmas* 11.7, pp. 3404–3408.
Gibbon, P. (2005). *Short pulse laser interactions with matter: an introduction*. Imperil College Press.
Hirayama, H., Y. Namito, W. R. Nelson, A. F. Bielajew, S. J. Wilderman, and U. Michigan (2005). *The EGS5 code system*. Tech. rep. United States. Department of Energy.

Huang, W., Q. Li, and Y. Lin (2005). “Calculation of photoneutrons produced in the targets of electron linear accelerators for radiography and radiotherapy applications”. In: *Nuclear Instruments and Methods in Physics Research Section B: Beam Interactions with Materials and Atoms* 229.3-4, pp. 339–347.

Carron, N. J. (2006). *An introduction to the passage of energetic particles through matter*. Taylor & Francis.

Doré, D., J. David, M. Giacri, J. Laborie, X. Ledoux, M. Petit, D. Ridikas, and A. Van Lauwe (2006). “Delayed neutron yields and spectra from photofission of actinides with bremsstrahlung photons below 20 MeV.” In: *Journal of Physics: Conference Series*. Vol. 41. IOP Publishing, p. 241.

Lisowski, P. W. and K. F. Schoenberg (2006). “The Los Alamos neutron science center”. In: *Nuclear Instruments and Methods in Physics Research Section A: Accelerators, Spectrometers, Detectors and Associated Equipment* 562.2, pp. 910–914.

Mangles, S. P., A. G. R. Thomas, M. Kaluza, O. Lundh, F. Lindau, A. Persson, F. Tsung, Z. Najmudin, W. B. Mori, C.-G. Wahlström, et al. (2006). “Laser-wakefield acceleration of monoenergetic electron beams in the first plasma-wave period”. In: *Physical review letters* 96.21, p. 215001.

Parise, J. B. (2006). “Introduction to neutron properties and applications”. In: *Reviews in Mineralogy and Geochemistry* 63.1, pp. 1–25.

Satoh, D., T. Sato, N. Shigyo, and K. Ishibashi (2006). “SCINFUL-QMD: Monte Carlo based computer code to calculate response function and detection efficiency of a liquid organic scintillator for neutron energies up to 3 GeV”. In: *JAEA-Data/Code* 23, p. 2006.

Yin, L., B. Albright, B. Hegelich, and J. Fernández (2006). “GeV laser ion acceleration from ultrathin targets: The laser break-out afterburner”. In: *Laser and Particle Beams* 24.2, pp. 291–298.

Bethge, K., G. Walter, and B. Wiedemann (2007). *Kernphysik: Eine Einführung*. Springer-Verlag.

Hamamatsu Photonics, K. (2007). “Photomultiplier tubes: Basics and applications”. In: *Edition 3a* 310.

Iida, K., A. Kohama, and K. Oyamatsu (2007). “Formula for proton–nucleus reaction cross section at intermediate energies and its application”. In: *Journal of the Physical Society of Japan* 76.4, p. 044201.

Lu, W., M. Tzoufras, C. Joshi, F. Tsung, W. Mori, J. Vieira, R. Fonseca, and L. Silva (2007). “Generating multi-GeV electron bunches using single stage laser wakefield acceleration in a 3D nonlinear regime”. In: *Physical Review Special Topics-Accelerators and Beams* 10.6, p. 061301.

Olsher, R. H., T. D. McLean, M. W. Mallett, L. L. Romero, R. T. Devine, and J. M. Hoffman (2007). “High-energy response of passive dosemeters in use at LANL”. In: *Radiation protection dosimetry* 126.1-4, pp. 326–332.

Petwal, V., V. Senecha, K. Subbaiah, H. Soni, and S. Kotaiah (2007). “Optimization studies of photo-neutron production in high-Z metallic targets using high energy electron beam for ADS and transmutation”. In: *Pramana* 68, pp. 235–241.

Stacey, W. M. (2007). *Nuclear reactor physics*. 2. ed., completely revised and enl. ISBN: 978-3527406791. Weinheim: Wiley-VCH Verlag GmbH & Co. KGaA.

Hofmann, H. (2008). *The physics of warm nuclei: with analogies to mesoscopic systems*. Vol. 25. OUP Oxford.

IAEA, N. I. (2008). “A Non-Destructive Tool for Materials Testing”. In: *Vienna: IAEA, September*.

Imaging, N. (2008). “A Non-Destructive Tool for Materials Testing”. In: *Physics Section International Atomic Energy Agency*.

Osterhoff, J., A. Popp, Z. Major, B. Marx, T. Rowlands-Rees, M. Fuchs, M. Geissler, R. Hörlein, B. Hidding, S. Becker, et al. (2008). “Generation of stable, low-divergence electron beams by laser-wakefield acceleration in a steady-state-flow gas cell”. In: *Physical review letters* 101.8, p. 085002.

Anderson, I. S., R. L. McGreevy, and H. Z. Bilheux (2009). “Neutron imaging and applications”. In: *Springer Science+ Business Media* 200.2209, pp. 987–.

Mor, I., D. Vartsky, D. Bar, G. Feldman, M. Goldberg, D. Katz, E. Sayag, I. Shmueli, Y. Cohen, A. Tal, et al. (2009). “High spatial resolution fast-neutron imaging detectors for pulsed fast-neutron transmission spectroscopy”. In: *Journal of Instrumentation* 4.05, P05016.

Rinaldi, R., L. Liang, and H. Schober (2009). *Neutron applications in earth, energy, and environmental sciences*. Springer.
Ye, T., Y. Watanabe, and K. Ogata (2009). "Analysis of deuteron breakup reactions on Li 7 for energies up to 100 MeV". In: *Physical Review C* 80.1, p. 014604.
Bagnoud, V., B. Aurand, A. Blazevic, S. Borneis, C. Bruske, B. Ecker, U. Eisenbarth, J. Fils, A. Frank, E. Gaul, et al. (2010). "Commissioning and early experiments of the PHELIX facility". In: *Applied Physics B* 100, pp. 137–150.
Buffler, A. and J. Tickner (2010). "Detecting contraband using neutrons: challenges and future directions". In: *Radiation Measurements* 45.10, pp. 1186–1192.
Knoll, G. F. (2010). *Radiation detection and measurement*. John Wiley & Sons.
Zeil, K., S. Kraft, S. Bock, M. Bussmann, T. Cowan, T. Kluge, J. Metzkes, T. Richter, R. Sauerbrey, and U. Schramm (2010). "The scaling of proton energies in ultrashort pulse laser plasma acceleration". In: *New Journal of Physics* 12.4, p. 045015.
Cengel, Y. (2011). "Ghajar". In: *Heat and Mass Transfer-Fundamentals and applications. Mc Graw Hill, foruth edition*.
Jung, D., R. Hörlein, D. Kiefer, S. Letzring, D. Gautier, U. Schramm, C. Hübsch, R. Öhm, B. Albright, J. Fernandez, et al. (2011). "Development of a high resolution and high dispersion Thomson parabola". In: *Review of Scientific Instruments* 82.1.
Mourou, G. A., G. Korn, W. Sandner, and J. L. Collier (2011). "ELI-Extreme Light Infrastructure: Science and Technology with Ultra-Intense Lasers, Whitebook". In: *THOSS Media GmbH*.
Shibata, K., O. Iwamoto, T. Nakagawa, N. Iwamoto, A. Ichihara, S. Kunieda, S. Chiba, K. Furutaka, N. Otuka, T. Ohsawa, et al. (2011). "JENDL-4.0: a new library for nuclear science and engineering". In: *Journal of Nuclear Science and Technology* 48.1, pp. 1–30.
Stroth, U. (2011). *Plasmaphysik*. Springer.
Banerjee, S., N. D. Powers, V. Ramanathan, I. Ghebregziabher, K. J. Brown, C. Maharjan, S. Chen, A. Beck, E. Lefebvre, S. Y. Kalmykov, et al. (2012). "Generation of tunable, 100–800 MeV quasi-monoenergetic electron beams from a laser-wakefield accelerator in the blowout regime". In: *Physics of Plasmas* 19.5, p. 056703.
Griffiths, D. J. (2012). *Introduction to quantum mechanics*. Vol. 2nd Edition. Pearson Education Inc.
Leo, W. R. (2012). *Techniques for nuclear and particle physics experiments: a how-to approach*. Springer Science & Business Media.
Bermejo, F. J. and F. Sordo (2013). "Neutron sources". In: *Experimental Methods in the Physical Sciences* 44, pp. 137–243.
Beyer, R., E. Birgersson, Z. Elekes, A. Ferrari, E. Grosse, R. Hannaske, A. Junghans, T. Kögler, R. Massarczyk, A. Matić, et al. (2013). "Characterization of the neutron beam at nELBE". In: *Nuclear Instruments and Methods in Physics Research Section A: Accelerators, Spectrometers, Detectors and Associated Equipment* 723, pp. 151–162.
Birks, J. B. (2013). *The theory and practice of scintillation counting: International series of monographs in electronics and instrumentation*. Vol. 27. Elsevier.
Boudard, A., J. Cugnon, J.-C. David, S. Leray, and D. Mancusi (2013). "New potentialities of the Liège intranuclear cascade model for reactions induced by nucleons and light charged particles". In: *Physical Review C* 87.1, p. 014606.
Corde, S., K. T. Phuoc, G. Lambert, R. Fitour, V. Malka, A. Rousse, A. Beck, and E. Lefebvre (2013). "Femtosecond x rays from laser-plasma accelerators". In: *Reviews of Modern Physics* 85.1, p. 1.
He, Z.-H., A. Thomas, B. Beaurepaire, J. Nees, B. Hou, V. Malka, K. Krushelnick, and J. Faure (2013). "Electron diffraction using ultrafast electron bunches from a laser-wakefield accelerator at kHz repetition rate". In: *Applied Physics Letters* 102.6.

Jung, D., K. Falk, N. Guler, O. Deppert, M. Devlin, A. Favalli, J. Fernandez, D. Gautier, M. Geissel, R. Haight, et al. (2013). “Characterization of a novel, short pulse laser-driven neutron source”. In: *Physics of Plasmas* 20.5.

Macchi, A. (2013). *A superintense laser-plasma interaction theory primer*. Springer Science & Business Media.

Petrov, G., D. Higginson, J. Davis, T. B. Petrova, C. McGuffey, B. Qiao, and F. Beg (2013). “Generation of energetic (> 15 MeV) neutron beams from proton-and deuteron-driven nuclear reactions using short pulse lasers”. In: *Plasma Physics and Controlled Fusion* 55.10, p. 105009.

Roth, M., D. Jung, K. Falk, N. Guler, O. Deppert, M. Devlin, A. Favalli, J. Fernandez, D. Gautier, M. Geissel, et al. (2013). “Bright laser-driven neutron source based on the relativistic transparency of solids”. In: *Physical review letters* 110.4, p. 044802.

Rus, B., P. Bakule, D. Kramer, G. Korn, J. Green, J. Nóvak, M. Fibrich, F. Batysta, J. Thoma, J. Naylon, et al. (2013). “ELI-Beamlines laser systems: status and design options”. In: *High-Power, High-Energy, and High-Intensity Laser Technology; and Research Using Extreme Light: Entering New Frontiers with Petawatt-Class Lasers*. Vol. 8780. International Society for Optics and Photonics, 87801T.

Sahai, A. A., F. S. Tsung, A. R. Tableman, W. B. Mori, and T. C. Katsouleas (2013). “Relativistically induced transparency acceleration of light ions by an ultrashort laser pulse interacting with a heavy-ion-plasma density gradient”. In: *Physical Review E—Statistical, Nonlinear, and Soft Matter Physics* 88.4, p. 043105.

Sari, A., F. Carrel, C. Jouanne, A. Lyoussi, and O. Petit (2013). “Optimization of the photoneutron flux emitted by an electron accelerator for neutron interrogation applications using MCNPX and TRIPOLI-4 Monte Carlo codes”. In: *Proc. IPAC*, pp. 3630–3632.

Zulick, C., F. Dollar, V. Chvykov, J. Davis, G. Kalinchenko, A. Maksimchuk, G. Petrov, A. Raymond, A. Thomas, L. Willingale, et al. (2013). “Energetic neutron beams generated from femtosecond laser plasma interactions”. In: *Applied Physics Letters* 102.12.

Alvarez, J., J. Fernández-Tobias, K. Mima, S. Nakai, S. Kar, Y. Kato, and J. Perlado (2014). “Laser driven neutron sources: characteristics, applications and prospects”. In: *Physics Procedia* 60, pp. 29–38.

Hashimoto, S., O. Iwamoto, Y. Iwamoto, T. Sato, and K. Niita (2014). “New approach for nuclear reaction model in the combination of intra-nuclear cascade and DWBA”. In: *Nuclear Data Sheets* 118, pp. 258–261.

Hashimoto, S., Y. Iwamoto, T. Sato, K. Niita, A. Boudard, J. Cugnon, J.-C. David, S. Leray, and D. Mancusi (2014a). “New approach to description of (d, xn) spectra at energies below 50 MeV in Monte Carlo simulation by intra-nuclear cascade code with Distorted Wave Born Approximation”. In: *Nuclear Instruments and Methods in Physics Research Section B: Beam Interactions with Materials and Atoms* 333, pp. 27–41.

Hashimoto, S., Y. Iwamoto, T. Sato, K. Niita, A. Boudard, J. Cugnon, J.-C. David, S. Leray, and D. Mancusi (2014b). “New approach to description of (d, xn) spectra at energies below 50 MeV in Monte Carlo simulation by intra-nuclear cascade code with Distorted Wave Born Approximation”. In: *Nuclear Instruments and Methods in Physics Research Section B: Beam Interactions with Materials and Atoms* 333, pp. 27–41.

Hoffmeister, G. (2014). “Influencing laser-accelerated ions by femtosecond-laser desorption”. PhD thesis. Technische Universität Darmstadt.

Sakurai, J. J., J. Napolitano, et al. (2014). *Modern quantum mechanics*. Vol. 185. Pearson Harlow.

Soppera, N., M. Bossant, and E. Dupont (2014). “JANIS 4: an improved version of the NEA java-based nuclear data information system”. In: *Nuclear Data Sheets* 120, pp. 294–296.

Wagner, F. (2014). “Kontrolle des zeitlichen Kontrastes am Lasersystem PHELIX”. PhD thesis. Technische Universität.

Alejo, A., H. Ahmed, A. Green, S. Mirfayzi, M. Borghesi, and S. Kar (2015). “Recent advances in laser-driven neutron sources”. In: *Il nuovo cimento C* 38.6, pp. 1–7.

Khabaz, R. (2015). “Analysis of neutron scattering components inside a room with concrete walls”. In: *Applied Radiation and Isotopes* 95, pp. 1–7.

Mirfayzi, S., S. Kar, H. Ahmed, A. Krygier, A. Green, A. Alejo, R. Clarke, R. Freeman, J. Fuchs, D. Jung, et al. (2015). “Calibration of time of flight detectors using laser-driven neutron source”. In: *Review of Scientific Instruments* 86.7.

Mor, I., V. Dangendorf, M. Reginatto, F. Kaufmann, D. Vartsky, M. Brandis, D. Bar, and M. B. Goldberg (2015). “Reconstruction of material elemental composition using fast neutron resonance radiography”. In: *Physics Procedia* 69, pp. 304–313.

Ogawa, T., T. Sato, S. Hashimoto, D. Satoh, S. Tsuda, and K. Niita (2015). “Energy-dependent fragmentation cross sections of relativistic C 12”. In: *Physical Review C* 92.2, p. 024614.

Schnell, M., A. Sävert, I. Uschmann, O. Jansen, M. C. Kaluza, and C. Spielmann (2015). “Characterization and application of hard x-ray betatron radiation generated by relativistic electrons from a laser-wakefield accelerator”. In: *Journal of Plasma Physics* 81.4, p. 475810401.

Sciences, E. P. and E. S. W. G. .-. N. Group (2015). *Neutron scattering facilities in Europe - Present status and future perspectives*. URL: https://www.esfri.eu/sites/default/files/NGL_CombinedReport_230816_Complete%20document_0209-1.pdf.

Smith, M., H. Andrews, H. Ing, and M. Koslowsky (2015). “Response of the bubble detector to neutrons of various energies”. In: *Radiation Protection Dosimetry* 164.3, pp. 203–209.

Wenz, J., S. Schleede, K. Khrennikov, M. Bech, P. Thibault, M. Heigoldt, F. Pfeiffer, and S. Karsch (2015). “Quantitative X-ray phase-contrast microtomography from a compact laser-driven betatron source”. In: *Nature communications* 6.1, p. 7568.

Alejo, A., D. Gwynne, D. Doria, H. Ahmed, D. Carroll, R. Clarke, D. Neely, G. Scott, M. Borghesi, and S. Kar (2016). “Recent developments in the Thomson Parabola Spectrometer diagnostic for laser-driven multi-species ion sources”. In: *Journal of Instrumentation* 11.10, p. C10005.

Chen, F. F. (2016). *Introduction to Plasma Physics and Controlled Fusion*. 3rd Edition. Springer International Publishing.

Kunieda, S., O. Iwamoto, N. Iwamoto, F. Minato, T. Okamoto, T. Sato, H. Nakashima, Y. Iwamoto, H. Iwamoto, F. Kitatani, et al. (2016). *Overview of JENDL-4.0/HE and benchmark calculations*. Tech. rep. JAEA.

Rücker, U., T. Cronert, J. Voigt, J. Dabruck, P.-E. Doege, J. Ulrich, R. Nabbi, Y. Beßler, M. Butzek, M. Büscher, et al. (2016). “The Jülich high-brilliance neutron source project”. In: *The European Physical Journal Plus* 131.1, p. 19.

Garoby, R., A. Vergara, H. Danared, I. Alonso, E. Bargallo, B. Cheymol, C. Darve, M. Eshraqi, H. Hassanzadegan, A. Jansson, et al. (2017). “The European spallation source design”. In: *Physica Scripta* 93.1, p. 014001.

Kleinschmidt, A. (2017). “Investigation of a laser-driven neutron source with respect to different fields of application”. In.

Obst, L., S. Göde, M. Rehwald, F.-E. Brack, J. Branco, S. Bock, M. Bussmann, T. E. Cowan, C. B. Curry, F. Fiuza, et al. (2017). “Efficient laser-driven proton acceleration from cylindrical and planar cryogenic hydrogen jets”. In: *Scientific reports* 7.1, p. 10248.

Roth, M. and M. Schollmeier (2017). “Ion acceleration-target normal sheath acceleration”. In: *arXiv preprint arXiv:1705.10569*.

Sabate Gilarte, M. (2017). “The n_TOF-EAR2 facility at CERN: neutron flux determination and ^{33}S(n,α)^{30}Si cross section measurement; implications in BNCT.” PhD thesis. Universidad de Sevilla.

Dabruck, J. P. (2018). *Target Station Optimization for the High-Brilliance Neutron Source HBS: Simulation Studies Based on the Monte Carlo Method*. ISBN: 978-3030056384. Springer.

Faure, J., D. Gustas, D. Guénot, A. Vernier, F. Böhle, M. Ouillé, S. Haessler, R. Lopez-Martens, and A. Lifschitz (2018). “A review of recent progress on laser-plasma acceleration at kHz repetition rate”. In: *Plasma Physics and Controlled Fusion* 61.1, p. 014012.

Kleinschmidt, A., V. Bagnoud, O. Deppert, A. Favalli, S. Frydrych, J. Hornung, D. Jahn, G. Schaumann, A. Tebartz, F. Wagner, G. Wurden, B. Zielbauer, and M. Roth (May 2018). "Intense, directed neutron beams from a laser-driven neutron source at PHELIX". In: *Physics of Plasmas* 25.5. ISSN: 1089-7674. DOI: 10.1063/1.5006613.

Kuschel, S. (2018). "Erzeugung dichter Elektronenpulse mit Laser-Plasma-Beschleunigern für QED Experimente in hohen Feldern". PhD thesis. Dissertation, Jena, Friedrich-Schiller-Universität Jena, 2018.

Kuschel, S., M. Schwab, M. Yeung, D. Hollatz, A. Seidel, W. Ziegler, A. Sävert, M. Kaluza, and M. Zepf (2018). "Controlling the self-injection threshold in laser wakefield accelerators". In: *Physical Review Letters* 121.15, p. 154801.

Morrison, J. T., S. Feister, K. D. Frische, D. R. Austin, G. K. Ngirmang, N. R. Murphy, C. Orban, E. A. Chowdhury, and W. Roquemore (2018). "MeV proton acceleration at kHz repetition rate from ultra-intense laser liquid interaction". In: *New Journal of Physics* 20.2, p. 022001.

Nelson, R. O., S. C. Vogel, J. F. Hunter, E. B. Watkins, A. S. Losko, A. S. Tremsin, N. P. Borges, T. E. Cutler, L. T. Dickman, M. A. Espy, et al. (2018). "Neutron imaging at LANSCE—from cold to ultrafast". In: *Journal of Imaging* 4.2, p. 45.

Obst, L., J. Metzkes, S. Bock, G. Cochran, T. Cowan, T. Oksenhendler, P. Poole, I. Prencipe, M. Rehwald, C. Rödel, et al. (2018). "Single plasma mirror temporal contrast improvement with on-shot characterization". In: *Plasma Phys. Controlled Fusion* 60.5, p. 054007.

Poole, P. L., L. Obst, G. E. Cochran, J. Metzkes, H.-P. Schlenvoigt, I. Prencipe, T. Kluge, T. Cowan, U. Schramm, D. W. Schumacher, et al. (2018). "Laser-driven ion acceleration via target normal sheath acceleration in the relativistic transparency regime". In: *New Journal of Physics* 20.1, p. 013019.

Siders, C. (2018). *New architectures for pw-scale high peak power lasers scalable to near-mw average powers*. Tech. rep. Lawrence Livermore National Lab.(LLNL), Livermore, CA (United States).

Silano, J. and H. Karwowski (2018). "Near-barrier photofission in Th 232 and U 238". In: *Physical Review C* 98.5, p. 054609.

Speicher, M., D. Haffa, M. A. Haug, J. Bin, Y. Gao, J. Hartmann, P. Hilz, C. Kreuzer, F. H. Lindner, T. M. Ostermayr, et al. (2018). "Integrated double-plasma-mirror targets for contrast enhancement in laser ion acceleration". In: *Journal of Physics: Conference Series*. Vol. 1079. IOP Publishing, p. 012002.

Tebartz, A. S. (2018). "Kryogene Wasserstoff-und Deuteriumtargets zur Laserionenbeschleunigung". PhD thesis. Technische Universität.

(2019). DOI: 10.1038/s42254-019-0042-6. URL: http://dx.doi.org/10.1038/s42254-019-0042-6.

Demtröder, W. (2019). *Electrodynamics and Optics*. Springer. DOI: https://doi.org/10.1007/978-3-030-02291-4.

Gonsalves, A., K. Nakamura, J. Daniels, C. Benedetti, C. Pieronek, T. De Raadt, S. Steinke, J. Bin, S. Bulanov, J. Van Tilborg, et al. (2019). "Petawatt laser guiding and electron beam acceleration to 8 GeV in a laser-heated capillary discharge waveguide". In: *Physical review letters* 122.8, p. 084801.

Guan, Y., H. Yang, L. Duan, J. Zhang, X. Yuan, Z. He, X. Zhang, R. Hu, C. Lu, P. Ma, et al. (2019). "Measurement of fast neutrons with 238 U-coated fission chamber". In: *Radiation Detection Technology and Methods* 3, pp. 1–5.

Koning, A., D. Rochman, J.-C. Sublet, N. Dzysiuk, M. Fleming, and S. Van der Marck (2019). "TENDL: complete nuclear data library for innovative nuclear science and technology". In: *Nuclear Data Sheets* 155, pp. 1–55.

Matsuda, N., S. Kunieda, T. Okamoto, K. Tada, and C. Konno (2019). "ACE library of JENDL-4.0/HE". In: *Prog Nucl Sci Technol* 6, pp. 225–229.

Brack, F.-E., F. Kroll, L. Gaus, C. Bernert, E. Beyreuther, T. E. Cowan, L. Karsch, S. Kraft, L. A. Kunz-Schughart, E. Lessmann, et al. (2020). “Spectral and spatial shaping of laser-driven proton beams using a pulsed high-field magnet beamline”. In: *Scientific reports* 10.1, p. 9118.

Feng, J., C. Fu, Y. Li, X. Zhang, J. Wang, D. Li, C. Zhu, J. Tan, M. Mirzaie, Z. Zhang, et al. (2020). “High-efficiency neutron source generation from photonuclear reactions driven by laser plasma accelerator”. In: *High Energy Density Physics* 36, p. 100753.

Hamamatsu (2020). *Photomultiplier Tubes R2083, R3377*. https://www.hamamatsu.com/content/dam/hamamatsu-photonics/sites/documents/99_SALES_LIBRARY/etd/R2083_R3377_TPMH1227E.pdf. Accessed on Feb 05, 2024.

Huebl, A., M. Rehwald, L. Obst-Huebl, T. Ziegler, M. Garten, R. Widera, K. Zeil, T. E. Cowan, M. Bussmann, U. Schramm, et al. (2020). “Spectral control via multi-species effects in PW-class laser-ion acceleration”. In: *Plasma Physics and Controlled Fusion* 62.12, p. 124003.

ISO, I. O. f. S. (2020). *Series 1 freight containers — Classification, dimensions and ratings*. https://www.iso.org/-standard/76912.html. Accessed on Jul 10, 2024.

Maier, A. R., N. M. Delbos, T. Eichner, L. Hübner, S. Jalas, L. Jeppe, S. W. Jolly, M. Kirchen, V. Leroux, P. Messner, et al. (2020). “Decoding sources of energy variability in a laser-plasma accelerator”. In: *Physical Review X* 10.3, p. 031039.

Malka, V. (2020). “Proceedings of the 2019 CERN–Accelerator–School course on High Gradient Wakefiled Accelerators Sesimbra”. In: CERN. Portugal. URL: https://cas.web.cern.ch/previous-schools.

Mirfayzi, S., A. Yogo, Z. Lan, T. Ishimoto, A. Iwamoto, M. Nagata, M. Nakai, Y. Arikawa, Y. Abe, D. Golovin, et al. (2020). “Proof-of-principle experiment for laser-driven cold neutron source”. In: *Scientific Reports* 10.1, p. 20157.

Mizutani, R., Y. Abe, Y. Arikawa, J. Nishibata, A. Yogo, S. Mirfayzi, H. Nishimura, K. Mima, S. Fujioka, M. Nakai, et al. (2020). “The avalanche image intensifier panel for fast neutron radiography by using laser-driven neutron sources”. In: *High Energy Density Physics* 36, p. 100833.

Otake, Y. (2020). “RIKEN accelerator-driven compact neutron systems, RANS project and their capabilities”. In: *Neutron News* 31.2-4, pp. 32–36.

Patrizio, M. (2020). “Development of an Actively Cooled Large Aperture Laser Amplifier at the GSI Helmholtzzentrum”. PhD thesis. Technische Universität Darmstadt.

Rovige, L., J. Huijts, I. Andriyash, A. Vernier, V. Tomkus, V. Girdauskas, G. Raciukaitis, J. Dudutis, V. Stankevic, P. Gecys, et al. (2020). “Demonstration of stable long-term operation of a kilohertz laser-plasma accelerator”. In: *Physical Review Accelerators and Beams* 23.9, p. 093401.

Wenz, J. and S. Karsch (2020). “Proceedings of the 2019 CERN–Accelerator–School course on High Gradient Wakefiled Accelerators Sesimbra”. In: CERN. Portugal. URL: https://cas.web.cern.ch/previous-schools.

Zimmer, M. (2020). “Laser-Driven Neutron Sources-A Compact Approach to Non-Destructive Material Analysis”. PhD thesis.

Albert, F., M. Couprie, A. Debus, M. C. Downer, J. Faure, A. Flacco, L. A. Gizzi, T. Grismayer, A. Huebl, C. Joshi, et al. (2021). “2020 roadmap on plasma accelerators”. In: *New Journal of Physics* 23.3, p. 031101.

Eljen Technology, E. (2021). *Fast Timing Plastic Scintillator EJ-232, EJ-232Q*. https://eljentechnology.com/products/plasti scintillators/ej-232-ej-232q. Accessed on Feb 05, 2024.

Haghighat, A. (2021). *Monte Carlo methods for particle transport*. 2nd Edition. ISBN: 978-0367188054. CRC Press.

Kobayashi, T., S. Ikeda, Y. Otake, Y. Ikeda, and N. Hayashizaki (2021). “Completion of a new accelerator-driven compact neutron source prototype RANS-II for on-site use”. In: *Nuclear Instruments and Methods in Physics Research Section A: Accelerators, Spectrometers, Detectors and Associated Equipment* 994, p. 165091.

Salehi, F., M. Le, L. Railing, M. Kolesik, and H. Milchberg (2021). “Laser-accelerated, low-divergence 15-MeV quasimonoenergetic electron bunches at 1 kHz”. In: *Physical Review X* 11.2, p. 021055.

Shaw, J., M. Romo-Gonzalez, N. Lemos, P. King, G. Bruhaug, K. Miller, C. Dorrer, B. Kruschwitz, L. Waxer, G. Williams, et al. (2021). “Microcoulomb (0.7±0.4 0.2 μC) laser plasma accelerator on OMEGA EP”. In: *Scientific Reports* 11.1, p. 7498.

Ziegler, T., D. Albach, C. Bernert, S. Bock, F.-E. Brack, T. E. Cowan, N. P. Dover, M. Garten, L. Gaus, R. Gebhardt, I. Goethel, U. Helbig, A. Irman, H. Kiriyama, T. Kluge, A. Kon, S. Kraft, F. Kroll, M. Loeser, J. Metzkes-Ng, M. Nishiuchi, L. Obst-Huebl, T. Püschel, M. Rehwald, H.-P. Schlenvoigt, U. Schramm, and K. Zeil (Apr. 2021). “Proton beam quality enhancement by spectral phase control of a PW-class laser system”. In: *Scientific Reports* 11.1. ISSN: 2045-2322. DOI: 10.1038/s41598-021-86547-x.

Zimmer, M., S. Scheuren, T. Ebert, G. Schaumann, B. Schmitz, J. Hornung, V. Bagnoud, C. Rödel, and M. Roth (2021). “Analysis of laser-proton acceleration experiments for development of empirical scaling laws”. In: *Physical Review E* 104.4, p. 045210.

Aswal, D. K., P. S. Sarkar, and Y. S. Kashyap (2022). *Neutron Imaging: Basics, Techniques and Applications*. Springer.

Iwamoto, Y., S. Hashimoto, T. Sato, N. Matsuda, S. Kunieda, Y. Çelik, N. Furutachi, and K. Niita (2022). “Benchmark study of particle and heavy-ion transport code system using shielding integral benchmark archive and database for accelerator-shielding experiments”. In: *Journal of Nuclear Science and Technology* 59.5, pp. 665–675.

Kulesza, J. A., T. R. Adams, J. C. Armstrong, S. R. Bolding, F. B. Brown, J. S. Bull, T. P. Burke, A. R. Clark, R. A. A. Forster III, J. F. Giron, et al. (2022). *MCNP® code version 6.3. 0 theory & user manual*. Tech. rep. LA-UR-22-30006, Rev. 1. Los Alamos, NM, USA: Los Alamos National Laboratory.

Lai, Y. and Y. Yang (2022). “A Design for the High Yield Photoneutron Source Target Station”. In: *Materials* 15.21, p. 7674.

Laplace, T. A., B. L. Goldblum, J. A. Brown, G. LeBlanc, T. Li, J. J. Manfredi, and E. Brubaker (2022). “Modeling ionization quenching in organic scintillators”. In: *Materials Advances* 3.14, pp. 5871–5881.

Losko, A. S. and S. Vogel (2022). “3D isotope density measurements by energy-resolved neutron imaging”. In: *Scientific Reports* 12.1, p. 6648.

Papp, D., A. Necas, N. Hafz, T. Tajima, S. Gales, G. Mourou, G. Szabo, and C. Kamperidis (2022). “Laser Wakefield Photoneutron Generation with Few-Cycle High-Repetition-Rate Laser Systems”. In: *Photonics*. Vol. 9. 11. MDPI, p. 826.

Satoh, D. and T. Sato (2022). “Improvements in the particle and heavy-ion transport code system (PHITS) for simulating neutron-response functions and detection efficiencies of a liquid organic scintillator”. In: *Journal of Nuclear Science and Technology* 59.8, pp. 1047–1060.

Zimmer, M., S. Scheuren, A. Kleinschmidt, N. Mitura, A. Tebartz, G. Schaumann, T. Abel, T. Ebert, M. Hesse, Ş. Zähter, et al. (2022). “Demonstration of non-destructive and isotope-sensitive material analysis using a short-pulsed laser-driven epi-thermal neutron source”. In: *Nature communications* 13.1, p. 1173.

Barbiero, G., Y. Pfaff, M. Rampp, H. Wang, S. Klingebiel, C. Y. Teisset, R. Jung, A. H. Woldegeorgis, J. Brons, A. R. Maier, et al. (2023). “High-energy, high-average power multipass cell spectral broadening of a thin disk regenerative amplifier (Conference Presentation)”. In: *High-power, High-energy Lasers and Ultrafast Optical Technologies*. SPIE, PC125770C.

Bubble Technology Industries (2023). URL: http://www.bubbletech.ca.

Iwamoto, O., N. Iwamoto, S. Kunieda, F. Minato, S. Nakayama, Y. Abe, K. Tsubakihara, S. Okumura, C. Ishizuka, T. Yoshida, et al. (2023). “Japanese evaluated nuclear data library version 5: JENDL-5”. In: *journal of nuclear science and technology* 60.1, pp. 1–60.

Jalas, S., M. Kirchen, C. Braun, T. Eichner, J. Gonzalez, L. Hübner, T. Hülsenbusch, P. Messner, G. Palmer, M. Schnepp, et al. (2023). “Tuning curves for a laser-plasma accelerator”. In: *Physical Review Accelerators and Beams* 26.7, p. 071302.

Konno, C. (2023). “New JENDL-4.0/HE neutron and proton ACE files”. In: *Journal of Nuclear Science and Technology*, pp. 1–6.

Lelièvre, R., W. Yao, T. Waltenspiel, I. Cohen, A. Beck, E. Cohen, D. Michaeli, I. Pomerantz, D. C. Gautier, F. Trompier, et al. (2023). “A Comprehensive Characterization of the Neutron Fields Produced by the Apollon Petawatt Laser”. In: *arXiv preprint arXiv:2311.12653*.

Liu, L., X. Ouyang, R. Gao, P. Wan, and X. Ouyang (2023). “Latest developments in room-temperature semiconductor neutron detectors: Prospects and challenges”. In: *Science China Physics, Mechanics & Astronomy* 66.3, p. 232001.

Mans, T. G., J. Brons, T. Eidam, T. Metzger, C. Grebing, M. Tschernajew, E. Shestaev, J. Limpert, Y. Pfaff, G. Barbiero, et al. (2023). “Nonlinear post-compression of mJ-class ytterbium-based ultrafast laser pulses”. In: *Frontiers in Ultrafast Optics: Biomedical, Scientific, and Industrial Applications XXIII*. SPIE, PC124110R.

Millán-Callado, M. A. (2023). “Compact neutron sources for Nuclear Physics: from accelerator-based to laser-driven neutron beams”. PhD thesis. Universidad de Sevilla.

Pfaff, Y., G. Barbiero, M. Rampp, S. Klingebiel, J. Brons, C. Y. Teisset, H. Wang, R. Jung, J. Jaksic, A. H. Woldegeorgis, et al. (2023). “Nonlinear pulse compression of a 200 mJ and 1 kW ultrafast thin-disk amplifier”. In: *Optics Express* 31.14, pp. 22740–22756.

Rehwald, M., S. Assenbaum, C. Bernert, F.-E. Brack, M. Bussmann, T. E. Cowan, C. B. Curry, F. Fiuza, M. Garten, L. Gaus, et al. (2023). “Ultra-short pulse laser acceleration of protons to 80 MeV from cryogenic hydrogen jets tailored to near-critical density”. In: *Nature communications* 14.1, p. 4009.

Rehwald, M., S. Assenbaum, C. Bernert, C. B. Curry, M. Gauthier, S. Glenzer, S. Göde, C. Schoenwaelder, U. Schramm, F. Treffert, et al. (2023). “Towards high-repetition rate petawatt laser experiments with cryogenic jets using a mechanical chopper system”. In: *Journal of Physics: Conference Series*. Vol. 2420. IOP Publishing, p. 012034.

Sato, T., Y. Iwamoto, S. Hashimoto, T. Ogawa, T. Furuta, S.-I. Abe, T. Kai, Y. Matsuya, N. Matsuda, Y. Hirata, et al. (2023). “Recent improvements of the particle and heavy ion transport code system–PHITS version 3.33”. In: *Journal of Nuclear Science and Technology*, pp. 1–9.

Treffert, F. (2023). “High Repetition-Rate Laser-Driven Particle Generation–Towards High Flux Fast Neutron Sources”. PhD thesis. Technische Universität Darmstadt.

Yogo, A., Y. Arikawa, Y. Abe, S. Mirfayzi, T. Hayakawa, K. Mima, and R. Kodama (2023). “Advances in laser-driven neutron sources and applications”. In: *The European Physical Journal A* 59.8, p. 191.

Yogo, A., Z. Lan, Y. Arikawa, Y. Abe, S. Mirfayzi, T. Wei, T. Mori, D. Golovin, T. Hayakawa, N. Iwata, et al. (2023). “Laser-driven neutron generation realizing single-shot resonance spectroscopy”. In: *Physical Review X* 13.1, p. 011011.

Al Qaaod, A. A., M. Reginatto, M. Zbořil, and A. Zimbal (2024). “The contribution of the air and room scattered neutrons in the PTB calibration facility”. In: *Radiation Physics and Chemistry* 217, p. 111490.

American Physical Society, A. (2024). *What Is Plasma and Why Does It Matter?* https://engage.aps.org/dpp/resources/wha is-plasma. Accessed on Feb 15, 2024.

Bubble Technology Industries, B. (2024). *BDR-III – BUBBLE DETECTOR READER III*. https://bubbletech.ca/product/bdr-iii-bubble-detector-reader-iii/. Accessed on Feb 05, 2024.

Ghasemi, A., S. Mirzanejhad, and T. Mohsenpour (2024). “Flying focus laser wake field acceleration by donut shape pulse”. In: *Applied Physics B* 130.6, p. 105.

Luxium Solutions, S. (2024). *Plastic Fiber*. https://www.luxiumsolutions.com/radiation-detection-scintillators/fibers. Accessed on May 05, 2024.

Monzac, J., S. Smartsev, J. Huijts, L. Rovige, I. A. Andriyash, A. Vernier, V. Tomkus, V. Girdauskas, G. Raciukaitis, M. Mackevičiūtė, et al. (2024). “Optical ionization effects in kHz laser wakefield acceleration with few-cycle pulses”. In: *arXiv preprint arXiv:2406.17426*.

Proxi Vision, P. (2024). *Gated Cameras (Nanosecond Gatable Cameras)*. https://www.proxivision.de/product/nanosecon gateable-cameras/. Accessed on May 05, 2024.

Sato, T., Y. Iwamoto, S. Hashimoto, T. Ogawa, T. Furuta, S.-I. Abe, T. Kai, Y. Matsuya, N. Matsuda, Y. Hirata, et al. (2024). “Recent improvements of the particle and heavy ion transport code system–PHITS version 3.33”. In: *Journal of Nuclear Science and Technology* 61.1, pp. 127–135.

Saves, P., R. Lafage, N. Bartoli, Y. Diouane, J. Bussemaker, T. Lefebvre, J. T. Hwang, J. Morlier, and J. R. Martins (Feb. 2024). “SMT 2.0: A Surrogate Modeling Toolbox with a focus on hierarchical and mixed variables Gaussian processes”. In: *Advances in Engineering Software* 188, p. 103571. ISSN: 0965-9978. DOI: 10.1016/j.advengsoft.2023.103571.

Scheuren, S., T. Jäger, J. Kohl, S. Kuschel, T. F. Rösch, B. Schmitz, M. Zimmer, C. Rödel, and M. Roth (2024). “Scaling of laboratory neutron sources based on laser wakefield accelerated electrons using Monte Carlo Simulations”. In: *Accepted for publication in the European Physical Journal Plus*.

Scheuren, S., M. A. Millan-Callado, J. Kohl, T. Jäger, M. Roth, C. Rödel, A. Alejo, F. Kroll, K. Zeil, A. Junghans, C. Guerrero, and B. Schmitz (2024). “On the Use of Bubble Detectors at Laser-Driven Neutron Sources”. In: *Submitted to Review of Scientific Instruments*.

Schweizer, A. (2024). *Emissionsgrad von verschiedenen Werkstoofen und Oberflächen*. https://www.schweizer-fn.de/stoff/strahlungswaerme/strahlungswaerme.php. Accessed on Jul 05, 2024.

Surface Concept, G. (2024). *Single Anode Delayline Detectors*. https://www.surface-concept.com/detectors/single-anode-delayline-detectors/. Accessed on Mar 10, 2024.

Trumpf Scientific, G. (2024). *Dira Series*. https://www.trumpf-scientific-lasers.com/products/dira-series/. Accessed on Jun 05, 2024.

Ziegler, T., I. Göthel, S. Assenbaum, C. Bernert, F.-E. Brack, T. E. Cowan, N. P. Dover, L. Gaus, T. Kluge, S. Kraft, et al. (2024). “Laser-driven high-energy proton beams from cascaded acceleration regimes”. In: *Nature Physics*, pp. 1–6.

A. Appendix

A.1. Resolution functions for LiF

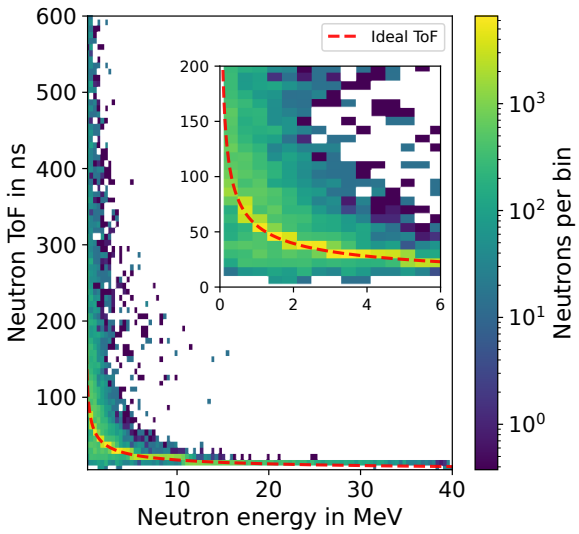

(a)

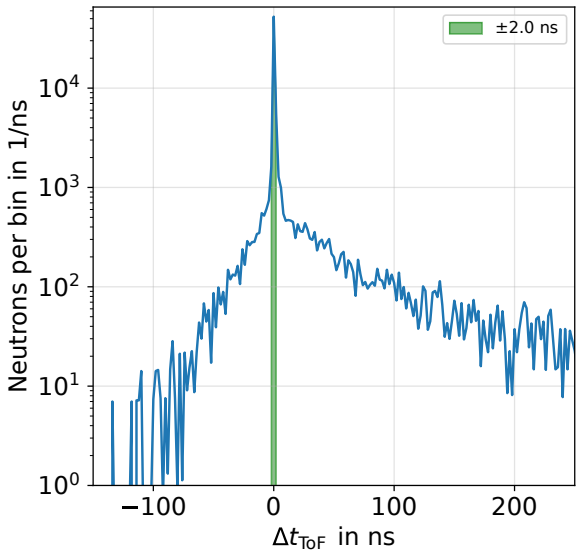

(b)

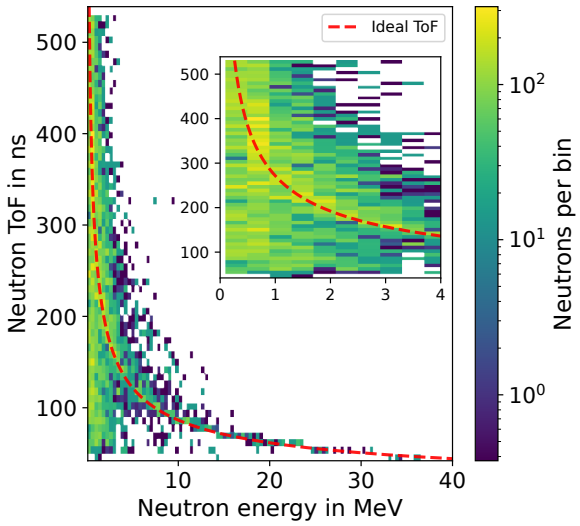

(c)

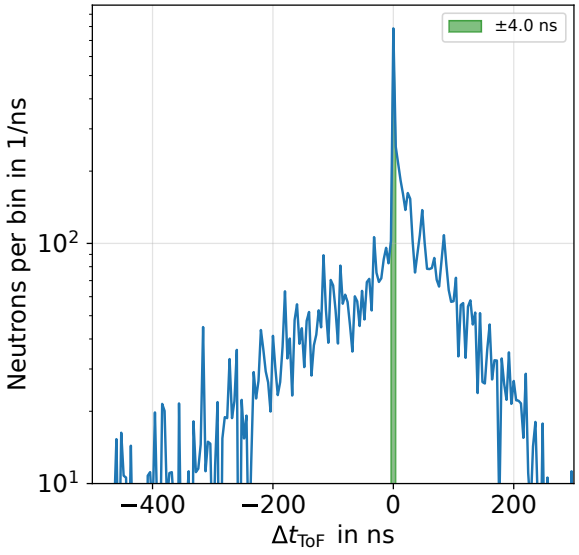

(d)

Figure A.1.: Results from PHITS simulations using a LiF catcher. (a) and (b) show the resolution function for the bubble detector placed at $0°$. (c) and (d) show the resolution function for the scintillator.

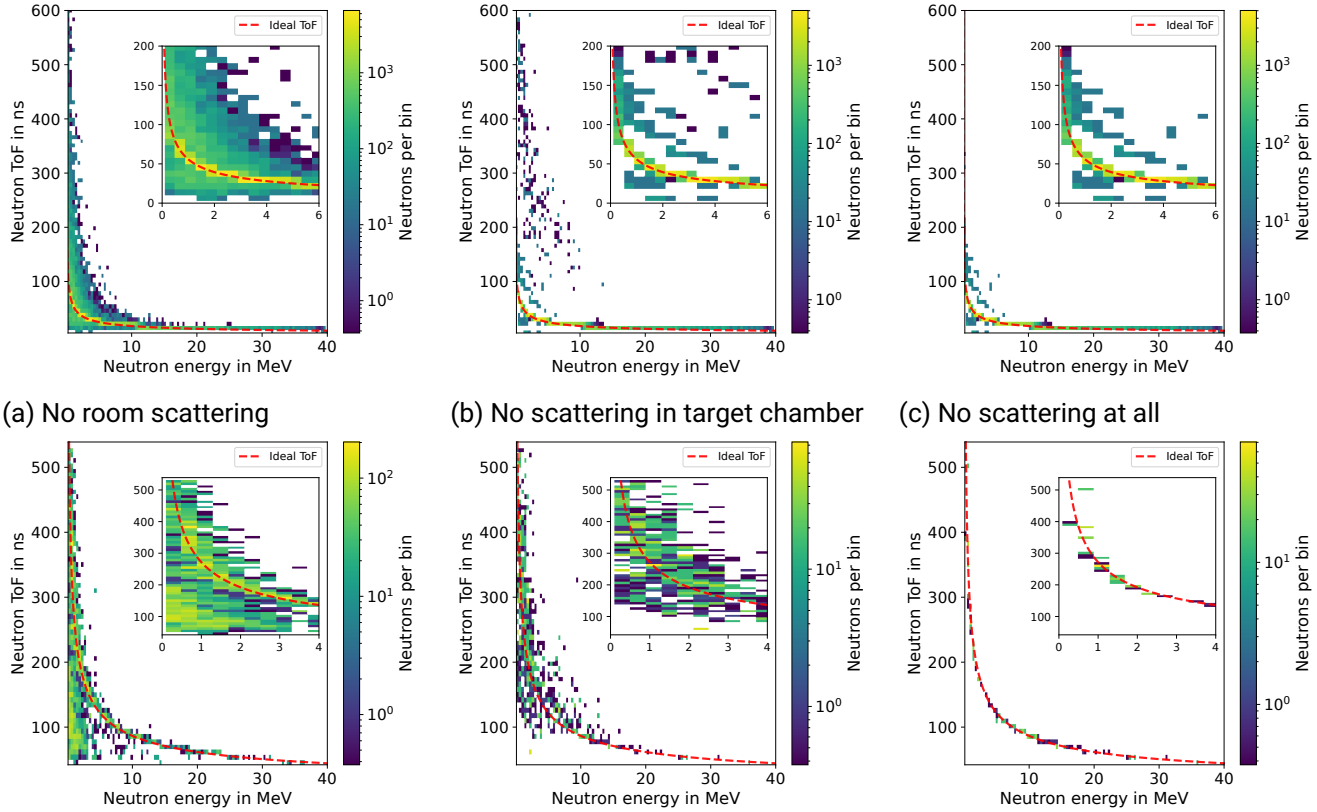

(a) No room scattering (b) No scattering in target chamber (c) No scattering at all

(d) No room scattering (e) No scattering in shielding (f) No scattering at all

Figure A.2.: Results are obtained from PHITS simulations using the LiF catcher. The top row shows results for the bubble detector at $0°$ with the bottoms row showing results for the scintillator. The figure contains the same information as Figure 4.21.

Acknowledgements

Zum Ende dieser Reise möchte ich mich bei allen bedanken, die mich während meiner Zeit als Doktorand unterstützt haben. Sei es fachlich oder auf einer persönlichen Ebene. Ohne euch hätte ich es nicht geschafft.

Ich möchte mich zu Beginn bei Markus für die Möglichkeit bedanken, dieses Thema bearbeiten zu dürfen. Insebsondere für die Freiheit bei der Bearbeitung meines Themas und für die Unterstützung während der Corona Zeit möchte ich mich bedanken. Ich möchte mich auch ausdrücklich dafür bedanken, dass du mir alle Mittel zur Verfügung gestellt hast, wie z. B. einen eigenen Simulationsrechner oder die Teilnahme an der DRACO Strahlzeit ermöglicht hast, um diese Arbeit abzuschließen. Dafür ein großes Danke! Auch möchte ich dir danken, dass ich die Möglichkeit hatte diese Arbeit in Kooperation mit Trumpf zusammen zu bearbeiten. Mein großer Dank gilt daher auch der Firma Trumpf.

In diesem Zusammenhang möchte ich mich insbesondere auch bei Max bedanken, welcher mich aus Trumpf heraus betreut hat. Die Einblicke die du mir in die Industrie ermöglicht hast haben mich definitiv bereichert und mir auch andere Herangehensweisen aufgezeigt. Dafür, für dein konstruktives und positives Feedback möchte ich dir sehr danken.

Ich möchte mich auch hier schon mal bei Stephan bedanken, dass er als zweiter Referent für meine Arbeit zur Verfügung steht und mir trotz seiner kurzen Zeit in Darmstadt doch sehr unter die Arme gegriffen hat und meine Arbeit bereichert hat. Ohne dich und Christian hätte ich vermutlich nie den Sprung zur Laser Wakefield Beschleunigung gemacht.

Ich möchte mich auch bei allen Kommilitonen und Kollegen bedanken, die mir unter die Arme gegriffen haben. Insbesondere möchte ich da Christian, Marc, Jonas und Gabriel hervorheben. Vielen Dank für eure Unterstützung durch Diskussionen bei Strahlzeiten, bei der Targetfertigung und einfach allem, was ihr zu dieser Arbeit beigetragen habt. Insbesondere Christian habe ich zu danken, der diese Arbeit doch maßgeblich beeinflusst hat, indem er mich mit zur DRACO Strahlzeit genommen hat

Bedanken möchte ich mich explizit auch noch bei Tim, Thomas R. und Benedikt bedanken, die sich seeeeehr viel Zeit genommen haben meine Arbeit oder meine Paper korrektur zu lesen. Ohne euch würde das alles ganz anders und definitiv nicht besser aussehen. Insbesondere möchte ich mich bei Tim bedanken, der mir geholfen hat die eine oder andere Strahlzeit besser zu überstehen als es ohne ihn der Fall gewesen wäre.

Außerdem gilt mein Dank auch noch allen Kollaborateuren, die mich unterstützt haben. Hier ist inbesondere die DRACO Kollaboration hervorzuheben. Daher vielen Dank an Llanlle, Carlos, Karl, Flo, Arnd und Roland. Ohne die Diskussionen mit euch. Ihr habt euch immer Zeit genommen und mich fachlich zu beraten, wenn ich es gebraucht habe. Dafür vielen Dank!

Ich muss mich auch ausdrücklich bei meiner Familie und meinen Freunden bedanken, einmal für ihre seelische und moralische Unterstützung, aber auch für das Verständnis, welches mir entgegengebracht wurde, wenn ich mal wieder lange gearbeitet habe. Besonders bedanken möchte ich mich bei meinen Eltern. Ohne eure Unterstützung hätte ich nicht nur diese Arbeit nicht geschafft, sondern das ganze Studium wäre vermutlich unmöglich gewesen. Dafür bin ich euch auf ewig dankbar. Auch wenn nur einer von euch die Fertigstellung dieser Arbeit miterleben kann, soweit ich doch das ihr beide immer bei mir seid und mich

unterstützt.

Zu guter Letzt gilt mein besonderer Dank noch Lea. Ohne dich, deine Unterstützung, deine Zuneigung und deine Witze hätte ich es nicht geschafft. Du hast mich durch meine schwierigsten Tage gebracht und mich immer wieder motiviert weiter zu machen. Dafür möchte ich mich aus tiefsten Herzen bei dir bedanken!

Education

Master of Science (Physics)
28.03.2018 - 28.01.2020

Technical University of Darmstadt
Karolinenplatz 5
64289 Darmstadt
Germany

Thesis: High repetition rate laser-driven neutron sources - A Monte Carlo based investigation

Bachelor of Science (Physics)
01.10.2014 - 27.03.2018

Technical University of Darmstadt
Karolinenplatz 5
64289 Darmstadt
Germany

Thesis: Theoretische Untersuchung der Wechselwirkung zwischen Rydberg-Atomen

General University Entrance Qualification
06.2014

Ernst-Ludwig-Schule
Am Solgraben 8
61231 Bad Nauheim
Germany

List of publications

Zimmer, M., **Scheuren, S.**, Kleinschmidt, A., Tebartz, A., Ebert, T., Ding, J., ... & Roth, M. (2020). Development of a setup for material identification based on laser-driven neutron resonance spectroscopy. In EPJ Web of Conferences (Vol. 231, p. 01006). EDP Sciences.

Hesse, M., Ebert, T., Zimmer, M., **Scheuren, S.**, Schaumann, G., & Roth, M. (2021). Spatially resolved online particle detector using scintillators for laser-driven particle sources. Review of Scientific Instruments, 92(9).

Zimmer, M., **Scheuren, S.**, Ebert, T., Schaumann, G., Schmitz, B., Hornung, J., ... & Roth, M. (2021). Analysis of laser-proton acceleration experiments for development of empirical scaling laws. Physical Review E, 104(4), 045210.

Zimmer, M., **Scheuren, S.**, Kleinschmidt, A., Mitura, N., Tebartz, A., Schaumann, G., ... & Roth, M. (2022). Demonstration of non-destructive and isotope-sensitive material analysis using a short-pulsed laser-driven epi-thermal neutron source. Nature communications, 13(1), 1173.

Schmitz, B., & **Scheuren, S.** (2024). Neutron Yield Predictions with Artificial Neural Networks: A Predictive Modeling Approach. Journal of Nuclear Engineering, 5(2), 114-127.

Scheuren, S., Jäger, T., Kohl, J., Kuschel, S., Rösch, T. F., Schmitz, B., ... & Roth, M. (2024). Scaling of laboratory neutron sources based on laser wakefield-accelerated electrons using Monte Carlo simulations. The European Physical Journal Plus, 139(8), 726.

Zimmer, M., Rösch, T.F., **Scheuren, S.**, Seupel, T., ... & Roth, M. (2024). Assessing the Potential of Upcoming Laser-Driven Neutron Sources and Their Practical Applications for Industry and Society. *Accepted for publication in The European Physical Journal Plus.*

Scheuren, S., Millan-Callado, M., Kohl, J., Jäger, T., Roth, M., Rödel, C., ... & Schmitz, B. (2024). On the Use of Bubble Detectors at Laser-Driven Neutron Sources. *Under review at Review of Scientific Instruments.*

Jäger, T., Tsviki, H., **Scheuren, S.**, Long, A., Losko, A., Wolfert, A., Zimmer, M., Roth, M., & Vogel, S. (2024). Energy-resolved MeV Neutron Analysis of a Mock-up Nuclear Waste Package. *Under review at Scientific Reports.*

Millan-Callado, M. A., **Scheuren, S.**, Junghans, A., Kroll, F., Schramm, U., Zeil, K., ... & Guerrero C. (2024). Single-event neutron time-of-flight spectroscopy with a petawatt-laser-driven neutron source. *In Preparation for Nature Communications.*